

**Biochemical and structural studies of NOD-like receptors  
and their inhibition by small molecule inhibitors**

**Dissertation**

zur

Erlangung des Doktorgrades (Dr. rer. nat.)

der

Mathematisch-Naturwissenschaftlichen Fakultät

der

Rheinischen Friedrich-Wilhelms-Universität Bonn

vorgelegt von

**Michael Marleaux**

aus

Düren

Bonn, 2022



Angefertigt mit Genehmigung der Mathematisch-Naturwissenschaftlichen Fakultät  
der Rheinischen Friedrich-Wilhelms-Universität Bonn

1. Gutachter: Prof. Dr. Matthias Geyer, Institut für Strukturbiologie, Universität Bonn
2. Gutachter: Prof. Dr. Walter Witke, Institut für Genetik, Universität Bonn

Tag der Promotion: 07.02.2023

Erscheinungsjahr: 2023



# Table of Contents

<b>Abstract</b> .....	<b>III</b>
<b>Acknowledgements</b> .....	<b>V</b>
<b>List of Abbreviations</b> .....	<b>VII</b>
<b>List of Figures</b> .....	<b>XVII</b>
<b>List of Tables</b> .....	<b>XIX</b>
<b>Chapter 1: Introduction</b> .....	<b>1</b>
1.1 The innate immune system .....	1
1.2 Pattern recognition receptors .....	3
1.3 The inflammasome – a multiprotein complex .....	21
1.4 The NOD domain and STAND ATPases .....	36
1.5 Pharmacological interference with the inflammasome pathway .....	42
1.6 Aims of the thesis .....	45
<b>Chapter 2: Biochemical and structural investigation of human NLRP9</b> .....	<b>47</b>
2.1 Initial functional analysis of human NLRP9 .....	48
2.2 Functional and structural investigation of the NLRP9 Pyrin domain.....	59
2.3 Discussion and Conclusion .....	74
<b>Chapter 3: Biochemical and structural investigation of human NLRP12</b> .....	<b>81</b>
3.1 Functional analysis of human NLRP12.....	82
3.2 Functional investigation of the NLRP12 Pyrin domain .....	93
3.3 Characterization of the NLRP12 NACHT domain .....	103
3.4 Discussion and Conclusion .....	113
<b>Chapter 4: Investigating NLRP3-specific small molecule inhibitors</b> .....	<b>121</b>
4.1 Molecular study of the NLRP3 inhibitor CRID3.....	122
4.2 Biochemical study of CRID3-containing probes and CRID3 analogs.....	141
4.3 Discussion and Conclusion .....	146
<b>5 Summary and Conclusion</b> .....	<b>153</b>
<b>6 Methods</b> .....	<b>159</b>
6.1 Molecular genetics .....	159
6.2 Expression of recombinant protein .....	166
6.3 Protein purification .....	168
6.4 Analytical methods.....	184
6.5 <i>In silico</i> methods.....	197
<b>7 Materials</b> .....	<b>199</b>
7.1 Chemicals .....	199
7.2 Consumables .....	199
7.3 Marker .....	200

7.4 Enzymes.....	200
7.5 Kits.....	200
7.6 Crystallization screens.....	201
7.7 Buffer and solutions .....	201
7.8 Bacterial strains and cell lines .....	202
7.9 Nucleic acids.....	202
7.10 Columns and affinity resins .....	205
7.11 Devices .....	206
7.12 Software .....	208
<b>References.....</b>	<b>211</b>
<b>List of Publications.....</b>	<b>239</b>

## Abstract

NOD-like receptors (NLRs) are innate immune sensors that can form inflammasomes driving pyroptosis. NLRP3 is the best studied member of the NLRs to date, and its dysregulation has been linked to human diseases relevant to our contemporary aging society. NLRP9 and NLRP12 are less well studied, but they have been described to form inflammasomes during infections. However, the existence of both inflammasomes has never been biochemically confirmed, and the mode of action of small molecule inhibitors is poorly understood. In this thesis, I show that recombinant human NLRP9 forms a defined and stable monomer in solution that is expected to adopt an ADP-bound and inactive conformation. Overexpression of NLRP9 in cells is not sufficient to nucleate ASC specks, which contradicts inflammasome formation and is in great contrast to NLRP3 or NLRP12. In line, the NLRP9 Pyrin domain (PYD) does not polymerize into filaments or interact with ASC. Based on a 1.95 Å crystal structure of NLRP9<sup>PYD</sup>, these observations can be explained by finding several mismatches in residues that would otherwise form interfaces in a filament.

Recombinant human NLRP12 associates with tubulin superfamily proteins, suggesting a role of microtubules in inflammasome formation. In addition, the detergent CHAPS can abrogate ATPase activity, which might indicate NLRP12 activation at lipid membranes. However, NLRP12<sup>PYD</sup> does not polymerize into filaments or interact with ASC, contradicting inflammasome formation. Based on a previously determined crystal structure of NLRP12<sup>PYD</sup>, this discrepancy was investigated but did not yield a clear explanation. Since recombinant NLRP12<sup>NACHT</sup> can assemble into oligomers, it is supposed that the NACHT domain acts as a scaffold for PYD polymerization. Crystals of NLRP12<sup>NACHT</sup> have been generated under various conditions, but have not yet diffracted sufficiently for structure determination.

The development of an optimized purification protocol allowed the determination of a 2.48 Å crystal structure of NLRP3 in complex with the prototypic inhibitor CRID3. NLRP3<sup>NACHT</sup> adopts an ADP-bound and inactive conformation stabilized by three intramolecular interdomain interfaces, each containing a disease-relevant mutation site. CRID3 binds NLRP3 with nanomolar affinity and inhibits ATPase activity. The binding site is formed by a cleft located on the backside of the Walker A motif and is also required to adopt the active state. In this way, CRID3 glues four subdomains of the NACHT

domain together with the transition LRR and locks NLRP3 in the inactive conformation. Binding experiments demonstrated that CRID3 can be extended at the eastern side without loss of interaction, and that substitution of the furan moiety could be an option for the development of advanced NLRP3 inhibitors with lower hepatotoxicity. I anticipate that these data could pave the way for rational and structure-guided drug optimization in the future not only for NLRP3 but for all NOD-like receptors.



## Acknowledgements

During my time as a PhD student, I have been accompanied and supported by a number of people to whom I would like to express my gratitude.

First of all, I would like to thank my supervisor Prof. Dr. Matthias Geyer for giving me the chance to work on such an interesting topic. Matthias, thank you for the freedom to pursue my own ideas and thank you for all the constructive discussions along the way. Thank you also for the opportunity to travel to conferences and for the invitations to the group retreats, which were always great occasions to have scientific conversations and make contacts. I would also like to thank you for the responsibilities I was able to take on beyond the PhD. In particular, I would like to mention the collaboration with IFM Therapeutics, which was an extremely valuable experience for me. I am convinced that it has been incredibly beneficial for my PhD projects but also for my further future. I would like to take this opportunity to thank all the people involved in this collaboration from IFM Therapeutics in Boston and Bonn. Thank you very much for your trust and for awakening my interest in drug development and research.

Many thanks also to Prof. Dr. Walter Witke, Prof. Dr. Peter Dörmann and Prof. Dr. Jan Hasenauer for joining my PhD committee.

I would also like to thank all current and former members of the working group. I am glad that we maintain a working atmosphere in which the work is really fun. Thank you for every professional but also private conversation. The PhD was certainly not an easy task but you have contributed so often that one does not despair. My special thanks go to Inga Hochheiser, Ines Kaltheuner, Anja Kopp, Dr. Karl Gatterdam, Dr. Jonas Möcking, Dr. Annemarie Steiner, Niels Schneberger, Dr. Martin Peter and Maximilian Schmitz. Thank you for all the mental support, all your help and for letting me "cry" to you in difficult times. Inga, thank you for all the measurements of samples at the electron microscope. Jonas and Anni, thank you for the FACS measurements you did for me. Karl, thank you for your support regarding SPR, even beyond your time with the group. Dr. Gregor Hagelüken and Dr. Kanchan Anand, thank you so much for all the help and support in structural biology. I am grateful that I was able to learn so much from you. Thank you also for your always open ear and constructive suggestions. Julia Hockling, thank you for your support with the purifications of NLRP3 protein. Thank you Dr. Rebecca Fusshöller (formerly Brinkschulte) for providing ASC-mCherry protein. A

special thank you also goes to my former master student Christoph Winterberg. Supervising you was really fun because you were always interested in the topic and gave your best. It was nice to watch your development and I am glad that you are now a PhD student with us yourself. Thank you also for your open ear and for your support, especially during the time I was writing this thesis.

I would also like to thank Dr. Anton Schmitz and Volkmar Fieberg for making my time at Caesar so much more enjoyable. Thank you for your support and thank you Volkmar for letting me learn so much about Aektas and columns. It was you who made me understand that these systems are actually not that complicated, but just pumps with a little bit around them. Thank you very much for this insight!

Thanks also to Prof. Dr. Eicke Latz and the entire Institute of Innate Immunity for the support during the time we were members of the institute but also beyond. Eicke, I would like to take this opportunity to thank you again for inviting me to the group retreats. They were fantastic experiences! My thanks also to Dr. Tomasz Prochnicki and the members of the core facility microscopy at the university clinics in Bonn, who instructed and supported me in the use of the microscopes. Thank you for your kind help!

Many thanks to Prof. Dr. Henning Urlaub and Monika Raabe for the mass spectrometric measurement of protein samples. Furthermore, I would like to thank all cooperation partners. At this point a special thank you to Prof. Dr. Michael Gütschow and Tim Keuler for the great cooperation on such interesting collaborative projects and the trust they have placed in me. It was really a pleasure!

I would also like to thank the beamline scientists at DESY and SLS for the nice briefing and the quick support in case of problems.

Finally, I would like to say a special thank you to my friends and family who have been incredibly supportive throughout this time. You gave me the support and confidence I needed. Grandma, unfortunately you passed away during my PhD years but I thank you for all the motivational talks. Mom and Dad, you always supported me and made me feel proud of myself. You always found the right words at the right time and made sure I never gave up. Thank you for everything! Patrick and Niclas, I am very happy to have you as brothers. We have actually always supported each other unconditionally and I am very grateful for that. Nora, as my girlfriend you probably got the most frustration during the whole time. I am very grateful to you for enduring it and bearing all the burdens together with me. You supported me in every way throughout and were always interested in my work. I could not have asked for more support. THANK YOU!

## List of Abbreviations

&	and
%	percent
°	degrees
°C	degrees Celsius
±	plus, minus
<	less than
>	greater than
~	approximately
≈	approximately equal
≥	greater or equal
2pRNA	5'-diphosphate dsRNA
3pRNA	5'-triphosphate dsRNA
Å	Angstrom (0.1 nm)
A <sub>x</sub>	absorbance at x nm
A/B	Walker A/B
aa	amino acids
AAA+	ATPases associated with diverse cellular activities
ABC	ATP binding cassette
ABRO1	Abraxas brother 1
AC	affinity chromatography
AD	acidic transactivation domain
ADP	adenosine diphosphate
AIM2	absent in melanoma 2
ALR	AIM2-like receptor
AMP	adenosine monophosphate
AMP-PCP	adenylyl methylenediphosphonate
AMP-PNP	adenylyl imidodiphosphate
Amp <sup>R</sup>	ampicillin resistance
ANOVA	analysis of variance
AP-1	activator protein 1
APAF-1	apoptotic protease activating factor-1
APBS	adaptive Poisson-Boltzmann solver
APS	ammonium persulfate
ARIH2	Ariadne homolog 2
ARMS	Ankyrin repeat-rich membrane spanning
ASC	apoptosis-associated speck-like protein containing a CARD
ASCE	additional strand, conserved glutamate
ATG16L1	autophagy related 16 like 1
ATP	adenosine triphosphate
ATPase	adenosine triphosphatase
ATP <sub>γ</sub> S	adenosine 5'-O-(3-thio)triphosphate
B-cell	bone marrow lymphocytes
BBB	blood brain barrier
BFP	blue fluorescent protein
BIR	baculovirus inhibitor of apoptosis protein repeat
Blimp-1	B lymphocyte-induced maturation protein 1
BMDMs	bone marrow-derived macrophages
bp	base pair

BRCA2	breast cancer 2
BRCC	BRCA2 containing complex subunit
BRET	bioluminescence resonance energy transfer
BSA	bovine serum albumin
BTK	Bruton's tyrosine kinase
bZIP	basic leucine zipper
C	carbon
c	concentration
C-term	carboxy-terminal, carboxy terminus
Ca <sup>2+</sup> -NFAT	calcineurin-nuclear factor of activated T-cells
CANTOS	Canakinumab anti-inflammatory thrombosis outcome study
CAPS	cryopyrin-associated periodic syndrome
CAPS, chemical	N-cyclohexyl-3-aminopropanesulfonic acid
CARD	caspase activation and recruitment domain
CARD9	CARD protein 9
CASP1	caspase-1 gene
Cbl-b	Casitas B-lineage lymphoma b
CC	correlation coefficient
CD14	cluster of differentiation 14
CED	<i>Caenorhabditis</i> cell death abnormal
cGAMP	cyclic GMP-AMP
cGAS	cyclic GMP-AMP synthase
CHAPS	3-[(3-cholamidopropyl)dimethylammonio]-1-propanesulfonate
cIAP1	cellular inhibitor of apoptosis protein
CIITA	class II, major histocompatibility complex, transactivator
CINCA	chronic infantile neurological cutaneous articular syndrome
CLR	C-type lectin receptor
cm	centimeter
CMD	carboxymethyl dextran
CMOS	complementary metal-oxide semiconductor
CMV	cytomegalovirus
cn	canonical
CNS	central nervous system
COP	CARD-only protein
COVID-19	coronavirus disease 2019
COX-2	cyclooxygenase type 2
CpG	5'-cytosine-phosphate-guanine-3'
CRD	carbohydrate recognition domain
CRID	cytokine release inhibitory drug
cryo	cryogenic
CSNK1K1	casein kinase I $\alpha$ 1
CTD	C-terminal domain
CTLD	C-type lectin-like domain
Cul1	Cullin-1
CV	column volume
d	distance
Da	Dalton
DAG	diacylglycerol
DAMP	damage-associated molecular pattern
DARK	<i>Drosophila</i> Apaf-1 related killer
DARTS	drug affinity responsive target stability
dATP	deoxyadenosine triphosphate

DC	dendritic cell
DC-SIGN	DC-specific intercellular adhesion molecule-3-grabbing non-integrin
DD	death domain
Dectin	dendritic cell-associated C-type lectin
DESY	Deutsches Elektronen Synchrotron
DHX	DEAH box helicase
DISC	death inducing signaling complex
DLS	dynamic light scattering
DMEM	Dulbecco's modified eagle's medium
DMSO	dimethyl sulfoxide
DNA	deoxyribonucleic acid
DNase	deoxyribonuclease
dNTP	deoxynucleotide triphosphates
DPBS	Dulbecco's PBS
DPP9	dipeptidyl peptidase 9
DRD1	dopamine D1 receptor
ds	double-stranded
dTGN	dispersed trans-Golgi network
DTT	dithiothreitol
DUB	deubiquitinating enzyme
E-S	glutamate switch
<i>E. coli</i>	<i>Escherichia coli</i>
e.g.	example given
$e_c$	charge of electron
EDTA	ethylenediaminetetraacetic acid
EEA1	endosome autoantigen 1
EM	electron microscopy
EphA2	ephrin type-A receptor 2
ER	endoplasmatic reticulum
ESCRT	endosomal sorting complexes required for transport
et al.	et alia, et alii, et aliae
etc.	et cetera
FADD	Fas-associated death domain protein
FAF-1	Fas-associated factor 1
FBS	fetal bovine serum
FBXL2	F-box/LRR-repeat protein 2
FBXO3	F-box only protein 3
Fc	flow cell
$F_{calc}$ , $F_c$	Structure factor (calculated)
FCAS	familial cold autoinflammatory syndrome
FDA	food and drug administration
FIIND	function to find domain
FISNA	fish-specific NACHT-associated domain
FMF	familial Mediterranean fever
$F_{obs}$ , $F_o$	structure factor (observed)
FPLC	fast protein liquid chromatography
fw	forward
GAP	GTPase activating protein
Gent <sup>R</sup>	gentamycin resistance
GFP	green fluorescent protein
GSDMD	gasdermin D
GST	glutathione-S-transferase

GTPases	guanosine triphosphatases
h	hour
HA	human influenza hemagglutinin
HAMPs	homeostasis-altering molecular processes
HD	helical domain
HEK	human embryonic kidney
HEPES	4-(2-hydroxyethyl)-1-piperazineethanesulfonic acid
HET-E	Incompatibility locus protein from <i>Podospora anserina</i>
HIN	hematopoietic expression, interferon-inducible nature, and nuclear localization
HIV	human immunodeficiency virus
hNLRP	human NLRP
HPLC	high performance liquid chromatography
HSP	heat shock protein
HSV-1	Herpes simplex virus type 1
Hz	hertz
I	intensity
i.e.	id est
IC <sub>50</sub>	half maximal inhibitory concentration
iE-DAP	$\gamma$ -D-glutamyl- <i>meso</i> -diaminopimelic acid
IEC	intestinal epithelial cell
IFI16	IFN- $\gamma$ -inducible protein 16
IFN	interferon
IFNAR	IFN- $\alpha/\beta$ receptor
Ig	immunoglobulin
IKK	I $\kappa$ B kinase
IKKi	IKK-related kinase
IL	interleukin
IL-18BP	IL-18 binding protein
IL-R	IL receptor
iNOS	inducible nitric oxide synthase
IPTG	isopropyl- $\beta$ -D-thiogalactopyranoside
IRAK	IL-1R associated kinase
IRES	internal ribosomal entry site
IRF	interferon regulatory factor
ISM	initiator-specific motif
ITAM	immunoreceptor tyrosine-based activation motif
ITIM	immunoreceptor tyrosine-based inhibitory motif
JNK1	c-Jun N-terminal kinase 1
k <sub>a</sub>	second-order association constant
KAP	acronym for Kidins220/ARMS and PifA
KAT5	lysine acetyltransferase 5
K <sub>av</sub>	partition coefficient
k <sub>B</sub>	Boltzmann constant
kb	kilobase
kbp	kilobase pair
K <sub>D</sub>	equilibrium dissociation constant
k <sub>d</sub>	first-order dissociation constant
kDa	kilodalton
kV	kilovolt
L	liter
l	length
LB	lysogeny broth

LBP	LPS-binding protein
LGP2	laboratory of genetics and physiology 2
LLPS	liquid-liquid phase separation
LPS	lipopolysaccharide
LRR	leucine-rich repeat
LTA	lipoteichoic acid
LTR	long terminal repeat
LUBAC	linear ubiquitination assembly complex
M	marker or molar
mA	milliampere
MALS	multi angle light scattering
MAMs	mitochondria-associated ER membranes
MAPK	mitogen-activated protein kinase
MAPL	mitochondrial-anchored protein ligase
MARCH7	membrane-associated RING finger protein 7
mAU	milli-absorbance unit
MAVS	mitochondrial antiviral-signaling protein
MBP	maltose binding protein
mCherry	monomeric Cherry
mCitrine	monomeric Citrine
MCS	multiple cloning site
MD-2	myeloid differentiation factor 2
MDA5	melanoma differentiation-associated protein 5
MDP	muramyl dipeptide
MES	2-(N-morpholino)ethanesulfonic acid
mg	milligram
MHC	major histocompatibility complex
min	minute
Mincle	macrophage inducible Ca <sup>2+</sup> -dependent lectin receptor
ml	milliliter
mM	millimolar
mMBP	mutant MBP
Mn	number average molar mass
mNLRP	mouse NLRP
MTOC	microtubule organizing center
MTS	mitochondrial targeting sequence
MW	molecular weight, weight average molar mass
MWCO	molecular weight cut-off
MWS	Muckle-Wells syndrome
MyD88	myeloid differentiation primary response 88
n	number of experiments
N-GSDMD	N-terminal cleavage fragment of GSDMD
N-term	amino-terminal, amino terminus
NACHT	acronym for NAIP, CIITA, HET-E, and TP1
NAIP	NLR family apoptosis inhibitory protein
nanoDSF	nano-format differential scanning fluorimetry
NASH	nonalcoholic steatohepatitis
NBD	nucleotide binding domain
NEK7	NIMA-related kinase 7
NF-κB	nuclear factor kappa B
ng	nanogram
NIK	NF-κB-inducing kinase

NK cell	natural killer cell
NKT cell	natural killer T cell
NLR	NOD-like receptor
NLRA	NLR family acidic transactivating domain containing protein
NLRB	NLR family BIR domain containing protein
NLRC	NLR family CARD containing protein
NLRP	NLR family PYD containing protein
NLRX	NLR family protein containing an unknown N-terminal effector domain
NLS	nuclear localization signal
nm	nanometer
nM	nanomolar
NMR	nuclear magnetic resonance
NO	nitric oxide
NOD	nucleotide-binding oligomerization domain
NOMID	neonatal-onset multisystem inflammatory disorder
ns	not significant
Nsp5	nonstructural protein 5
NTA	nitritriacetic acid
NTase	nucleotidyltransferase
NTPases	nucleoside-triphosphatase
OD	optical density
OptiMEM	Improved serum-free minimal essential medium
P	probability
P2X7	P2X purinoceptor 7
PAGE	polyacrylamide gel electrophoresis
PAK1	PI-3K/Rac1/p21-activated kinase 1
PAMP	pathogen-associated molecular pattern
PBMC	peripheral blood mononuclear cells
PBS	phosphate-buffered saline
PCR	polymerase chain reaction
PDB	protein data bank
PE	polyethylene
PEG	polyethylene glycol
PEI	polyethylenimine
PELI2	Pellino2
PGE2	prostaglandin-E2
PGK	3-phosphoglycerate kinase
PGN	peptidoglycan
pH	potentia hydrogenii
pI	isoelectric point
PIDD	p53-induced protein with a death domain
pKa	acid dissociation constant
PKN/D	protein kinase N/D
PLA2	phospholipase A2
PLK4	polo-like kinase 4
PMSF	phenylmethylsulfonylfluoride
POP	PYD-only protein
PP2A	protein phosphatase 2A
PRR	pattern recognition receptor
PSTPIP1	proline serine threonine phosphatase interacting protein 1
PtdIns4P	phosphatidylinositol-4-phosphate
PTEN	phosphatase and tensin homolog



PTM	post-translational modification
PTPase	protein tyrosine phosphatase
PTPN22	protein tyrosine phosphatase non-receptor type 22
PYD	Pyrin domain
Pyk2	proline-rich tyrosine kinase 2
R factor/value	residual factor/value
R protein	resistance protein
R-F	arginine finger
RAF-1	rapidly accelerated fibrosarcoma 1
RD	repressor domain
rev	reverse
$r_H$	hydrodynamic radius
Rho	Ras homolog
RI	refractive index
RIG-I	retinoic acid-inducible gene-I
RING	really interesting new gene
RIPK	receptor-interacting serine/threonine-protein kinase
RLR	RIG-I-like receptor
$R_{max}$	maximum response
RMSD	root-mean-square deviation
RNA	ribonucleic acid
RNF	RING finger protein
ROS	reactive oxygen species
rpm	revolutions per minute
RT	room temperature
RU	response unit
S-I	sensor I
s, sec	second
SA	streptavidin
SARS-CoV-2	severe acute respiratory syndrome coronavirus 2
SD	standard deviation
SDS	sodium dodecyl sulfate
SEC	size-exclusion chromatography
SEM	standard error of the mean
SENP	SUMO-specific protease
<i>Sf9</i>	<i>Spodoptera Frugiperda</i> 9
SHP	Src homology region 2 domain-containing phosphatase
SIRT2	sirtuin 2
SLS	Swiss Light Source
SMILES	simplified molecular input line entry specification
SMOC	supramolecular organizing center
SPR	surface plasmon resonance
ss	single-stranded
STAND	signal transduction ATPases with numerous domains
STING	stimulator of IFN genes
SUMO	small ubiquitin-like modifier
SUP	supernatant
Syk	spleen tyrosine kinase
T	temperature
T-cell	thymus lymphocytes
T3SS	type III bacterial secretion system
TAE	tris-acetate-EDTA

TAK	TGF- $\beta$ -activated kinase
TBA-Br	tetrabutylammonium bromide
TBK1	TANK-binding kinase
TCEP	tris(2-carboxyethyl)phosphine
TEM	transmission electron microscope
TEMED	tetramethyl ethylenediamine
Tet	tetracycline
TEV	tobacco etch virus
TGF	transforming growth factor
Th	T helper
THP1	human leukemia monocytic cell line
TIR	Toll-interleukin-1 receptor
TIRAP	Toll/interleukin-1 receptor domain-containing adapter protein
TLR	Toll-like receptor
™	trademark
T <sub>m</sub>	melting temperature
T <sub>n</sub>	transposon
TNF	tumor necrosis factor
TNFR	TNF receptor
TOFIE	time-of-flight inflammasome activation method
TP1	telomerase-associated protein 1
tr	transition
TRAF	TNF-receptor associated factor
TRAM	TRIF-related adaptor molecule
TRAPS	TNF receptor-associated periodic syndrome
TRIF	TIR-domain-containing adapter-inducing interferon- $\beta$
TRIM	tripartite motif containing protein
Tris	tris(hydroxymethyl)aminomethane
TUB	tubulin
U	units
UBA	ubiquitin-associated domain
UPA	acronym for UNC5, PIDD, and Ankyrins
USP	ubiquitin-specific peptidase
UT	untreated
UV	ultraviolet
V	volt
v/v	volume for volume
V <sub>0</sub> , V <sub>1</sub> , V <sub>2</sub>	viral stocks
VDR	vitamin D receptor
V <sub>e</sub> , V <sub>c</sub> , V <sub>0</sub>	peak retention volume, total column volume, void volume
Vis	visible spectroscopy
w/	with
w/o	without
w/v	weight for volume
w/w	weight for weight
WHD	winged helix domain
x g	times g-force
X-gal	5-bromo-4-chloro-3-indolyl $\beta$ -D-galactopyranoside
X-ray	roentgen radiation
ZAK $\alpha$	zipper-sterile- $\alpha$ -motif kinase
ZU5	acronym for ZO-1 and UNC5
$\alpha$	alpha, alpha helix

$\beta$	beta, beta strand
$\beta$ ME	$\beta$ -mercaptoethanol
$\gamma$	gamma
$\Delta$	delta, difference, without
$\varepsilon$	extinction coefficient
$\eta$	$3_{10}$ -helix
$\lambda$	wavelength
$\mu$ g	microgram
$\mu$ l	microliter
$\mu$ M	micromolar
$\mu$ m	micrometer
$\sigma$	sigma

In general, elements and their ions as well as chemicals, including nucleotides and amino acids are abbreviated according to the IUPAC nomenclature.



## List of Figures

Figure 1-1: Toll-like receptors and their signaling pathways.....	6
Figure 1-2: The human NOD-like receptor family and functions in innate immunity .....	9
Figure 1-3: Nod-like receptors and their signaling .....	14
Figure 1-4: Current model of canonical inflammasome formation.....	23
Figure 1-5: PYD and CARD filaments formed by inflammasome components.....	33
Figure 1-6: The class of STAND ATPases.....	36
Figure 1-7: Conformational change and oligomerization of NLRC4 .....	39
Figure 2-1: Sequence alignment of NLRP3 and NLRP9.....	51
Figure 2-2: Analysis of ASC speck formation in cells overexpressing NLRP9.....	53
Figure 2-3: Purification and analysis of human NLRP9.....	54
Figure 2-4: Thermal destabilization of NLRP9 in the presence of ATP .....	56
Figure 2-5: Dimerization of NLRP9 in the presence of ATP .....	57
Figure 2-6: Analysis of NLRP9 using electron microscopy.....	59
Figure 2-7: Purification of human NLRP9 <sup>PYD</sup> protein .....	61
Figure 2-8: Molecular dispersion of recombinant NLRP9 <sup>PYD</sup> protein .....	62
Figure 2-9: Analysis of PYD polymerization and ASC speck formation in cells.....	63
Figure 2-10: Crystals and diffraction image of human NLRP9 <sup>PYD</sup> .....	65
Figure 2-11: Crystal structure of human NLRP9 <sup>PYD</sup> .....	67
Figure 2-12: Molecular characteristics of the NLRP9 <sup>PYD</sup> .....	68
Figure 2-13: Conformational analysis of NLRP9 <sup>PYD</sup> .....	70
Figure 2-14: Structural comparison of NLRP9 <sup>PYD</sup> with filament-forming PYDs.....	71
Figure 2-15: Molecular analysis of ASC nucleation capability of NLRP9 <sup>PYD</sup> .....	73
Figure 3-1: Sequence alignment of NLRP3 and NLRP12.....	84
Figure 3-2: Analysis of ASC speck formation in cells overexpressing NLRP12.....	86
Figure 3-3: Purification and electron microscopy of human NLRP12.....	87
Figure 3-4: ATPase and adenylate kinase activity of human NLRP12.....	90
Figure 3-5: ATPase activity of mutant NLRP12.....	91
Figure 3-6: Purification of human NLRP12 <sup>PYD</sup> .....	94
Figure 3-7: Molecular dispersion of recombinant NLRP12 <sup>PYD</sup> .....	95

Figure 3-8: Analysis of ASC interaction and PYD polymerization in cells .....	96
Figure 3-9: Conformational analysis of NLRP12 <sup>PYD</sup> .....	98
Figure 3-10: Structural comparison of NLRP12 <sup>PYD</sup> with filament-forming PYDs.....	99
Figure 3-11: Purification and electron microscopy of the NLRP12 <sup>PYD</sup> W45R mutant...	101
Figure 3-12: Molecular analysis of ASC nucleation capability of NLRP12 <sup>PYD</sup> .....	102
Figure 3-13: Purification of NLRP12 constructs containing the NACHT domain .....	104
Figure 3-14: Spontaneous oligomerization of monomeric NLRP12 <sup>NACHT</sup> .....	105
Figure 3-15: Effect of nucleotides on NLRP12 <sup>NACHT</sup> oligomerization .....	107
Figure 3-16: Binding study of the NLRP3-specific inhibitor CRID3 on NLRP12 .....	109
Figure 3-17: Purification of NLRP12 <sup>NACHT</sup> protein after buffer optimization .....	110
Figure 3-18: Purification of NLRP12 <sup>NACHT</sup> with cleaved MBP affinity tag.....	112
Figure 4-1: Purification of NLRP3 <sup>NACHT</sup> .....	124
Figure 4-2: Binding study of the inhibitor CRID3 to NLRP3 .....	126
Figure 4-3: Crystal forms and diffraction image of human NLRP3 <sup>NACHT</sup> protein.....	127
Figure 4-4: High-resolution crystal structure of the NLRP3-CRID3 complex .....	130
Figure 4-5: Conformation of the NLRP3-CRID3 complex.....	132
Figure 4-6: Interdomain interactions and CAPS mutants in the NLRP3 NACHT domain .....	134
Figure 4-7: The CRID3 binding site in NLRP3 .....	135
Figure 4-8: Mutational study on the CRID3 binding site in NLRP3 .....	137
Figure 4-9: The polybasic cluster and nucleotide binding site of NLRP3.....	139
Figure 4-10: CRID3 binding site in the active state and comparison with NLR family members .....	141
Figure 4-11: CRID3-containing probes and CRID3 analogs.....	142
Figure 4-12: Binding study of CRID3-containing probes.....	143
Figure 4-13: Binding study of CRID3 analogs.....	145

## List of Tables

Table 2-1: Crystallographic data collection and refinement statistics of NLRP9 <sup>PYD</sup> .....	66
Table 4-1: Crystallographic data collection and refinement statistics of NLRP3 <sup>NACHT</sup> ..	129
Table 6-1: Reaction mix for standard and mutagenesis PCR.....	159
Table 6-2: Protocol for standard PCR .....	159
Table 6-3: Reaction mix for restriction enzyme digestion.....	160
Table 6-4: Reaction mix for ligation of DNA .....	161
Table 6-5: Protocol for mutagenesis PCR .....	162
Table 6-6: Usage of antibiotics .....	162
Table 6-7: Subcloning strategies for the preparation of expression vectors .....	164
Table 6-8: Recipe for the preparation of polyacrylamide gels .....	184
Table 7-1: Amplification primers for subcloning .....	203
Table 7-2: Primers for site-directed mutagenesis .....	203
Table 7-3: Primers used in Sanger sequencing.....	204
Table 7-4: DNA template vectors .....	205
Table 7-5: Destination vectors .....	205
Table 7-6: Columns and resins used for affinity chromatography .....	205
Table 7-7: Gel filtration and reversed phase columns .....	206





# Chapter 1: Introduction

## 1.1 The innate immune system

A major challenge for all living organisms is to counteract diverse threats with the potential to compromise cellular homeostasis. These include cellular stress, malfunction, injury, and infection (Medzhitov, 2008). Through billions of years of evolution, the immune system evolved as a network of biological processes that enable the host to eliminate diverse microbial pathogens and abnormal or damaged cells (Marshall et al., 2018; Paludan et al., 2021). Notably, the human skin, gut, and lung collectively form a large surface area (estimated  $> 110 \text{ m}^2$ , (Gallo, 2017)) that is permanently exposed to potentially harmful microbes (including bacteria, fungi, and parasites), viruses, and toxins (Marshall et al., 2018). However, only a limited number of these contacts will effectively cause disease symptoms. This is due to the great efficacy of the vertebrate immune system, which is commonly subdivided into innate and adaptive branches (Murphy, 2017). Both branches are activated through recognition of pathogens via mainly two types of receptor systems: The germline-encoded and less specific pattern recognition receptors (PRRs), which initiate immediate innate immune responses; and somatically recombined antigen-specific receptors (i.e., T-cell and B-cell receptors), that can mediate delayed but long-lasting protective immunity against virtually any pathogen by e.g., the production of antibodies (Murphy, 2017; Takeuchi & Akira, 2010).

As an initial level of defense, intruding pathogens will encounter anatomical barriers that are provided by the body's epithelial surfaces. This includes the intact skin, oral mucosa, respiratory epithelium, and intestine (Murphy, 2017). They retard the entry and growth of pathogenic microbes via establishment of an acidic environment, promotion of commensal bacteria and normal flora, or mucociliary clearance mechanisms that entrap foreign microbes and propel them out of the body (Carrillo et al., 2017; Marshall et al., 2018; Turvey & Broide, 2010). In addition, a large range of constitutive immune mechanisms, including the production of antimicrobial proteins and peptides (such as lysozyme and defensins), have been identified to further strengthen host defense mechanisms (Marshall et al., 2018; Murphy, 2017; Paludan et al., 2021).

In case these barriers are breached, the innate immune system is ready to counteract further invasion with a collection of plasma proteins known as the complement system

(Murphy, 2017). Activation of the complement system via the classical- (which involves antibodies), alternative- (which occurs in the presence of a pathogen alone), or lectin- (which involves the recognition of carbohydrates on the pathogen surface) pathway can mediate direct lysis of a microbe or opsonization and subsequent phagocytosis of the invader by immune cells (Mathern & Heeger, 2015; Murphy, 2017).

Pathogens that evade both anatomical and chemical barriers finally encounter tissue-resident sensor cells, such as macrophages, dendritic cells (DCs), and mast cells (Murphy, 2017). These cell types are able to detect a variety of inflammatory mediators/inducers through the expression of PRRs. Such inducers include simple molecular components and regular patterns of molecular structure, which are evolutionary conserved among many pathogens because they are essential for their survival (Marshall et al., 2018; Murphy, 2017). Since these components generally have unique molecular or subcellular characteristics not present in the host, they allow for discrimination between “self” and “non-self” and are referred to as pathogen-associated molecular patterns (PAMPs) (Janeway & Medzhitov, 2002; Murphy, 2017). Apart from PAMPs, certain PRRs can also recognize damage-associated molecular patterns (DAMPs) and homeostasis-altering molecular processes (HAMPs). DAMPs are immunogenic self-derived host molecules that are released by damaged or dying cells and act as danger signals (Gong et al., 2020). HAMPs collectively summarize other immunogenic danger signals, such as stress or dyshomeostasis-associated molecular patterns or processes (Gong et al., 2020).

Triggering of PRRs can activate immune cells to produce and release various mediators that directly eliminate invading pathogens or propagate the immune response. Latter include chemokines and cytokines, which recruit and activate further immune cells (mostly polymorphonuclear leukocytes) to support in phagocytosis of microbes or damaged cells and to produce toxic chemical mediators, such as antimicrobial peptides, degradative enzymes, and reactive oxygen species (ROS) to inactivate or lyse pathogens (Murphy, 2017). Importantly, dendritic cells (DCs) are a class of professional antigen-presenting cells and specialized in activating other immune cells. Uptake and recognition of pathogens via PRRs can stimulate DCs to mature and migrate to lymphoid organs to activate naïve T- and B-cells, which in turn mount adaptive immune responses (Murphy, 2017; Patente et al., 2018). Thus, activation of immune cells via PRRs represents an important link between the innate and adaptive immune system, which have to act in concert to successfully clear the body from many infections, toxins, or cancerous cells.

## 1.2 Pattern recognition receptors

PRRs are a class of germline-encoded receptors of the innate immune system that evolved to directly recognize specific molecular structures of pathogens (PAMPs) and danger signals generated by damaged, transformed, or dying host cells (DAMPs and HAMPs) (Gong et al., 2020). In this way, our immune system is able to immediately react on threats potentially compromising homeostasis by utilizing only a confined set of available receptors (Bardoel & Strijp, 2011). PRRs are predominantly expressed in professional immune cells, such as macrophages and DCs, but also in many nonprofessional immune cells and even non-immune cells (Kumar et al., 2013; Takeuchi & Akira, 2010). They commonly localize on the outer cell membrane, intracellular compartment membranes, or the cytoplasm and are basically composed of ligand recognition domains, central regulatory or transmembrane domains, and effector domains (Li & Wu, 2021). Based on domain homology, most PRRs can be classified into five different types of receptors: Toll-like receptors (TLRs), nucleotide-binding oligomerization domain (NOD)-like receptors (NLRs), C-type lectin receptors (CLRs), retinoic acid-inducible gene-I (RIG-I)-like receptors (RLRs), and absent in melanoma 2 (AIM2)-like receptors (ALRs) (Li & Wu, 2021). Triggering of these receptors initiates downstream signal transduction via common mechanisms such as oligomerization, recruitment of adaptor proteins, proximity-induced activation of effector proteins including protein kinases or caspases, and activation of transcription factors that cross-talk and converge into common antimicrobial, antiviral, and inflammatory signaling pathways. These pathways include nuclear factor (NF)- $\kappa$ B signaling, mitogen-activated protein kinase (MAPK) signaling, TANK-binding kinase 1 (TBK1)-interferon regulatory factor (IRF) signaling, and inflammasome signaling, which regulate the expression and maturation of key molecules, such as the previously mentioned chemokines and cytokines, but also type I interferons (IFNs) and many proteins of the immune system machinery (Li & Wu, 2021; Takeuchi & Akira, 2010).

Because the focus of this thesis is on NLR family proteins, embracing the full complexity of PRRs and their downstream signaling pathways would go beyond the scope of this introduction. Thus, the following description of the different types of PRRs is not comprehensive and only intended to provide an overview about their similarities and differences in domain architecture, structure, and function including ligand sensing mechanisms and the subsequent immune response.

### 1.2.1 Toll-like receptors

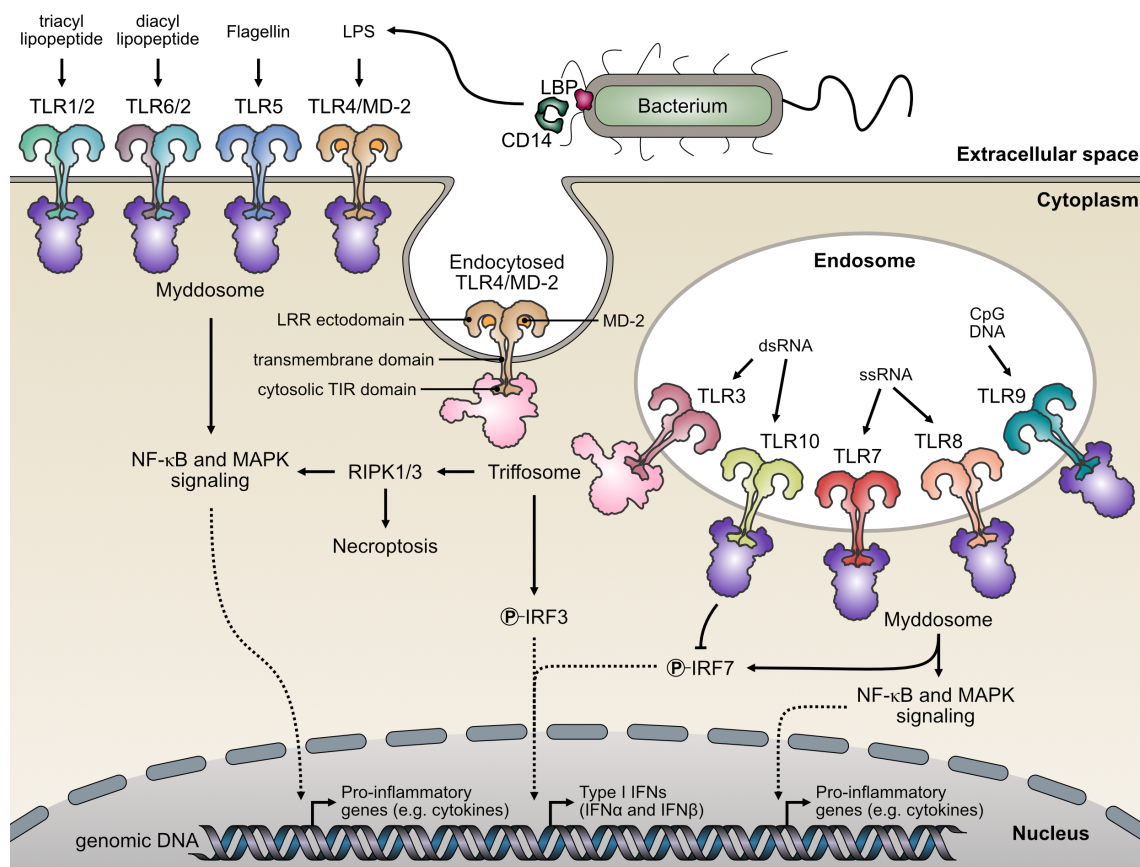
The TLR family was discovered when the Toll protein from *Drosophila* was identified as a receptor important for fly immunity against fungal infection (Lemaitre et al., 1996). This finding marks a milestone in immunology because subsequent discovery of a human homolog (TLR4) enabled scientists for the first time to answer the long-standing question of how pathogens can be sensed by the innate immune system (Medzhitov et al., 1997). Today we know that TLRs are a class of type I transmembrane proteins that are evolutionary conserved among organisms ranging from corals to humans (Fitzgerald & Kagan, 2020). However, a distinct number of TLRs is encoded by individual organisms. As an example, purple sea urchin encodes 222 different TLRs, whereas only ten functional TLRs (TLR1-10) were identified in human (Fitzgerald & Kagan, 2020; Vijay, 2018). In mammals, TLRs can be located on the plasma or endosomal membranes, where they primarily recognize bacterial cell surface components or diverse nucleic acid ligands (Fitzgerald & Kagan, 2020). TLRs located at the plasma membrane include TLR1, TLR2, TLR4, TLR5, and TLR6, whereas TLR3, TLR7, TLR8, TLR9, and TLR10 are found at endosomal membranes (Figure 1-1) (Kawasaki & Kawai, 2014; S. M. Lee et al., 2018). However, upon ligand sensing, TLR4 can be endocytosed and translocate to endosomal membranes, which can alter its downstream signaling (Hornef et al., 2003; Kagan et al., 2008; Zanoni et al., 2011). Interestingly, trafficking of TLR9 to its final destination includes similar but ligand-independent delivery to the plasma membrane and subsequent endocytosis (Lee et al., 2013). This might also be the case for TLR10, which has mostly been described in the literature to locate at the plasma membrane but was more recently found to signal from the endosomal compartment (Kawasaki & Kawai, 2014; S. M. Lee et al., 2018). The rationale behind this is not yet understood.

All TLRs have the same basic domain architecture: The amino (N)-terminal ectodomain containing several leucine-rich repeats (LRRs) is followed by a single transmembrane domain and the carboxy (C)-terminal cytosolic Toll-interleukin-1 receptor (TIR) homology domain (Fitzgerald & Kagan, 2020). Pattern recognition is facilitated by direct interaction of variable numbers of ligand molecules with the LRR domains of TLR dimers causing allosteric conformational changes that promote interaction of cytosolic TIR domains, which is a prerequisite for signal transduction (Fitzgerald & Kagan, 2020; Jin & Lee, 2008; Latz et al., 2007). Most TLRs form homodimers with M-type structure of their ectodomains but TLR1 and TLR6 or TLR2 and TLR6 are functional as heterodimers (Fitzgerald & Kagan, 2020). Typically, LRR

domains are composed of 20-30 amino acid modules that fold into an  $\alpha/\beta$  'horseshoe-like' structure with a parallel  $\beta$ -sheet on the concave side and various mostly helical secondary structures on the convex side (Enkhbayar et al., 2004; Park et al., 2015). In TLRs, these modules are flanked by cysteine clusters forming disulfide bridges to protect the central hydrophobic core that is established by conserved leucine-rich motifs and further residues from a more variable region (Jin & Lee, 2008; Matsushima et al., 2007). Variability of the ligand binding site within the LRR domain allows for the detection of diverse pathogenic structures (Figure 1-1) (Fitzgerald & Kagan, 2020; Kawai & Akira, 2010; S. M. Lee et al., 2018; Li & Wu, 2021): Triacyl lipopeptide (TLR1/TLR2), diacyl lipopeptide (TLR2/TLR6), double-stranded (ds) ribonucleic acid (RNA; TLR3 and TLR10), lipopolysaccharide (LPS, TLR4), flagellin (TLR5), single-stranded (ss) RNA (TLR7 and TLR8), and unmethylated CpG (5'-cytosine-phosphate-guanine-3') containing single-stranded deoxyribonucleic acid (ssDNA; TLR9). Interestingly, TLR10 is the only receptor that was described to transmit anti-inflammatory signaling, whereas other TLRs mediate inflammatory responses (S. M. Lee et al., 2018). Noteworthy, activation of endosomal TLRs requires cleavage by endosomal cathepsins in their ectodomain, low pH, and presence of free nucleosides (produced by acid-dependent nucleases) to allow for efficient dimerization. These mechanisms likely ensure that nucleic acid sensing only occurs in the endosomal compartment to prevent unintended activation by self-molecules and concomitant autoimmune responses (Fitzgerald & Kagan, 2020).

Recognition of LPS via TLR4 is dependent on auxiliary proteins and thus represents a special case that deserves particular attention (Li & Wu, 2021). LPS is a major cell surface component of gram-negative bacteria and is composed of a hydrophobic membrane anchor known as Lipid A and a central hydrophilic core polysaccharide that is extended by a repeating oligosaccharide chain called the O-antigen (Chandler & Ernst, 2017). Lipid A is a glucosamine backbone connected to varying number of acyl chains with different length and represents the component responsible for recognition by TLR4 (Chandler & Ernst, 2017; Fitzgerald & Kagan, 2020). Upon infection with bacteria, the serum LPS-binding protein (LBP) associates with the bacterial membrane and facilitates the extraction of LPS molecules. Next, one molecule of LPS is transferred from LBP to a CD14 (cluster of differentiation 14) dimer, which is a LRR protein on the host cell surface or a secreted or shed soluble protein. Finally, LPS is transferred to a heterodimer of TLR4 and MD-2 (myeloid differentiation factor 2), which is bound to the concave side of the

TLR4 LRR domain with parts of its  $\beta$ -sandwich fold (Figure 1-1) (Yin et al., 2015). In case of hexacylated Lipid A, five acyl chains integrate into a hydrophobic pocket formed by MD-2, whereas the last acyl chain is exposed to the surface and makes contact with a TLR4 component of another TLR4/MD-2 heterodimer ultimately leading to TLR4 dimerization and subsequent signal transduction (Park et al., 2009). These structural and mechanistic insights explained how complex formation enables picomolar activity of LPS in macrophages and why TLR4 alone only forms weak interactions with LPS *in vitro* (Gioannini et al., 2004).



**Figure 1-1: Toll-like receptors and their signaling pathways.** Toll-like receptors (TLRs) are type I transmembrane proteins that can be located at plasma or endosomal membranes. They can detect PAMPs and DAMPs directly by utilizing their leucine-rich repeat (LRR)-containing ectodomains. However, sensing of bacteria-derived lipopolysaccharide (LPS) by TLR4 is dependent on the auxiliary proteins LBP, CD14, and MD-2. LBP binds to the bacterial membrane to extract LPS molecules, while CD14 facilitates the transfer of a single molecule onto the TLR-4/MD-2 heterodimer. Upon ligand-binding, TLRs dimerize to transduce signals with their cytosolic Toll-interleukin-1 receptor (TIR) domain. TIR domain oligomerization can recruit the Myddosome or Trifosome multiprotein complexes to primarily induce expression of pro-inflammatory genes and type I interferons (IFNs). Additionally, activation of proteins of the RIPK family can result in inflammatory killing of the cell by a mechanism called necroptosis. The circled ‘P’ represents phosphorylation. LBP: LPS binding protein, CD14: cluster of differentiation 14, MD-2: myeloid differentiation factor 2, NF- $\kappa$ B: nuclear factor  $\kappa$ B, MAPK: mitogen-activated protein kinase, RIPK: receptor-interacting serine/threonine-protein kinase, IRF: interferon regulatory factor, dsRNA: double-stranded ribonucleic acid, ssRNA: single-stranded RNA, CpG DNA: 5'-cytosine-phosphate-guanine-3' containing deoxyribonucleic acid.

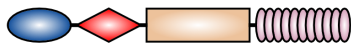













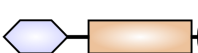


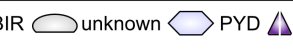
After dimerization or oligomerization of cytosolic TIR domains, TLR signaling leads to significant changes in cellular activity, including gene transcription, splicing, translation efficiency, autophagy, glycolysis, and oxidative phosphorylation (Fitzgerald & Kagan, 2020). While the downstream mechanisms linked to these responses are not completely understood, two possible signaling pathways including the formation of large multiprotein scaffold complexes called supramolecular organizing centers (SMOCs) have been unveiled (Figure 1-1) (Fitzgerald & Kagan, 2020). One SMOC termed as the Myddosome is seeded by the TIR domain-containing peripheral membrane protein TIRAP (Toll/interleukin-1 receptor domain-containing adapter protein), which binds TLRs to recruit MyD88 (myeloid differentiation primary response 88) (Fitzgerald & Kagan, 2020). MyD88 also consists of a C-terminal TIR domain and an N-terminal death domain (DD) (Fitzgerald & Kagan, 2020). DDs belong to the death-fold superfamily whose members are well known to assemble into helical filamentous structures that are typical for inflammatory and apoptotic signaling complexes (Ferrao & Wu, 2012; Kersse et al., 2011). Helical assembly of MyD88 results in association of members of the interleukin-1 receptor (IL-1R) associated kinase (IRAK) family of serine threonine kinases, which also comprise DDs. Proximity-induced activation of IRAKs drives autophosphorylation and recruitment of the E3 ubiquitin ligase TRAF6 (TNF [tumor necrosis factor] receptor-associated factor 6), which can finally induce activation of NF- $\kappa$ B and AP-1 (activator protein 1) transcription factors via TAK1 (TGF- $\beta$ -activated kinase 1) or IFN-inducing transcription factors, such as IRF7 (Fitzgerald & Kagan, 2020; Kawasaki & Kawai, 2014). Apart from the Myddosome, another supposed SMOC termed the Trifosome can induce TLR-dependent immune responses through the peripheral membrane protein TRAM (TRIF-related adaptor molecule) (Fitzgerald & Kagan, 2020). TRAM is thought to form a complex with TLRs and TRIF (TIR-domain-containing adapter-inducing IFN- $\beta$ ), TRAF3, and TBK1. This complex can promote NF- $\kappa$ B and MAPK signaling via the RIPK1 (receptor-interacting serine/threonine-protein kinase 1) axis or TRAF3-dependent activation of TBK1, which in turn recruits and activates IRF3 to ultimately induce the expression of type I IFNs and IFN-stimulated genes (Fitzgerald & Kagan, 2020). RIPK1 can further activate RIPK3 to initiate an inflammatory mode of cell death called necroptosis (Bertheloot et al., 2021; Fitzgerald & Kagan, 2020).


### 1.2.2 NOD-like receptors

In humans, NLRs constitute a family of 22 cytosolic PRRs that are thought to detect a wide range of pathogen and danger-associated molecular pattern to mount an innate immune response against perpetrators of cellular imbalance (Motta et al., 2015; Platnich & Muruve, 2019; Shaw et al., 2008; Shaw et al., 2010). Such ligands may include microbial components (peptidoglycan, flagellin, viral RNA, fungal hyphae, etc.), host cell components (ATP, cholesterol crystals, uric acid, etc.), or environmental triggers (alum, asbestos, silica, alloy particles, UV radiation, etc.) (Kim et al., 2016). NLRs are primarily expressed in immune cells but some NLRs are also found in non-immune cells, where they have many roles beyond pathogen recognition, including the regulation of antigen presentation or even stem cell survival and embryonic development (Meunier & Broz, 2017; Motta et al., 2015; Shaw et al., 2008). However, the function of many family members is currently unknown or their pathways have been incompletely characterized.

NLRs share a similar **tripartite domain architecture** with a C-terminal LRR domain, a central NACHT (acronym for NAIP [NLR family apoptosis inhibitory protein], CIITA [class II, major histocompatibility complex, transactivator], HET-E [incompatibility locus protein from *Podospora anserina*], and TP1 [telomerase-associated protein]) domain, and N-terminal death-fold superfamily effector domains (Meunier & Broz, 2017; Platnich & Muruve, 2019). Based on the type of effector domain, NLRs are further classified into four subfamilies: NLRAs, NLRBs, NLRCs, and NLRPs (Figure 1-2) (Kim et al., 2016). CIITA is the only representant of the NLRA family, which contains an N-terminal caspase activation and recruitment domain (CARD) and an acidic transactivation domain (AD). Members of the NLRB family comprise BIR (baculovirus inhibitor of apoptosis protein repeat) domains. In humans, this family is represented by the NLR family apoptosis inhibitory protein (NAIP). The NLRC family consists of six members: NLRC1 (NOD1), NLRC2 (NOD2), NLRC3, NLRC4, NLRC5, and NLRX1. NOD1, NOD2, and NLRC3 contain one or two N-terminal CARD domains, whereas NLRC3, NLRC5, and NLRX1 comprise an unknown N-terminal effector domain. The NLRP family includes 14 members (NLRP1-14), which all contain an N-terminal Pyrin domain (PYD) (Meunier & Broz, 2017). Of note, CARDS and PYDs are members of the death-fold superfamily, which typically adopt a six-helical bundle fold and are known for mediating homotypic CARD-CARD or PYD-PYD interactions in oligomers (Ferraro & Wu, 2012; Kersse et al., 2011; Park et al., 2007).



Subfamily	Protein	Function	Domain architecture
NLRA	CIITA	MHC II expression	
NLRB	NAIP	T3SS and flagellin recognition	
NLRC	NOD1	NF-κB and MAPK signaling, autophagy	
	NOD2	NF-κB and MAPK signaling, autophagy, type I IFN	
	NLRC3	negative regulator of T-cell activation	
	NLRC4	inflammasomal signaling with NAIP	
	NLRC5	MHC I expression, antiviral response	
	NLRX1	antiviral response, type I IFN inhibition, ROS regulation, autophagy	
NLRP	NLRP1	inflammasomal signaling	
	NLRP2,-7,-9	inflammasomal signaling, embryonic development	
	NLRP3	inflammasomal signaling	
	NLRP5	embryonic development	
	NLRP6	inflammasomal signaling, NF-κB and MAPK signaling inhibition, type I IFNs	
	NLRP8,-13	unknown	
	NLRP10	NF-κB regulation	
	NLRP11	NF-κB and MAPK signaling inhibition	
	NLRP12	inflammasomal signaling, NF-κB and MAPK signaling inhibition	
	NLRP14	spermatogenesis	



**Figure 1-2: The human NOD-like receptor family and functions in innate immunity.** NOD-like receptors (NLRs) mostly comprise a tripartite domain architecture with an N-terminal effector domain, a central NACHT domain, and C-terminal LRRs. Depending on the type of effector domain, the family is further classified into four subfamilies (NLRA, NLRB, NLRC, NLRP). NLRs fulfill diverse functions in innate immunity. However, most family members have currently not been well characterized. Figure is based on (Meunier & Broz, 2017) and complemented with known NLR functions reported in the literature and described in the text. CIITA: Class II, major histocompatibility complex, transactivator, NAIP: NLR family apoptosis inhibitory protein, NOD: nucleotide-binding oligomerization domain, MHC: major histocompatibility complex, T3SS: Type III bacterial secretion system, NF-κB: nuclear factor κB, MAPK: mitogen-activated protein kinase, IFN: interferon, ROS: reactive oxygen species, CARD: caspase activation and recruitment domain, AD: acidic transactivation domain, NACHT: acronym for NAIP, CIITA, HET-E, and TP1, LRR: leucine-rich repeat, BIR: baculovirus inhibitor of apoptosis protein repeat, PYD: Pyrin domain, FIIND: function to find domain, MTS: mitochondrial targeting sequence.

NLRP1 and NLRP10 are distinct from other NLRPs because they do not share the tripartite domain architecture. NLRP1 comprises an additional function to find (FIIND) and CARD domain at its C-terminus. The FIIND domain is composed of interlaced ZU5-UPA domains that undergo autolytic cleavage and thereafter remain associated, which is necessary but insufficient for activation of NLRP1 (Finger et al., 2012). Association of the cleavage fragments is supported by interaction with dipeptidyl peptidase 9 (DPP9) (Hollingsworth et al., 2021; Huang et al., 2021). Additionally, in NLRP1 the C-terminal CARD is the effector domain, whereas the N-terminal PYD might mediate autoinhibitory interaction (Finger et al., 2012; Mitchell et al., 2019; Zhong et al., 2016). NLRP10 does only contain a PYD and NACHT domain but not the C-terminal LRR domain. Thus, it was suggested as a signaling adaptor rather than an NLR sensor, because ligand recognition or activator sensing is proposed to typically appear at the LRR domain of NLRs (Meunier & Broz, 2017; Shaw et al., 2008; Zhong et al., 2013).

**Ligand recognition** was investigated by a structural study on murine NAIP5, which recognizes bacterial flagellin by direct interaction with its LRR domain and a portion of the NACHT domain (Tenthorey et al., 2017). In line, mutagenic disruption/removal of the LRR domains of NAIPs or NOD1/2 renders the proteins defective in pathogen recognition (Meunier & Broz, 2017; Motta et al., 2015). However, removal of the LRR domain can also result in hyperactive protein thus arguing for a second role in autoinhibition (Meunier & Broz, 2017). The mechanism behind this was revealed by a structural study on inactive NLRC4, where the LRR domain folds back towards one side of the NACHT domain to sterically occlude oligomerization interfaces and stabilize the inactive conformation (Hu & Chai, 2016; Hu et al., 2013). Similar with the structurally reminiscent family of plant R proteins, ligand recognition is thought to result in conformational changes from an inactive and ‘closed’ state to an active and ‘open’ state leading to subsequent oligomerization (Danot et al., 2009; Maruta et al., 2022; Sandall et al., 2020). This proposes a model of NLR activation by modification or ligand-induced displacement of the **autoinhibiting intramolecular contacts** between the NACHT and LRR domains leading to conformational change, concomitant oligomerization, and signaling by the N-terminal effector domain. However, in case of NOD2 the LRR domain is not attached to the NACHT domain, suggesting a different mode of autoinhibition that relies on interdomain interactions in the NACHT domain itself (Maekawa et al., 2016). Furthermore, the LRR domain of NLRP3 was reported to be dispensable for autoinhibition and activation, indicating other domains might facilitate ligand sensing and

activation in some NLRs (Hafner-Bratkovic et al., 2018). LRRs have also been shown to aid in oligomerization (as shown for NLRC4), but the key domain driving self-assembly is thought to be the central NACHT domain (Danot et al., 2009; Moghaddas et al., 2018).

**The NACHT domain** is composed of four subdomains, which classify NLR proteins as members of the family of signal transduction ATPases with numerous domains (STAND): The nucleotide binding domain (NBD), helical domain 1 (HD1), the winged helix domain (WHD), and helical domain 2 (HD2) harbor conserved motifs involved in nucleotide binding and hydrolysis, such as the Walker A and Walker B motifs and specific sensor motifs (Sandall et al., 2020). Nucleotide exchange from adenosine diphosphate (ADP) to adenosine triphosphate (ATP) and subsequent hydrolysis are known to be essential regulatory events for the oligomerization and downstream functions of NLRs but the precise role of these events remains to be determined (Duncan et al., 2007; Platnich & Muruve, 2019; Ye et al., 2008). Some NLRs, such as NLRP3, contain a fish-specific NACHT associated domain (FISNA) upstream of the NBD that was first identified as a distinct domain in zebrafish (Stein et al., 2007).

Although NLRs are functionally quite diverse, certain receptors are related in their ability to directly regulate transcription (i.e., CIITA, NLRC5), mediate NF- $\kappa$ B and MAPK signaling (e.g., NOD1, NOD2) or to form multimeric complexes driving pyroptosis – a rapid mode of inflammatory and lytic cell death that relies on the activation of caspases (Platnich & Muruve, 2019). These complexes have been termed **inflammasomes** (Martinon et al., 2002) and will be explained in more detail in section 1.3. In short, inflammasome formation results in bursting of cells together with maturation and release of pro-inflammatory cytokines (i.e., IL-1 $\beta$ , IL-18). Inflammasome formation has been validated for different NLRs, including NAIP/NLRC4, NLRP1, NLRP3, and NLRP6, while existence of NLRP2, NLRP7, NLRP9, and NLRP12 inflammasomes remains to be proven biochemically (Kim et al., 2016; Platnich & Muruve, 2019; Shen et al., 2019). The following descriptions shall give an overview of exemplary NLRs where functional insights have been reported (Figure 1-3).

**CIITA** and **NLRC5** are upregulated upon IFN $\gamma$  signaling. Both proteins can translocate to the nucleus and act as transactivators of MHC I and MHC II gene expression, respectively (Motta et al., 2015; Shaw et al., 2010). NLRC5 can also associate with RIG-I to drive robust antiviral responses against influenza virus (Ranjan et al., 2015). **NOD1** and **NOD2** can recognize bacterial peptidoglycan (PGN) derivatives (i.e.,  $\gamma$ -D-glutamyl-*meso*-diaminopimelic acid [iE-DAP] and muramyl dipeptide [MDP],

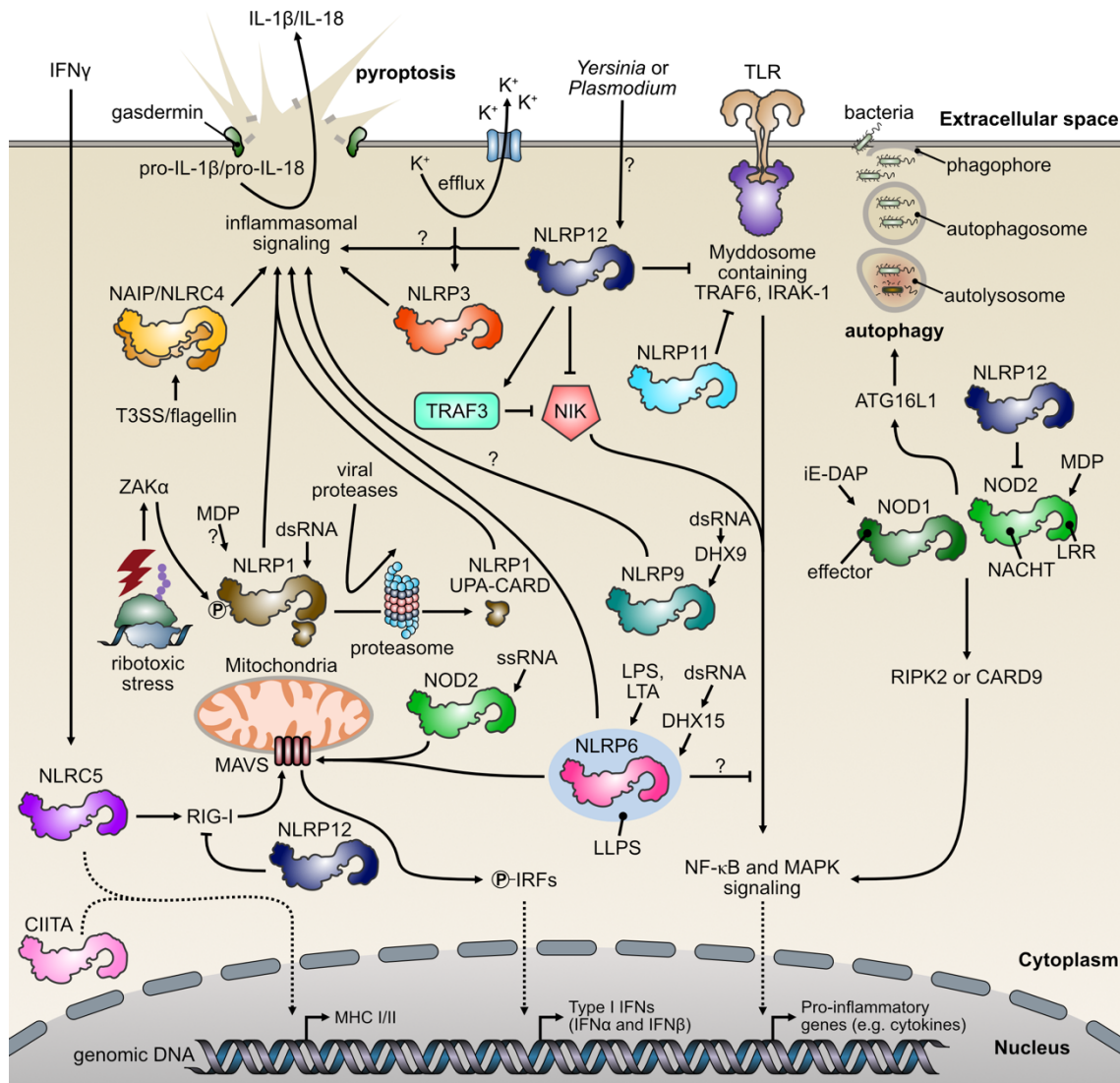
respectively), which may derive from bacterial cell division in the cytosol of infected cells or leak from lysosomal compartments where phagocytosed bacteria have been lysed (Shaw et al., 2010). Ligand binding triggers oligomerization and subsequent recruitment of RIPK2 or CARD9 (CARD protein 9) via homotypic CARD interactions, which drives downstream activation of NF- $\kappa$ B or MAPK signaling, respectively (Platnich & Muruve, 2019; Shaw et al., 2010). Additionally, NOD2 was implicated in the recognition of viral ssRNA, which stimulates interaction with MAVS (mitochondrial antiviral-signaling protein) at the mitochondrial membrane and culminates in the expression of type I IFNs via activation of IRF3 (Negroni et al., 2018). Furthermore, NOD1 and NOD2 might be related to autophagic processes, since they were described to interact with autophagy related 16 like 1 (ATG16L1), which results in the recruitment of the autophagy machinery to the site of bacterial entry on the plasma membrane (Travassos et al., 2010).

Human **NAIP** is implicated in recognizing components of the bacterial type III secretion system (T3SS) (Platnich & Muruve, 2019). Interestingly, expression of a second, extended isoform of human NAIP possess capability to bind to *Salmonella* flagellin (Kortmann et al., 2015). As demonstrated for the murine system, activated NAIP is able to directly interact with **NLRC4** and drive conformational changes that lead to activation, oligomerization, and cooperative inflammasomal signaling (Zhang et al., 2015). Importantly, the concept of cooperative signaling is not new to the field of innate immunity (see e.g., TLR heterodimers) but just emerged in the field of NLRs. It can be assumed that future studies will identify more pairs of sensory and executive NLRs, which together form a functional inflammasome or even other signaling complexes.

Activity of lethal toxin, a secreted protease of *Bacillus anthracis*, is sensed by murine **NLRP1** (Boyden & Dietrich, 2006). Instead, human NLRP1 was supposed to be activated by MDP, which is a membrane component of gram-positive and gram-negative bacteria (Faustin et al., 2007). Although recognition of MDP by human NLRP1 is controversial (Martino et al., 2016; Reubold et al., 2014), this is an important example for differential pattern recognition and regulatory mechanisms adapted by an ortholog receptor. More recently, interaction of the NLRP1 LRR domain with viral dsRNA was also identified to trigger activation and inflammasomal signaling (Bauernfried et al., 2021). NLRP1 can further be activated by LRR-independent mechanisms. After self-processing of the FIIND domain, a number of viral 3C proteases have been identified to cleave and destabilize the autoinhibiting N-terminus of NLRP1, causing ubiquitination and subsequent proteasomal degradation, thereby releasing the C-terminal fragment for inflammasome formation

(Robinson et al., 2020; Tsu et al., 2021). Notably, activation of murine NLRP1b via lethal toxin was shown to be mediated by a similar mechanism (Levinsohn et al., 2012). Additionally, ubiquitination can also be induced by microbial E3 ubiquitin ligases, such as IpaH7.8 from *Shigella flexneri* (Sandstrom et al., 2019). Of note, ubiquitination of proteins is utilized by cells as a common signal for proteasomal degradation (Ciechanover, 1994). These findings suggest that the majority of the PYD-NACHT-LRR domain assembly of NLRP1 is dispensable for its activity. Indeed, CARD8 is a protein considered a ‘minimized’ NLRP1 ortholog that harbors only the FIIND and CARD domains and can be activated via proteolytic processing by HIV protease (Mitchell et al., 2019; Wang et al., 2021). It is a reasonable hypothesis that NLRP1 and CARD8 evolved as a ‘tripwire’ for these pathogens by sensing the activity of viral proteases and microbial E3 ubiquitin ligases that often target and inactivate host proteins with immune functions (Fenini et al., 2022). Lately, bacterial toxins (e.g., anisomycin) and ultraviolet B (UVB) radiation, which both trigger ribotoxic stress, were found to activate the NLRP1 inflammasome. In this pathway, the zipper-sterile- $\alpha$ -motif kinase (ZAK $\alpha$ ) is activated, whereafter it hyperphosphorylates NLRP1 in a disordered region between the PYD and NACHT domain, thereby activating the NLRP1 inflammasome (Robinson et al., 2022).

A plethora of pathogen and host-derived molecular stimuli, including ATP, nigericin, particulate matter, ROS, and many more have been described to act in common pathways that activate the **NLRP3** inflammasome (Paik et al., 2021). However, none of these stimuli could be demonstrated to directly bind and activate NLRP3. Thus, it is currently thought that the pathways they trigger culminate in one specific activator. Most of these pathways (e.g., potassium and chloride efflux, calcium signaling, lysosomal disruption) can be associated with rupture of cellular and organellar membranes thus demonstrating that NLRP3 is a general sensor for disturbances in cellular homeostasis (Platnich & Muruve, 2019). Strikingly, one particular convergence point of common NLRP3 agonists is potassium ion efflux. Indeed, it was demonstrated that presence of low intracellular potassium results in an ‘open’ conformation of NLRP3 that promotes inflammasome assembly, whereas blockage of potassium efflux can abrogate NLRP3 inflammasome activation downstream of aforementioned stimuli (Munoz-Planillo et al., 2013; Tapia-Abellan et al., 2021). Additionally, the mitotic NIMA-related kinase 7 (NEK7) interacts with the NLRP3 LRR domain to potentially license inflammasome formation. However, its precise role in activating NLRP3 remains to be determined (He et al., 2016; Schmid-Burgk et al., 2016; Sharif et al., 2019; H. Shi et al., 2016).



**Figure 1-3: Nod-like receptors and their signaling.** NOD-like receptors (NLRs) are cytosolic PRRs that comprise a tripartite domain architecture with an N-terminal effector domain, a central NACHT domain and a number of C-terminal leucine-rich repeats (LRRs). Functionally, the family is quite diverse but related in their ability to directly regulate transcription, mediate NF- $\kappa$ B and MAPK signaling or to form multimeric complexes driving pyroptosis. These complexes have been termed inflammasomes. Pyroptosis is defined as gasdermin-mediated lytic cell death in concert with maturation and release of the pro-inflammatory cytokines IL-1 $\beta$  and IL-18. NLRC5 and CIITA are upregulated in response to stimulation with IFN $\gamma$  and translocate to the nucleus to induce the expression of MHC I and MHC II genes, respectively. Additionally, NLRC5 can form a complex with RIG-I to induce a robust anti-viral immune response against infection with influenza virus. NOD1 and NOD2 can sense microbial peptidoglycan derivatives and mediate NF- $\kappa$ B and MAPK signaling to induce the expression of pro-inflammatory genes or recruit the autophagy machinery to bacterial entry sites at the cell membrane. NOD2 can also sense viral RNA and induce the expression of type I IFNs via MAVS at the mitochondrial membrane. NAIP can sense components of the bacterial T3SS or flagellin and activate NLRC4 to form an inflammasome. NLRP1 might also form an inflammasome upon recognition of MDP or cytosolic RNA. Recently, ribotoxic stress, which activates ZAK $\alpha$ , was found to result in hyperphosphorylation of the NLRP1 N-terminus and thereby drive inflammasome formation. Furthermore, viral proteases can cleave and thus destabilize the NLRP1 N-terminus promoting proteasomal degradation. Since NLRP1 is autolytically cleaved in its FIIND domain, proteasomal degradation releases the C-terminal UPA-CARD fragment for inflammasome formation. The NLRP3 inflammasome is activated by cellular imbalances that mostly culminate in the efflux of potassium ions. NLRP6, NLRP11, and NLRP12 have anti-inflammatory function and can inhibit NF- $\kappa$ B and MAPK signaling as well as anti-viral responses. While the pathway for NLRP6 has not been determined, NLRP12 was shown to interact with IRAK-1, TRAF3, NIK, NOD2, and RIG-I. As a consequence, IRAK-1 hyperphosphorylation is inhibited, TRAF3 is stabilized, and proteasomal degradation of NIK, NOD2, and

RIG-I is promoted. Instead, NLRP11 promotes proteasomal degradation of TRAF6. Additionally, NLRP6 can sense LPS, LTA, and viral RNA via the RNA helicase DHX15. Recent insights revealed that activated NLRP6 can form condensates, which enables the formation of an inflammasome or the induction of type I IFNs via MAVS. NLRP12 was proposed as an inflammasome sensor for specific strains of *Yersinia* and *Plasmodium* but its definitive ligand is still unknown. The NLRP12 inflammasome was also not proven biochemically. Another inflammasome that needs verification is formed by NLRP9, which might recognize cytosolic RNA via DHX9. The circled 'P' represents phosphorylation. NOD: nucleotide-binding oligomerization domain, IFN: interferon, CIITA: class II, major histocompatibility complex, transactivator, MHC: major histocompatibility complex, IL-1 $\beta$ : interleukin-1 $\beta$ , IL-18: interleukin-18, NAIP: NLR family apoptosis inhibitory protein, T3SS: type III secretion system, ZAK $\alpha$ : zipper-sterile- $\alpha$ -motif kinase, MDP: muramyl dipeptide, dsRNA: double-stranded ribonucleic acid, ssRNA: single-stranded ribonucleic acid, IRF: interferon regulatory factor, UPA: acronym for UNC5, PIDD, and Ankyrins, CARD: caspase activation and recruitment domain, MAVS: mitochondrial antiviral-signaling protein, RIG-I: retinoic acid-inducible gene-I, K<sup>+</sup>: potassium ion, TLR: Toll-like receptor, TRAF3: TNF receptor-associated factor 3, TRAF6: TNF receptor-associated factor 6, IRAK-1: IL-1 receptor associated kinase 1, NIK: NF- $\kappa$ B-inducing kinase, DHX9: DEAH box helicase 9, DHX15: DEAH box helicase 15, LPS: lipopolysaccharide, LTA: lipoteichoic acid, LLPS: liquid-liquid phase separation, NF- $\kappa$ B: nuclear factor  $\kappa$ B, MAPK: mitogen-activated protein kinase, ATG16L1: autophagy related 16 like 1, iE-DAP:  $\gamma$ -D-glutamyl-*meso*-diaminopimelic acid, NACHT: acronym for NAIP, CIITA, HET-E, and TP1, LRR: leucine-rich repeat, RIPK2: receptor-interacting serine/threonine-protein kinase 2, CARD9: CARD protein 9.

Among others, **NLRP6** and **NLRP12** have been reported to have a dual role in innate immunity. Apart from forming inflammasomes, they can negatively regulate NF- $\kappa$ B and MAPK signaling (Allen et al., 2012; Anand et al., 2012; Krauss et al., 2015; Zaki et al., 2011). More precisely, murine *Nlrp6*-deficient (*Nlrp6*<sup>-/-</sup>) bone marrow-derived macrophages (BMDMs) that were exposed to *Listeria monocytogenes* or known TLR agonists showed enhanced NF- $\kappa$ B and MAPK pathway activation, as if compared with *Nlrp6* wildtype (*Nlrp6*<sup>wt</sup>) BMDMs (Anand et al., 2012). However, the molecular details of the anti-inflammatory effects of NLRP6 have never been elucidated. In contrast, structural and biochemical studies investigated mechanistic detail about NLRP6 inflammasome formation. LPS was shown to directly bind to recombinant NLRP6, which results in conformational change and homodimerization (Leng et al., 2020). However, oligomerization into linear molecular platforms and inflammasome formation via the PYD effector domain required further presence of ATP (Leng et al., 2020). Interestingly, lipoteichoic acid (LTA, membrane component of gram-positive bacteria) and long stretches of viral dsRNA were also found as ligands for NLRP6 (Hara et al., 2018; Shen et al., 2021; Zhu et al., 2017). Importantly, recognition of dsRNA requires interaction with DHX15 (DEAH box helicase 15) (Xing et al., 2021). Upon activation, NLRP6 forms condensates by a mechanism called liquid-liquid phase separation (LLPS). Following, NLRP6 can interact with MAVS to promote the expression of type I IFNs or participate in inflammasome formation, which will solidify NLRP6 condensates and mediate pyroptosis (Shen et al., 2021; Xing et al., 2021).

**NLRP12** has been shown to shut down TLR and TNF receptor (TNFR)-driven NF- $\kappa$ B and MAPK signaling by preventing the hyperphosphorylation of IRAK1 and regulating the degradation of important molecules of the signaling cascade, including NIK (NF- $\kappa$ B-inducing kinase) and TRAF3 (Allen et al., 2012; Arthur et al., 2007; Lich et al., 2007; Tuladhar & Kanneganti, 2020; Williams et al., 2005; Ye et al., 2008; Zaki et al., 2011). Additionally, NLRP12 can interact with NOD2 and induce its proteasomal degradation (Normand et al., 2018). More recently, NLRP12 was implicated in regulating anti-viral response by enhancing proteasomal degradation of RIG-I and inhibiting the ubiquitin ligase TRIM25 (tripartite motif-containing protein 25), which is important for RIG-I activation (Chen et al., 2019). Consistent with its role as a negative regulator of inflammation, NLRP12 is transcriptionally suppressed via Blimp-1 (B lymphocyte-induced maturation protein 1) downstream of certain TLR stimuli, whereas expression of inflammatory NLRs is typically induced (Lord et al., 2009). The anti-inflammatory function was proposed to be especially important to maintain a quiescent state during resting and after infection, when NLRP12 is upregulated to (re-)establish homeostasis. Additionally, NLRP12 might manage pathogen discrimination in the gut, where permanent presence of commensal bacteria shall not cause unintended or excessive inflammation. This was especially investigated in models of experimental colitis, which revealed that NLRP12 suppresses colon inflammation and tumorigenesis (Allen et al., 2012; Chen et al., 2017; Shaw et al., 2010). Conflicting, earlier reports on NLRP12 suggested a role in inflammasomal signaling upon infection with strains of *Yersinia pestis* and *Plasmodium vivax* (Ataide et al., 2014; Vladimer et al., 2012). This is indeed supported by the finding that mutations in the *Nlrp12* gene lead to the same phenotypic disease as is the case for NLRP3, which is well known to form an inflammasome (Wang, 2022). However, the defined molecular structure sensed by NLRP12 is unknown and biochemical validation of the existence of the NLRP12 inflammasome still remains.

Similar with NLRP6 and NLRP12, also **NLRP11** was shown to attenuate TLR-driven NF- $\kappa$ B and MAPK signaling (Ellwanger et al., 2018; Wu et al., 2017). Mechanistically, NLRP11 can mediate proteasomal degradation of TRAF6 via the ubiquitin ligase RNF19A (RING finger protein 19A) (Wu et al., 2017).

The **NLRP9** inflammasome is another example where its existence and underlying molecular mechanisms remain to be determined by biochemical studies. NLRP9 was first discovered as a protein with implications in embryonic development and only later proposed as an intestinal sensor for infections with rotavirus (Mullins & Chen, 2021). In



detail, it was found that short stretches of viral dsRNA bind to DHX9, which mediates the interaction with NLRP9b (a murine isoform of NLRP9). Successive activation of NLRP9b results in inflammasome formation and maturation of IL-18 but not IL-1 $\beta$ . Importantly, the study also revealed intestinal expression of human NLRP9 and association with DHX9 and inflammasome components in rotavirus-infected HEK293T cells (Zhu et al., 2017). While lysis of infected cells might limit the viral infection, the role of IL-18 in eliminating this pathogen could not be finally elucidated. IL-18-deficient mice did not exhibit increased susceptibility to infection with rotavirus, whereas administration of IL-18 to mice helped to prevent or eliminate the infection (B. Zhang et al., 2014; Zhu et al., 2017).

Further studies are needed to unravel the undoubtedly important role of NLRs in innate immunity and beyond, not least because many family members not mentioned here have not been adequately explored, especially given that NLR function and dysregulation have been linked to a variety of human diseases (Caruso et al., 2014; Christgen & Kanneganti, 2020; Guo et al., 2015; Kim et al., 2016; Lunemann et al., 2021; Mangan et al., 2018; Strowig et al., 2012; Zhong et al., 2013).

### **1.2.3 C-type lectin receptors**

The CLR family comprises a large number of mostly transmembrane proteins that are classified into seventeen subgroups (I-XVII) according to their features including domain organization and phylogeny (Hoving et al., 2014; Sancho & Reis e Sousa, 2012). They commonly share one or more extracellular C-type lectin-like domains (CTLDs), which is a conserved structural motif arranged as two loops that are connected by four conserved cysteine residues forming disulfide bridges at the bases of the loops. The more flexible second loop generally contains the ligand binding site (Zelensky & Gready, 2005). CTLDs can specifically recognize a number of different ligands, including the molecular structure of carbohydrates, proteins, lipids, or even inorganic molecules, enabling CLRs to recognize various fungi, viruses, bacteria, and parasites (Geijtenbeek & Gringhuis, 2009; Sancho & Reis e Sousa, 2012). The most common CTLD function is to provide Ca<sup>2+</sup>-dependent lectin (carbohydrate binding) activity (Hoving et al., 2014; Sancho & Reis e Sousa, 2012). In this case, the CTLD is a carbohydrate recognition domain (CRD), which encompasses four Ca<sup>2+</sup> binding sites. Ligand recognition and specificity is determined at site 2, which contains two amino acids with long carbonyl side chains

separated by a *cis*-proline and is responsible for specific binding of individual monosaccharides. In this way, CRDs can be separated in one group that contains an EPN (glutamate-proline-asparagine) motif and confers specificity for mannose-based ligands and another group with an QPD (glutamine-proline-aspartic acid) motif with preference for galactose-based ligands (Kingeter & Lin, 2012; Sancho & Reis e Sousa, 2012; Zelensky & Gready, 2005). Different ligand specificity is well exemplified by the prominent family members Dectin-1 (dendritic cell-associated C-type lectin 1), Dectin-2, and Mincle (macrophage inducible Ca<sup>2+</sup>-dependent lectin receptor), which preferentially bind to  $\beta$ -glucan, high mannose, and  $\alpha$ -mannose, respectively (Kingeter & Lin, 2012).

Based on the cytoplasmic tail, CLRs can be further classified as activating and Syk (spleen tyrosine kinase)-coupled CLRs, inhibitory CLRs, and CLRs without clear cytoplasmic motifs for signal transduction. Activation of Syk can be indirect via the interaction with adaptor proteins that contain a Syk-recruiting immunoreceptor tyrosine-based activation motif (ITAM), or direct in case the CLR cytoplasmic tail comprises an ITAM motif itself (Hoving et al., 2014; Sancho & Reis e Sousa, 2012). Activated Syk can promote NF- $\kappa$ B, MAPK, and Ca<sup>2+</sup>-NFAT (calcineurin-nuclear factor of activated T-cells) signaling for the production of pro-inflammatory cytokines and phosphorylation of ASC (apoptosis-associated speck-like protein containing a CARD), which is an important adaptor protein in inflammasomal signaling (Goodridge et al., 2007; Hara et al., 2013; Hoving et al., 2014; Sancho & Reis e Sousa, 2012). Indeed, activation of Dectin-1 and Dectin-2 additionally triggers ROS production and potassium efflux, which are known activators of the NLRP3 inflammasome (Kankkunen et al., 2010; Sancho & Reis e Sousa, 2012). Inhibitory CLRs bear an immunoreceptor tyrosine-based inhibitory motif (ITIM), which upon activation, recruits the tyrosine phosphatases SHP-1 (Src homology 2 domain-containing protein tyrosine phosphatase 1) and SHP-2 to modulate signaling induced by other PRRs (Hoving et al., 2014; Sancho & Reis e Sousa, 2012). CLRs without a cytoplasmic signaling domain are mainly implicated in endocytic activity and antigen presentation but can in some cases also have similar modulating functions as ITIM-containing CLRs (Sancho & Reis e Sousa, 2012). However, the mechanism was only clarified for DC-SIGN (dendritic cell-specific intercellular adhesion molecule-3-grabbing non-integrin), which can oligomerize and activate a kinase called RAF-1 (rapidly accelerated fibrosarcoma 1) to positively modulate TLR signaling (Gringhuis et al., 2007; Valverde et al., 2020).

#### **1.2.4 RIG-I-like receptors**

The RLR family encompasses three known members: RIG-I (retinoic acid-inducible gene-I), MDA5 (melanoma differentiation-associated protein 5), and LGP2 (laboratory of genetics and physiology 2). They are all described to mediate antiviral immune responses by the recognition of viral dsRNA in the cytosol (Hartmann, 2017). RIG-I consists of a central DExD/H helicase domain with ATPase and helicase activity, two N-terminal CARD effector domains, a repressor domain (RD) and a C-terminal domain (CTD) for ligand binding (Li & Wu, 2021). In the resting state the RD interacts with one of the CARDS to keep the protein in an autoinhibited conformation (Saito et al., 2007). Upon RNA binding at the helicase domain and the CTD, conformational change and ATP hydrolysis mediate activation and subsequent exposure of CARDS for oligomerization and signal transduction (Li & Wu, 2021; Patel et al., 2013). Notably, ATP hydrolysis is further able to displace bound self-RNA from RIG-I, which prevents unintended activation and signaling (Lassig et al., 2015). MDA5 has basically the same domain architecture but misses the RD, whereas LGP2 does not comprise CARDS (Li & Wu, 2021). Thus, LGP2 is not able to signal itself but interacts with RIG-I or MDA5 to regulate their antiviral immune responses (Rehwinkel & Gack, 2020).

RIG-I and MDA5 can recognize short and long-chain dsRNA, respectively. In detail, RIG-I is capable of recognizing uncapped and unmethylated 5'-triphosphate or 5'-diphosphate dsRNA (3pRNA or 2pRNA) that is typical for some viruses but mostly capped or modified in eukaryotes (Goubau et al., 2014; Hornung et al., 2006; Lu et al., 2010; Schmidt et al., 2009; Schuberth-Wagner et al., 2015). MDA5 recognizes a specific sequence corresponding to the L region antisense RNA of encephalomyocarditis virus (Deddouche et al., 2014). Activated RIG-I or MDA5 can bind to downstream signaling molecules such as MAVS via homotypic CARD interactions to mediate the activation of the transcription factors NF- $\kappa$ B, IRF3, and IRF7, which finally drive the expression of pro-inflammatory cytokines and type I IFNs (Yoneyama & Fujita, 2009).

#### **1.2.5 AIM2-like receptors**

In healthy conditions, DNA is confined to the nucleus and mitochondria, whereas cytosolic DNA is rapidly degraded by endogenous nucleases. However, during infection or cellular damage, DNA can accumulate in the cytosol (Hopfner & Hornung, 2020). ALRs are cytosolic receptors that recognize the presence of intracellular foreign or self-

DNA. They comprise an N-terminal PYD domain and one or two C-terminal HIN (acronym for hematopoietic expression, IFN-inducible nature, and nuclear localization) domains responsible for the direct recognition of dsDNA (Li & Wu, 2021). In contrast to other receptors of intracellular DNA, activation of ALRs does not induce an IFN response (Gray et al., 2016). As demonstrated for AIM2 and IFI16 (IFN- $\gamma$ -inducible protein 16), ligand binding liberates the autoinhibited conformation to induce oligomerization and subsequent inflammasomal signaling via the PYD (Jin et al., 2012; Zheng et al., 2020).

### 1.2.6 Other PRRs

Further important PRRs that have not been classified include the Pypin protein and cGAS (cyclic GMP-AMP synthase). The Pypin protein is eponymous for the PYD domain, which is also contained at its N-terminus. The protein includes an additional basic leucine zipper (bZIP) transcription factor domain, two overlapping nuclear localization signals (NLS), a B-box domain, an  $\alpha$ -helical coiled-coil domain, and a C-terminal B30.2 domain (Schnappauf et al., 2019). As for many other PRRs, the PYD domain is implicated in inflammasome formation (Richards et al., 2001). In contrast, the B30.2 domain was shown to directly interact with caspase-1 and attenuate its activation (Chae et al., 2006). The B-box and PYD domains form intramolecular interactions in an autoinhibited state, which results in coiled-coil domain-mediated homotrimer formation of Pypin. Additionally, Pypin was shown to interact with PSTPIP1 (proline serine threonine phosphatase interacting protein 1), which might release the PYD and thus functionally link Pypin activation with cytoskeleton organization (Yu et al., 2007). While full-length Pypin is mainly located in the cytoplasm, a shorter variant lacking a domain encoded by exon 2 can translocate to the nucleus (Papin et al., 2000). Pypin is also a substrate of caspase-1. The N-terminal cleavage fragment can interact with the p65 subunit of NF- $\kappa$ B and promote its activation and translocation to the nucleus. This interaction is thought to be mediated by the bZIP transcription factor domain (Chae et al., 2008). Activation of the Pypin inflammasome is downstream of pathogen-induced inactivation of host Rho GTPases (Ras homolog [Rho] guanosine triphosphatases). Mechanistically, RhoA-dependent serine/threonine-protein kinase N1 (PKN1) and PKN2 phosphorylate Pypin, which facilitates interaction with 14-3-3 chaperones that stabilize Pypin in the inactive state. Decreased phosphorylation results in release of 14-3-3 proteins and concomitant activation of the Pypin inflammasome (Gao et al., 2016; Park et al., 2016).

Similar to ALRs, cGAS was identified as a sensor of cytoplasmic DNA. It comprises an unstructured and highly basic N-terminal domain and a more globular C-terminal domain that contains a catalytic nucleotidyltransferase (NTase) core domain and a Mab21 domain that facilitates direct binding of dsDNA (Wu et al., 2014). Under resting conditions, cGAS predominantly resides in the nucleus and is tightly sequestered to chromatin or associated with the inner leaflet of the plasma membrane, which is thought to enable discrimination between self and non-self. Its localization preference to membranes is thought to be mediated by the N-terminal domain, which can interact with phosphatidylinositol 4,5-bisphosphate (Barnett et al., 2019; Volkman et al., 2019). The NTase domain folds into two structural lobes that form the active site at their interface and contain a catalytic activation loop that becomes only suitably structured for the enzymatic reaction upon DNA binding (Civril et al., 2013). To obtain the final catalytic active state, two cGAS proteins need to dimerize and sandwich two DNA strands in between (Li et al., 2013; X. Zhang et al., 2014). However, not all DNA molecules that bind to cGAS fully activate the receptor. New insights revealed that a certain length threshold allows for the formation of oligomeric complexes on the same DNA molecule that drive LLPS, which might have consequences for cGAS activity (Du & Chen, 2018; Hopfner & Hornung, 2020). Activated cGAS synthesizes the second messenger cyclic GMP-AMP (cGAMP) from ATP and GTP. cGAMP is sensed by STING (stimulator of IFN genes), which is a dimeric transmembrane protein at the endoplasmic reticulum (ER). Following, STING undergoes conformational change and translocates to the Golgi where it activates TBK1, which in turn drives phosphorylation of IRF3 resulting in induction of type I IFN expression (Hopfner & Hornung, 2020; Ishikawa & Barber, 2008).

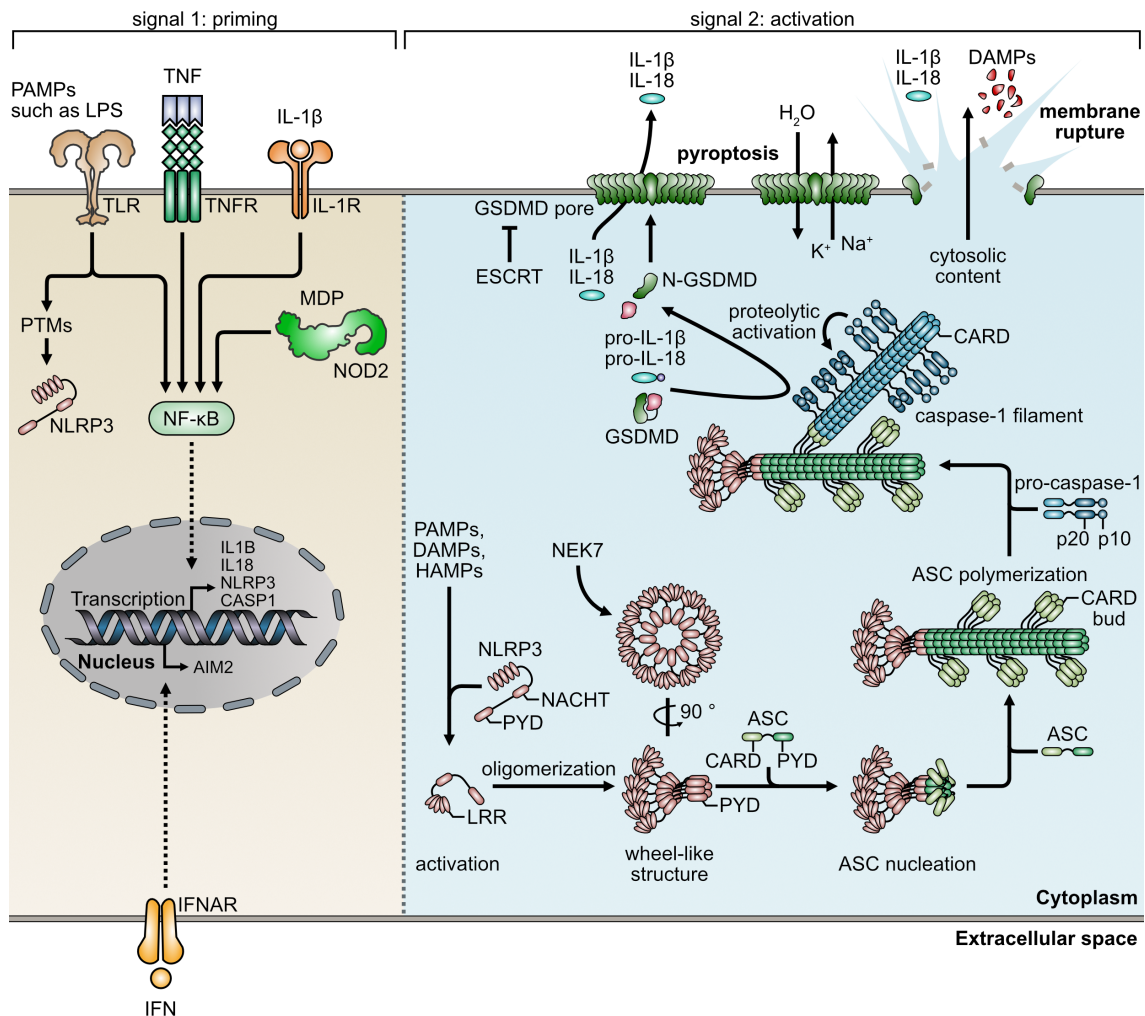
Finally, the innate immune system also comprises many soluble and extracellular pattern recognition molecules, including pentraxins, collectins, and ficolins, which bind to pathogens and function through complement activation, opsonization, aggregation, or modulation of cellular PRRs (Li & Wu, 2021).

### **1.3 The inflammasome – a multiprotein complex**

The term ‘inflammasome’ was originally coined by Martinon and colleagues in 2002, who introduced a newly discovered caspase-activating complex – the NLRP1 inflammasome (Martinon et al., 2002). Since then, follow-up studies identified a number of distinct inflammasomes, assembled upon recognition of PAMPs, DAMPs, or HAMPs

by individual PRRs (see previous section). The current model of inflammasome formation involves a two-step mechanism where each signal acts as a critical regulatory checkpoint for activation (Figure 1-4). This is best studied for the prototypic NLRP3 inflammasome but was also basically reported for other inflammasomes, including NLRC4 or AIM2 (Latz et al., 2013; Zheng et al., 2020). The first signal, also referred to as ‘priming’, is provided upon activation and signal transduction of certain PRRs (such as TLRs or NOD2), cytokine receptors (such as TNFR or IL-1R), or other receptors that culminate in the activation of the NF- $\kappa$ B and MAPK signaling pathways (Paik et al., 2021; Swanson et al., 2019). NF- $\kappa$ B as a transcription factor induces transcriptional upregulation of inflammasome components, such as pro-IL-1 $\beta$ , pro-IL-18, pro-caspase-1, and the sensor protein e.g., NLRP3 (Bauernfeind et al., 2009; Lee et al., 2015; McKee & Coll, 2020). Similarly, other inflammasome sensors, such as AIM2, are transcriptionally upregulated downstream of IFN signaling via the IFN- $\alpha/\beta$  receptor (IFNAR) (F. Liu et al., 2017). Of note, pro-IL-18 is constitutively expressed in many cells but its expression can be further increased and sustained by TLR signaling (Zhu & Kanneganti, 2017). Furthermore, priming activates certain enzymes that regulate post-translational modifications (PTMs) on inflammasome components, which enable activation and assembly into the inflammasome complex (McKee & Coll, 2020; Song et al., 2017).

Priming was shown to be dispensable for activating the NLRP3 inflammasome in human monocytes, which express low levels of basal NLRP3. Treatment of monocytes with the potassium ionophore nigericin in an unprimed setting did result in robust NLRP3 inflammasome formation as well as maturation and release of constitutively expressed IL-18. Interestingly, this observation was strictly cell dependent, as NLRP3 activation in monocyte-derived macrophages required priming (Gritsenko et al., 2020). Another study revealed the possibility of immediate priming of NLRP3 via IRAK-1 together with rapid caspase-1 activation in response to specific TLR stimuli and extracellular ATP, suggesting that both receptors can be activated simultaneously and independent from *de novo* protein synthesis to mediate early host defense (Fernandes-Alnemri et al., 2013; Fitzgerald & Kagan, 2020; Lin et al., 2014). Another exception to the two-step activation model is the sustained stimulation of TLR4 with LPS, which drives an alternative NLRP3 inflammasome pathway that relies on TLR4-TRIF-RIPK1-FADD (Fas-associated death domain protein)-caspase-8 signaling and leads to processing of IL-1 $\beta$ , which occurs independently of ASC speck formation, pyroptosis, potassium efflux, or activation of the purinergic P2X7 ATP-gated ion channel (Kelley et al., 2019; Swanson et al., 2019).



**Figure 1-4: Current model of canonical inflammasome formation.** Inflammasome formation is a two-step mechanism. The initial priming step (signal 1) involves the activation of certain immune receptors, such as TLRs, TNFR, IL-1R, or NOD2. Signal transduction culminates in the activation of the transcription factor NF- $\kappa$ B and transcriptional upregulation of typical inflammasome components. Additionally, activity of specific enzymes that mediate necessary post-translational modifications of the inflammasome receptor is induced. Other components including AIM2 are transcriptionally upregulated upon IFN signaling via IFNAR. The activation step (signal 2) includes the recognition of intracellular PAMPs, DAMPs, or HAMPs and subsequent assembly of the inflammasome complex, which is here exemplified for the prototypic NLRP3 inflammasome. Upon ligand sensing and activation, NLRP3 undergoes conformational change and assembles into an oligomeric structure. Based on structural studies on inflammasome complexes, NLRP3 might form wheel-like structures similarly as seen for NLRC4. At this stage adapter proteins, such as NEK7, might be required to mediate intermolecular interactions that bridge adjacent subunits, thereby stabilizing the oligomer. The oligomeric assembly provides a nucleation seed for polymerization of ASC, which interacts with NLRP3 via homotypic PYD interactions. The ASC<sup>PYD</sup> forms filaments surrounded by ASC<sup>CARD</sup> buds that in turn serve as a platform for the recruitment and polymerization of pro-caspase-1. Proximity-induced proteolytic activation results in catalytically active caspase-1, which cleaves precursors of the pro-inflammatory cytokines IL-1 $\beta$  and IL-18 into their mature biologically active form. Caspase-1 also cleaves GSDMD, thereby releasing the pore forming N-terminal fragment from the autoinhibiting C-terminus. N-GSDMD inserts into membranes where it undergoes conformational change and forms large oligomeric transmembrane pores, which allow the passage of cytokines and preferably small cations such as potassium and sodium ions. The GSDMD pore further allows free diffusion of water across the osmotic gradient leading to rapid swelling of the cell and eventually membrane rupture. GSDMD-mediated membrane pores can be repaired by the ESCRT machinery. In case of membrane rupture, cytosolic content including pro-inflammatory cytokines and DAMPs are released from the cell and can be sensed by recipient immune cells. This specific morphotype of caspase-1-mediated cell-death was termed pyroptosis. Figure is modified from (Broz & Dixit, 2016; Swanson et al., 2019). PAMPs: pathogen-associated molecular pattern, DAMPs: damage-associated molecular pattern, HAMPs: homeostasis-altering molecular processes, LPS:

lipopolysaccharide, TNF: tumor necrosis factor, IL-1 $\beta$ : interleukin-1 $\beta$ , IL-18: interleukin-18, IFN: interferon, MDP: muramyl dipeptide, TLR: Toll-like receptor, TNFR: TNF receptor, IL-1R: IL-1 receptor, IFNAR: IFN- $\alpha/\beta$  receptor, PTM: post-translational modification, NOD2: nucleotide-binding and oligomerization domain-containing protein 2, NLRP3: NOD-like receptor containing a Pyrin domain 3, NF- $\kappa$ B: nuclear factor  $\kappa$ B, IL1B: IL-1 $\beta$  gene, IL18: IL-18 gene, CASP1: caspase-1 gene, AIM2: absent in melanoma 2, PYD: Pyrin domain, NACHT: acronym for NAIP, CIITA, HET-E, and TP1, LRR: leucine-rich repeat, CARD: caspase activation and recruitment domain, ASC: apoptosis-associated speck-like protein containing a CARD, GSDMD: gasdermin D, N-GSDMD: N-terminal cleavage fragment of GSDMD, H<sub>2</sub>O: water, K<sup>+</sup>: potassium ion, Na<sup>+</sup>: sodium ion, ESCRT: endosomal sorting complexes required for transport, NEK7: NIMA-related kinase 7.

Activation of the PRR by signal two triggers a conformational switch from the inactive to the active conformer with concomitant self-oligomerization into wheel-like structures that recruit the adaptor protein ASC via homotypic death-fold domain interactions (Martinon et al., 2009). Such oligomers were initially hypothesized due to the relationship between inflammasomes and apoptosomes (Broz & Dixit, 2016; Martinon et al., 2009) and finally confirmed for NLRs by biochemical and cryogenic (cryo)-electron microscopy studies on purified flagellin-NAIP5-NLRC4 and PrgJ-NAIP2-NLRC4 complexes (Diebolder et al., 2015; Halff et al., 2012; Hu et al., 2015; Tenthorey et al., 2017; Zhang et al., 2015). However, ALR family inflammasome sensors that lack the NACHT domain might assemble in a different manner. A structural study of HIN domain-DNA complexes proposed the sensed dsDNA itself to act as an oligomerization scaffold in ALR inflammasome assembly (Jin et al., 2012).

ASC consists of two death-fold domains: PYD-CARD. Upon nucleation at PRR oligomers, polymerization of ASC<sup>PYD</sup> into filaments and cross-linking of these filaments by homotypic ASC<sup>CARD</sup> interactions results in the formation of a large perinuclear structure termed the ASC speck. This micrometer-sized structure is a hallmark of inflammasome formation and acts as a platform for the recruitment and proximity-induced autoprocessing of caspase-1 (Broz & Dixit, 2016; Dick et al., 2016). Importantly, a recent cryo-EM tomography study of the physiological ASC speck confirmed these observations and provided additional insights of the structural organization and potential dynamics within the ASC network (Liu et al., 2021). Interestingly, CARD-containing receptors (such as NAIP/NLRC4, NLRP1) can also directly recruit and activate caspase-1 in the absence of ASC, but presence of ASC increases the processing of the pro-inflammatory cytokine IL-1 $\beta$  by presumably providing a vast number of caspase-1 activation sites (Broz & Dixit, 2016; Dick et al., 2016). Recently, also caspase-8 was found to bind to ASC via FADD, which mediates apoptosis (Zheng et al., 2020).



Caspases are a family of cysteine proteases that are central players in inflammation and apoptosis. In humans, inflammatory caspases include caspase-1, caspase-4, caspase-5, and caspase-12. They consist of an N-terminal CARD domain and a C-terminal protease effector domain, which is formed by a large and a small subunit. During resting state, caspase-1 exists as an inactive zymogen in the cytosol of the cell but after dimerization and proteolytic activation it cleaves the pro-inflammatory cytokines IL-1 $\beta$  and IL-18 into their mature biologically active form (Man & Kanneganti, 2016; Schroder & Tschopp, 2010). In detail, dimers of full-length caspase-1 (p46) and a transient species produced by autolytic cleavage (p33/p10 heterotetramer) represent the active forms at the inflammasome. Further processing into the p20/p10 heterotetramer removes the CARD domain from the p33 fragment and results in dissociation from the inflammasome. Protease activity is subsequently terminated due to intrinsic instability of the p20/p10 heterotetramer thus self-limiting the duration of caspase-1 activity (Boucher et al., 2018).

Caspase-1 can also cleave gasdermin D (GSDMD), which comprises a cytotoxic N-terminal domain and an autoinhibitory C-terminal domain similar to other gasdermin family members (Broz et al., 2020). Cleavage of GSDMD by caspase-1 releases the N-terminal fragment, which in turn inserts into membranes and undergoes conformational change to subsequently form large oligomeric transmembrane pores of 10-20 nanometer (nm) diameter that ultimately drive pyroptosis and the release of pro-inflammatory cytokines (Burdette et al., 2021; He et al., 2015; X. Liu et al., 2016; Shi et al., 2015; Xia et al., 2021). As a consequence of plasma membrane permeabilization, ions and water can diffuse freely across the cellular osmotic gradient and cause a rapid swelling of the cell that finally results in membrane rupture and release of the cytosolic content (Jorgensen & Miao, 2015). While cell-death related membrane rupture was thought to be a rather passive event, a recent study suggests that the process relies on disruption of the phospholipid bilayer following oligomerization of the transmembrane protein Ninjurin 1 (Kayagaki et al., 2021). However, the exact mechanism remains to be elucidated. Interestingly, inflammasome complexes released from pyroptotic cells can themselves act as DAMPs and are phagocytosed by nearby macrophages. In the recipient cell they induce lysosomal damage, exit the phagolysosome, recruit the cytosolic ASC from the recipient cell, and propagate the inflammatory response (Baroja-Mazo et al., 2014; Franklin et al., 2014). Additionally, extracellular ATP is well known to stimulate potassium efflux via the P2X7 receptor, which activates NLRP3 (Munoz-Planillo et al., 2013; Schroder & Tschopp, 2010). Noteworthy, GSDMD-mediated membrane pores can be repaired by the

ESCRT (endosomal sorting complexes required for transport) machinery, which is recruited to the site of membrane damage by calcium ion ( $\text{Ca}^{2+}$ ) influx through GSDMD pores (Ruhl et al., 2018). In this context, it was found that macrophages can release IL-1 $\beta$  while maintaining viability – a condition termed hyperactivation (Evavold et al., 2018). Two independent studies demonstrated that GSDMD pores were required for the release of IL-1 $\beta$  and IL-18 across the intact plasma membrane (Evavold et al., 2018; Heilig et al., 2018). While Heilig and colleagues proposed that the GSDMD pore is large enough to facilitate passive release of small cytosolic proteins, a more recent structural study of the GSDMD pore revealed that the pore conduit is predominantly negatively charged (Xia et al., 2021). This study demonstrated that secretion of mature cytokines is preferred over their respective precursors that still contain the acidic pro-domain. Thus, GSDMD pores might only license the secretion of cargo with a specific size and charge.

### **1.3.1 Non-canonical inflammasome formation**

The term ‘non-canonical inflammasome’ describes a TLR4-independent signaling pathway that indirectly activates the NLRP3 inflammasome upon recognition of cytoplasmic LPS (Kelley et al., 2019; Swanson et al., 2019). Human caspase-4 and caspase-5 or murine caspase-11 are able to act as cytoplasmic PRRs that directly bind to and thereby recognize pentacylated or hexacylated LPS (Baker et al., 2015; Hagar et al., 2013; Shi et al., 2014). Because human cells constitutively express high levels of caspase-4, priming is dispensable for this pathway. In contrast, murine caspase-11 is expressed at low basal level. Thus, priming enhances the inflammatory response by transcriptional upregulation (Kelley et al., 2019). Upon LPS binding, caspase-11 was shown to oligomerize and become activated by auto-proteolytic cleavage (B. L. Lee et al., 2018). Subsequently, activated human caspase-4 and caspase-5 or murine caspase-11 cleave GSDMD, resulting in pore formation (Kayagaki et al., 2015; Shi et al., 2015).

Murine caspase-11 was also shown to cleave pannexin-1, which is essential for non-canonical inflammasome formation in mice. Pannexin-1 releases ATP from the cell, which is subsequently recognized by the P2X7 receptor (Pelegrin & Surprenant, 2006; Yang et al., 2015). It is not yet clear whether these events are also important for the formation of non-canonical inflammasomes in humans. However, P2X7 activation leads to potassium efflux and the recruitment of NLRP3 via Paxillin, culminating in inflammasome formation and the secretion of IL-1 $\beta$  (Wang, Hu, Feng, et al., 2020).

### 1.3.2 Post-translational regulation of inflammasome components

Aberrant inflammasome formation is known to drive the pathogenesis of many inflammatory disorders (Kim et al., 2016; Y. Li et al., 2021). For that reason, inflammasome formation is precisely regulated not only by transcriptional priming but also by several post-translational mechanisms some of which shall be described in this section. Regulation of the NLRP3 inflammasome is the best studied and thus prototypical example (Kelley et al., 2019; McKee & Coll, 2020; Paik et al., 2021; Swanson et al., 2019; Yang et al., 2017). Therefore, this section is mainly focused on NLRP3.

One of the key post-translational modifications (PTMs) is **ubiquitination**. Ubiquitin contains seven lysine residues that can themselves be ubiquitinated, thereby forming ubiquitin chains. Depending on the position of the linkage, ubiquitin chains can have different effects. As an example, Lys48-linked ubiquitin chains target proteins to the proteasome for degradation, whereas Lys63-linked ubiquitin chains have non-degradative roles in regulation (Swatek & Komander, 2016). Upon LPS stimulation, ABRO1 (Abraxas brother 1) binds to NLRP3 and recruits the deubiquitinating enzyme (DUB) BRCC36 (BRCA2 containing complex subunit 36; BRCC3 in rodents), which removes Lys63-linked ubiquitin from the NLRP3 LRR to allow its oligomerization (Py et al., 2013; Ren et al., 2019). Interestingly, BRCC3 was found to be blocked by vitamin D receptor (VDR) activation (Rao et al., 2019). Additionally, STING was found to recruit NLRP3 to the ER, where it activates NLRP3 by attenuating Lys48- and Lys63-linked polyubiquitination during Herpes simplex virus type 1 (HSV-1) infections (Wang, Hu, Wu, et al., 2020). Furthermore, USP7 (ubiquitin-specific peptidase 7) and USP47 were shown to function as DUBs in response to NLRP3 activation signals (Palazon-Riquelme et al., 2018). In contrast, FBXL2 (F-box/LRR-repeat protein 2), ARIH2 (Ariadne homolog 2), and TRIM31 (tripartite motif containing protein 31) facilitate proteasomal degradation by ubiquitinating NLRP3 (Han et al., 2015; Kawashima et al., 2017; Song et al., 2016). Upon LPS stimulation, FBXO3 (F-box only protein 3) mediates the degradation of FBXL2, thereby inhibiting NLRP3 ubiquitination (Han et al., 2015). However, LPS stimulation upregulates the expression of TRIM31, suggesting a negative feedback mechanism for inflammasome activation (McKee & Coll, 2020; Song et al., 2016). Another way of NLRP3 degradation is the sequential ubiquitination by the RING finger protein 125 (RNF125) and Cbl-b (Casitas B-lineage lymphoma b). First, RNF125 modifies the NLRP3 LRR with Lys63-linked polyubiquitin, which in turn recruits Cbl-b that mediates modification of Lys496 in NLRP3 with Lys48-linked ubiquitin chains, thus

promoting proteasomal degradation (Tang et al., 2020). The NLRP3 LRR is further targeted for Lys48-linked ubiquitination by the membrane-associated RING finger protein 7 (MARCH7), which mediates degradation of NLRP3 via autophagy in response to DRD1 (dopamine D1 receptor) activation (Yan et al., 2015). Two additional E3 ubiquitin ligases that modify NLRP3 are Cullin-1 (Cul1) and Pellino2 (PELI2). In resting cells, Cul1 ubiquitinates NLRP3 at Lys689, thereby inhibiting inflammasome formation in a non-degradative manner. After LPS stimulation, Cul1 dissociates from NLRP3 to allow inflammasome formation (Wan et al., 2019). PELI2 licenses NLRP3 activation by inducing Lys63-linked ubiquitination during LPS priming (Humphries et al., 2018).

Ubiquitination is also important for regulating ASC, caspase-1, and pro-IL-1 $\beta$ . Removal of Lys63-linked ubiquitin chains by USP50 (ubiquitin specific peptidase 50) is important for ASC activity (Lee et al., 2017). In contrast, ubiquitination of ASC via TRAF3 and LUBAC (linear ubiquitination assembly complex) are pivotal for inflammasome assembly (Guan et al., 2015; Rodgers et al., 2014). LUBAC can also ubiquitinate the CARD of caspase-1, which inhibits activation (Douglas & Saleh, 2020). On the other hand, LPS stimulation can induce Lys63-linked polyubiquitination of caspase-1 by cIAP1 (cellular inhibitor of apoptosis protein 1) and cIAP2, which is prerequisite for its activity (Labbe et al., 2011). Additionally, the zinc finger protein A20 regulates ubiquitination of pro-IL-1 $\beta$ , which is an essential event enabling its proteolytic processing (Duong et al., 2015).

Similar with ubiquitination, modification of NLRP3 with the small ubiquitin-like modifier (**SUMO**) regulates its activity. Sumoylation via MAPL (mitochondrial-anchored protein ligase) inhibits inflammasome formation, whereas desumoylation by SENP6 (SUMO-specific protease 6) and SENP7 allows NLRP3 activation (Barry et al., 2018). In contrast, sumoylation of Lys204 in NLRP3 by SUMO1 (small ubiquitin-related modifier 1) was found to be essential for NLRP3 activation, which can be attenuated by SENP3 (Shao et al., 2020).

**Phosphorylation** is another key PTM that regulates the activity of inflammasome components. Phosphorylation of NLRP3 at Ser5 prevents NLRP3<sup>PYD</sup>-mediated polymerization. Thus, dephosphorylation by PP2A (protein phosphatase 2A) is an important event to allow inflammasome assembly after activating signals (Stutz et al., 2017). Interestingly, PP2A activity is inhibited by BTK (Bruton's tyrosine kinase), which binds to NLRP3 following priming and dissociates after activation (Mao et al., 2020). In contrast, phosphorylation of Ser198 in NLRP3 by JNK1 (c-Jun N-terminal kinase 1) is

an essential priming event that enables deubiquitination by BRCC36 (Song et al., 2017). Additionally, LPS priming and presence of NLRP3 activating signals trigger NLRP3 phosphorylation at Ser295 via PKD (protein kinase D) at the Golgi membrane. Indeed, spatial separation of inflammasome components into different cellular compartments provides an additional level of regulation. Upon activation, NLRP3 can oligomerize and associate with mitochondria-associated ER membranes (MAMs), which localize close to Golgi membranes. Following, the concentration of diacylglycerol (DAG) at the Golgi increases, recruiting PKD to phosphorylate NLRP3 and releasing it from the membrane for subsequent inflammasome formation (Zhang et al., 2017). At the same time, PKA can also phosphorylate Ser295 in NLRP3, which in this case inhibits NLRP3 ATPase activity and oligomerization (Mortimer et al., 2016). How phosphorylation of the same residue can have opposing effects is not yet understood (Swanson et al., 2019). In addition, the NLRP3 LRR domain can be phosphorylated at Ser803 by CSNK1K1 (casein kinase I $\alpha$ 1) upon priming and later dephosphorylated upon activation. Phosphorylation at Ser803 is known to regulate the interaction with NEK7 and deubiquitination by BRCC3 (Niu et al., 2021). NLRP3 can also be phosphorylated at Tyr32 in the PYD and its dephosphorylation by PTEN (phosphatase and tensin homolog) is necessary for inflammasome formation (Huang et al., 2020). Similarly, phosphorylation of Tyr132 in murine NLRP3 by EphA2 (ephrin type-A receptor 2) inhibits inflammasome assembly (Zhang et al., 2020). Phosphorylation of Tyr861 mediates degradation of NLRP3 via autophagy and PTPN22 (protein tyrosine phosphatase non-receptor type 22) is essential for its dephosphorylation following activating stimuli (Spalinger et al., 2016; Spalinger et al., 2017). Of note, NEK7 kinase function is dispensable for NLRP3 activation (He et al., 2016).

Again, phosphorylation is also important for the regulation of other inflammasome components. The I $\kappa$ B kinase (IKK) complex can regulate the localization of ASC. Phosphorylation of Ser16 and Ser193 by IKK $\alpha$  prevents translocation from the nucleus, whereas phosphorylation at Ser58 by IKKi (IKK-related kinase) promotes localization to the perinuclear region, where ASC speck formation can be induced after LPS stimulation (Martin et al., 2014). Additionally, ASC must be phosphorylated at multiple tyrosine residues to enable speck formation and interaction with caspase-1. Syk is involved in the phosphorylation of ASC at Tyr146. Mechanistically, Syk phosphorylates Pyk2 (proline-rich tyrosine kinase 2) in response to inflammasome activating signals and Pyk2 subsequently phosphorylates ASC (Chung et al., 2016; Hara et al., 2013; McAndrew et al., 2018). In contrast, dephosphorylation of ASC at Tyr60 and Tyr137 by protein tyrosine

phosphatases (PTPases) is as well required for speck formation (Mambwe et al., 2019). Upon LPS stimulation, PAK1 (PI-3K/Rac1/p21-activated kinase 1) phosphorylates caspase-1 at residue Ser376, which promotes its activation (Basak et al., 2005). Interestingly, phosphorylation of NEK7 at Ser204 by PLK4 (polo-like kinase 4) was shown to suppress interaction with NLRP3 (Yang et al., 2020).

NLRP3 activation is also regulated by **acetylation** of residues Lys21 and Lys22, which is mediated by KAT5 (lysine acetyltransferase 5) and can be removed by the deacetylase sirtuin 2 (SIRT2) (He et al., 2020; McKee & Coll, 2020). Other important but less characterized PTMs that regulate inflammasome components include **S-nitrosylation**, **alkylation**, **ADP-ribosylation**, and **deglutathionylation** (McKee & Coll, 2020).

Noteworthy, inflammasomes are also regulated by a set of **proteins**. Hsp90 (heat shock protein 90) protects NLRP3 from degradation via the proteasome and autophagy (Mayor et al., 2007; Piippo et al., 2018). NEK7 is not only implicated in NLRP3 inflammasome formation but also in mitosis and thus coordinates both events to be mutually exclusive because a limiting amount of cellular NEK7 does not allow both events to occur at the same time (H. Shi et al., 2016). Additionally, a number of PYD-only proteins (POPs) and CARD-only proteins (COPs) act as cytoplasmic decoy proteins that interact with PYDs and CARDS of inflammasome components, thus blocking homotypic interactions essential for functional inflammasome assembly (Indramohan et al., 2018; McKee & Coll, 2020). This is indeed reminiscent of some actin-binding proteins that regulate the formation of the actin filament (Lee & Dominguez, 2010). Interestingly, POPs and COPs are not expressed in rodents, indicating a more complex regulation of inflammasomes in humans (McKee & Coll, 2020; Swanson et al., 2019).

### 1.3.3 Release of pro-inflammatory cytokines – What's next?

The IL-1 cytokine family encompasses 11 members from which some are known to function as pro-inflammatory signaling molecules (e.g., IL-1 $\beta$ , IL-18), whereas others are known receptor antagonists (e.g., IL-1RA) or anti-inflammatory mediators (e.g., IL-37) (Dinarello, 2018). While most cytokines (e.g., TNF, IL-10) comprise a signal sequence that targets them to ER/Golgi-dependent secretory pathways, some of them act differently (Monteleone et al., 2015). In addition to IL-1 $\beta$  and IL-18, IL-37 is activated by caspase-1, leading to its nuclear translocation and transcriptional suppression of pro-inflammatory mediators (Bulau et al., 2014; Nold et al., 2010), which might likely represent a negative

feedback loop in response to inflammasome activation. IL-1 $\beta$  and IL-18 are so called leaderless secretory signaling molecules, which means that they lack the signal sequence for the ER/Golgi route and are released via unconventional mechanisms (Monteleone et al., 2015). In recent years, three different mechanisms have been proposed, including inflammasome-dependent and independent pathways (Monteleone et al., 2018). As described before, mature IL-1 $\beta$  and IL-18 can be released via GSDMD pores or upon membrane rupture downstream of inflammasome formation (Cullen et al., 2015; Evavold et al., 2018). Interestingly, GSDMD and mature IL-1 $\beta$  (but not its inactive precursor) were shown to be recruited to membrane ruffles enriched in phosphatidylinositol phosphates, thus enabling rapid secretion (Ding et al., 2016; X. Liu et al., 2016; Monteleone et al., 2018). In contrast, slow secretion of IL-1 $\beta$  was revealed to be in fact dependent on caspase-1 but independent from GSDMD pores and membrane permeabilization. Instead, EEA1 (endosome autoantigen 1), which is also a target of caspase-1, was found to be implicated in a pyroptosis-independent vesicular secretion pathway (Baroja-Mazo et al., 2019; Semino et al., 2018). If also IL-18 can follow this route for its secretion is currently unknown.

The family of IL-1 receptors contains 10 members, which are all integral membrane proteins that share a similar domain architecture. They comprise extracellular immunoglobulin (Ig)-like domains for the binding of cytokines and a cytosolic TIR domain for signaling (Garlanda et al., 2013). After secretion, IL-1 $\beta$  binds to IL-1R1 and induces a conformational change that allows interaction with IL-1R3. Similar with TLR signaling, heterodimer formation leads to approximation of the TIR domains and signal transduction via the MyD88 adapter, which culminates in NF- $\kappa$ B activation (Dinarello, 2018). As a consequence, the production of several inflammatory mediators is induced. Transcriptional upregulation of COX-2 (cyclooxygenase type 2), PLA2 (phospholipase A2), and iNOS (inducible nitric oxide synthase) leads to the production of prostaglandin-E2 (PGE2), platelet activating factor, and nitric oxide (NO), which are classical mediators of fever, lowered pain threshold, vasodilation, and hypotension. Additionally, IL-1 $\beta$  increases the expression of cell adhesion molecules, chemokines, and cytokines that collectively recruit tissue-infiltrating immune cells to the site of damage or infection and amplify the synthesis of acute-phase proteins via IL-6 in the liver (Dinarello, 2009; Garlanda et al., 2013; Rider et al., 2011). Importantly, cytokines that are transcriptionally upregulated by IL-1 $\beta$  include IL-1 $\beta$  itself, which results in more persistent upregulation as if compared with stimulation by microbial ligands (Dinarello, 2018). Interestingly,

IL-1 $\beta$  signaling can be antagonized by soluble IL-1R3 or the decoy receptor IL-1R2, which lacks the cytoplasmic signaling domain and exists as both a soluble or an integral membrane protein (Dinarello, 2018). In addition, not all cells constitutively express both components of the IL-1 receptor, thus signaling can be regulated transcriptionally (Dinarello et al., 2013).

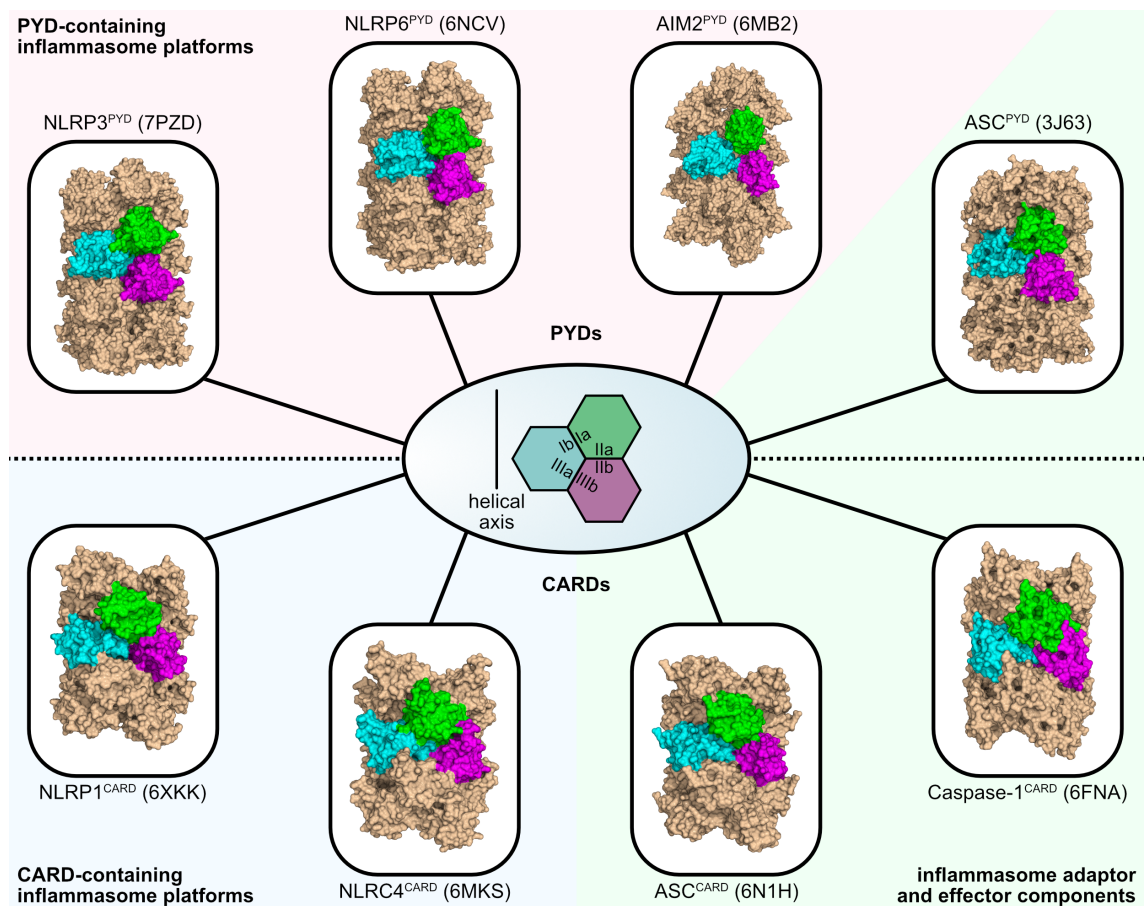
In many aspects IL-18 functions similar to IL-1 $\beta$  and signaling accounts for the same downstream effects. After secretion, IL-18 binds to its receptor IL-1R5, which forms a heterodimer with IL-1R7. Interestingly, the affinity towards IL-1R5 is low but significantly increased in the presence of IL-1R7. Again, approximation leads to signaling via the adapter MyD88 and nearly the same downstream effects as described for IL-1 $\beta$  (Dinarello, 2018; Dinarello et al., 2013). However, there are also differences. First, IL-18 precursor is constitutively expressed in macrophages and dendritic cells but also endothelial cells, keratinocytes, and intestinal epithelial cells, whereas IL-1 $\beta$  is mainly expressed upon stimulation in myeloid cells (Dinarello, 2018; Mantovani et al., 2019). Second, much higher concentrations of IL-18 are needed for the formation of a functional signaling complex as if compared with IL-1 $\beta$  (Dinarello et al., 2013). Third, IL-18 fails to induce fever because levels of COX-2 are not upregulated, suggesting that IL-18 primarily activates the MAPK signaling pathway instead of NF- $\kappa$ B (Lee et al., 2004). Fourth, IL-18 can act in concert with either IL-12 or IL-15 (which upregulate IL-1R7) to induce the production of IFN $\gamma$  in T helper (Th) and natural killer (NK) cells (Dinarello et al., 2013; Novick et al., 2013). However, in the absence of IL-12 but presence of IL-2 or IL-3, IL-18 also facilitates stimulation of NK, NKT, and Th1 cells or mast cells and basophils, respectively to produce diverse sets of cytokines (Nakanishi, 2018). Similar with IL-1 $\beta$ , signaling can be transcriptionally regulated because not all cells constitutively express IL-1R7, or antagonized with secretion of the decoy receptor IL-18BP (IL-18 binding protein) that comprises a single IgG domain for the binding of IL-18 but no cytoplasmic tail for signaling (Dinarello, 2018; Dinarello et al., 2013).

In conclusion, both IL-1 $\beta$  and IL-18 regulate a number of important immune processes that are generally host-protective during damage or infection but detrimental when dysregulated. IL-1 responses are implicated in contributing to the pathology of several hereditary autoinflammatory and acquired chronic inflammatory diseases, including cryopyrin-associated periodic syndromes (CAPS), familial Mediterranean fever (FMF), TNF receptor-associated periodic syndrome (TRAPS), rheumatoid arthritis, osteoarthritis, gout, and type 2 diabetes (Chan & Schroder, 2020).



### 1.3.4 Structural aspects of inflammasome assembly

Assembly of inflammasomes as supramolecular complexes critically relies on events of homotypic and heterotypic interactions between PYDs or CARDs of the individual inflammasome components (Broz & Dixit, 2016; Malik & Kanneganti, 2017). During the last years, biochemical and structural studies helped to deepen our molecular understanding of their assembly and identified unified mechanisms of nucleated polymerization, explaining the observed ‘all or none’ response kinetics (Cheng et al., 2010; Lu & Wu, 2015). Similar with death domains (DDs), PYDs and CARDs can assemble into filaments via three conserved asymmetric interfaces (type I, II, and III) that form respective intra- and interstrand interactions between subunits (Ferrao & Wu, 2012; Kersse et al., 2011; Lu et al., 2014) (Figure 1-5). However, subunits of PYD or CARD filaments show significant differences in their relative orientation when compared with their DD filament counterparts (Lu et al., 2014).



**Figure 1-5: PYD and CARD filaments formed by inflammasome components.** Inflammasome formation and inherent signal transduction relies on nucleated polymerization mechanisms of PYDs and CARDs. These domains are contained in each inflammasome component, which can be categorized into PYD-containing inflammasome platforms, CARD-containing inflammasome platforms, inflammasome adaptors, and effector components. PYD filaments commonly assemble with three-start helical symmetry

and right-handed rotation, whereas CARD filaments typically possess one-start helical symmetry and left-handed rotation. Independent from these different helical parameters, filament assembly is mediated by conserved type I, II, and III asymmetric interfaces. The type I interface is established between two subunits that form intrastrand interactions (blue and green). Type II and III interactions occur between subunits of different strands (type II: green and magenta; type III: blue and magenta). The code in brackets represents the PDB identifier of the respective filament structure. NLRP: NOD-like receptor containing a Pyrin domain, PYD: Pyrin domain, AIM2: absent in melanoma 2, CARD: caspase activation and recruitment domain, ASC: apoptosis-associated speck-like protein containing a CARD, NLRC: NOD-like receptor containing a CARD.

PYDs of NLRP3, NLRP6, AIM2, and ASC commonly polymerize with three-start helical symmetry of  $\sim 54.8^\circ$  right-handed rotation and an axial rise of  $\sim 14$  Å per subunit, whereas CARDS of NLRP1, NLRC4, ASC, and caspase-1 commonly assemble into filaments with one-start helical symmetry of approximately  $-100.5^\circ$  left-handed rotation and  $\sim 5.1$  Å axial rise per subunit (Gong et al., 2021; Hochheiser, Behrmann, et al., 2022; Li et al., 2018; Lu et al., 2016; Lu et al., 2014; Matyszewski et al., 2018; Matyszewski et al., 2021; Shen et al., 2019). An exception to this was the finding that the AIM2<sup>PYD</sup> assembles into a filament with one-start helical symmetry of  $138.9^\circ$  right-handed rotation and an axial rise of 6 Å per subunit when a GFP (green fluorescent protein) tag was introduced at the N-terminus (Lu et al., 2015). This completely different filament architecture was proposed to be induced due to steric restraints caused by the tag. Interestingly, filament assembly was still mediated by type I interactions forming intrastrand contacts, and type II and type III interactions forming interstrand contacts, suggesting plasticity in filament assembly and tolerance to different helical parameters. This is supported by the fact that tagged AIM2<sup>PYD</sup> or NLRP6<sup>PYD</sup> can still induce ASC<sup>PYD</sup> polymerization (Lu et al., 2015).

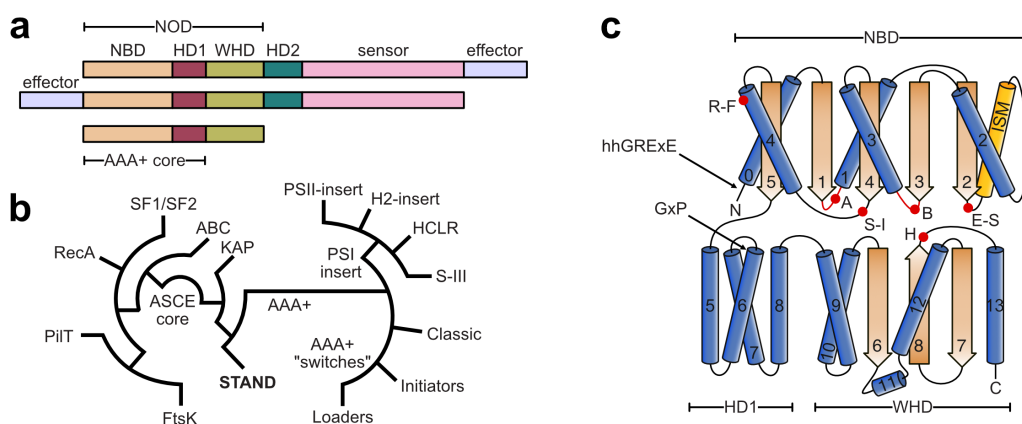
Indeed, one key finding made by different studies was the capability of PYD and CARD filaments to mediate signal transduction by nucleating polymerization of PYDs or CARDS from other inflammasome components. This heterotypic transition appears along the helical trajectory of the nucleating filament and is mediated by the same asymmetric interfaces that also facilitate homotypic interactions, thus providing a structural template for ensuing polymerization (Lu et al., 2014; Lu & Wu, 2015). Using a fluorescence polarization assay and negative stain EM, Lu and colleagues showed that substoichiometric amounts of recombinant AIM2 or NLRP3 nucleate unidirectional formation of ASC<sup>PYD</sup> filaments through PYD-PYD interactions. Indeed, site-directed mutagenesis of selected residues in AIM2<sup>PYD</sup> and NLRP3<sup>PYD</sup> reduced or impaired their ability to promote ASC<sup>PYD</sup> polymerization. In addition, presence of oligomerized ASC<sup>CARD</sup> was found to promote the polymerization of caspase-1<sup>CARD</sup> into filaments,

suggesting a unified mechanism of nucleated polymerization (Lu et al., 2014). Later, Li and colleagues showed that not only ASC<sup>CARD</sup> but also NLRC4<sup>CARD</sup> is able to nucleate caspase-1 polymerization and that the transition is again disrupted when asymmetric interfaces are mutated (Li et al., 2018). Importantly, NLRC4<sup>CARD</sup> can also engage ASC<sup>CARD</sup> and seed its polymerization (Gong et al., 2021; Man et al., 2014). In terms of signal amplification, this is advantageous because in this way one NLRC4 oligomer can seed not only one filament of caspase-1 but ASC, which can subsequently crosslink with other filaments to form a platform with multiple caspase-1 nucleation sites. Mechanistically, self-polymerization can occur in a bidirectional manner, whereas the transition from one filament to another is unidirectional (Hochheiser, Behrmann, et al., 2022; Lu et al., 2014; Matyszewski et al., 2021). This is because the type II interface is critically involved in the recognition of the engaged inflammasome component (Matyszewski et al., 2021). In line, a specific motif on the type IIb surface of NLRP1<sup>CARD</sup> was found to be responsible for its preferential interaction with ASC<sup>CARD</sup> and why it disfavors caspase-1<sup>CARD</sup> interactions (Gong et al., 2021).

In late 2015, Zhang and colleagues determined the cryo-EM structure of an activated murine NAIP2/NLRC4 complex that revealed how this polymerization cascade might be regulated. They found that a single activated NAIP2 molecule initiates a domino-like activation and directional oligomerization of several NLRC4 $\Delta$ CARD molecules into mostly 11-bladed wheel-like structures (Zhang et al., 2015). The intermolecular interactions in the oligomer were accompanied by electrostatic interactions between large surface patches in the NLRC4 NACHT domain, which formed the inner ring, and small patches at the LRR domain forming the outer ring. In context of full-length NLRC4, it was hypothesized that a CARD filament might assemble within the central hole formed by the ~11 subunits (Zhang et al., 2015). This is supported by cryo-EM tomography and negative stain EM studies, which found that activated full-length NAIP5/NLRC4 and full-length NLRP6 assemble along a helical axis, respectively (Diebolder et al., 2015; Shen et al., 2019). Additionally, the NACHT domain of NLRP6 was found to synergize with the PYD and amplify its polymerization at lower concentrations (Shen et al., 2019). Finally, a structural study of the NLRC4<sup>CARD</sup> filament showed that the dimensions correspond well to the central hole of the wheel-like structure of NLRC4 $\Delta$ CARD and the NLRC4 tomography map (Li et al., 2018). Since then, the model of active NLRC4 was established as a prototypic example on how activated inflammasome sensors regulate and arrange their respective effector domains (PYD, CARD) to initiate the polymerization cascade.

### 1.4 The NOD domain and STAND ATPases

The NOD module is eponymous for the family of NOD-like receptors (Inohara & Nunez, 2001) and a hallmark typifying the class of signal transduction ATPases with numerous domains (STAND), which has first been recognized by Leipe and co-workers in 2004 (Danot et al., 2009; Leipe et al., 2004). Besides inflammasomal sensors in humans, the class includes a number of signaling and transcription regulatory proteins from all kingdoms of life (Leipe et al., 2004; Sandall et al., 2020). Prominent examples are bacterial transcription regulators, regulatory proteins involved in apoptosis in e.g., nematodes, and the NLR family plant-resistance (R) proteins (Danot et al., 2009). STAND class members are capable of these diverse functions by modular extension of their NOD module with strictly C-terminal sensor domains that specifically recognize an inducer and various effector domains that can be tethered to either the N- or C-terminus for signal transduction (Danot et al., 2009). The bulky sensor domain is often separated from the NOD module by a structural spacer or arm element that was later termed HD2 (Danot et al., 2009). The NOD module consists of the NBD, HD1, and the regulatory WHD. The NBD-HD1 architecture is derived from the highly related ATPase core module of the family of ATPases associated with diverse cellular activities (AAA+ family, Figure 1-6a) (Danot et al., 2009; Erzberger & Berger, 2006; Leipe et al., 2004). Indeed, it has been proposed that STAND ATPases evolved from a structurally related member of an AAA+ subclade containing a C-terminal WHD with non-regulatory but sensory function (Danot et al., 2009). Hence, others have even classified STANDs as part of the AAA+ superfamily (MacDonald et al., 2013; Sandall et al., 2020).



**Figure 1-6: The class of STAND ATPases.** (a) The different possible domain architectures of signal transduction ATPases with numerous domains (STANDs) are shown. The typifying hallmark of the class is the nucleotide-binding oligomerization domain (NOD) module, which is composed of the AAA+ (ATPases associated with diverse cellular activities) core module and the regulatory winged helix domain

(WHD). The AAA+ core is composed of the nucleotide binding domain (NBD) and helical domain 1 (HD1). The NOD module can be extended by a strictly C-terminal sensor domain and an effector domain that can be tethered either at the N- or C-terminus. The bulky sensor domain is separated from the NOD module by a structural spacer, termed helical domain 2 (HD2). Figure is adapted from (Danot et al., 2009). (b) Schematic representation of main ASCE (additional strand, conserved glutamate) subgroups. Branches are according to defining structural elements. Figure is adapted from (Erzberger & Berger, 2006). (c) Topology map of the NOD module. Helices are depicted as tubes and  $\beta$ -strands are depicted as arrows. The amino (N)- and carboxy (C)-termini are marked. Conserved features are highlighted and include the hhGRExE motif, arginine finger (R-F), Walker A (A), Walker B (B), sensor I (S-I), glutamate switch (E-S), GxP motif, and the conserved histidine (H) in the WHD. The letters h and x denote a hydrophobic and any amino acid, respectively. The initiator-specific motif (ISM) is specific for the STAND class and the AAA+ initiator clade. Figure according to (Danot et al., 2009).

The AAA+ core module is composed of a classical NBD and a C-terminal helical lid domain, which is the HD1 in STANDs. The NBD forms a typical five-stranded  $\alpha$ - $\beta$ - $\alpha$  Rossmann-like fold and is characterized by a 5-1-4-3-2 order of the central parallel  $\beta$ -sheet. Implemented at the tip of  $\beta$ 1 and  $\beta$ 3, the well conserved Walker A (P-loop) and Walker B motifs are crucially involved in nucleotide binding and hydrolysis by coordinating the  $\beta$ - and  $\gamma$ -phosphates of ATP and the catalyzing magnesium ion (Wendler et al., 2012). In AAA+ proteins and STANDs the Walker A and B motifs are separated by an additional strand ( $\beta$ 4) in the core sheet and thus both classes belong to the ASCE (additional strand, catalytic E) division of P-loop NTPases (Figure 1-6b), which among others also contains the ABC (ATP binding cassette) transporters and the family of KAP (acronym for Kidins220/ARMS and PifA) NTPases (Erzberger & Berger, 2006; Leipe et al., 2004; Wendler et al., 2012). The tip of  $\beta$ 4 typically contains a polar residue that participates in hydrolysis and is the so-called ‘sensor I’ motif (Wendler et al., 2012). Other important motifs are the ‘glutamate switch’, the ‘arginine finger’ and the ‘sensor II’ motif. The glutamate switch motif is typically represented by a conserved asparagine on  $\beta$ 2 that interacts with the conserved glutamate in the Walker B motif when the protein is in the inactive and ATP bound state. This interaction is released upon ligand binding, thereby regulating hydrolysis activity (Wendler et al., 2012; Zhang & Wigley, 2008). Upon activation, AAA+ ATPases can oligomerize into mostly ring-shaped hexameric structures with the nucleotide bound at the interface between two subunits (Danot et al., 2009; Jessop et al., 2021). The arginine finger motif located at the end of helix  $\alpha$ 4 interacts *in trans* with the  $\gamma$ -phosphate of the nucleotide bound in a neighboring subunit (Jessop et al., 2021; Ogura et al., 2004; Wendler et al., 2012). This resembles the hydrolysis mechanism of small guanosine triphosphatases (GTPases) involving the GTPase activating protein (GAP), which provides an arginine that interacts with the bound nucleotide to stabilize the transition state during GTP hydrolysis, thereby significantly

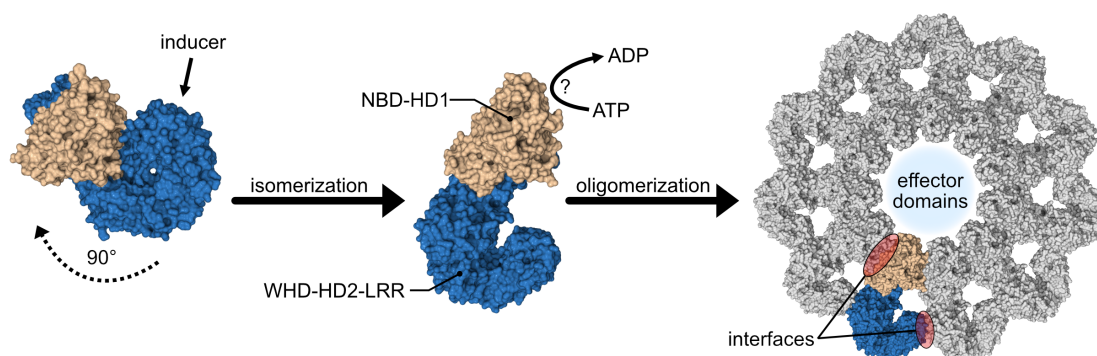
enhancing GTPase activity (Scheffzek et al., 1997). Another well-conserved arginine that interacts with the nucleotide is the sensor II motif that is located in the C-terminal lid domain of AAA+ ATPases. Notably, not all members of the AAA+ superfamily present with the sensor I, sensor II, and arginine finger motifs (Wendler et al., 2012).

Similarly, the NOD module of most STAND proteins is not equipped with an arginine finger or the sensor II motif (Danot et al., 2009). However, STAND ATPases share other distinctive features, such as a special Walker B motif that varies in the position of the catalytic acidic residue (depending on the clade), an adenine moiety-interacting hhGRExE sequence (the letter 'h' denotes for a hydrophobic and 'x' for any amino acid) located upstream of the Walker A motif, a GxP motif at the end of HD1, and a conserved histidine in the regulatory WHD domain (Figure 1-6c). Importantly, the conserved histidine interacts with the  $\beta$ -phosphate of the bound nucleotide, which leads to an autoinhibition mechanism where the WHD folds back towards the NBD to bury the nucleotide and render it unexchangeable. In combination with the specific architecture of the STAND ATPase module this allows for its regulation by the 'STAND binary switch' mechanism (Danot et al., 2009).

#### **1.4.1 The STAND binary switch mechanism**

The emerging picture from comprehensive structural studies is that STANDs function as molecular switches with the 'off' state being a long-lived ADP-bound and monomeric resting form, whereas the 'on' position corresponds to a deoxyadenosine triphosphate (dATP) or ATP-bound conformer, competent to assemble into wheel-like structures that bring together the effector domains of several subunits, thereby facilitating signal transduction (Danot et al., 2009). In the 'closed' 'off' state, the WHD is rotated towards the NBD and interacts with the bound nucleotide, thereby shielding oligomerization interfaces. Upon inducer binding or displacement of inhibitory factors, interdomain interactions are thought to be initially destabilized and subsequently rearranged to allow protein isomerization from the inactive to the active state (Danot et al., 2009). This process involves dramatic conformational changes together with consecutive nucleotide exchange from ADP to ATP, finally displacing the WHD from the NBD. As a consequence, the WHD is rotated away from the NBD by  $\sim 90^\circ$  with the pivot point (hinge region) being located within the linker region connecting the HD1 with the WHD domain. This leads to exposure of the AAA+ multimerization interface and subsequent

oligomerization (Danot et al., 2009; Sandall et al., 2020). Importantly, common ADP-bound ‘closed’ and (d)ATP-bound ‘open’ conformations as well as wheel-shaped oligomeric assemblies of active signaling complexes have been reported for several STAND ATPases, including the bacterial MalT transcriptional activator, plant R proteins, the DARK (*Drosophila* Apaf-1 related killer) apoptosome, the CED4 (*Caenorhabditis* cell death abnormal 4) apoptosome, the mouse and human APAF-1 (apoptotic protease activating factor-1) apoptosome, and inflammasomal components such as NAIP/NLRC4, NLRP3, and NLRP6, indicating that the ‘binary switch mechanism’ is widely conserved throughout this class of functionally diverse proteins (Arya & Acharya, 2018; Cheng et al., 2017; Cheng et al., 2016; Halff et al., 2012; Hu et al., 2013; Hu et al., 2015; Huang et al., 2013; Larquet et al., 2004; Lukasik & Takken, 2009; Reubold et al., 2011; Riedl et al., 2005; Sharif et al., 2019; Shen et al., 2019; Tenthorey et al., 2017; Zhang et al., 2015; Zhou et al., 2015). The example of NLRC4 as a representative of the NLR family is given in Figure 1-7.



**Figure 1-7: Conformational change and oligomerization of NLRC4.** The resting form of NLRC4 is an ADP-bound monomer. Upon inducer binding, which is activated NAIP, NLRC4 switches its conformation from an autoinhibited and closed conformation to an active and open conformation. This isomerization step is characterized by the release of autoinhibiting interdomain interactions and a  $\sim 90^\circ$  rotation of the WHD-HD2-LRR region relative to the NBD-HD1 region. Exposure of oligomerization interfaces leads to wheel-like NLRC4 assemblies bringing together effector domains for subsequent downstream signaling. Oligomerization might include ADP to ATP exchange. Structures taken from inactive mouse NLRC4 $\Delta$ CARD (PDB: 4KXF) and an activated NAIP2/NLRC4 oligomer (PDB: 3JBL). NBD: nucleotide binding domain, HD1: helical domain 1, WHD: winged helix domain, HD2: helical domain 2, LRR: leucine rich repeat, ADP: adenosine diphosphate, ATP: adenosine triphosphate.

#### 1.4.2 The role of nucleotide binding and hydrolysis

Apart from the recognition that several structures of STAND ATPases were determined in an ADP-bound inactive or a (d)ATP-bound active conformation, there is not much known about the distinct roles of nucleotide binding and hydrolysis in the regulation and assembly of STANDs. Nevertheless, these molecular snapshots provide pivotal insight to

different steps in a potential nucleotide cycling process, which is complemented by biochemical data. First of all, related AAA<sup>+</sup> ATPases are thought to couple ATP hydrolysis to the generation of mechanochemical work, thereby driving conformational change – a mechanism that is still poorly understood (Ammelburg et al., 2006; Wendler et al., 2012). However, this concept was largely applied to STAND ATPases and initially proposed to be at the basis of the extensive and global conformational reorganization needed to adopt the active conformer (MacDonald et al., 2013; Sandall et al., 2020). Indeed, most STAND ATPases preferentially bind and respond to (d)ATP and possess intrinsic ATPase activity but with generally very low turnover rate (Danot et al., 2009; Sandall et al., 2020). In line, ATP was shown to induce NLRP1 inflammasome assembly in a concentration-dependent manner, whereas presence of the nonhydrolyzable ATP analogs AMP-PNP (adenylyl imidodiphosphate) and ATP $\gamma$ S failed to promote NLRP1-dependent caspase-1 activation (Faustin et al., 2007). Importantly, ATP was also reported to be required for the assembly of other inflammasomes (Sandall et al., 2020). In addition, mutations that abolish ATP binding in NLRC4, NLRP3, NLRP7, and NLRP12 were demonstrated to prevent self-oligomerization and downstream signaling (Duncan et al., 2007; Lu et al., 2005; Radian et al., 2015; Ye et al., 2008). Interestingly, the archaeal STAND ATPase SSO1545 was crystallized in the open conformation and bound to ADP instead of ATP (Xu et al., 2009). This might actually imply that ATP is hydrolyzed to drive conformational change of SSO1545 leaving the protein bound to ADP, which is subsequently exchanged with ATP to enable oligomerization. This model was also supposed in case of APAF-1, which hydrolyzes dATP upon cytochrome c binding and is reloaded with dATP before apoptosome assembly occurs (Kim et al., 2005). However, the biochemical data underlying this model is controversial, since APAF-1 irreversibly aggregates when incubated with cytochrome c (Danot et al., 2009). As an alternative, ADP-bound SSO1545 in the open conformation might represent an intermediate after conformational change and before nucleotide exchange and oligomerization, meaning that ATP hydrolysis is not required for the transition from an inactive to an active state. In line with this concept, the inactive conformation of STAND ATPases suggests that bound ADP is shielded from being exchanged and thus the protein needs to open up first before the nucleotide is able to dissociate (Danot et al., 2009). However, other nucleotide exchange mechanisms might be possible and it is indeed not yet clarified how and when this event occurs.



Oligomerization is thought to stabilize the ATP-bound state because ATP is bound at the interface of two subunits in the oligomer (Danot et al., 2009). A structural study on CED-4 in complex with the CED-9 inhibitor protein reported an open and ATP-bound but not oligomeric conformation (Yan et al., 2005), suggesting that ATP is bound prior to oligomerization. In contrast, oligomeric structures of NLRC4 were reported to be free from nucleotides (Hu et al., 2015; Tenthorey et al., 2017; Zhang et al., 2015). One explanation could be that the NLRC4 oligomer might have low affinity towards ATP leading to its dissociation during the purification process, but NLRC4 and the related family members NLRP3 and NLRP12 were each shown to display high affinity towards ATP with dissociation constants in the range of ~50-100 nM (Duncan et al., 2007; Lu et al., 2005; Ye et al., 2008). Although the conformation of ATP-bound NLRC4, NLRP3 and NLRP12 is unknown, it is likely that ATP is bound in the open form, thus suggesting that ATP binding in NLRC4 occurs after oligomerization.

Regarding the role of ATP hydrolysis, an interesting finding was that mutation of the catalytic residue in the Walker B motif of tomato R protein I-2 leads to its autoactivation (Tameling et al., 2006). Importantly, hyperactive I-2 mutants were shown to be only impaired in ATP hydrolysis activity but not nucleotide binding (Tameling et al., 2006), indicating that hydrolysis is not needed to adopt the active conformation but rather important for inactivating the protein. Thus, these mutants are likely trapped in an ATP-bound active conformation, which would explain their reported hyperactivity (Danot et al., 2009). Similarly, mutation of the ATPase module in the *Arabidopsis* RPS5 protein, the bacterial MalT or the NLR family proteins NOD2 and NLRP3 were shown to lead to hyperactivation when the mutation abolished ATPase activity, or on the contrary, protein inhibition when nucleotide binding was affected (Ade et al., 2007; Marquenet & Richet, 2007; Proell et al., 2008). Additionally, presence of AMP-PNP and another nonhydrolyzable ATP analog AMP-PCP (adenylyl methylenediphosphonate) are able to promote the activation and signaling of MalT and APAF-1, respectively (Jiang & Wang, 2000; Marquenet & Richet, 2007), indicating that ATP binding but not hydrolysis is essential for downstream signaling (Danot et al., 2009). Incongruously, a mutant of murine NLRP1b defective in nucleotide binding was reported to render the protein constitutively active and similar with human NLRP1, presence of ATP $\gamma$ S failed to activate the APAF-1 apoptosome (Faustin et al., 2007; Jiang & Wang, 2000; Liao & Mogridge, 2013).

Importantly, some inconsistent findings from biochemical studies can be explained by the fact that mutations within the ATPase module can affect either nucleotide binding or ATP hydrolysis, which should be considered as distinct events in the activation process. In addition, it is likely that STAND proteins display different affinity for ATP and nonhydrolyzable ATP analogs. Low affinity binding might not be sufficient for activation. However, it is as well possible that discrepancies come along with more complex dynamics of nucleotide binding and hydrolysis. In conclusion, the emerging activation mechanism of STANDs might include ADP to ATP exchange that is most likely required for activation and oligomerization, and ATP hydrolysis that might return the active conformer back to the inactive resting state. Due to the lack of conclusive data, the steps in between cannot be ultimately resolved yet (Danot et al., 2009).

### **1.5 Pharmacological interference with the inflammasome pathway**

Accumulation of sterile danger signals is a common instigator of chronic inflammation, which drives a variety of diseases arising in ageing populations (Mangan et al., 2018). NLRP3 was determined as a key mediator of inflammation in conditions of cellular dyshomeostasis (Platnich & Muruve, 2019). Thus, many links between the pathology of age-related diseases and aberrant or excessive activation of NLRP3 could be established (Mangan et al., 2018; Schwaid & Spencer, 2021). Diseases with NLRP3-dependent pathology can be broadly categorized as systemic autoinflammatory diseases, diseases of the central nervous system (CNS), and peripheral inflammatory diseases that are most often associated with metabolic dysfunction. Cryopyrin-associated periodic syndromes (CAPS) are a group of rare and inherited autoinflammatory disorders that are caused by different gain-of-function mutations in the *Nlrp3* gene (Booshehri & Hoffman, 2019). They include familial cold autoinflammatory syndrome (FCAS), Muckle-Wells syndrome (MWS), and neonatal-onset multisystem inflammatory disorder (NOMID), which present with increasing symptoms and severity. Patients commonly suffer from blood neutrophilia, fever, and inflammation of the skin, joints, and conjunctiva. In addition, hearing loss and kidney amyloidosis can occur in MWS and NOMID, whereby the latter can also lead to CNS inflammation (Mangan et al., 2018).

Excessive activation of the NLRP3 inflammasome is also the driving force for the pathology of important non-hereditary diseases of the brain and the periphery. A mutual finding in Alzheimer disease, Parkinson disease, amyotrophic lateral sclerosis, multiple

sclerosis, epilepsy, stroke, and traumatic brain injury was an increase in the expression levels of NLRP3 inflammasome components and elevated secretion of mature IL-1 $\beta$ , indicating that pyroptosis might be the common denominator of neurodegeneration. Importantly, mouse models revealed that depletion or inhibition of NLRP3 is paralleled by decreased disease progression (Lunemann et al., 2021). In addition, metabolic dysbiosis can lead to the accumulation of lipids that provide a priming signal for NLRP3 as well as the formation of NLRP3-activating crystals that drive lysosomal rupture and chronic low-grade inflammation. Examples of NLRP3-associated diseases driven by metabolic alterations include type II diabetes, nonalcoholic steatohepatitis (NASH), rheumatoid arthritis, atherosclerosis (coronary artery disease), gout, kidney dysfunction, and certain types of cancer (Mangan et al., 2018; Schwaid & Spencer, 2021). Importantly, the development of metabolic diseases is strongly associated with increasingly sedentary lifestyles and a Western diet, which adds up to the aging population of these days (Mangan et al., 2018). Notably, the here described diseases are all associated with NLRP3, whereas the function of other NLR family members have been linked with many more human diseases (Zhong et al., 2013). Thus, NLRs and their signaling pathways are an attractive target for pharmacological inhibition with broad therapeutic potential in especially autoinflammatory and chronic inflammatory diseases (Mangan et al., 2018).

Inhibition of the NLRP3 inflammasome pathway has been explored in some detail. The most advanced and clinically approved therapeutics today are the human anti-IL-1 $\beta$  monoclonal antibody canakinumab and anakinra, which is the recombinantly produced form of the endogenous IL-1 receptor antagonist (Mangan et al., 2018; Schwaid & Spencer, 2021). Canakinumab is an approved treatment option in patients with CAPS (Lachmann et al., 2009). In addition, the antibody was tested as an anti-inflammatory therapy in the CANTOS (Canakinumab anti-inflammatory thrombosis outcome study) phase III trial and showed safety and efficacy in treating atherosclerosis by significantly lowering the rate of recurrent cardiovascular events in at-risk patients (Ridker et al., 2017). It was also observed that symptoms of chronic inflammation and cancer mortality could be decreased during therapy with Canakinumab (Schwaid & Spencer, 2021). Anakinra is approved by the U.S. food and drug administration (FDA) for the use in rheumatoid arthritis, when patients do not experience improvements in disease symptoms with at least one other antirheumatic drug. Unfortunately, anakinra is reported to have only modest efficacy in this indication (Mertens & Singh, 2009). This is likely due to the fact that pathology in many diseases is often driven by factors beyond IL-1 $\beta$  (Mangan et

al., 2018). Anakinra was also approved to be efficacious in treating patients with CAPS (Kuemmerle-Deschner et al., 2013). Because anakinra has a relatively short half-life of 4-6 h and modest oral bioavailability, frequent injections are needed. Most often these injections cause pain at the injection site, thus therapy with canakinumab (half-life of 26 days) is generally preferred (Schwaid & Spencer, 2021). However, one important side effect of both therapies is a compromised immune response with concomitant risk for serious opportunistic infections due to the central role of IL-1 $\beta$  as a cytokine that is produced by multiple inflammasomes (Mangan et al., 2018; Schwaid & Spencer, 2021).

Another target more upstream in the inflammasome pathway is caspase-1. VX-765 and VX-740 are so far the most selective caspase-1 inhibitors that were tested in the clinic but did not demonstrate sufficient efficacy and safety. Both compounds are prodrugs that become active by the modification of plasma esterases and were developed for rheumatoid arthritis and psoriasis and epilepsy, respectively. However, phase IIb clinical trials were discontinued due to concerns of hepatotoxicity. Importantly, caspase-1 inhibitors increase the risk for opportunistic infections as does inhibition of IL-1 $\beta$  (Mangan et al., 2018; Schwaid & Spencer, 2021). Other concepts with similarly broad side effects include the inhibition of priming signals or activating stimuli. As an example, data on BTK inhibitors show an effect on the inflammasome with positive phase II data in multiple sclerosis and rheumatoid arthritis (Cohen et al., 2020; X. Liu et al., 2017; Montalban et al., 2019). But strikingly, BTK inhibitors are non-selective NLRP3 inflammasome inhibitors because interfering with BTK function will also affect several other cell processes besides inflammasome activation (Schwaid & Spencer, 2021).

For that reason, direct and selective inhibition of single inflammasome sensors is the most recent strategy in the development of potent inflammasome inhibitors (Schwaid & Spencer, 2021). The most important compound in this group is the NLRP3-selective small molecule inhibitor CRID3, which has been shown to be effective in dozens of preclinical disease models (Corcoran et al., 2021; Mangan et al., 2018). However, clinical development of CRID3 was discontinued after phase Ib testing due to increased risk of hepatotoxicity, but next-generation CRID3-inspired compounds have recently progressed into clinical trials (El-Sharkawy et al., 2020; Schwaid & Spencer, 2021). Importantly, structural data of the NLRP3-CRID3 inhibitor complex would provide vital information to accelerate and improve the development of advanced NLRP3 antagonists, which could be the medicine of tomorrow.

## 1.6 Aims of the thesis

Existence of the NLRP9 and NLRP12 inflammasomes has not yet been confirmed in biochemical studies. Therefore, one objective of this thesis is the investigation and confirmation of the putative NLRP9 and NLRP12 inflammasomes using biochemical approaches and ultimately the acquisition of structural data that would gain mechanistic insights into their regulation and assembly. For that purpose, full-length protein and single-domain constructs shall be expressed in the *Sf9* insect cell system and purification strategies shall be developed. It has been reported that purification of NLR proteins is difficult, probably because these proteins have a tight folding and tend to oligomerize with their PYD and NACHT domains. For that reason, the establishment of purification strategies is a major aim of this thesis.

Because signal transduction in NLRP proteins is facilitated via nucleated polymerization of Pyrin domains, this domain shall be of particular focus of the research. It is expected that Pyrin domain-only constructs of NLRP proteins can largely escape the autoinhibition mechanisms of the full-length proteins, which might be subject to complex regulation mechanisms involving steps of post-translational modification (priming) and inducer binding. Therefore, investigation of PYD-only constructs might be less sophisticated. CARDS and PYDs of certain inflammasome components were reported to polymerize into filaments via three conserved asymmetric interfaces. Thus, it shall be investigated whether PYDs of NLRP9 and NLRP12 are assembled in a similar manner or if differences exist, what might be their functional consequences.

NLRP12 is highly related to the prototypic inflammasome sensor NLRP3, which has been studied extensively in the past. However, NLRP12 but not NLRP3 is implicated in anti-inflammatory regulation of the NF- $\kappa$ B pathway. For that reason, regulatory mechanisms that allow downstream signaling might be different and shall be investigated. This primarily includes analysis of the regulatory NACHT domain of NLRP12 regarding its capability to bind to and hydrolyze nucleotides and to self-oligomerize into higher order structures. Ideally, structural information shall be obtained to gain mechanistic insight into NLRP12 conformation, regulation, and function.

This thesis shall provide new mechanistic understanding on human inflammasomes and how potent pharmacological interference can be achieved. As a prototypic example of direct inflammasome inhibition, the structure of NLRP3 in complex with the small molecule inhibitor CRID3 shall be determined to ultimately reveal its mode of action.



## Chapter 2: Biochemical and structural investigation of human NLRP9

Some work presented in this chapter was accomplished in cooperation with Inga Hochheiser and Dr. Kanchan Anand (University of Bonn). Inga Hochheiser performed grid preparation and imaging using the facility for electron microscopy at the Max Planck Institute for Neurobiology of Behavior – Caesar (Bonn). Dr. Kanchan Anand performed crystallization of NLRP9<sup>PYD</sup>, data collection at the Swiss Light Source (SLS) – Paul Scherrer Institute (Villigen, Switzerland), as well as data processing, structure determination, and refinement.

Part of this chapter is published in:

**Marleaux, M.**, Anand, K., Latz, E., & Geyer, M. Crystal structure of the human NLRP9 Pyrin domain suggests a distinct mode of inflammasome assembly. *FEBS Lett* **594**, 2383-2395 (2020). DOI: 10.1002/1873-3468.13865

## 2.1 Initial functional analysis of human NLRP9

Rotavirus is a genus of double-stranded RNA viruses that are the leading cause of severe acute diarrhea among infants and young children worldwide, causing an estimated 200,000-450,000 deaths annually and 36% of all diarrhea hospitalizations (Crawford et al., 2017; Dennehy, 2015). While NLRP9 has initially been shown to play a role in preimplantation embryo development (Kanzaki et al., 2020; Kufer & Sansonetti, 2011), a study in 2017 established the mouse analogue NLRP9b as an inflammasome sensor that drives ASC and caspase-1 mediated pyroptosis in intestinal epithelial cells (IECs) of mice challenged with rotavirus infection (Zhu et al., 2017). They found that, in concert with the RNA sensor DHX9, NLRP9b recognizes short double-stranded RNA (dsRNA) from rotavirus and drives pyroptosis resulting in subsequent abortive infection. Also, expression of human NLRP9 in IECs and association with DHX9 and ASC in rotavirus-infected HEK293T cells has been shown (Zhu et al., 2017). NLRP9 was moreover found to be expressed and upregulated upon inflammatory stimuli in brain pericytes (Nyul-Toth et al., 2017) and cerebral endothelial cells (Nagyoszi et al., 2015), suggesting an additional function in the human brain. Besides, NLRP9 has been linked to neutrophilic inflammation in a mouse model of acute lung injury (Yanling et al., 2018) and a number of other inflammatory diseases, including urothelial carcinoma (Poli et al., 2015), multiple sclerosis (Gil-Varea et al., 2018), familial late onset Alzheimer's disease (Fernandez et al., 2018), systemic-onset juvenile idiopathic arthritis (Tadaki et al., 2011), and *Helicobacter pylori* infection (Castano-Rodriguez et al., 2014). However, existence of an NLRP9 inflammasome was never confirmed biochemically. Thus, the specific role of NLRP9 in disease and mechanistic understanding of its regulation is still enigmatic.

Since no biochemical and structural information about human NLRP9 was known, this part of the thesis provides an initial analysis. The primary structure of NLRP9 is compared to NLRP3, a NLR family member that has been studied intensively in recent years. Protein domains and important motifs as well as similarities and differences that reflect protein structure and function are assigned. Moreover, it is shown in a HEK293T cell system, that full-length NLRP9 does not nucleate ASC speck formation in the absence of rotavirus. Functionally, recombinant NLRP9 is found to exist as a monomer in solution and to adopt a less stable dimeric conformation upon exposure with ATP. Finally, monomeric NLRP9 is analyzed using electron microscopy and the shape of the imaged particles is compared to a structural model.



### 2.1.1 Domain architecture and sequence motifs in NLRP9

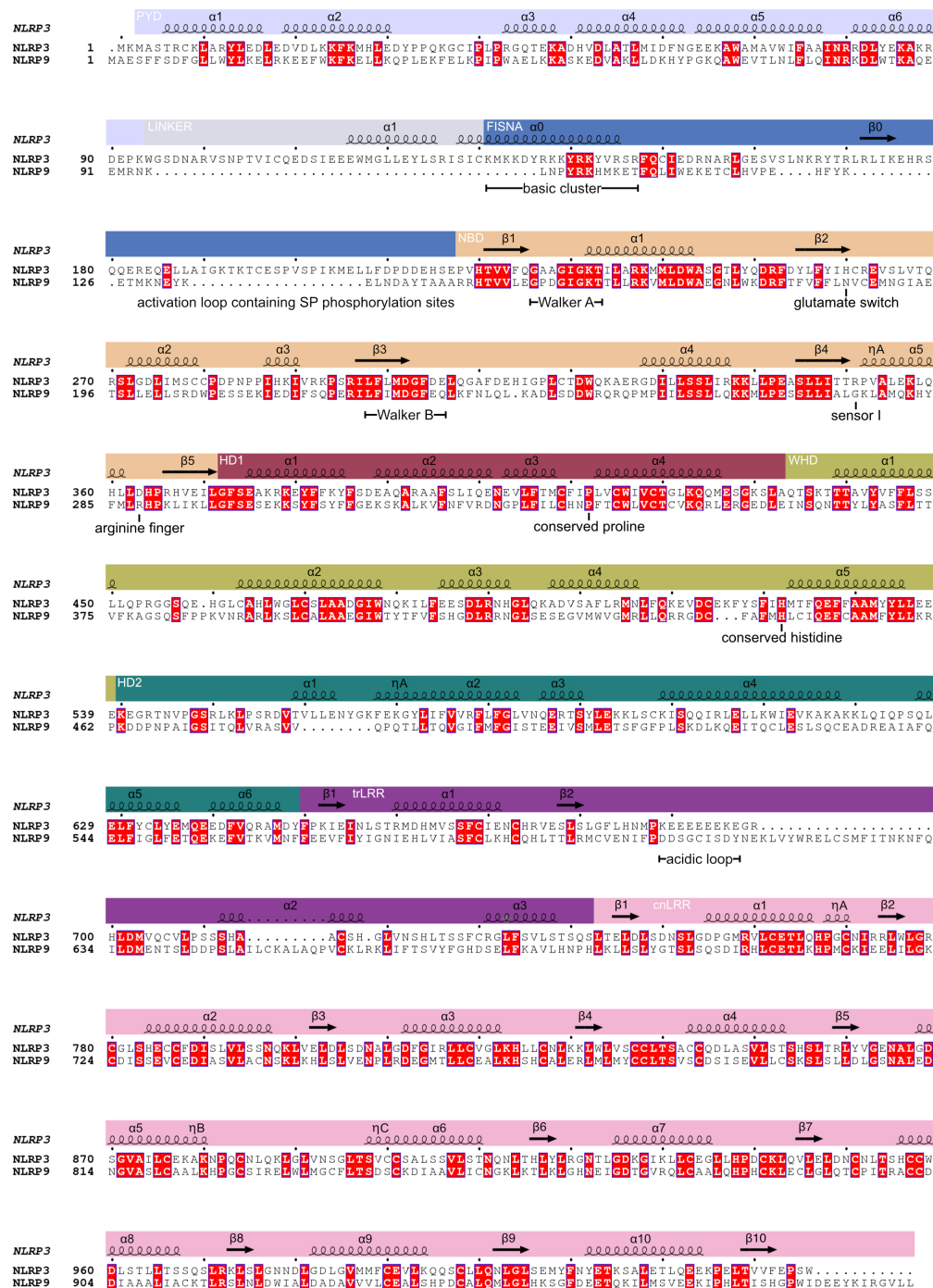
In contrast to mice, which harbor three *Nlrp9* genes (*mNlrp9a*, *mNlrp9b*, *mNlrp9c*), humans have only one *Nlrp9* gene located on the reverse strand of chromosome 19. The gene contains 9 coding exons, which encode two isoforms produced by alternative splicing (Ensembl: ENSG00000185792). Isoform 1 has been defined as the canonical sequence (Uniprot: Q7RTR0). The protein consists of 991 amino acids with a calculated mass of approximately 113 kDa and a theoretical isoelectric point (pI) of 6.08. To determine the domain architecture of NLRP9 as well as functional and structural relationships with the well-studied family member NLRP3, a detailed primary structure analysis combined with a sequence alignment was performed (Figure 2-1). Interestingly, both proteins show a remarkably high conservation at the C-terminus. However, the overall sequence identity between full-length NLRP3 and NLRP9 was determined to be 35.0%. Corresponding to the upper ‘twilight zone’ (Rost, 1999), this value reflects that both proteins are homologous and share the basic tripartite architecture that is widely conserved within the NLR family and contains an N-terminal effector domain, a central NACHT domain and a C-terminal region with a series of LRRs (Martinon et al., 2009). Besides this parent organization, the NACHT and LRR regions can be subdivided into different subdomains.

In NLRP9, the N-terminal effector domain is a PYD that spans amino acids (aa) 1-97 and is followed by the central NACHT domain continuing until aa 563. While both domains are separated by a 37 amino acid flexible linker in NLRP3, this linker is completely absent in NLRP9. It was proposed recently, that this linker region in NLRP3 might be important to position the PYDs of different subunits into the helical assembly that forms a seed for ASC polymerization (Tapia-Abellan et al., 2021). In NLRP3, the linker is followed by the FISNA domain that contains two functionally important motifs. The first motif is a polybasic cluster with 10 out of 17 aa being positively charged and found to be key for NLRP3 inflammasome activation upon cellular potassium efflux (Tapia-Abellan et al., 2021). The second motif is a loop containing SP phosphorylation sites, which become phosphorylated during priming and are prerequisite for NLRP3 deubiquitination and subsequent inflammasome activation (Paik et al., 2021). In NLRP9, the sequence identity with the NLRP3 FISNA domain is very poor and does neither contain the polybasic cluster, nor the activation loop. One distinctive feature of STAND ATPases in this particular region is an hhGRExE motif roughly 25-30 residues upstream of Walker A that interacts with the adenine moiety of a bound nucleotide (Danot et al.,

2009; Leipe et al., 2004). This motif seems not well conserved in NLRP3 or NLRP9, but a sequence with some similarity (**HFYKETM**) could be found at the expected position in NLRP9. Interestingly, a structural model of human NLRP9 generated with the AlphaFold2 server (Jumper et al., 2021) predicts two helices between the PYD and the first  $\beta$ -strand of the NBD (Figure 2-6b). Existence of a helix directly upstream of the first NBD  $\beta$ -strand would essentially be in line with the common NBD topology previously described for STAND ATPases that differs from NLRP3 (Figure 1-6c) (Danot et al., 2009). Thus, the beginning of this helix (aa 121) reflects the start of the NBD in NLRP9, whereas the other predicted helix might serve as a rigid linker between the PYD and NBD.

The NLRP9 NBD spans until aa 296 and harbors a classical Walker A and an extended Walker B motif, which are both key for nucleotide binding and hydrolysis (Danot et al., 2009). With the sequence LFIMDGFEQ, the Walker B motif in NLRP9 shows significant variation from the hhhhD[G/A/S]hDE consensus sequence that is typically shared among the NACHT clade (Leipe et al., 2004). STAND ATPases are thought to be regulated by a molecular switch mechanism, that renders the bound nucleotide unexchangeable (Danot et al., 2009). However, in AAA+ proteins a ‘glutamate switch’ mechanism has been found to regulate hydrolysis activity dependent on ligand binding (Zhang & Wigley, 2008). The mechanism relies on a single residue that is affected by a ligand binding event and suited to establish or cease an interaction with the catalytic acidic residue of the Walker B motif (Zhang & Wigley, 2008). This residue is usually located at the tip of the second NBD  $\beta$ -strand (Wendler et al., 2012). No ligand binding site is known for NLRP9 but residue Asn186 was found at the expected position in close proximity to the Walker B site.

The sensor I motif is typically a polar residue embedded at the tip of the central beta strand and thought to fulfill several putative functions, including stabilization of the negative charge of the reaction intermediate during hydrolysis (Leipe et al., 2004). In NLRP3, Arg351 is found as the expected polar residue. In contrast, NLRP9 contains a glycine residue (Gly276) at the equivalent position, suggesting the sensor I motif is missing. Another polar residue that is most often conserved across AAA+ proteins is referred to as the arginine finger. In an oligomeric assembly, the residue is thought to interact *in trans* with the nucleotide bound in a neighboring subunit (Wendler et al., 2012). Interestingly, in the MNS clade of STAND ATPases a putative arginine finger motif was reported to be complementary present with the sensor I motif (Leipe et al., 2004). Although very rare in NLRs, Arg288 might be a similar candidate residue located at the tip of a helix right before the terminal  $\beta$ -strand of the NLRP9 NBD.



**Figure 2-1: Sequence alignment of NLRP3 and NLRP9.** The amino acid sequence of human NLRP3 isoform 2 (Uniprot accession number: Q96P20) and human NLRP9 isoform 1 (Uniprot accession number: Q7RTR0) was aligned using Clustal Omega (Madeira et al., 2019). Identical amino acids in both proteins are boxed. The secondary structure assignment was generated from NLRP3 (PDB: 7PZC, (Hochheiser, Pils, et al., 2022)) using ESPript 3.0 (Robert & Gouet, 2014). Helices are shown as squiggles and beta strands are shown as arrows. Domain boundaries are based on the NLRP3 structure and highlighted as Pyrin domain (PYD, bluewhite), fish-specific NACHT associated domain (FISNA, skyblue), nucleotide binding domain (NBD, wheat), helical domain 1 (HD1, raspberry), winged helix domain (WHD, deepolive), helical domain 2 (HD2, deepteal), transition leucine-rich repeat domain (trLRR, violetpurple), and canonical leucine-rich repeat domain (cnLRR, lightpink). Important motifs in NLRP3 are depicted below the sequence.  $\alpha$ : alpha-helix,  $\eta$ :  $3_{10}$ -helix,  $\beta$ : beta-strand.

Helical domain 1 (HD1) spans aa 297-358 in NLRP9 and, in STAND ATPases, typically contains a conserved GxP motif (Danot et al., 2009). NLR proteins largely lack the glycine residue but the proline that interacts with the adenine moiety of the nucleotide is highly conserved throughout the family, including NLRP9 (Sandall et al., 2020).

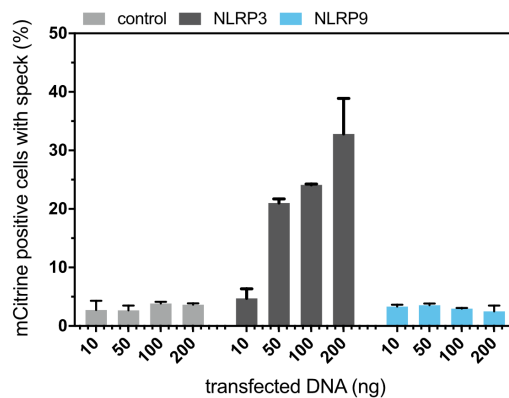
The sequential winged helix domain (WHD) starts at aa 359 and ties into helical domain 2 (HD2) at position 464. It contains a highly conserved histidine residue (H445) that is likely to substitute for the function of a conserved arginine residue implicated in hydrolysis, nucleotide-sensing, and inter-subunit interaction in AAA+ ATPases, termed sensor II (Ogura et al., 2004; Sandall et al., 2020).

HD2 spans until aa 564 and is then followed by the C-terminal LRR domain, which can be subdivided into two different segments. The first segment defines as a region with varying length and composition of the individual LRR repeats, termed transition LRR (trLRR, aa 565-637; based on AlphaFold2 model). The second segment is a region containing canonical LRR repeats (cnLRR, aa 638-991) with a conserved array of helices, turns and beta strands. The trLRR in NLRP3 harbors an acidic loop that extends from an LRR transition segment and folds back into the concave side of the cnLRR to mediate contacts between two opposing LRRs in an inactive decameric conformation (Hochheiser, Pilsl, et al., 2022). While this loop is important for the autoinhibition of NLRP3, it is absent in NLRP9, suggesting a different mode of regulation.

### **2.1.2 NLRP9 is not capable of nucleating ASC specks in the absence of rotavirus**

A previous study showed that reconstitution and overexpression of inflammasome components in a HEK293T cell system is sufficient to promote spontaneous ASC speck formation (Sester et al., 2015), which is considered a reliable readout for inflammasome activation (Stutz et al., 2013). In a first functional experiment, the capability of NLRP9 to promote ASC specks was investigated. HEK293T cells stably expressing low levels of ASC-BFP (blue fluorescent protein) fusion protein were transfected with increasing concentrations of a plasmid encoding human full-length NLRP9. For comparison, also human full-length NLRP3 was transfected as the closest relative that is well known to form an inflammasome with ASC (Swanson et al., 2019). Subsequently, the number of ASC specks has been determined using flow cytometry experiments (Figure 2-2). Expression of NLRP3 resulted in robust formation of ASC specks in a dose-dependent manner. Importantly, this effect was specific for NLRP3, since a control plasmid did not

promote ASC speck formation in transfected cells. In contrast, transfection of NLRP9 was not sufficient to form ASC specks in the tested system. Thus, opposite to NLRP3, NLRP9 is not capable of nucleating ASC specks in the absence of its ligand, suggesting two possible explanations: (1) A more stable autoinhibited state due to a different mode of regulation or (2) its inability to interact with ASC to form an active inflammasome.

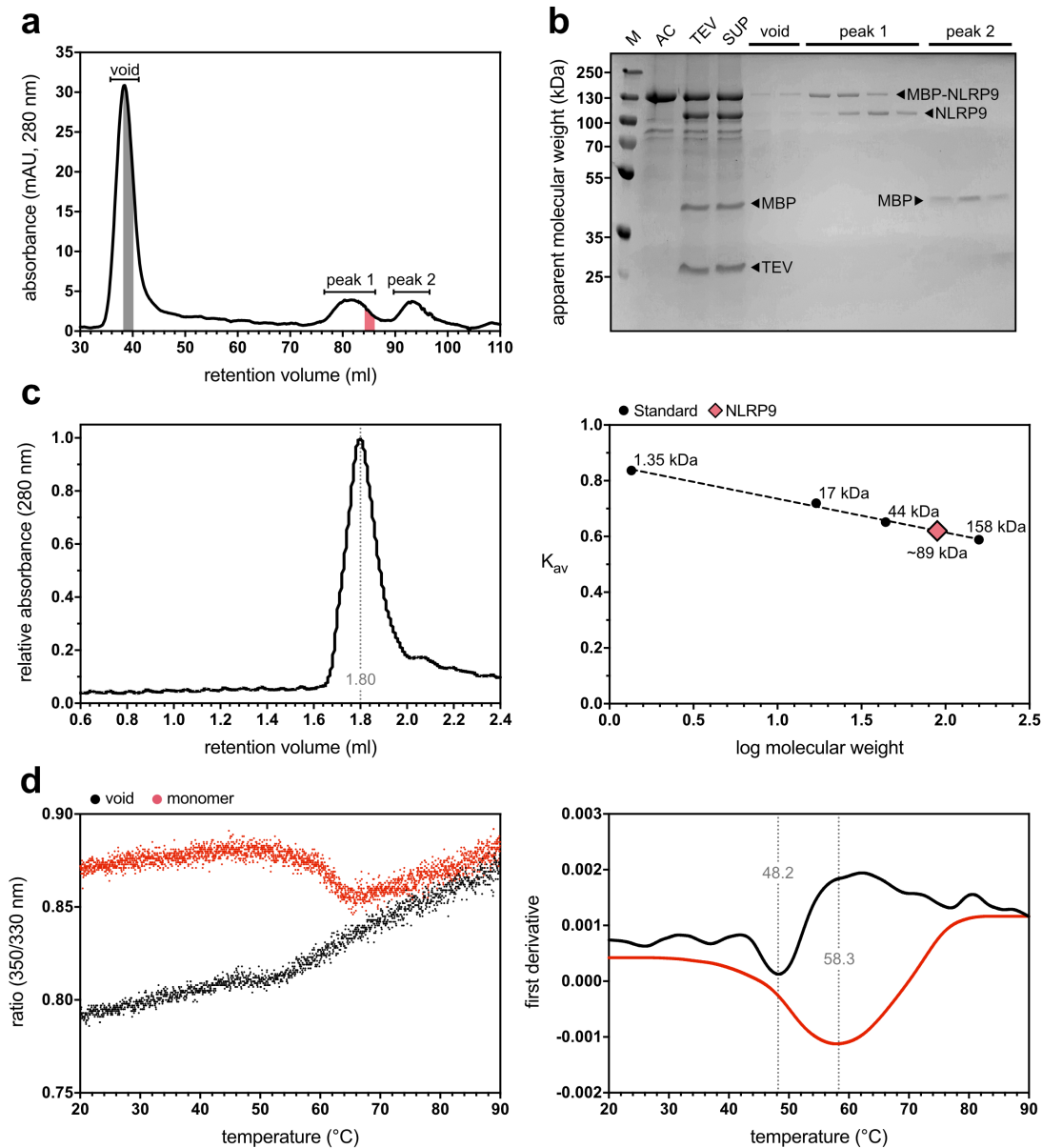


**Figure 2-2: Analysis of ASC speck formation in cells overexpressing NLRP9.** Plasmids coding for human NLRP3 or NLRP9 under a CMV promoter were transfected into HEK293T cells stably expressing ASC-BFP fusion protein. To follow promoter activity, mCitrine was simultaneously expressed via an internal ribosomal entry site (IRES). In case of the control, the transfected plasmid did not contain the NLRP3 or NLRP9 coding sequence. mCitrine positive cells have been analyzed by flow cytometry for the presence of ASC specks. Bars are representative of two technical replicates.  $n = 1 \pm SD$ .

### 2.1.3 Recombinant full-length NLRP9 forms a stable monomer in solution

To gain more insights into the regulation and autoinhibition mechanisms, human NLRP9 was recombinantly expressed as N-terminal MBP-fusion protein in the *Sf9* insect cell system. The MBP tag was chosen based on its stabilizing and solubilizing properties and the experience that full-length NLR proteins tend to aggregate at higher concentrations. NLRP9 was purified to homogeneity by affinity chromatography (AC), tag cleavage, and size-exclusion chromatography (SEC) in the absence of nucleotides. A representative SEC run of NLRP9 after AC and tag cleavage is shown in Figure 2-3a. The protein eluted as one major peak close to the void volume at around 40 ml and two minor peaks at 82 ml and 96 ml, respectively. The void volume fraction corresponds to a protein mass of  $> 6,000$  kDa and contains large protein aggregates that are most likely not well folded and thus not an appropriate conformation for autoinhibition. In contrast, peak 1 eluted at a retention volume that is expected for monomeric NLRP9. Peak 2 represents a fraction of defined protein such as the cleaved MBP tag. The SDS gel with samples from different steps of the purification process shows a high excess of target protein with an intense

band above 130 kDa for uncleaved MBP-NLRP9 (MW = 154,808 Da) and 100 kDa for tag-cleaved NLRP9 (MW = 113,459 Da, Figure 2-3b).



**Figure 2-3: Purification and analysis of human NLRP9.** (a) Representative chromatogram of NLRP9 injected onto a Superose 6 PG XK 16/70 size-exclusion column after affinity purification and tag cleavage. Elution of protein was followed via the absorbance at 280 nm wavelength. Grey and red areas indicate individually pooled fractions of the void and first peak, respectively. (b) Coomassie-stained samples from different steps of the purification process and fractions from (a) after reducing SDS-PAGE. M: marker, AC: affinity chromatography, TEV: tag cleavage using TEV protease, SUP: supernatant after centrifugation. (c) Elution profile from analytical gel filtration of  $\sim 10 \mu\text{g}$  NLRP9 peak 1 protein injected onto a Superose 6 Increase 3.2/300 column and calculation of the molecular weight from the peak retention volume. Linear regression was used to fit the calibration curve to the partition coefficient ( $K_{av}$ ) versus the logarithm of the molecular weight of a standard ( $R^2 = 0.9943$ ). (d) Thermal shift assay of 80 nM full-length NLRP9 void (black) or monomer (peak 1, red) in the absence of nucleotides. The measurement was setup with a temperature ramp ranging from 15-95°C, a slope of  $2^\circ\text{C}\cdot\text{min}^{-1}$ , and a 100% laser intensity. Shown data is representative of 2-3 technical replicates. Apparent melting temperatures ( $T_M$ ) of the samples are depicted as dashed lines.

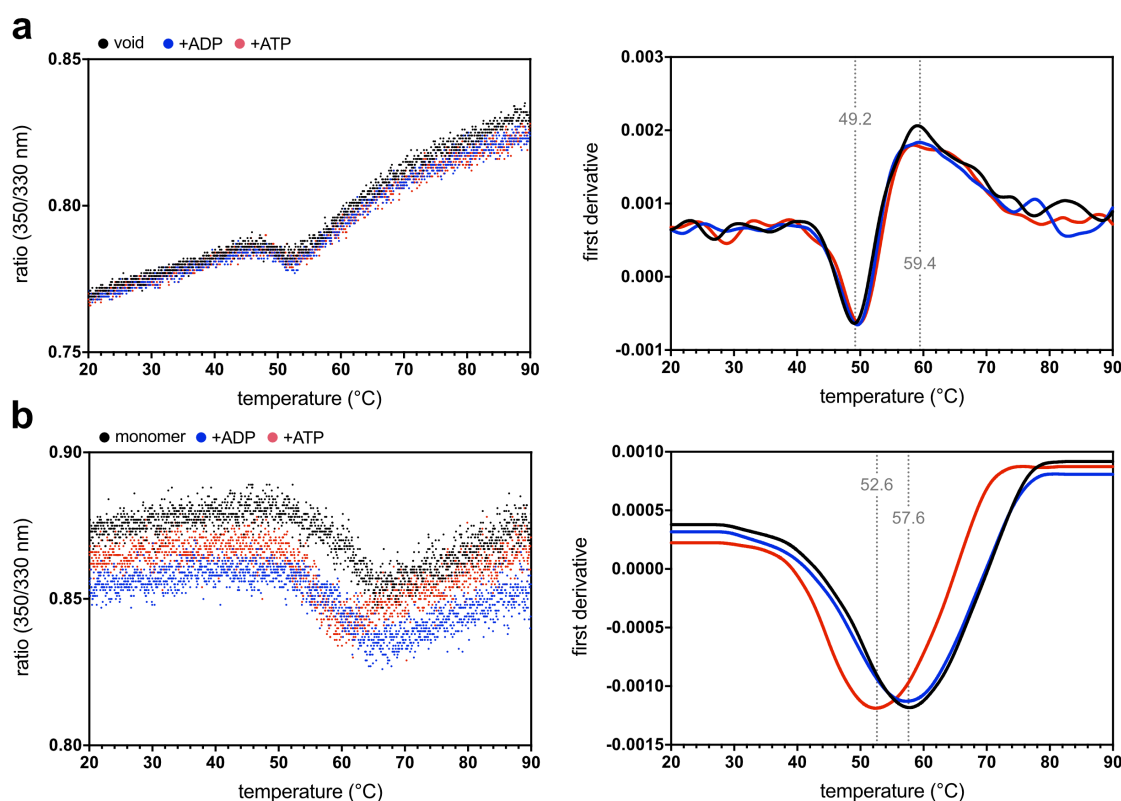
The two additional protein bands at lower molecular weights correspond to the cleaved MBP tag (MW = 41,349 Da) and the TEV protease that was supplemented for tag cleavage (MW = 28,400 Da). As already suggested, the Coomassie-stained SDS gel proves that the void fraction and the peak 1 fraction both contain NLRP9, whereas the peak 2 fraction contains the cleaved MBP (Figure 2-3b). Additionally, it indicates that the tag cleavage worked only partially, since the MBP tag could not be cleaved from all NLRP9 molecules. While the void peak mainly consists of uncleaved NLRP9, the peak 1 fractions contain a mixture of both, cleaved and uncleaved protein. However, the right shoulder of peak 1 is comprised of pure and cleaved protein with minimal amounts of impurities and thus, was pooled for further analyses.

To determine the molecular weight and ensure protein integrity, the sample was investigated by analytical gel filtration (Figure 2-3c). Injected at a low concentration, NLRP9 eluted as a single peak with a retention volume of 1.80 ml, which corresponds to an approximate molecular weight of 89 kDa. Since the theoretical molecular weight of monomeric NLRP9 is 113 kDa, it can be concluded that NLRP9 from the peak 1 fraction corresponds to a stable monomer in solution.

Based on this result, the difference between monomeric NLRP9 and the aggregated protein collected from the void volume was examined in thermal shift denaturation assays (Figure 2-3d). Using nanoDSF (differential scanning fluorimetry) for thermal denaturation, NLRP9 void protein denatured in two steps as reflected by the different melting temperatures ( $T_M$ ) at 48.2°C and ~60°C, whereas monomeric NLRP9 denatured in only one defined event ( $T_M = 58.3^\circ\text{C}$ ). The protein from the void volume is significantly less stable compared to the monomeric NLRP9 protein ( $\Delta T_M = 10.1^\circ\text{C}$ ), suggesting a different conformation together with potential improper folding. With respect to the highly stabilizing effect of the MBP tag it should be mentioned again that the void volume fraction mainly consists of uncleaved protein, whereas the pooled right flank of the monomeric fraction only contains cleaved NLRP9. Furthermore, the melting curves of NLRP9 from both fractions show a different course, which likely reflects diverse local positions of tryptophan residues within the protein and therefore also provides evidence for different conformations. In conclusion, recombinant full-length NLRP9 forms a stable monomer in solution that is different from the void volume protein fraction.

### 2.1.4 ATP drives conformational change and dimerization of NLRP9

Mechanistically, one model for the regulation of STAND ATPases includes the binding of an inducer that results in the exchange from ADP to ATP and subsequent interconversion from an inactive to an active state (Danot et al., 2009). The subsequent ATP hydrolysis might couple to the generation of mechanochemical work that turns off the protein (Danot et al., 2009). In line, intrinsic ATPase activity was associated with all functions of NLRP3 and NLRP12, suggesting that ATP binding and hydrolysis play an important role in regulation (Duncan et al., 2007; MacDonald et al., 2013; Ye et al., 2008). Therefore, the effect of ADP and ATP on the conformation of NLRP9 was investigated using thermal shift denaturation assays (Figure 2-4).

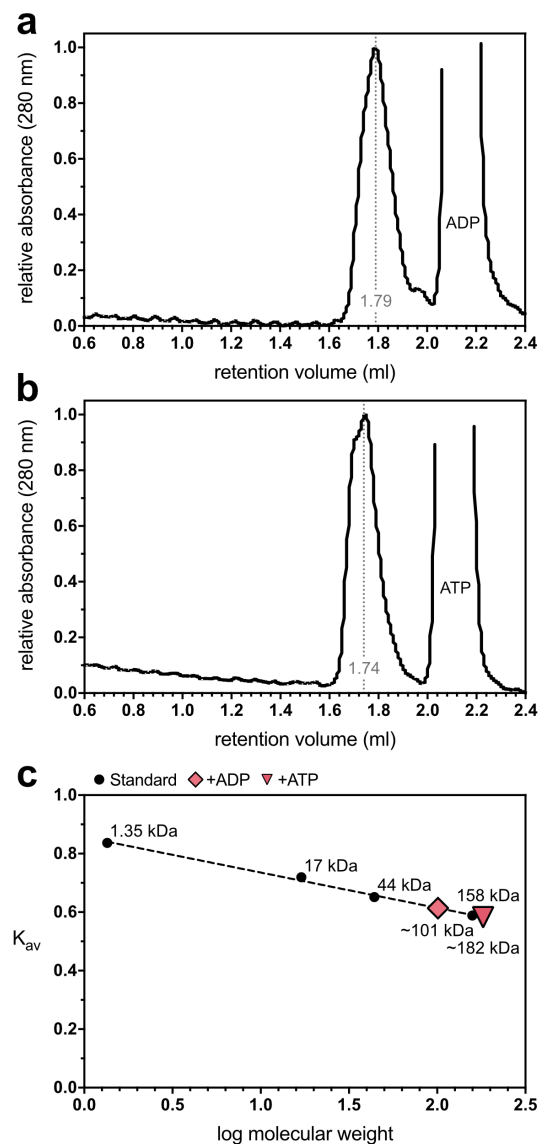


**Figure 2-4: Thermal destabilization of NLRP9 in the presence of ATP.** Thermal shift denaturation assay of (a) 350 nM NLRP9 void protein or (b) 80 nM NLRP9 monomer either in the absence or in the presence of 1 mM ADP or ATP. MgCl<sub>2</sub> at a concentration of 5 mM is already included in the purification buffer. The measurement was setup with a temperature ramp ranging from 15-95°C, a slope of 2°C·min<sup>-1</sup>, and a 100% laser intensity. Shown data is representative of 3 technical replicates. Apparent melting temperatures ( $T_M$ ) of the samples are depicted as dashed lines.

As expected, incubation with 1 mM ADP or ATP did not change the thermal stability of aggregated NLRP9 (void) as if compared with the protein incubated alone (Figure 2-4a). It is likely, although binding of ADP or ATP still might be possible, that the protein is



not well folded and thus not able to switch between the autoinhibited and active conformation. In contrast, incubation of monomeric NLRP9 with the same concentration of ATP did result in a significant destabilization of the protein ( $\Delta T_M = 5^\circ\text{C}$ ). Interestingly, incubation with ADP did not show such effect as the thermal stability of NLRP9 that was incubated with ADP was comparable to the untreated control (Figure 2-4b). These results indicate that monomeric NLRP9 is likely in an ADP-bound autoinhibited conformation. High concentration of ATP might promote nucleotide exchange together with a potential conformational change to an ATP-bound active conformation.



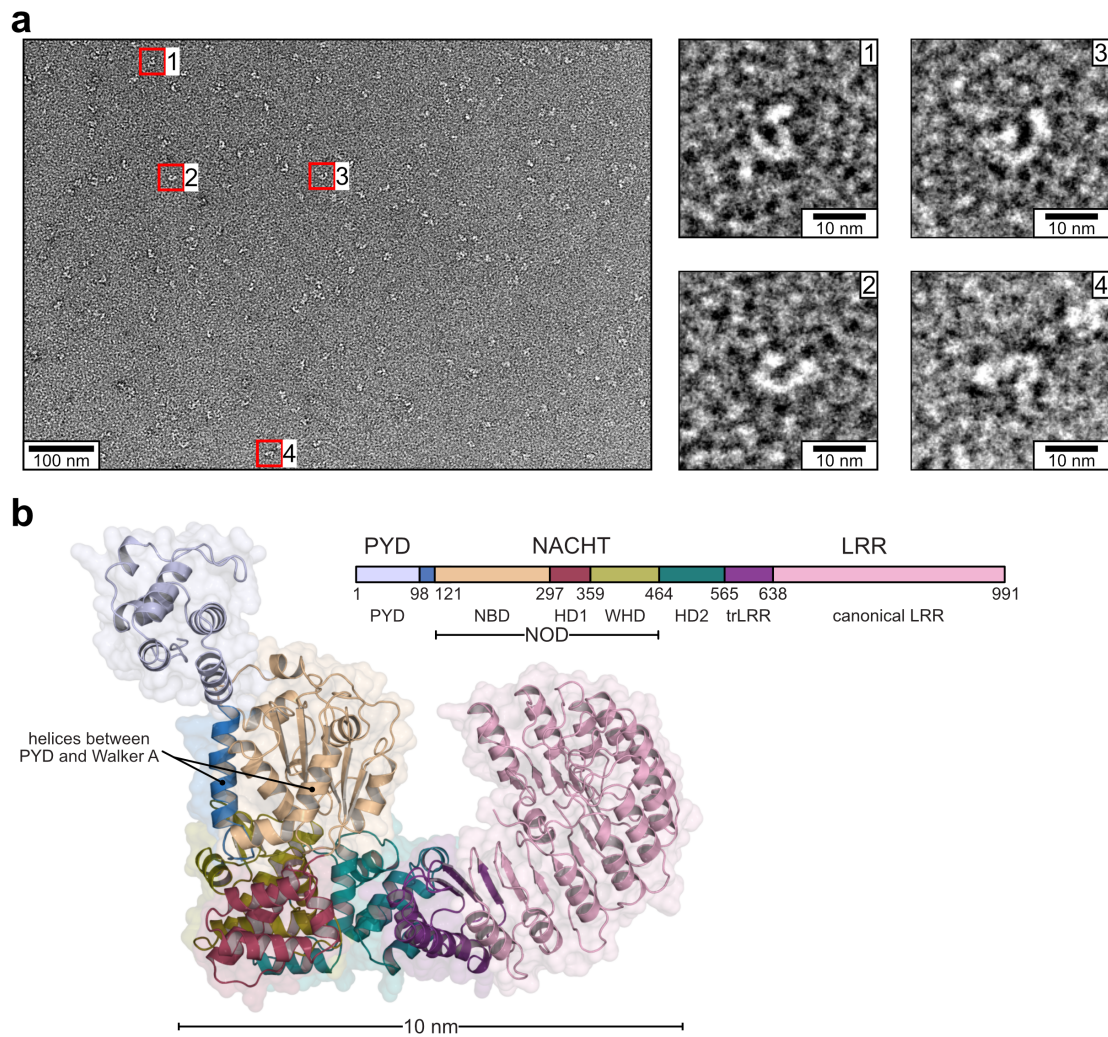
**Figure 2-5: Dimerization of NLRP9 in the presence of ATP.** Elution profile from analytical gel filtration of  $\sim 10 \mu\text{g}$  monomeric NLRP9 preincubated with 1 mM (a) ADP or (b) ATP for 30 minutes on ice before injection onto a Superose 6 Increase 3.2/300 column.  $\text{MgCl}_2$  at a concentration of 5 mM is already included in the purification buffer. (c) Calculation of the molecular weight from the peak retention volume obtained from (a, b). Linear regression was used to fit the calibration curve to the partition coefficient ( $K_{av}$ ) versus the logarithm of the molecular weight of a standard ( $R^2 = 0.9943$ ).

As exemplified by NLRC4 (Zhang et al., 2015) and NLRP6 (Shen et al., 2019), the current model of inflammasome formation includes oligomerization. To analyze the oligomerization status of NLRP9 after incubation with nucleotides, the protein was subjected to analytical gel filtration (Figure 2-5). Monomeric NLRP9 incubated with 1 mM ADP eluted at a retention volume of 1.79 ml, corresponding to a molecular weight of ~101 kDa (Figure 2-5a, c). If incubated with 1 mM ATP instead of ADP, the retention volume changed to 1.74 ml with a shoulder to the left side of the peak (Figure 2-5b). The measured retention volume corresponds to a molecular weight of ~182 kDa (Figure 2-5c). Since monomeric NLRP9 has a theoretical mass of 113 kDa it can be concluded that incubation with ADP has no effects on NLRP9 while incubation with ATP drives conformational change together with destabilization and dimerization.

### **2.1.5 Shape of particles obtained by electron microscopy fits model of NLRP9**

To address whether monomeric NLRP9 resembles the ‘closed’ and autoinhibited state of the NLR, the protein was analyzed using electron microscopy. The negative stain image shows single and homogeneous particles with an average diameter of approximately 10 nm (Figure 2-6a). The overall particle density was low and unfortunately the protein could not be further concentrated due to subsequent aggregation. While the homogeneity and size of the particles appeared to suit well for solving the protein structure using cryo-EM, the particle density opposed the performance of such trials. Thus, the shape of representative particles from the negative stain EM was further investigated.

Particles of monomeric human NLRP9 have a horseshoe-like shape with an additional density at one side (Figure 2-6a, right panels). This highly resembles the overall fold of the NACHT and LRR domains that has already been structurally determined in other NLR family proteins, including NLRC4 (PDB: 4KXF (Hu et al., 2013)), NOD2 (PDB: 5IRN (Maekawa et al., 2016)), and NLRP3 (PDB: 6NPY (Sharif et al., 2019)). In line, a surface representation from a model of human NLRP9 generated with the AlphaFold2 server (Jumper et al., 2021) shows clear similarities with the overall shape and size of the obtained EM particles (Figure 2-6b). While it is not possible to conclude about the active or inactive conformation of monomeric NLRP9 without determination of average class sums or ultimately the protein structure, the individual domains of NLRP9 likely fold and arrange in a similar way to other NLR family proteins. Therefore, regulation by a molecular switch mechanism and concomitant rearrangements might be conserved.



**Figure 2-6: Analysis of NLRP9 using electron microscopy.** (a) Negative stain EM image of  $\sim 0.01$   $\text{mg}\cdot\text{ml}^{-1}$  monomeric NLRP9, recorded by Inga Hochheiser (University of Bonn). Red squares (1-4) represent regions of interest that contain representative particles shown as close-ups on the right side. (b) Cartoon and transparent surface representation of a model of human NLRP9 generated using AlphaFold2 (Jumper et al., 2021). The domain composition is shown color-coded as in Figure 2-1 with domain boundaries being indicated.

## 2.2 Functional and structural investigation of the NLRP9 Pyrin domain

The NLRP9-dependent inflammasome in IECs relies on the formation of ASC specks and subsequent activation of the downstream effector cysteine protease caspase-1 (Zhu et al., 2017). In turn, activated caspase-1 is capable to process the highly pro-inflammatory cytokines pro-IL-1 $\beta$  and pro-IL-18 into their mature forms (Man & Kanneganti, 2016; Mariathasan et al., 2004). Additionally, caspase-1 cleaves gasdermin D, which incorporates into the host cell membrane to form pores that induce the release of cytokines and pyroptotic cell death (Burdette et al., 2021; Shi et al., 2015). In case of rotavirus, this process might drive abortive infection and thereby effectively reduce the viral replication rate in the host.

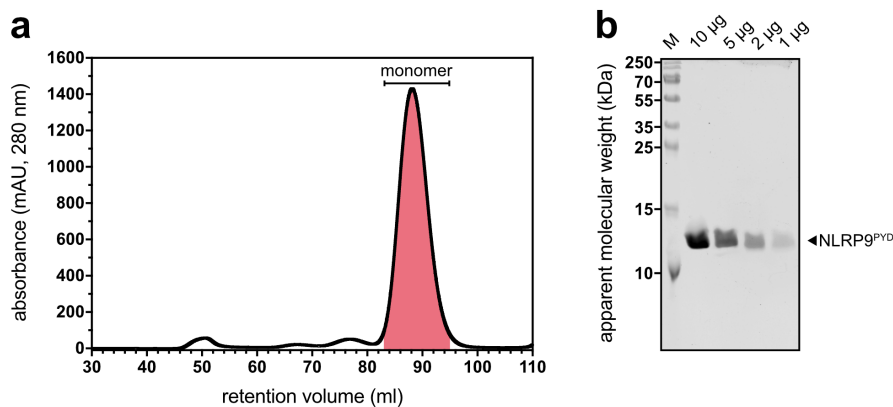
Importantly, inflammasome formation is facilitated by unified nucleation-driven polymerization of the individual inflammasome components (Li et al., 2018; Lu et al., 2014; Lu & Wu, 2015). As exemplified by NLRP3, NLRP6, and AIM2, the Pyrin domain of a sensor protein can polymerize to form the nucleation seed for ASC filament assembly by using three major types of asymmetric interfaces (Hochheiser, Behrmann, et al., 2022; Lu et al., 2015; Lu et al., 2014; Shen et al., 2019). Utilizing CARD-CARD interactions, caspase-1 extends the ASC filament, which finally leads to proximity-induced autoproteolytic activation (Lu et al., 2014). Thus, inflammasome assembly and signal amplification significantly relies on homotypic PYD-PYD and CARD-CARD interactions of the respective inflammasome components. However, such interactions have not been reported for NLRP9 until now.

To gain understanding of NLRP9 inflammasome assembly, this part of the thesis provides new insights on the capability of NLRP9<sup>PYD</sup> to self-polymerize into filaments and to nucleate ASC speck formation. It is found that recombinant human NLRP9<sup>PYD</sup> exists as a stable monomer *in vitro* and in cells. In line, human and also murine NLRP9<sup>PYD</sup> does not polymerize into filaments nor nucleate ASC speck formation, which is found to be in great contrast to filament-forming Pyrin domains such as human NLRP3<sup>PYD</sup>. Finally, a high-resolution crystal structure of human NLRP9<sup>PYD</sup> is determined, to study these differences on molecular level. While the conformation of NLRP9<sup>PYD</sup> seems compatible with filament formation, several charge inversions at positions of otherwise interfacing residues are identified. Repulsive effects might prohibit self-oligomerization of NLRP9<sup>PYD</sup>, which consequently suggests a distinct mode of inflammasome assembly, including the interaction with other NLRs.

### 2.2.1 Purification of recombinant human NLRP9<sup>PYD</sup>

To study NLRP9 inflammasome assembly, human NLRP9<sup>PYD</sup> (aa 1-97) was expressed as N-terminal GST-fusion protein in *E. coli*. The protein was purified to homogeneity by affinity chromatography, subsequent tag cleavage, and size-exclusion chromatography at near physiological buffer conditions (methods section). To enable separation of NLRP9<sup>PYD</sup> (MW = 11.83 kDa) from the cleaved GST tag (MW = ~27 kDa), the size-exclusion column was equipped with a tandem GSTrap affinity column for prolonged retention of GST. The chromatogram of a representative SEC run after AC and tag cleavage is shown in Figure 2-7a. The vast majority of NLRP9<sup>PYD</sup> eluted as one single

symmetrical peak at around 88 ml, corresponding to a retention volume expected for an approximately 12 kDa protein on this particular type of column. The monomeric protein fractions were pooled and readily concentrated up to  $120 \text{ mg}\cdot\text{ml}^{-1}$  without any signs of precipitation or aggregation. Different amounts of purified NLRP9<sup>PYD</sup> were analyzed with reducing SDS-PAGE to ensure the purity and integrity of the protein sample (Figure 2-7b). The SDS-gel shows only one intense single band at an apparent molecular weight of ~12 kDa, demonstrating crystallization-grade quality of recombinant NLRP9<sup>PYD</sup>.

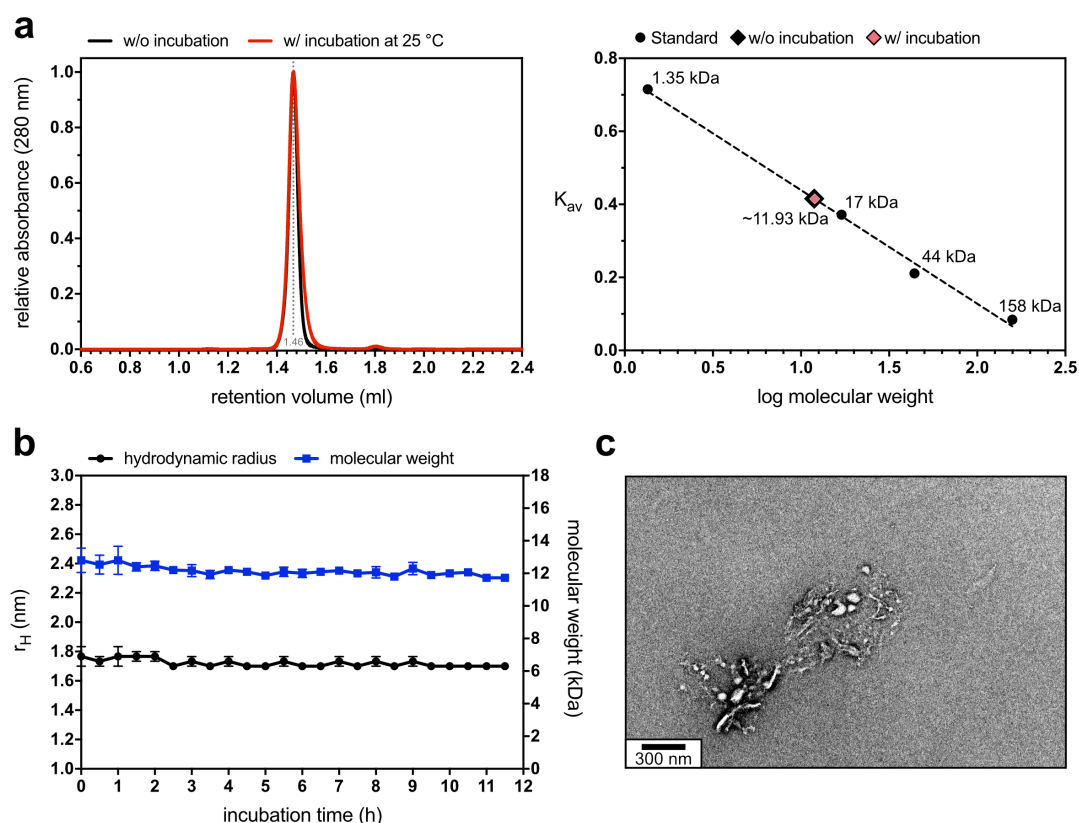


**Figure 2-7: Purification of human NLRP9<sup>PYD</sup> protein.** (a) Representative chromatogram of NLRP9<sup>PYD</sup> injected onto a Superdex 75 PG 16/600 size-exclusion column after affinity purification and tag cleavage. The column was connected to a tandem GSTRap column for prolonged retention of the GST tag. Elution of protein was followed via the absorbance at 280 nm wavelength. The red area indicates pooled fractions of the monomeric peak. (b) Coomassie-stained samples of NLRP9<sup>PYD</sup> after reducing SDS-PAGE. Different amounts of protein have been loaded onto the gel to determine the purity of the sample. M: marker.

### 2.2.2 NLRP9<sup>PYD</sup> is monomeric and does not self-polymerize *in vitro*

To answer the question whether NLRP9<sup>PYD</sup> features the ability to form filaments, the protein was analyzed using different methods that are common to determine the size distribution and experimental molecular weight of a protein sample. First, NLRP9<sup>PYD</sup> was diluted to  $2 \text{ mg}\cdot\text{ml}^{-1}$  and incubated for 12 h at  $25^\circ\text{C}$ . Subsequently, the protein sample was analyzed by analytical gel filtration and dynamic light scattering (Figure 2-8a, b). Analytical gel filtration revealed an average retention volume of 1.46 ml corresponding to an average molecular weight of 11.93 kDa independent of the incubation time (Figure 2-8a). Consistently, NLRP9<sup>PYD</sup> particles showed an average hydrodynamic radius of 1.7 nm that equals a molecular weight of approximately 12 kDa and was stable over the full 12 h incubation period (Figure 2-8b). Since the theoretical molecular weight of monomeric NLRP9<sup>PYD</sup> is 11.96 kDa, it was concluded that NLRP9<sup>PYD</sup> is monomeric in

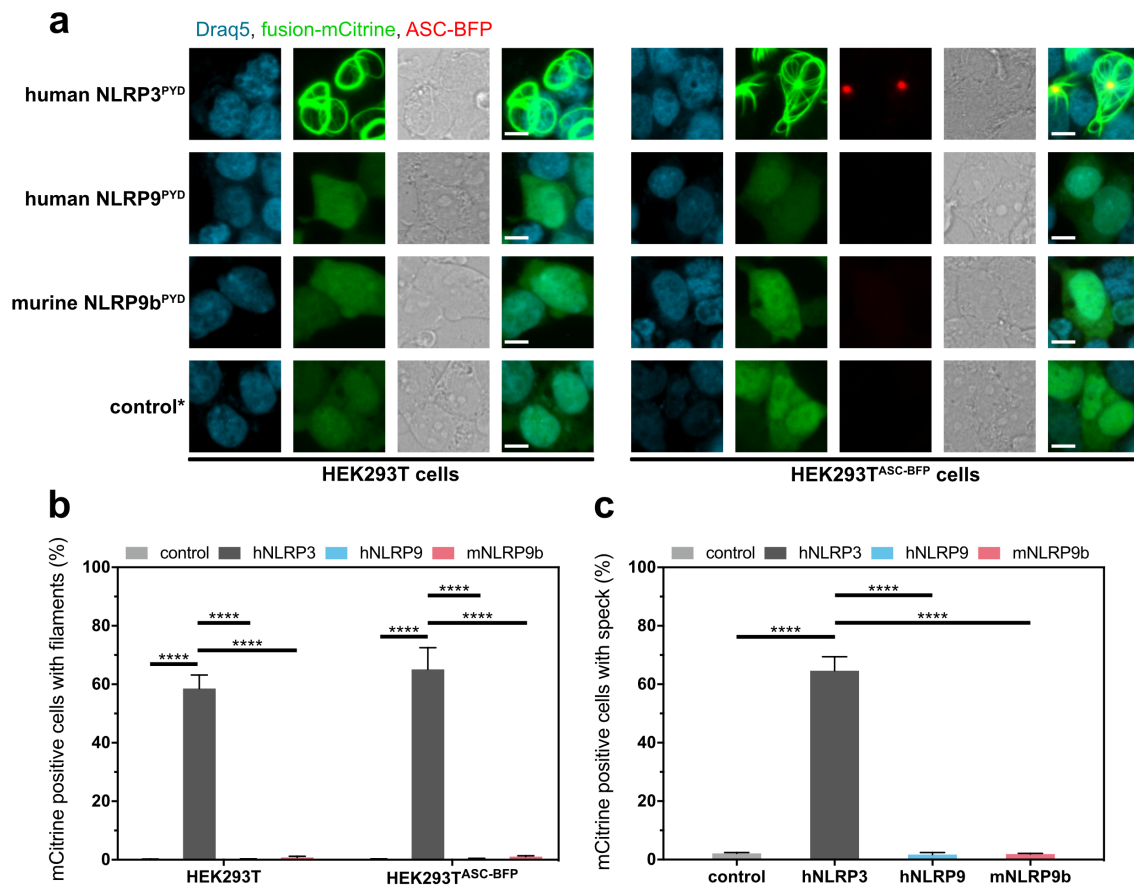
solution and does not self-polymerize *in vitro*. To rule out that a small fraction of NLRP9<sup>PYD</sup> is still able to form filaments, the protein was next diluted to 1.2 mg·ml<sup>-1</sup> and incubated overnight at 37°C. The sample was then analyzed by negative stain EM, which revealed only three small spots on the otherwise completely ‘empty’ grid with some protein aggregates but not filaments (Figure 2-8c). Since monomeric NLRP9<sup>PYD</sup> is too small to be resolved as a visible particle in electron microscopy, this finding underlines the aforementioned conclusion.



**Figure 2-8: Molecular dispersion of recombinant NLRP9<sup>PYD</sup> protein.** (a) Representative elution profile from analytical gel filtration of 50  $\mu$ g NLRP9<sup>PYD</sup> injected onto a Superdex 75 Increase 3.2/300 column and calculation of the molecular weight from the peak retention volume. Linear regression was used to fit the calibration curve to the partition coefficient ( $K_{av}$ ) versus the logarithm of the molecular weight of a standard ( $R^2 = 0.9948$ ). The molecular weight of NLRP9<sup>PYD</sup> was determined before and after 12 h of incubation time at 25°C. Data points are representative of three independent experiments.  $n = 3 \pm$  SEM. (b) Hydrodynamic radius and corresponding molecular weight of NLRP9<sup>PYD</sup> (2 mg·ml<sup>-1</sup>) as determined by DLS. Sample was measured every 30 min during 11.5 h of incubation at 25°C. Data points are representative of three independent experiments.  $n = 3 \pm$  SEM. (c) Negative stain EM image of 1.2 mg·ml<sup>-1</sup> NLRP9<sup>PYD</sup>, recorded by Inga Hochheiser (University of Bonn). Prior analysis, the sample was incubated overnight at 37°C. The depicted aggregates are representative of one of three small spots on the otherwise completely ‘empty’ grid.

### 2.2.3 NLRP9<sup>PYD</sup> does not self-polymerize nor nucleate ASC speck formation in cells

Since NLRP9<sup>PYD</sup> did not tend to form filamentous structures under the conditions tested *in vitro*, the next step was to validate its behavior in the more physiological setting of HEK293T cells. This cell line was previously shown to be suitable for NLRP9 inflammasome reconstitution (Zhu et al., 2017) and to endogenously express the potential binding partner DHX9 (The Human Protein Atlas, (Karlsson et al., 2021)). To track filament formation, human NLRP9<sup>PYD</sup> was overexpressed as C-terminal mCitrine fusion protein and compared to overexpression of human NLRP3<sup>PYD</sup> fusion protein, which is known to form filaments in cells (Stutz et al., 2017). As expected, an average of  $58.5 \pm 4.7\%$  of cells overexpressing NLRP3<sup>PYD</sup>-mCitrine displayed large filamentous structures with ring-shaped morphology (Figure 2-9a, b).



**Figure 2-9: Analysis of PYD polymerization and ASC speck formation in cells.** (a) Images of indicated mCitrine fusion proteins overexpressed in HEK293T or HEK293T<sup>ASC-BFP</sup> cells. (\*) Plasmid coding for mCitrine-HA was transfected as a control and due to IRES expression had to be imaged with higher exposure time. Bar, 10  $\mu$ m. Images are representative of three independent experiments. (b) Quantification of mCitrine-positive cells with filaments. Bars are representative of three independent experiments.  $n = 3 \pm$  SEM; \*\*\*\* $P < 0.0001$  (two-way ANOVA followed by the Holm-Sidak's multiple comparisons test). (c) Quantification of mCitrine-positive cells with ASC speck. Bars are representative of three independent experiments.  $n = 3 \pm$  SEM; \*\*\*\* $P < 0.0001$  (ordinary one-way ANOVA followed by the Holm-Sidak's multiple comparisons test).

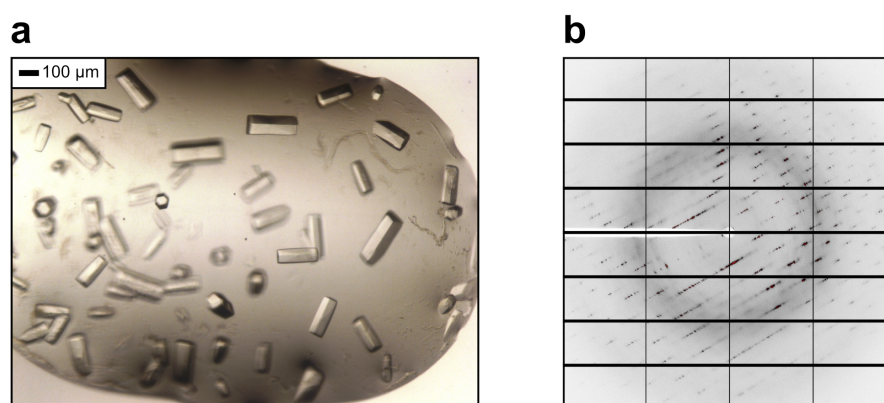
In contrast, fluorescent protein was found to diffusively locate within cells overexpressing human NLRP9<sup>PYD</sup>-mCitrine or mCitrine control under otherwise identical experimental conditions (Figure 2-9a, b). Conclusively, no NLRP9<sup>PYD</sup> filaments could be detected in the cellular system thus supporting findings from the *in vitro* experiments (Figure 2-8). However, all experiments have been performed using human NLRP9<sup>PYD</sup> whereas previous studies more extensively focused on the murine system. Given the relatively low sequence identity of 52.1% between human NLRP9 (aa 1-94) and murine NLRP9b (aa 1-91), it is reasonable to anticipate different abilities of its respective PYDs. For that reason, also murine NLRP9b<sup>PYD</sup> fusion protein was overexpressed in HEK293T cells and tested for its ability to form filaments. As observed for human NLRP9<sup>PYD</sup>, no filaments formed when murine NLRP9b<sup>PYD</sup> was overexpressed in cells (Figure 2-9a, b).

In comparison, most of the ASC-dependent inflammasomes studied so far rely on proper polymerization of the Pyrin effector domain as mutations within the PYD that prevent filament formation also abrogate nucleation of ASC specks (Shen et al., 2019; Stutz et al., 2017). Despite, with the established ASC-dependent Pyrin or NLRP12 inflammasomes, examples exist where as well no hints for filament formation of their respective effector domains have been found, yet (Jin et al., 2018; Schnappauf et al., 2019; Vladimer et al., 2012). Consequently, the ability of NLRP9<sup>PYD</sup> to nucleate ASC speck formation independent from self-polymerization was investigated. For this purpose, the PYD fusion proteins were overexpressed in HEK293T cells stably expressing an ASC-BFP fusion protein (HEK293T<sup>ASC-BFP</sup>). No significant difference between the number of cells with filaments could be found between HEK293T and HEK293T<sup>ASC-BFP</sup> cells, indicating that presence of ASC has no effect on the capability of Pyrin domains to self-polymerize (Figure 2-9a, b). But interestingly, NLRP3<sup>PYD</sup> filaments changed to a more star-like morphology that colocalized with ASC specks at its center (Figure 2-9a). Indeed, NLRP3<sup>PYD</sup> filaments were found to nucleate ASC speck formation, as the number of cells with filaments ( $65.1 \pm 7.4\%$ , Figure 2-9b) clearly correlated with the number of cells that formed ASC specks ( $64.6 \pm 4.8\%$ , Figure 2-9c). Importantly, these numbers differed significantly from mCitrine control cells ( $2.1 \pm 0.3\%$ ) and cells overexpressing human NLRP9<sup>PYD</sup> ( $1.74 \pm 0.67\%$ ) or murine NLRP9b<sup>PYD</sup> ( $1.92 \pm 0.23\%$ , Figure 2-9c). Thus, unlike NLRP3<sup>PYD</sup>, NLRP9<sup>PYD</sup> does not self-polymerize nor nucleate ASC specks in cells.



### 2.2.4 Determination of a high-resolution structure of the human NLRP9<sup>PYD</sup>

To investigate the differences between NLRP9<sup>PYD</sup> and filament-forming PYDs (as NLRP3, NLRP6, ASC, AIM2) at the molecular level, recombinant protein was subjected to crystallization trials for the determination of a high-resolution X-ray crystal structure. For that purpose, NLRP9<sup>PYD</sup> protein (aa 1-97) was concentrated to 31.7 mg·ml<sup>-1</sup> and tested in several commercially available and in house crystallization screens. Already after short period of time, initial crystals could be found in many conditions but suffered from heavy twinning. After extensive optimization, the final hexagonal-shaped crystals appeared in 0.1 M Bicine pH 9.0, 0.2 M sodium thiocyanate, 0.1 M sodium formate, and 25-27% (w/v) PEG3350 (Figure 2-10a). After the crystals had grown large enough for diffraction experiments, they were measured using the PX1 beamline and Eiger detector of the Swiss Light Source (SLS) located at the Paul Scherrer Institute in Villigen, Switzerland. The recorded diffraction images revealed single spots with a resolution of up to 1.95 Å and a diffraction pattern clearly indicative of protein crystals, thus ruling out the possibility of salt crystals (Figure 2-10b).



**Figure 2-10: Crystals and diffraction image of human NLRP9<sup>PYD</sup>.** (a) Representative hexagonal-shaped crystals of NLRP9<sup>PYD</sup> that appeared in one of the optimization conditions. (b) Diffraction image of NLRP9<sup>PYD</sup> with single spots that diffracted up to 1.95 Å resolution. Crystallization, data collection, processing, structure determination, and structure refinement was performed by Dr. Kanchan Anand (University of Bonn).

Although the particular crystal used to determine the structure suffered from some diffraction anisotropy, the dataset could be successfully processed in space group P6<sub>5</sub>22 at a final resolution of 1.95 Å (Table 2-1). Initial phases were obtained by molecular replacement using the coordinates of the NLRP4<sup>PYD</sup> crystal structure (PDB: 4EWI, 59.6% sequence identity) as a search model. Based on the resulting electron density map, the

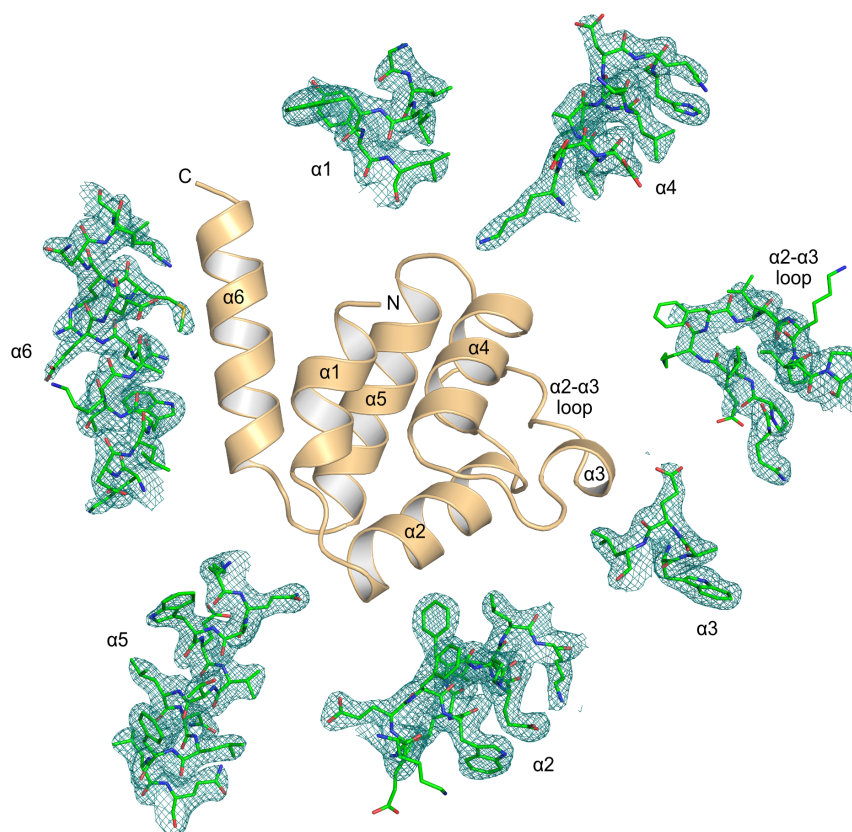
model of NLRP9<sup>PYD</sup> was built as a continuous chain spanning residues 9-97 and was refined to  $R_{\text{work}}$  of 21.5% and  $R_{\text{free}}$  of 22.2% with excellent stereochemistry (Table 2-1, Figure 2-11). In contrast, the N-terminal region (residues 1-8) of the molecule that corresponds to almost 10% of the structure and several sidechains facing towards solvent channels were found to be disordered and were not resolved in the electron density map (Figure 2-11). Additional details of the data collection, quality, and refinement statistics are given in Table 2-1.

**Table 2-1: Crystallographic data collection and refinement statistics of NLRP9<sup>PYD</sup>**

Data collection	
Space group	<i>P</i> 6 <sub>5</sub> 22
<i>a</i> , <i>b</i> , <i>c</i> (Å)	33.33, 33.33, 311.09
Resolution (Å) <sup>a</sup>	28.74-1.95 (2.02-1.95)
$R_{\text{merge}}$ (%)	8.25 (98.49)
$I/\sigma$ ( <i>I</i> )	18.58 (1.84)
Completeness (%)	99.52 (99.23)
$CC_{1/2}$	0.998 (0.916)
Redundancy	22.3 (16.7)
Refinement	
Resolution (Å)	28.74-1.95
Number of reflections	14 097
$R_{\text{work}}/R_{\text{free}}$ <sup>b</sup>	0.215/0.222
Number of atoms	
Protein	772
Water	17
<i>B</i> factors	
Protein	68.96
Water	75.60
RMSD	
Bond lengths (Å)	0.006
Bond angles (°)	0.74
Residues in Ramachandran	
Favored regions (%)	98.86
Allowed regions (%)	1.14
PDB	
Accession number	6Z2G

<sup>a</sup> Values in parentheses are for the highest resolution shell.

<sup>b</sup>  $R_{\text{free}}$  value is equivalent to the  $R$  value but is calculated for 5% of the reflections chosen at random and omitted from the refinement process.

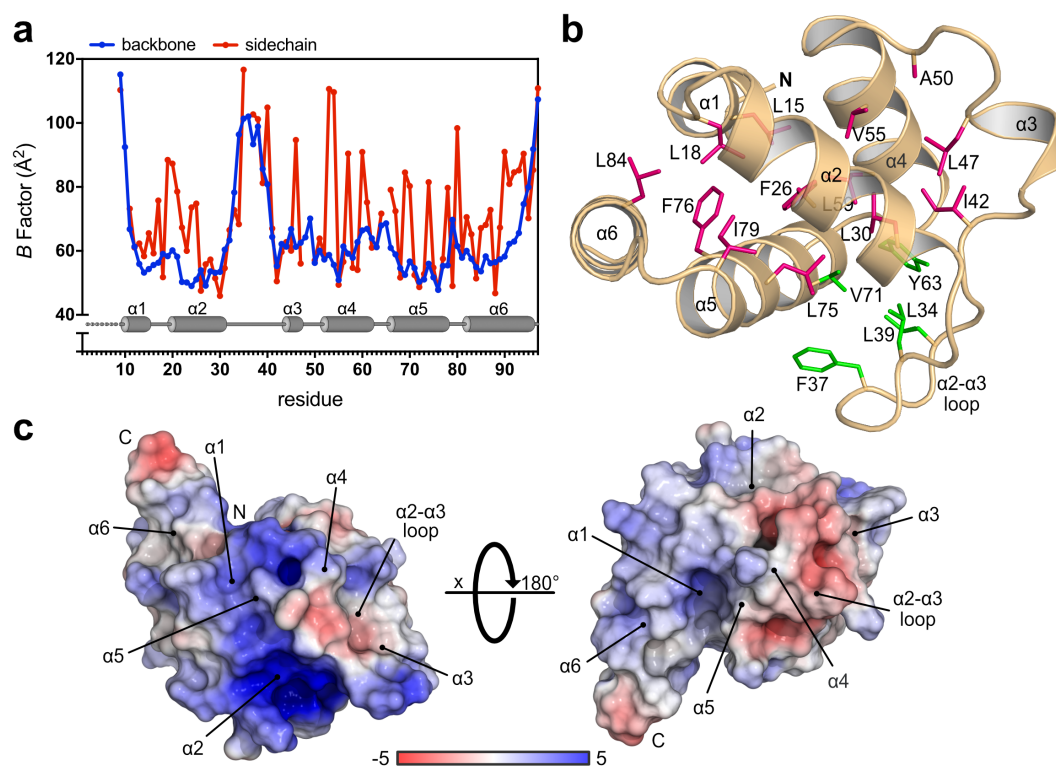


**Figure 2-11: Crystal structure of human NLRP9<sup>PYD</sup>.** Cartoon representation of the NLRP9<sup>PYD</sup> crystal structure with six antiparallel helices and long  $\alpha 2$ - $\alpha 3$  loop, surrounded by detailed views of the respective residues fitted into the electron density map ( $2F_o - F_c$  map contoured at 1.0 sigma). The N- and C-terminus of NLRP9<sup>PYD</sup> are indicated.

### 2.2.5 Hydrophobic core residues stabilize a polar surface of NLRP9<sup>PYD</sup>

Consistent with other members of the death-fold superfamily, NLRP9<sup>PYD</sup> is made from six antiparallel helices, connected by five loops and arranged in the typical death domain fold (Ferraro & Wu, 2012) (Figure 2-11). While residues 10-15 ( $\alpha 1$ ), 20-31 ( $\alpha 2$ ), 52-62 ( $\alpha 4$ ), 66-78 ( $\alpha 5$ ), and 82-96 ( $\alpha 6$ ) form five of the six helices as alpha helices, residues 44-47 ( $\alpha 3$ ) form a short  $3_{10}$ -helix. The helices are interconnected by residues with lower  $B$  factors that establish a central hydrophobic core (Figure 2-12a, b). Experimental  $B$  factors are commonly used to predict the flexibility of amino acids and their sidechains, since they describe the attenuation of X-ray scattering caused by dynamic disorder, due to the temperature-dependent vibration of atoms, and static disorder within the protein structure (Sun et al., 2019). Because lower  $B$  factors predict lower flexibility, it is assumed that the hydrophobic core residues substantially stabilize the overall fold of NLRP9<sup>PYD</sup>. These residues include Leu15 of  $\alpha 1$ , Leu18 in the  $\alpha 1$ - $\alpha 2$  loop, Phe26 and Leu30 of  $\alpha 2$ , Ile42 in the  $\alpha 2$ - $\alpha 3$  loop, Leu47 of  $\alpha 3$ , Ala50 in the  $\alpha 3$ - $\alpha 4$  loop, Val55 and Leu59 of  $\alpha 4$ , Leu75 and Phe76 of  $\alpha 5$ , Ile79 in the  $\alpha 5$ - $\alpha 6$  loop, and Leu84 of  $\alpha 6$ . As the hydrophobicity at positions

in the central core of NLRP9<sup>PYD</sup> is conserved across other PYDs, the importance of the hydrophobic core residues for domain stability is further confirmed (Figure 2-14a).



**Figure 2-12: Molecular characteristics of the NLRP9<sup>PYD</sup>.** (a) Plot of individual  $B$  factors for each residue of NLRP9<sup>PYD</sup>. Values for backbone (blue) and sidechains (red) were calculated separately. Sidechains without occupancy were excluded. Secondary structure elements of NLRP9<sup>PYD</sup> are plotted above the corresponding residue numbers. (b) Bottom view of NLRP9<sup>PYD</sup> (rotated by  $90^\circ$  about the  $x$ -axis relative to Figure 2-11). Hydrophobic core residues stabilizing the six-helical fold in NLRP9<sup>PYD</sup> are shown as pink sticks. A second hydrophobic cluster stabilizing the  $\alpha 2$ - $\alpha 3$  loop is shown as green sticks. (c) Color-coded (blue: positive, red: negative) electrostatic surface representation of NLRP9<sup>PYD</sup> generated with APBS (Jurrus et al., 2018). Electrostatic potentials are given in units of  $k_B T/e_c$  where  $k_B$  is the Boltzmann constant,  $T$  is the temperature and  $e_c$  is the charge of the electron.

In contrast, residues with highest  $B$  factors for backbone and sidechains were found at the N-terminus of  $\alpha 1$ , the C-terminus of  $\alpha 6$  and within the  $\alpha 2$ - $\alpha 3$  loop (Figure 2-12a). Interestingly, the  $\alpha 2$ - $\alpha 3$  loop is stabilized by a second hydrophobic cluster formed by residues Leu34, Phe37, and Leu39 interacting with Tyr63 of the  $\alpha 4$ - $\alpha 5$  loop, and Val71 of  $\alpha 5$  (Figure 2-12b). Because raw  $B$  factors are dependent on resolution, crystal lattice, and refinement procedures, they do not represent an absolute quantitative measure and need normalization to allow comparison between different structures (Sun et al., 2019; Zhang & Kurgan, 2014). However, the relative distribution of regions with lower and higher raw  $B$  factors is equivalent for PYDs of other NLRPs (Bae & Park, 2011; Hiller et al., 2003; Pinheiro et al., 2010), supposing regions with similar flexibility.

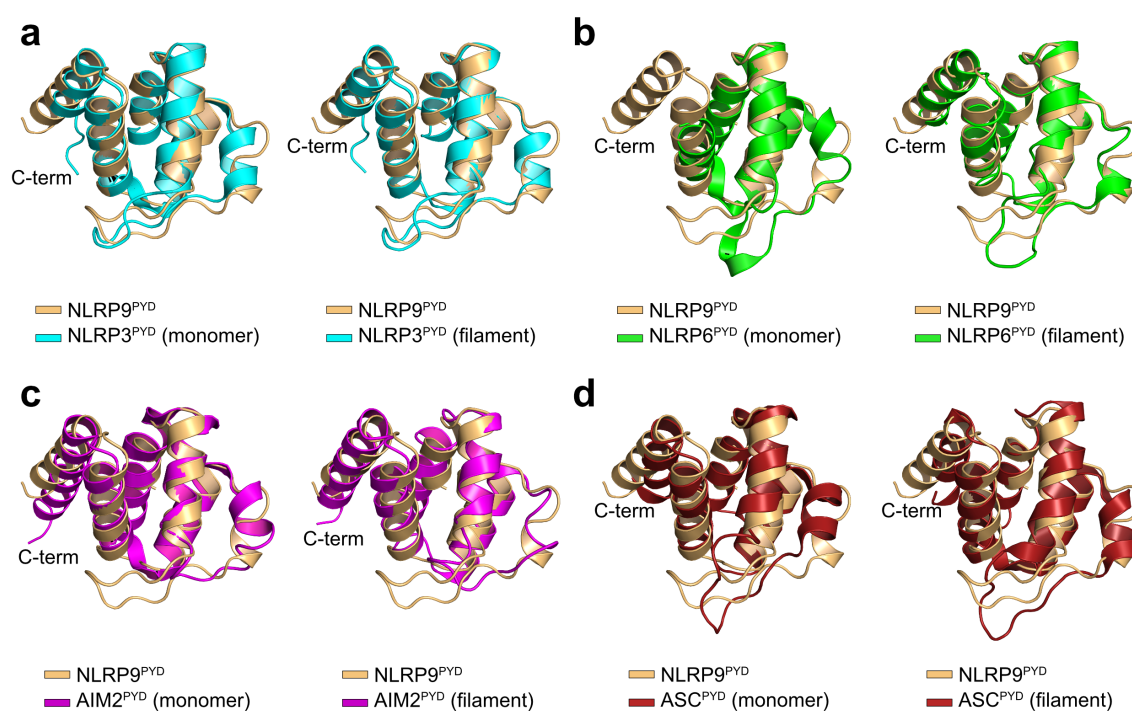
While seeking for explanations why NLRP9<sup>PYD</sup> is not able to self-polymerize, next, the electrostatic surface of the protein domain was analyzed (Figure 2-12c). It was striking that the surface of NLRP9<sup>PYD</sup> mainly consists of polar residues with basic character (theoretical pI of NLRP9<sup>PYD</sup> is 9.1), whereas clear acidic surface patches could only be found in a rather small region of the  $\alpha$ 2- $\alpha$ 3 loop and the very C-terminus of  $\alpha$ 6 (Figure 2-12c). As the filament-forming Pyrin domains of NLRP3, NLRP6 and AIM2 display significantly different distribution of basic and acidic surface patches (data not shown), this result prompted further investigation.

### **2.2.6 NLRP9<sup>PYD</sup> adopts a conformation compatible with filament formation**

To draw conclusions about filament formation based on amino acids on the surface of NLRP9<sup>PYD</sup>, it is essential to analyze their relative location in the protein, meaning their three-dimensional conformation. It is known that, upon formation of the filament, PYDs can undergo large conformational changes with most prominent translational and rotational transition of the flexible  $\alpha$ 2- $\alpha$ 3 loop and its connected  $\alpha$ 2 and  $\alpha$ 3 helices (Lu et al., 2015; Lu et al., 2014; Shen et al., 2019). Therefore, it was analyzed how the conformation of these regions would change upon filament formation and whether NLRP9<sup>PYD</sup> could undergo such transition without steric hindrance. For this purpose, the structure of NLRP9<sup>PYD</sup> was overlaid and compared with structures of NLRP3<sup>PYD</sup>, NLRP6<sup>PYD</sup>, AIM2<sup>PYD</sup>, and ASC<sup>PYD</sup> obtained from monomeric and filamentous assemblies (Figure 2-13). Interestingly, conformations of NLRP3<sup>PYD</sup> were found to be almost non-distinguishable between the monomeric and filamentous state. They both closely resemble monomeric NLRP9<sup>PYD</sup> and superimpose well with root-mean-square deviation (RMSD) values of 1.0 Å and 0.8 Å, respectively (Figure 2-13a). In contrast, NLRP6<sup>PYD</sup> undergoes conformational changes upon filament formation (Shen et al., 2019). But surprisingly, it was found that NLRP6<sup>PYD</sup> from the filament superimposes better with NLRP9<sup>PYD</sup> (RMSD value of 1.2 Å) as if compared with monomeric NLRP6<sup>PYD</sup> (RMSD value of 1.6 Å). Especially the orientation of the  $\alpha$ 2- $\alpha$ 3 loop region and the downstream  $\alpha$ 3 helix of filamentous NLRP6<sup>PYD</sup> is highly similar to NLRP9<sup>PYD</sup>, whereas those regions in monomeric NLRP6<sup>PYD</sup> are oriented differently (Figure 2-13b).

For validation of these findings, NLRP9<sup>PYD</sup> was also compared to structures of the less related AIM2<sup>PYD</sup> and ASC<sup>PYD</sup> (Figure 2-13c, d). Opposing the previous findings, both, monomeric AIM2<sup>PYD</sup> and ASC<sup>PYD</sup> superimpose better with monomeric NLRP9<sup>PYD</sup> as if

compared with their filamentous counterparts. They superimpose with RMSD values of 1.1 Å and 1.7 Å for AIM2<sup>PYD</sup>, and 1.3 Å and 1.5 Å for ASC<sup>PYD</sup>, respectively. However, by comparing only the  $\alpha$ 2- $\alpha$ 3 loop regions and the C-terminal helices of those molecules, it is apparent that NLRP9<sup>PYD</sup> resembles the conformation of filamentous but not monomeric AIM2 and ASC PYDs. Recapitulating, NLRP9<sup>PYD</sup> shares the orientation of not only but especially the  $\alpha$ 2- $\alpha$ 3 loop region with different filamentous Pyrin domains and thus might already exist in a conformation compatible with filament formation.

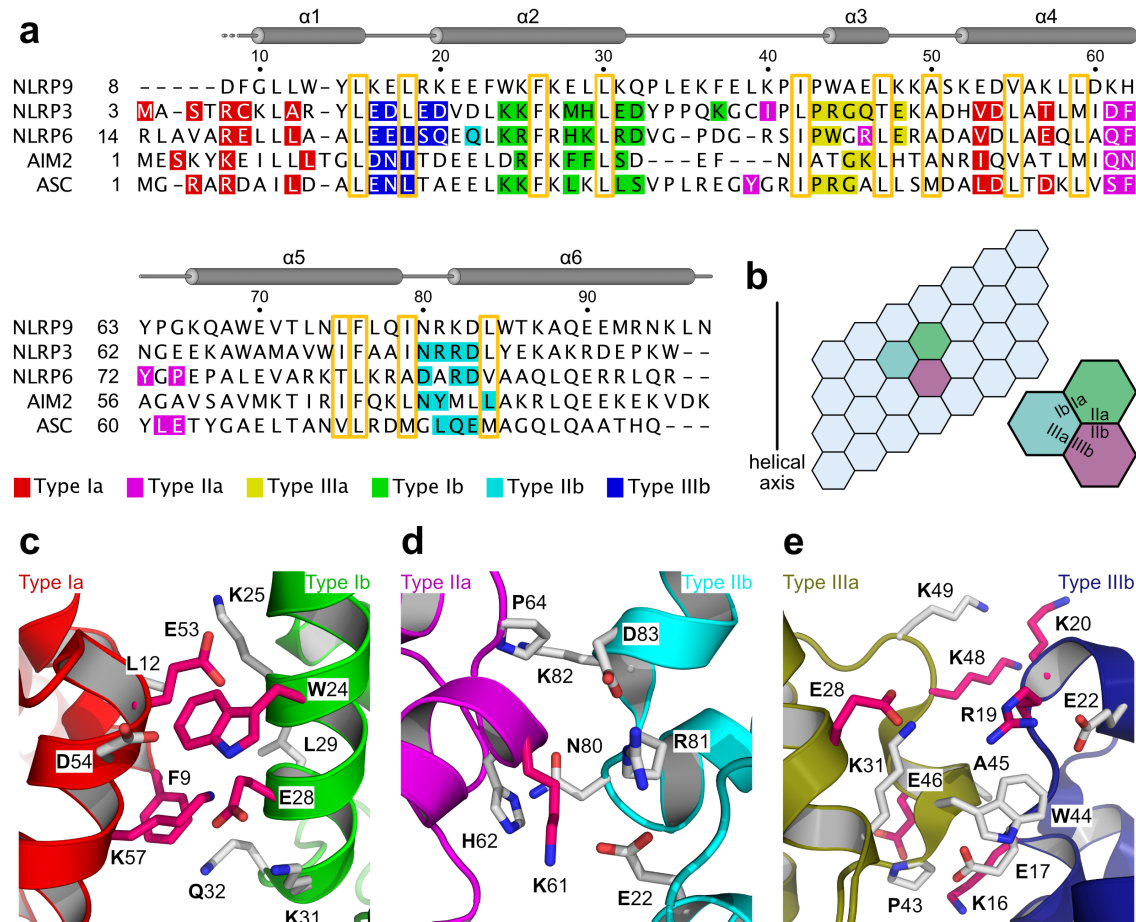


**Figure 2-13: Conformational analysis of NLRP9<sup>PYD</sup>.** Overlays of the here determined NLRP9<sup>PYD</sup> crystal structure (PDB: 6Z2G) with different structures of filament-forming PYDs. **(a)** Overlay with the NLRP3<sup>PYD</sup> crystal structure (PDB: 3QF2, chain A) and the NLRP3<sup>PYD</sup> filament structure (PDB: 7PZD). **(b)** Overlay with the MBP-NLRP6<sup>PYD</sup> crystal structure (PDB: 6NDJ, chain A) and the NLRP6<sup>PYD</sup> filament structure (PDB: 6NCV). **(c)** Overlay with the MBP-AIM2<sup>PYD</sup> crystal structure (PDB: 3VD8) and the GFP-AIM2<sup>PYD</sup> filament structure (PDB: 6MB2). **(d)** Overlay with the monomeric ASC<sup>PYD</sup> structure (PDB: 1UCP) and the ASC<sup>PYD</sup> filament structure (PDB: 3J63).

### 2.2.7 Several amino acids of NLRP9 interfere with PYD filament formation

The high-resolution structural data of NLRP9<sup>PYD</sup> was used to address its inability to self-polymerize at the molecular level. For this purpose, a structure-based sequence alignment of NLRP9<sup>PYD</sup> and the filament-forming PYDs of NLRP3, NLRP6, AIM2, and ASC was performed (Figure 2-14a). NLRP9<sup>PYD</sup> (residues 8-94) displays sequence identities of 28.7%, 26.4%, 25.0%, and 21.8% with NLRP3<sup>PYD</sup>, NLRP6<sup>PYD</sup>, AIM2<sup>PYD</sup>, and ASC<sup>PYD</sup>, respectively (Figure 2-14a). As depicted in Figure 2-14b, assembly of PYD filaments

relies on the formation of three asymmetric interfaces that mediate intra- and interstrand interactions (Lu et al., 2015; Lu et al., 2014; Shen et al., 2019). It was hypothesized that residues located in such interfaces and matching by charge or hydrophobicity in filament-forming Pyrin domains might be mismatching in NLRP9<sup>PYD</sup>.



**Figure 2-14: Structural comparison of NLRP9<sup>PYD</sup> with filament-forming PYDs.** (a) Structure-based sequence alignment of the PYDs of NLRP9 with the filament-forming PYDs of NLRP3, NLRP6, AIM2, and ASC. Asp8 was included in the alignment, since density of the mainchain could be seen at lower sigma level. For NLRP3, NLRP6, AIM2, and ASC, the filament structures are known (Hochheiser, Behrmann, et al., 2022; Lu et al., 2015; Lu et al., 2014; Shen et al., 2019) and the residues forming the asymmetric interfaces are highlighted with the indicated colors. Residues that form the hydrophobic core in NLRP9<sup>PYD</sup> are shown in yellow boxes. Secondary structure elements of NLRP9<sup>PYD</sup> are plotted above the corresponding sequence. (b) Chart of three flanking subunits in a typical PYD filament. They form unified type I, type II, and type III interfaces with interface sides a and b, respectively. Subunits are labeled light blue, light green and light magenta. (c-e) Detailed view of the residues forming the (c) type I, (d) type II, and (e) type III interfaces in a modeled and hypothetical filament of NLRP9<sup>PYD</sup> that is based on the NLRP3<sup>PYD</sup> and NLRP6<sup>PYD</sup> filament structures. Residues of NLRP9 not matching conserved properties of amino acids at equivalent positions in filament-forming PYDs are highlighted as pink sticks.

In fact, many residues at positions that are typically involved in filament formation, were found to be charge inverted in NLRP9. This includes Asp8, Lys16, Arg19, Lys20, Glu46, Lys48, Lys57, and Lys61 (Figure 2-14a). As well, positions with conserved

hydrophobicity in filament-forming Pyrin domains were found to be substituted by charged residues, such as Glu28 and Glu53 in NLRP9<sup>PYD</sup> (Figure 2-14a). Conversely, Phe9 and Trp24 were found as large hydrophobic substitutions potentially prohibiting NLRP9<sup>PYD</sup> filament formation due to steric clashes (Figure 2-14a).

While these findings could indeed explain the inability of NLRP9<sup>PYD</sup> to self-polymerize, the presumed mismatches could compensate each other in the interfaces. This would for example be the case, if residues not only being charge inverted on the ‘a’ side but equally on the ‘b’ side, thereby preserving important interactions. To understand the significance of the differences between NLRP9<sup>PYD</sup> and filament-forming PYDs, a hypothetical NLRP9<sup>PYD</sup> filament was modeled based on the NLRP3<sup>PYD</sup> (PDB: 7PZD, (Hochheiser, Behrmann, et al., 2022)) and NLRP6<sup>PYD</sup> (PDB: 6NCV, (Shen et al., 2019)) filament structures. It was found that in the hypothetical type I interface Lys57 and Glu28 would indeed compensate each other and form a potential salt bridge (Figure 2-14c). Moreover, Phe9 might be able to adopt a different conformation and orient in direction of the proximal Leu12 and Leu29 to form hydrophobic interactions (Figure 2-14c). In contrast, Trp24 and Glu53 might cause a plausible mismatch that interferes with NLRP9<sup>PYD</sup> filament formation (Figure 2-14c).

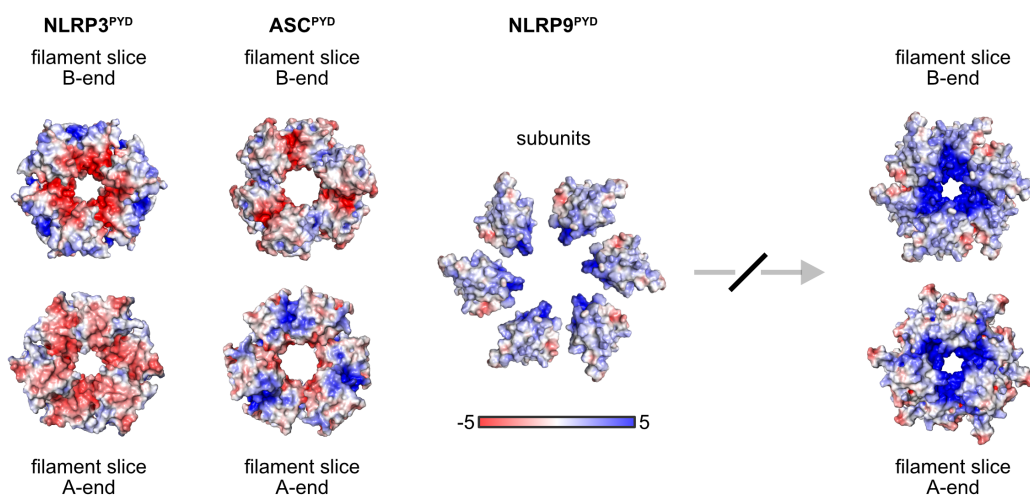
In the type II interface, the only charge inversion found is Lys61 (type IIa, Figure 2-14d). Since both, positively and negatively charged residues (Glu22, Arg81, Asp83) would be provided by the putative ‘b’ side, Lys61 could probably establish a salt bridge similar to its acidic counterparts in filament-forming PYDs.

In the putative type III interface, it is apparent that Trp44 would cause a steric clash with the mainchain of Glu17 in case the residue cannot adopt a different conformation that allows to avoid this close proximity (Figure 2-14e). However, in NLRP6<sup>PYD</sup> a tryptophan residue is found at the same position but with different orientation of its sidechain (Figure 2-14a, (Shen et al., 2019)). While Lys16 and Glu46 might form a salt bridge and thereby compensate each other in a hypothetical filament, Arg19, Lys20, Lys48, and Lys49 will most likely cause repulsive effects that prevent formation of such interface in NLRP9<sup>PYD</sup> (Figure 2-14e). In theory, Arg19 could interact with the close by Glu28, which is otherwise part of the type I interface. But intramolecular interactions with Lys31 and Glu22, respectively, might hinder the rearrangements needed for such intermolecular interaction to occur (Figure 2-14e). Taken together, several amino acids of NLRP9<sup>PYD</sup> were found to likely interfere with the formation of type I and type III interfaces, which are prerequisite for self-polymerization into filaments.



### 2.2.8 NLRP9<sup>PYD</sup> does not display charge matching surface patches with ASC

To investigate the differences between human NLRP3<sup>PYD</sup> and NLRP9<sup>PYD</sup> in its ability to nucleate ASC speck formation, the model of a hypothetical NLRP9<sup>PYD</sup> filament was further analyzed. One ring of the human NLRP3<sup>PYD</sup> (PDB: 7PZD) and ASC<sup>PYD</sup> (PDB: 3J63) filament structures and a slice of the hypothetical NLRP9<sup>PYD</sup> filament was used to calculate APBS-generated surface electrostatics (Jurrus et al., 2018) (Figure 2-15). Many charged clusters in NLRP3<sup>PYD</sup> (pI = 6.1) are found to be inverted in NLRP9<sup>PYD</sup> (pI = 9.1), which might disrupt intra- and interstrand interactions in the filament. Additionally, basic residues centering at the inner core ring of the hypothetical NLRP9<sup>PYD</sup> filament, might cause strong repulsive forces that likely contradict such assembly (Figure 2-15, NLRP9<sup>PYD</sup> top and bottom views). However, in the NLRP3<sup>PYD</sup> filament, similar forces are caused by acidic residues that line the inner core ring and must be overcome by strong attractive forces in the asymmetric interfaces to allow self-polymerization (Figure 2-15, NLRP3<sup>PYD</sup> top and bottom views). In contrast, two rings of ASC<sup>PYD</sup> show three surface patches matching by charge from the outer to the inner core ring (Figure 2-15, ASC<sup>PYD</sup> top and bottom views), possibly explaining its high intrinsic tendency to form filaments at neutral pH (Lu et al., 2014).



**Figure 2-15: Molecular analysis of ASC nucleation capability of NLRP9<sup>PYD</sup>.** Color-coded (blue: positive, red: negative) electrostatic surface representation of subunits of NLRP9<sup>PYD</sup> and filament slices of NLRP3<sup>PYD</sup>, ASC<sup>PYD</sup>, and NLRP9<sup>PYD</sup> generated with APBS (Jurrus et al., 2018). The filament slice of NLRP3<sup>PYD</sup> and ASC<sup>PYD</sup> was adapted from the NLRP3<sup>PYD</sup> (PDB: 7PZD) and the ASC<sup>PYD</sup> (PDB: 3J63) filament structures, respectively. Based on the NLRP3<sup>PYD</sup> and NLRP6<sup>PYD</sup> filament structures, the slice representation of a hypothetical NLRP9<sup>PYD</sup> filament was modeled using the crystal structure of the NLRP9<sup>PYD</sup> monomer determined here (PDB: 6Z2G). Bottom views (A-ends) represent a superjacent slice of the respective filament that was rotated by 180° about the y-axis and mirrored horizontally to show interfacing regions in the filament at the same x/y coordinates of top and bottom views. Electrostatic potentials are given in units of  $k_B T / e_c$  where  $k_B$  is the Boltzmann constant, T is the temperature and  $e_c$  is the charge of the electron.

Regarding nucleation of ASC specks, it is known that the ‘B-end’ of the NLRP3<sup>PYD</sup> filament forms a seed for an interaction with the ‘A-end’ of a globular ASC<sup>PYD</sup> molecule to subsequently induce ASC polymerization (Hochheiser, Behrmann, et al., 2022). Indeed, surface patches formed at the ‘B-end’ of the NLRP3<sup>PYD</sup> filament and the ‘A-end’ of the ASC<sup>PYD</sup> filament are matching by charge, which is in great contrast to NLRP9<sup>PYD</sup> (Figure 2-15). Although not excluding potential hydrophobic interactions between NLRP9<sup>PYD</sup> and ASC<sup>PYD</sup>, no charge matching surface patches at interfacing positions could be found. This might be another explanation why NLRP9<sup>PYD</sup> is not nucleating the homotypic transition to ASC<sup>PYD</sup>.

### 2.3 Discussion and Conclusion

Already five years ago, rodent and human NLRP9 have been described to form an ASC and caspase-1 dependent inflammasome in intestinal epithelial cells infected with rotavirus (Zhu et al., 2017). While we have learned about molecular details of other inflammasomes, understanding of the NLRP9 inflammasome is still widely elusive. Only very recently, structural details about bovine NLRP9 $\Delta$ PYD could be achieved by using a combination of electron microscopy and X-ray crystallography (Kamitsukasa et al., 2022). The researchers were able to purify a monomer of bovine NLRP9 $\Delta$ PYD and to determine its X-ray crystal structure at 2.75 Å resolution, revealing NLRP9 in the ADP-bound inactive state. Interestingly, the structure of bovine NLRP9 is closely resembling the NACHT-LRR region of a model of human NLRP9 generated using the AlphaFold2 server (Jumper et al., 2021) (Figure 2-6b). Using a variety of techniques, from thermal shift denaturation to analytical gel filtration, it was found that full-length human NLRP9 also exists as a stable monomer in solution (Figure 2-3). Additionally, electron microscopy revealed particles that fit in size and shape with both, the structure and model of bovine and human NLRP9 (Figure 2-6a), respectively, indicating that monomers of human NLRP9 are likely to represent the same ADP-bound inactive state.

NLRP9 comprises all motifs relevant for nucleotide binding and hydrolysis, including the well conserved Walker A and Walker B motifs within the central NACHT domain (Figure 2-1). However, the NLRP9 Walker B motif LFIMDGFEQ differs significantly from the hhhhD[G/A/S]hDE consensus sequence that was described for the NACHT clade of STAND ATPases (Leipe et al., 2004). Importantly, mutational experiments on the Walker B motif in NLRP3 (LFLMDGFDE) were performed by our group and

revealed that the last acidic residue has an important function in ATP hydrolysis (Brinkschulte, 2020). Therefore, it is reasonable to assume that NLRP9 hydrolysis activity should generally be very low. In addition, hydrolysis activity is likely controlled by the ‘glutamate switch’ mechanism (Zhang & Wigley, 2008). To my knowledge, yet, no regulatory factor is known to drive this mechanism in NLRP proteins, but the importance of this motif is strongly evidenced by the disease-related mutation R262W in NLRP3, which is only two residues downstream of the expected position of the ‘glutamate switch’ motif and known to cause spontaneous inflammasome activation in patients with CAPS (Baroja-Mazo et al., 2014). Interestingly, NLRP9 misses a polar residue at the position where the sensor I motif is usually found (Figure 2-1) (Sandall et al., 2020). Again, this suggests that NLRP9 might possess only very low ATP hydrolysis activity, because the sensor I motif is thought to play an important role in the hydrolysis reaction (Leipe et al., 2004). Instead, NLRP9 contains an arginine residue at a position expected to be exposed and suitable to function as an arginine finger motif (Figure 2-1). Such motif is rather rare in NLRP proteins (Sandall et al., 2020) but suggests that NLRP9 hydrolysis activity is increased in a multimeric assembly as is the case for some AAA+ ATPases (Tafuya & Bustamante, 2018). Indeed, upon incubation with ATP·Mg<sup>2+</sup>, NLRP9 adopts a different conformation and dimerizes, which is evidenced by a shift in thermal shift denaturation (Figure 2-4b) and analytical gel filtration assays (Figure 2-5). However, dimerization differs largely from the 10-12-mer found for active NLRC4 (Zhang et al., 2015) or the closely related and often ring-shaped hexameric AAA+ ATPases (Jessop et al., 2021), compromising the hypothesis of a fully active NLRP9. For NLR proteins, that belong to the STAND ATPase family, it is thought that the topologically conserved NACHT and LRR domains adopt a ‘closed’ and inactive conformation and upon ATP binding shear open into the active conformation allowing for subsequent oligomerization (Danot et al., 2009). In turn, nucleotide hydrolysis is thought to convert energy for the rearrangement back to the inactive state (Danot et al., 2009). For NLRP9 it is yet unknown if, and under which conditions, the protein hydrolyses ATP to ADP. This question should be addressed in future studies by using a multi-cycle turnover ATP hydrolysis assay established in the laboratory.

NLR proteins are kept autoinhibited in the inactive state by a combination of regulatory mechanisms, including post-translational modifications (PTMs) (Yang et al., 2017). Yet, differences in regulation are evidenced by the finding that, in contrast to NLRP9, incubation of NLRP3 with 1 mM ATP·Mg<sup>2+</sup> does not alter its inactive decameric

conformation (Hochheiser, Pilsl, et al., 2022). Interestingly, the tertiary structure of the HD2 domain in bovine NLRP9 was reported to be different from NLRP3, NOD2, and NLRC4, thus a different function was proposed (Kamitsukasa et al., 2022). One more apparent difference between NLRP3 and NLRP9 is the decameric versus monomeric assembly of the inactive state. Notably, one intermolecular interface in the NLRP3 oligomer is established by an acidic loop that extends from an LRR transition segment and is missing in NLRP9 (Figure 2-1) (Hochheiser, Pilsl, et al., 2022). Probably, high concentrations of ATP are able to force the release of ADP in monomeric NLRP9, which might result in a ‘semi-open’ conformation with formation of partial oligomerization interfaces that allow for dimerization of the protein. Consequently, regulatory elements still preserved in the inactive state might prohibit full activation of NLRP9 and further oligomerization. However, initial observations should be confirmed by follow-up experiments to strengthen conclusions.

Unique to NLRP9 is a C-terminal helix, which folds back into the concave site of the NLRP9 LRR domain and was supposed to have regulatory function (Kamitsukasa et al., 2022). Likewise, the NLRP3 acidic loop interacts with the concave site of the LRR domain (Hochheiser, Pilsl, et al., 2022). Moreover, interaction of the NBD with the concave site of the LRR domain has been shown and assumed for inactive NLRC4 and NOD2, respectively (Hu et al., 2013; Maekawa et al., 2016). Additionally, also ligand binding in NOD2 is supposed to happen at the concave site of the LRR domain (Maekawa et al., 2016) and the NIMA-related kinase NEK7 was shown to bind to this same site in NLRP3 to potentially license the NLRP3 inflammasome (Sharif et al., 2019). These observations suggest a common autoinhibition mechanism based on intramolecular interactions that can be abrogated by the binding of a corresponding ligand molecule. This could explain why overexpression of NLRP9 in the absence of its rotavirus ligand does not lead to ASC speck formation (Figure 2-2), but raises the question why other inflammasome sensors such as NLRP3 (Figure 2-2, (Hochheiser, Behrmann, et al., 2022)), NLRP6 (Shen et al., 2019), or AIM2 (Sester et al., 2015) behave quite differently.

As demonstrated by cellular and structural studies on NLRP3 and NLRP6, activation of the inflammasome includes homotypic filament formation of then accessible PYDs and successive nucleation of ASC polymerization (Hochheiser, Behrmann, et al., 2022; Shen et al., 2019; Stutz et al., 2017). To simplify investigation of the NLRP9 inflammasome and unlink from potential regulatory mechanisms, PYDs of NLRP3 and NLRP9 were further examined. Recapitulating, it could be shown that filamentous

NLRP3<sup>PYD</sup> is indeed a robust nucleator of ASC specks in cells (Figure 2-9). In contrast, findings on murine and human NLRP9<sup>PYD</sup> suggest that these molecules are neither able to self-polymerize into filaments, nor to nucleate ASC speck formation (Figure 2-8, Figure 2-9). Importantly, these results contradict the existence of an NLRP9-dependent inflammasome and instead resemble the results of a study on NLRP11, which claimed that the protein does not interact with ASC but rather suppresses NF- $\kappa$ B and type I interferon response - two key pathways in innate immunity (Ellwanger et al., 2018).

Determination of a high-resolution structure of human NLRP9<sup>PYD</sup> allowed for the analysis of molecular characteristics that differ from filament-forming PYDs. In addition to several residues that form a conserved hydrophobic core and stabilize the typical death domain fold, additional residues were identified that form a hydrophobic cluster with the  $\alpha$ 2- $\alpha$ 3 loop region potentially restricting its conformation (Figure 2-12b). In contrast, this loop region was reported to be flexible and undergo most prominent conformational changes upon formation of the filament in e.g., NLRP6<sup>PYD</sup> (Shen et al., 2019). Strikingly, monomeric NLRP9<sup>PYD</sup> was found to resemble the conformation of filamentous but not monomeric NLRP6, AIM2, and ASC PYDs in terms of the  $\alpha$ 2- $\alpha$ 3 loop and the conformation of the C-terminal helix (Figure 2-13). Similar with NLRP9<sup>PYD</sup>, also NLRP3<sup>PYD</sup> features a hydrophobic cluster that stabilizes the conformation of the  $\alpha$ 2- $\alpha$ 3 loop region. Thus, it was not surprising that the conformation of NLRP9<sup>PYD</sup> is similar with both, monomeric and filamentous NLRP3<sup>PYD</sup> (Figure 2-13). In conclusion, this supports the hypothesis that the conformation of monomeric NLRP9<sup>PYD</sup> is already compatible with filament formation and in consequence, its inability to form filaments might not result from conformational restraints. Instead, a number of residues that likely interfere with the formation of type I and type III asymmetric interfaces could be identified (Figure 2-14). Particularly basic residues that dominate the inner core ring of a hypothetical NLRP9<sup>PYD</sup> filament, cause strong repulsive forces that most likely disrupt filament formation, since they cannot be compensated by interfacing residues matching by charge or hydrophobicity (Figure 2-15). Furthermore, by assessing surface electrostatics of the ASC<sup>PYD</sup> filament, no interfaces that would match in charge complementarity with NLRP9<sup>PYD</sup> could be found, whereas such interfaces were clearly present for NLRP3<sup>PYD</sup> (Figure 2-15). However, these results are of rather low evidence, since investigation of polar and hydrophobic contacts as well as potential post-translational modifications were not included in the analysis. To examine and conclusively show such relationships, extensive mutational studies would be needed.

In a similar study by Ha & Park, the results obtained on the structure of NLRP9<sup>PYD</sup> have been widely confirmed (Ha & Park, 2020). They found in addition that NLRP9<sup>PYD</sup> is also able to form dimers in solution and proposed that a bent N-terminal loop might sterically clash with subunits in the filament, thereby regulating its assembly. Interestingly, this loop was found to be disordered in the crystal structure presented here (Figure 2-11), indicating rather loose interaction after cleavage of the N-terminal GST tag. Still, no signs of self-polymerization could be found, arguing against a hypothesis that this regulatory element might solely be responsible for the inability of NLRP9<sup>PYD</sup> to form filaments. While ‘dimer domain swapping’ was described as a mechanism of how Pyrin domains might be able to dimerize (Eibl et al., 2014), it cannot explain the ability of NLRP9<sup>PYD</sup> to form dimers in solution. The study introduced a cluster of three residues in  $\alpha 6$  of PYDs, that are described as the Glu-Arg-Asp charge relay, which were found to stabilize the arrangement of helix  $\alpha 6$  and its preceding loop through salt bridge formation with helix  $\alpha 2$  (Eibl et al., 2014). In NLRP14<sup>PYD</sup> the central arginine is substituted by a leucine, resulting in rather loose coordination of  $\alpha 6$  and the concomitant formation of a long  $\alpha 5$ - $\alpha 6$  stem helix, which provides an interface for the concentration-dependent transition from monomer to dimer (Eibl et al., 2014). In contrast, the pattern of charged residues is contained in NLRP9 (E22–R81–D83). Thus, the observation of stable and completely monomeric but not dimeric NLRP9<sup>PYD</sup> (Figure 2-8) is in accordance with the described mechanism. However, presence of the Glu-Arg-Asp charge relay does not exclude dimer formation by a different mechanism or account for the inability of NLRP9<sup>PYD</sup> to form filaments.

Post-translational modifications represent a common mechanism for the regulation of inflammasomes (Yang et al., 2017) but also other PRRs (J. Liu et al., 2016). The delicate balance of activation and inhibition by PTM regulation is exemplified by the well-studied NLR family member NLRP3. While a single phosphorylation of Ser5 in the Pyrin domain completely abrogates self-polymerization, phosphorylation of Ser198 is known to be essential for NLRP3 activation and inflammasome formation (Song et al., 2017; Stutz et al., 2017). Likewise, one can easily imagine that a single phosphorylation in NLRP9<sup>PYD</sup> could drive interaction of the otherwise basic and repulsive interfaces to enable filament formation. Thinking in the same direction, enzymes, interaction partners, or cofactors regulating NLRP9 activity might be missing in the experimental setup, which hitherto relies on the expression of recombinant protein and use of the artificial HEK293T cell system. Thus, fundamental knowledge about proteins and cofactors that regulate NLRP9

could improve future attempts to successfully assay the NLRP9 inflammasome. For instance, DHX9 is known to be endogenously expressed by HEK293T cells (The Human Protein Atlas, (Karlsson et al., 2021)) but it is so far unknown which domains participate in the interaction with NLRP9, what is the consequence of this interaction, and how viral RNA might trigger such event while endogenous RNA does not.

Because NLRP6 is highly expressed together with NLRP9 in the intestine of mammals (Zhu et al., 2017), it is quite possible that NLRP6 and NLRP9 function synergistically to form an inflammasome. This would be in line with the ‘domino-like’ activation mechanism of murine NLRC4 that is induced by ligand-bound and activated NAIPs (Hu et al., 2015; Tenthorey et al., 2017; Zhang et al., 2015). Significant hints might be the findings, that the intestines of NLRP6-deficient mice show increased viral loads when challenged with rotavirus and that both sensors detect viral RNA by utilizing RNA helicases of the DHX family (Mullins & Chen, 2021; Xing et al., 2021). Importantly, NLRP6 is not expressed by HEK293T cells (The Human Protein Atlas, (Karlsson et al., 2021)), which could explain the inability of NLRP9 to form filaments and induce ASC polymerization in this cellular system. To meet the need of further interaction partners not expressed in HEK293T cells, NLRP9 inflammasome formation could be examined in organoid cultures of IECs. For completion, it is also possible that NLRP9<sup>PYD</sup> is not involved in oligomerization, or vice versa, synergism with the NACHT or LRR domain is required. But since a number of previous studies on different inflammasome effector domains (Li et al., 2018; Lu et al., 2015; Shen et al., 2019) together with the findings on NLRP3<sup>PYD</sup> (Figure 2-9) showed their sufficiency in filament formation and inflammasome activation, these hypotheses are rather unlikely. Furthermore, homotypic interaction motifs of the death-fold superfamily are indeed well known to be involved in the assembly of other multimeric signaling complexes, such as the Myddosome, the p53-induced protein with a death domain (PIDD)osome, and the Fas receptor/FADD death inducing signaling complex (DISC) (Kersse et al., 2011).

While also highly expressed in reproductive organs, mammalian NLRP9 has been implicated to play a role in preimplantation embryo development (Kufer & Sansonetti, 2011). Since mice harbor three *Nlrp9* genes with potential functional redundance (Mullins & Chen, 2021; Tian et al., 2009), this connection was difficult to be investigated and could only recently been proven by a study of NLRP9 triple mutant mice (Kanzaki et al., 2020). Interestingly, interleukin-1 $\beta$  was found to be a critical player in mouse blastocyst hatching and implantation (Pathak et al., 2021) but NLRP9 could also have a distinct role

that does not link with inflammasome formation in the reproductive system. These observations emphasize the need to extend investigations on the tissue specific functions of NLRP9, which further underline its likely tight regulation.

In conclusion, the function of NLRP9 and the formation of an NLRP9-mediated inflammasome are controversial, and the molecular details of its regulation are still largely unknown. However, further insights would be valuable to develop strategies for therapeutic interventions in diseases related to its dysregulation.



## Chapter 3: Biochemical and structural investigation of human NLRP12

Some work presented in this chapter was accomplished in cooperation with other members of the Institute of Structural Biology (University of Bonn). Inga Hochheiser performed grid preparation and imaging using the facility for electron microscopy at the Max Planck Institute for Neurobiology of Behavior – Caesar (Bonn). Christoph Winterberg performed ATPase assays with mutant NLRP12 as part of his master thesis that was supervised by me. Dr. Rebecca Brinkschulte provided ASC-mCherry protein for pulldown experiments with NLRP12<sup>PYD</sup>. Dr. Kanchan Anand performed crystallization trials of human NLRP12<sup>NACHT</sup> protein. Dr. Karl Gatterdam instructed me in performing surface plasmon resonance spectroscopy (SPR) experiments. All mass spectrometry analyses were conducted by the group of Prof. Dr. Henning Urlaub at the Max Planck Institute for Multidisciplinary Sciences in Göttingen.

### 3.1 Functional analysis of human NLRP12

NLRP12 was first described in 2002 as an inflammasome component that interacts with ASC to activate caspase-1 (Wang et al., 2002). In line, mutations in the *Nlrp12* gene have been reported to cause autoinflammatory disease, which is accompanied by hereditary periodic fever and spontaneous secretion of IL-1 $\beta$  from peripheral blood mononuclear cells (PBMCs) (Jeru et al., 2008; Jeru et al., 2011; Wang, 2022). Later the NLRP12 inflammasome was demonstrated to recognize strains of *Yersinia pestis* and *Plasmodium vivax* but its direct ligand remained unknown (Ataide et al., 2014; Vladimer et al., 2012). In contrast, NLRP12 was shown to antagonize pro-inflammatory TLR and TNFR signaling by interfering with the central NF- $\kappa$ B and MAPK pathways (Tuladhar & Kanneganti, 2020). Mechanistically, NLRP12 has been shown to associate with IRAK1, NIK, TRAF3, and NOD2 to prevent hyperphosphorylation or regulate proteasomal degradation (Allen et al., 2012; Lich et al., 2007; Normand et al., 2018; Williams et al., 2005). Physiologically, NLRP12 regulates tissue homeostasis and diversity of commensal bacteria to prevent adverse autoinflammation and tumorigenesis, especially in the gastrointestinal tract and liver (Allen et al., 2012; Castano-Rodriguez et al., 2014; Chen et al., 2017; Khan & Zaki, 2020; Truax et al., 2018). This might also include localization, recruitment, and differentiation of dendritic cells, neutrophils, and T-cells (Arthur et al., 2010; Cai et al., 2016; Gharagozloo et al., 2018; Ulland et al., 2016; Wang et al., 2018; Zamoshnikova et al., 2016). However, NLRP12 can also regulate anti-viral response. In steady state, NLRP12 inhibits the ubiquitin ligase TRIM25 and upon infection with vesicular stomatitis virus is downregulated to allow activation of RIG-I (Chen et al., 2019). In contrast, NLRP12 was found to enhance type I interferons and interferon-stimulated genes upon infection with dengue virus (X. Li et al., 2021). NLRP12 is also cleaved by the Nsp5 (nonstructural protein 5) main protease of SARS-CoV-2, which might result in enhanced production of cytokines in COVID-19 patients (Moustaqil et al., 2021). An article that reviewed the controversial function of NLRP12 in more detail is given elsewhere (Tuladhar & Kanneganti, 2020).

Dysregulation of NLRP12 has been linked with many inflammatory diseases, including Kawasaki disease, acute glaucoma, arthritis, multiple sclerosis, lung inflammation, and glioma (Chen et al., 2020; Gharagozloo et al., 2018; Huang et al., 2018; Y. Jin et al., 2017; Sharma et al., 2019; Wang et al., 2022). However, its regulation and diverse activation mechanisms have barely been investigated. Here I present data that provides a basic functional analysis of NLRP12. The primary structure of human NLRP12 is

compared to NLRP3, which allows the assignment of important sequence motifs. Moreover, NLRP12-dependent ASC speck formation is shown in a HEK293T cell overexpression system. Functionally, recombinant NLRP12 is found to mainly form aggregates that possess ATPase and adenylate kinase activity with unknown implication.

### **3.1.1 Domain architecture and sequence motifs in NLRP12**

Together with the *hNlrp9* gene, the gene coding for human NLRP12 (*hNlrp12*) is located on the reverse strand of chromosome 19. It contains 10 coding exons, encoding six isoforms produced by alternative splicing (Ensembl: ENSG00000142405), of which isoform 1 has been defined as the canonical sequence (Uniprot: P59046). The protein consists of 1,061 amino acids with a calculated mass of approximately 120 kDa and a theoretical isoelectric point (pI) of 6.59. Except for the PYD, no structural information is yet available for NLRP12 (T. Jin et al., 2017; Pinheiro et al., 2011). Thus, as already performed for NLRP9 (Figure 2-1), a detailed primary structure analysis of NLRP12 combined with a sequence alignment with NLRP3 was conducted (Figure 3-1). The overall sequence identity between full-length NLRP3 and NLRP12 was determined to be 49.16%, which reflects that both proteins are highly related in terms of their structure but still different enough to allow for distinct functions.

In NLRP12, the N-terminal Pyrin domain spans amino acids 1-95 and is connected with the following FISNA domain (aa 120-208) by a 24 amino acid linker. As stated previously, the FISNA domain in NLRP3 contains a polybasic cluster with 10 out of 17 aa being positively charged and found to be key for NLRP3 inflammasome activation upon cellular potassium efflux (Tapia-Abellan et al., 2021). Additionally, SP phosphorylation sites, which become phosphorylated during priming and are prerequisite for NLRP3 deubiquitination and subsequent inflammasome activation, are found in the NLRP3 FISNA domain (Paik et al., 2021). Similar to NLRP3, in NLRP12 a polar cluster with yet unknown function spans aa 120-136 and contains 6 basic residues together with 3 acidic residues. Although the cluster contains less basic and more acidic residues as if compared with NLRP3, the overall basic charge of this cluster is shared among both proteins. In contrast, the phosphorylation site Ser198 in human NLRP3 is not conserved in human NLRP12, where the serine is substituted with a histidine and followed by a glutamine (aa 188-189). But a second SP motif is found in both proteins (aa 192-193; NLRP3: aa 201-202) and might be phosphorylated to potentially regulate their activation.



**Figure 3-1: Sequence alignment of NLRP3 and NLRP12.** The amino acid sequence of human NLRP3 isoform 2 (Uniprot accession number: Q96P20) and human NLRP12 isoform 1 (Uniprot accession number: P59046) was aligned using Clustal Omega (Madeira et al., 2019). Identical amino acids in both proteins are boxed. The secondary structure assignment was generated from NLRP3 (PDB: 7PZC, (Hochheiser, Pils, et al., 2022)) using ESPrnt 3.0 (Robert & Gouet, 2014). Helices are shown as squiggles and beta strands are shown as arrows. Domain boundaries are based on the NLRP3 structure and highlighted as Pyrin domain (PYD: bluewhite), fish-specific NACHT associated domain (FISNA: skyblue), nucleotide binding domain (NBD: wheat), helical domain 1 (HD1: raspberry), winged helix domain (WHD: deepolive), helical domain 2 (HD2: deepteal), transition leucine-rich repeat domain (trLRR: violetpurple), and canonical leucine-rich repeat domain (cnLRR: lightpink). Important motifs in NLRP3 are depicted below the sequence.  $\alpha$ : alpha-helix,  $\eta$ : 3<sub>10</sub>-helix,  $\beta$ : beta-strand.

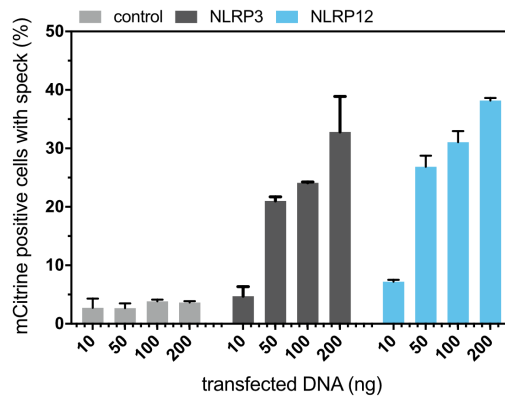
Apart from differences in the FISNA domain, the NACHT domain is well conserved between both proteins. The NBD of NLRP12 (aa 209-363) contains a classical Walker A and an extended Walker B motif, typical for STAND ATPases of the NACHT clade (Danot et al., 2009; Leipe et al., 2004). Moreover, Asn251 and Arg343 correspond well to the putative 'glutamate switch' and 'sensor I' motifs, respectively. Also, the HD1 (aa 364-425) and WHD (aa 426-531) of NLRP12 contain the residues Pro404 and His514, which are highly conserved in the NLRP family and essential for nucleotide binding and protein conformation (Sandall et al., 2020). The HD2 spans aa 532-632 and completes the NACHT domain, which ties into the C-terminal LRR domain.

Depending on the variability in length and composition of the individual repeats, the LRR domain can be subdivided in a transition and a canonical segment. While the canonical LRR region of NLRP3 aligns well with the very C-terminal sequence of NLRP12 (aa 772-1061), the region of the transition LRR (aa 633-771) differs significantly. The region is much longer in NLRP12 as if compared with NLRP3 and therefore difficult to be predicted by sequence alignment. However, a model of human NLRP12 generated with AlphaFold2 (Jumper et al., 2021) predicts four LRR repeats with alternating beta strands and alpha helices but variable length of the beta strands. This alternating pattern is interrupted by an extension of aa 667-698 that forms a loop similarly found in NLRP3 (Hochheiser, Pils, et al., 2022). In NLRP3, this loop contains an acidic cluster, which mediates contact between two opposing LRRs in an inactive decameric conformation (Hochheiser, Pils, et al., 2022). Interestingly, charged residues but no acidic cluster could be found in the supposed loop region in NLRP12. In summary, NLRP12 displays a similar overall architecture with NLRP3 by sharing the fundamental domain composition and many of the functionally important motifs, but with slight variations that might indicate different regulation and function.

### **3.1.2 Overexpression of NLRP12 triggers ASC speck formation**

As shown in the previous chapter, NLRP3 has the capability to nucleate ASC speck formation when overexpressed in the HEK293T<sup>ASC-BFP</sup> cell system (Figure 2-2). Since it has been previously demonstrated that also NLRP12 cooperates with ASC to promote caspase-1 activation and production of IL-1 $\beta$  in a PYD-dependent manner (Wang et al., 2002), the protein has been assayed in the same experiment (Figure 3-2). In contrast to the control and similar with NLRP3, transfection of NLRP12 induced robust formation

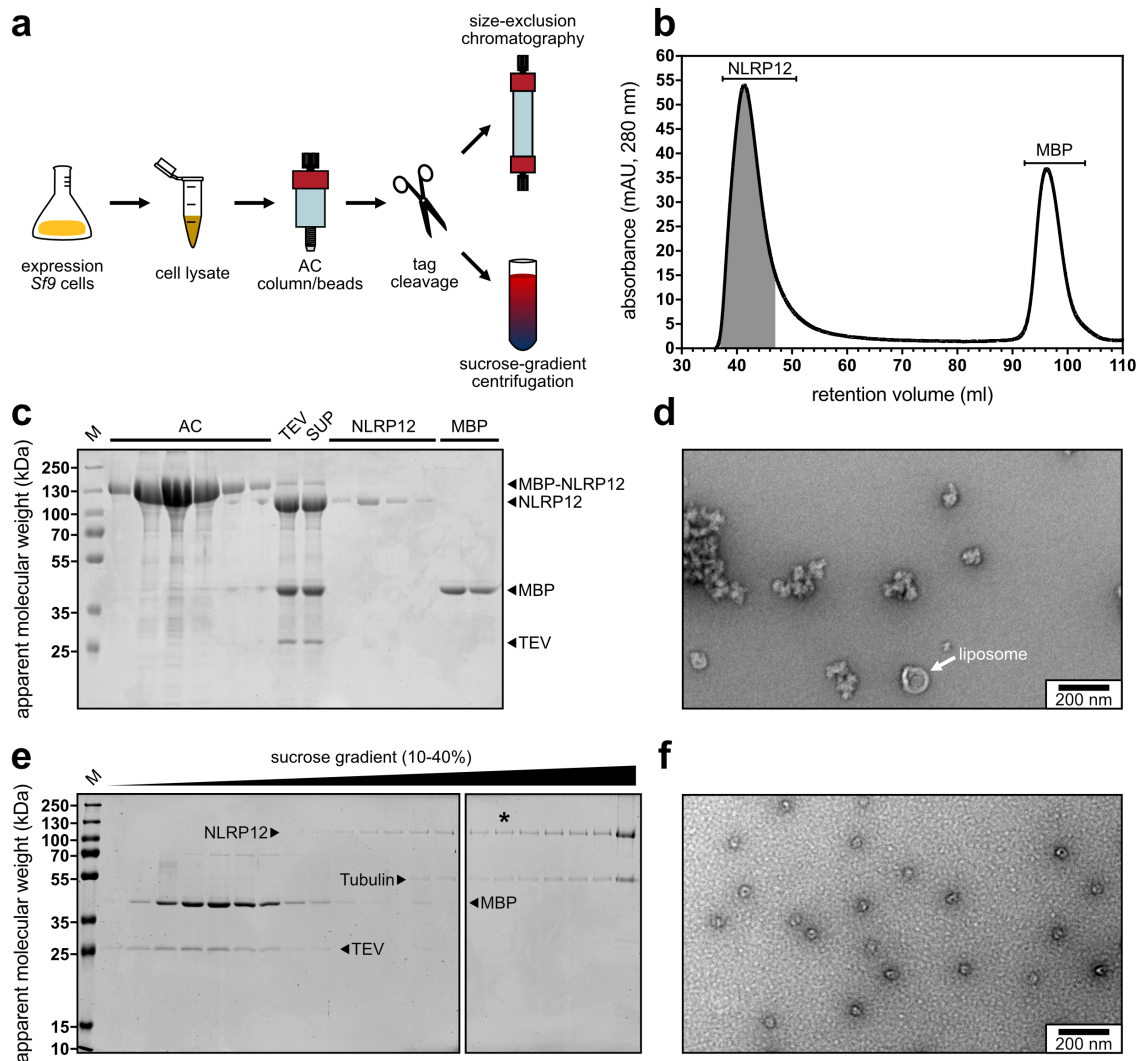
of ASC specks in a dose-dependent manner. This result confirms the capability of NLRP12 to interact with ASC and trigger its polymerization, which is a hallmark of ASC-dependent inflammasomes (Lu et al., 2014).



**Figure 3-2: Analysis of ASC speck formation in cells overexpressing NLRP12.** Plasmids coding for human NLRP3 or NLRP12 under a CMV promoter were transfected into HEK293T cells stably expressing ASC-BFP fusion protein. To follow promoter activity, mCitrine was simultaneously expressed via an internal ribosomal entry site (IRES). In case of the control the transfected plasmid did not contain the NLRP3 or NLRP12 coding sequence. mCitrine positive cells have been analyzed by flow cytometry for the presence of ASC specks. Data for control and NLRP3 are also shown in Figure 2-2. Bars are representative of two technical replicates.  $n = 1 \pm SD$ .

### 3.1.3 Towards the structure determination of full-length NLRP12

To gain mechanistic insights into the regulation and function of the NLRP12 inflammasome, structural information about NLRP12 was tried to be obtained following different purification strategies (Figure 3-3a). First, the protein was recombinantly expressed as N-terminal MBP-fusion protein in the *Sf9* insect cell system and purified by affinity chromatography. Since cleavage of the MBP tag led to precipitation and complete loss of the protein, the buffer conditions have been extensively optimized to stabilize and solubilize NLRP12 (data not shown). Using subsequent size-exclusion chromatography the cleaved MBP tag could be separated but NLRP12 eluted in the void volume corresponding to a molecular weight of  $>6,000$  kDa (Figure 3-3b). The solubility and purity of the protein was confirmed by SDS-PAGE analysis (Figure 3-3c) but as already apparent from the elution volume, electron microscopy revealed that NLRP12 was mostly aggregated and not applicable to structure determination (Figure 3-3d).



**Figure 3-3: Purification and electron microscopy of human NLRP12.** (a) Graphical representation of two different NLRP12 purification strategies based on size-exclusion chromatography and sucrose density gradient centrifugation. (b) Representative chromatogram of NLRP12 injected onto a Superose 6 PG XK 16/70 size-exclusion column after affinity purification and tag cleavage. Elution of protein was followed via the absorbance at 280 nm wavelength. Grey area indicates pooled fractions. (c) Coomassie-stained samples from different steps of the purification process and fractions from (b) after reducing SDS-PAGE. M: marker, AC: affinity chromatography, TEV: tag cleavage using TEV protease, SUP: supernatant after centrifugation. (d) Negative stain EM image of 0.075 mg·ml<sup>-1</sup> NLRP12 after size-exclusion chromatography, recorded by Inga Hochheiser (University of Bonn). (e) Coomassie-stained samples from fractions of the sucrose gradient after reducing SDS-PAGE. The star indicates the fraction analyzed in electron microscopy. M: marker. (f) Negative stain EM image of NLRP12 after sucrose density gradient centrifugation, recorded by Inga Hochheiser (University of Bonn).

In contrast, full-length NLRP3 was found to exist in two distinct species that classify by the phosphorylation status of Ser198 in the FISNA domain (Hochheiser, Pilsl, et al., 2022). While phosphorylated NLRP3 also forms aggregates, dephosphorylated NLRP3 is a defined and stable decamer (Hochheiser, Pilsl, et al., 2022). Indeed, peptide mass fingerprint analysis of NLRP12 revealed enrichment of phosphorylation at Ser192 in the FISNA domain but also Ser755 in the LRR domain. The consequence of phosphorylated

Ser755 is completely unknown but assuming phosphorylation of Ser192 in NLRP12 is redundant with phosphorylation of Ser198 in NLRP3, recombinant NLRP12 might have a primed status with higher tendency to self-associate (Swanson et al., 2019).

One more hypothesis was that the fluid flow generated by the pumps used in column-based purification methods could create shear forces that might have disrupted the delicate ‘closed’ conformation of inactive NLRP12. Thus, the purification strategy was changed to a milder approach including gravity-based affinity purification and sucrose density gradient centrifugation (Figure 3-3a). SDS-PAGE analysis of the fractionated sucrose gradient revealed that NLRP12 (MW = 120,317 Da) peaked in higher concentrations of sucrose and could be separated from TEV protease (MW = 28,400 Da) supplemented for the tag cleavage, and the cleaved MBP tag (MW = 41,349 Da, Figure 3-3e). Strikingly, the SDS-PAGE analysis revealed another protein with an apparent molecular weight of roughly 55 kDa that is found to form a 1:1 complex with NLRP12 (Figure 3-3e). Peptide mass fingerprint analysis identified proteins of the tubulin superfamily, including  $\alpha$ -tubulin subtype TUBA2 and  $\beta$ -tubulin subtypes TUBB2A and TUBB2C. Interestingly, this indicates that NLRP12 can associate with microtubules in cells – an observation that was previously made in a study on the NLRP3 and Pyrin inflammasomes (Magupalli et al., 2020). Investigation of this complex by electron microscopy, showed single particles with a diameter of  $\sim$ 38 nm (Figure 3-3f), corresponding to an oligomeric assembly but not tubular structures. The particles have been homogenous in size but still, attempts to determine their structure failed, since no defined class sums could be calculated from the negative stain EM datasets. This indicates that the particles are not well enough structured and inhomogeneous in conformation, reflecting the possibility that they might rather represent fractured aggregates instead of defined oligomers.

#### **3.1.4 NLRP12 shows ATPase and adenylate kinase activity *in vitro***

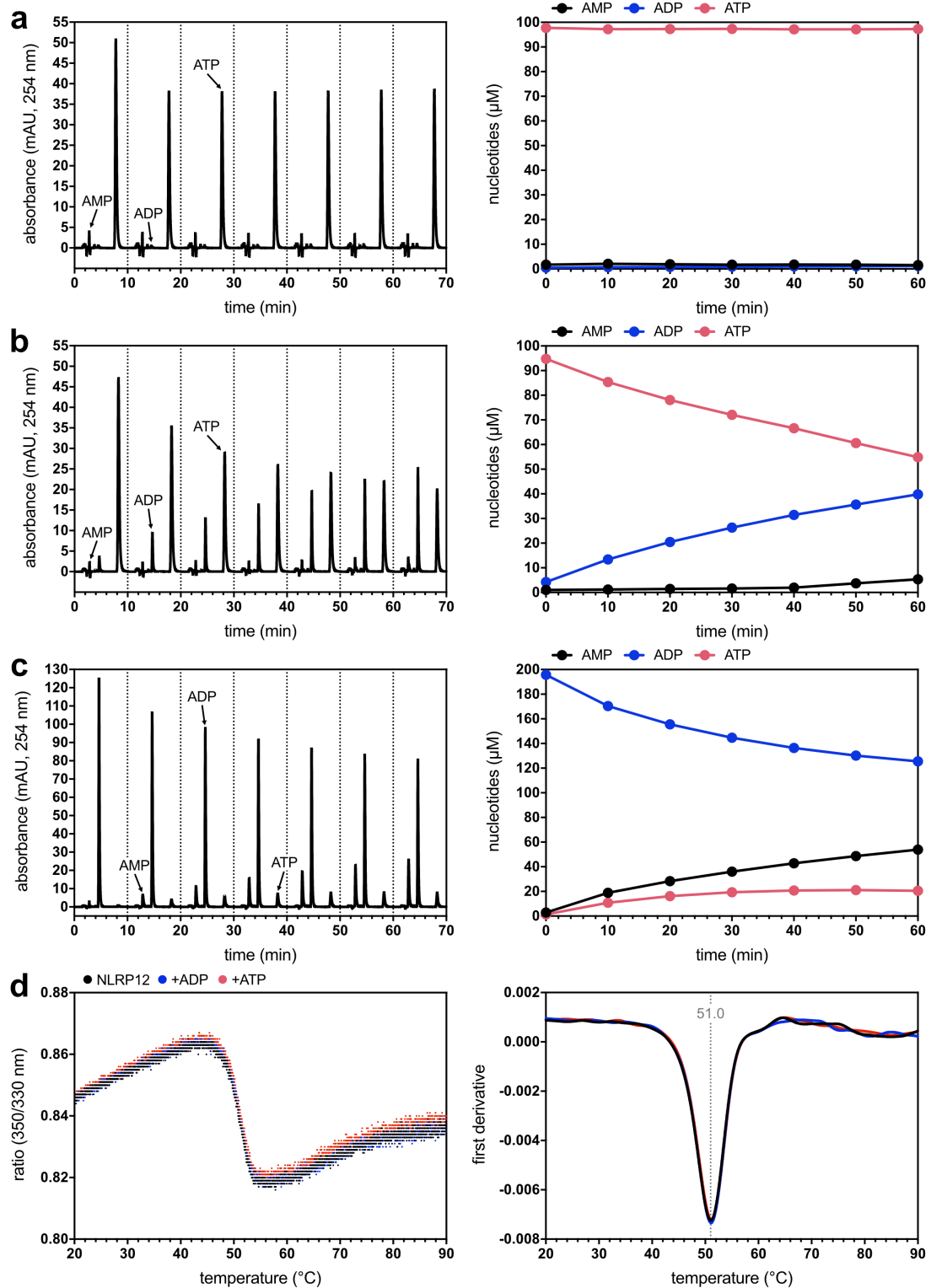
All known functions of NLRP3 and NLRP12 were found to rely on intrinsic ATPase activity of the proteins, emphasizing an important role for ATP binding and hydrolysis in the regulation of inflammasomes (Duncan et al., 2007; MacDonald et al., 2013; Ye et al., 2008). To investigate the hydrolysis activity of NLRP12, an assay based on ion-pairing reverse phase HPLC was established (methods section). Surprisingly and in contrast to a previous study (Ye et al., 2008), MBP-tagged NLRP12 did not exhibit ATPase activity



under the conditions tested (Figure 3-4a). In addition, it was already established in the laboratory that MBP-NLRP3 purified under more simplified buffer conditions was able to hydrolyze ATP and that the products of this enzymatic reaction could indeed be measured and quantified using the HPLC-based method (Brinkschulte, 2020; Hochheiser, Pils, et al., 2022). Thus, MBP-NLRP12 was purified under different buffer conditions screening the reason for inhibition of hydrolysis activity. Presence of the zwitterionic surfactant CHAPS during lysis of the cells did render NLRP12 inactive, while excluding CHAPS from the lysis buffer resulted in active protein (Figure 3-4b). Altering other conditions, such as salt or pH, did not inhibit ATPase activity of NLRP12 (data not shown).

Interestingly, it was observed that not only ATP is converted to ADP but a minor fraction is also further converted to AMP (Figure 3-4b). A similar finding was made previously for MBP-NLRP3 and it was proposed that NLRP3 has adenylate kinase activity (Brinkschulte, 2020). Adenylate kinases catalyze the conversion of two molecules of ADP into one molecule of AMP plus ATP and vice versa (Dzeja & Terzic, 2009). To elucidate if NLRP12 is able to conduct this enzymatic reaction, MBP-NLRP12 was next incubated in the presence of magnesium chloride and ADP to monitor the generation of AMP as a potential product of such reaction. Since NLRP12 possesses ATPase activity, it was assumed that the generated ATP product might be instantly hydrolyzed. However, the consumption of ADP together with the generation of AMP but also ATP could be observed (Figure 3-4c), indicating that NLRP12 has adenylate kinase activity.

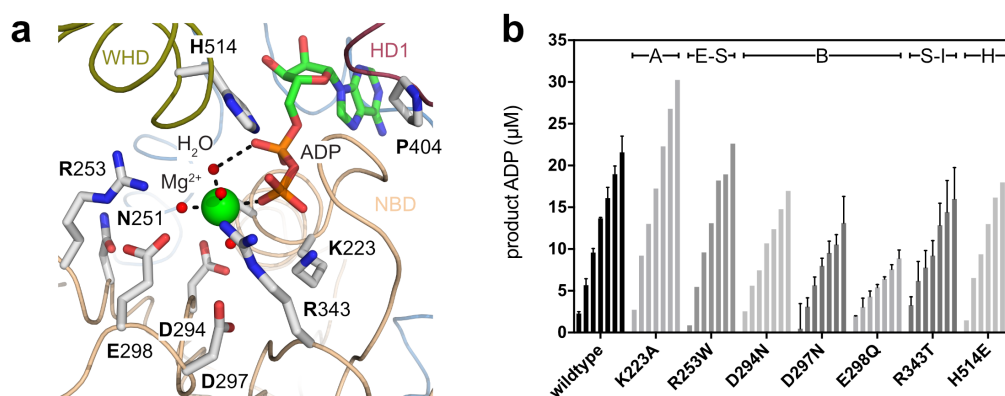
To understand whether nucleotide binding or hydrolysis induces conformational changes in MBP-NLRP12, thermal stability was investigated using thermal shift denaturation assays (Figure 3-4d). Incubation of MBP-NLRP12 with 100  $\mu$ M ADP or ATP and in the presence of 5 mM magnesium chloride did not alter its apparent melting temperature and thus the thermal stability. This suggests that NLRP12 does not undergo extensive and thus measurable conformational changes upon binding and hydrolysis of ATP or ADP. In line with the finding that NLRP12 is mostly aggregated, it is likely, that the protein is not well folded and thus, not able to switch between the autoinhibited and active conformation. It can be rather predicted that due to oligomerization and aggregation, NLRP12 is trapped in an artificially 'open' but still enzymatically intact conformation where the exchange of nucleotides occurs freely and the molecular switch mechanism is undermined.



**Figure 3-4: ATPase and adenylate kinase activity of human NLRP12.** (a-c) Hydrolysis assay based on ion-pairing reverse phase HPLC. MBP-NLRP12 was purified (a) in the presence or (b-c) in the absence of the zwitterionic surfactant CHAPS and thereafter 3  $\mu\text{M}$  of the protein was incubated with 5 mM  $\text{MgCl}_2$  and (a-b) 100  $\mu\text{M}$  ATP or (c) 200  $\mu\text{M}$  ADP at 25 $^{\circ}\text{C}$ . Every 10 minutes a sample was injected onto a Chromolith Performance RP-18 HPLC column and elution of nucleotides was followed via the absorbance at 259 nm wavelength. The area under the curve was used to calculate the peak ratios and subsequently estimate the concentration of nucleotides. Dashed lines indicate injections. (d) Thermal shift assay of 3  $\mu\text{M}$  MBP-NLRP12 in the presence of 5 mM  $\text{MgCl}_2$  and 100  $\mu\text{M}$  ADP or ATP. The measurement was setup with a temperature ramp ranging from 20-95 $^{\circ}\text{C}$ , a slope of 2 $^{\circ}\text{C}\cdot\text{min}^{-1}$ , and a 50% laser intensity. Apparent melting temperatures ( $T_M$ ) of the samples are depicted as dashed lines.

### 3.1.5 NLRP12 mutants show decreased ATPase activity

To investigate the mechanism of ATP hydrolysis and to further validate that measured enzymatic activity is indeed dependent on NLRP12, several mutations in the ATP binding site were introduced by site-directed mutagenesis. To anticipate the mechanistic effect of such mutation, a model of the nucleotide binding site in human NLRP12 bound to ADP·Mg<sup>2+</sup> was generated (Figure 3-5a). The model is based on the structure prediction from AlphaFold2 (Jumper et al., 2021) and the crystal structure of NLRP3 presented in a subsequent chapter of this thesis (Figure 4-4). Of note, all mutations were designed to affect ATPase activity but maintain the integrity of the NLRP12 fold in the nucleotide binding site. However, purification of most mutants did yield significantly less protein as if compared with wildtype NLRP12, limiting the number of experiments.



**Figure 3-5: ATPase activity of mutant NLRP12.** (a) Ribbon representation of a model of the nucleotide binding site in human NLRP12. Important sidechains are represented as sticks. The model is based on the structure prediction from AlphaFold2 (Jumper et al., 2021) and the NLRP3 crystal structure presented in a subsequent chapter of this thesis. Coloring of the ribbon representation is based on the domain boundaries established in Figure 3-1. (b) Hydrolysis assay based on ion-pairing reverse phase HPLC performed by Christoph Winterberg (University of Bonn). NLRP12 was mutated in Walker A (A), glutamate switch (E-S), Walker B (B), sensor I (S-I), or the conserved histidine (H) in the winged helix domain. 2.5 μM of wildtype or mutant MBP-NLRP12 was incubated with 5.5 mM MgCl<sub>2</sub> and 111 μM ATP at 25°C. Every 10 minutes a sample was injected onto a Chromolith Performance RP-18 HPLC column and elution of nucleotides was followed via the absorbance at 259 nm wavelength. The area under the curve was used to calculate the peak ratios and subsequently estimate the concentration of ADP as the product of the enzymatic reaction. Each set of six bars represents data for one variant with measurements at 0, 10, 20, 30, 40, 50, and 60 minutes, respectively. Data are mean ± SD of *n* = 1-2 independent experiments.

The overall requirement for the catalysis of the ATP hydrolysis reaction is the correct positioning of the phosphate groups of the nucleotide, the magnesium ion, the coordinated water molecules, and the catalytic residues of the Walker B motif. The Walker A motif (or P-loop) includes the most commonly mutated lysine residue that makes contact with the β- and γ-phosphates of the nucleotide (Figure 3-5a, (Wendler et al., 2012)). Since exchange typically abrogates nucleotide binding (Wendler et al., 2012), this residue was

substituted with an alanine (K223A). When ATP hydrolysis experiments were performed, this mutant showed unexpectedly high activity compared to the wildtype protein (Figure 3-5b). For that reason, the experiment should be repeated in future studies to confirm initial observations with independently purified protein.

In patients suffering from CAPS disease, the mutation R262W was found to cause hyperactivation of NLRP3 and spontaneous inflammasome activation (Booshehri & Hoffman, 2019). Arg262 in NLRP3 corresponds to Arg253 in NLRP12 and is only two residues downstream of Asn251, which was described above to be a potential ‘glutamate switch’ motif. In the model however, the catalytic Glu298 from the Walker B motif is oriented towards Arg253 and not Asn251 (Figure 3-5a), which suggests that Arg253 is the ‘glutamate switch’ motif that regulates ATPase activity in NLRP12. Thus, Arg253 was exchanged with a tryptophan and its effect was investigated using the ATPase assay (Figure 3-5b). Interestingly, the mutant showed no change in ATPase activity, suggesting that this mutation may instead destabilize the autoinhibited resting state of NLRP12.

The negatively charged residues of the Walker B motif are important for the positioning of the water activating magnesium ion and the priming of this water molecule for a nucleophilic attack on the  $\gamma$ -phosphate of ATP (Wendler et al., 2012). While Asp297 might align the nearby Arg343 (sensor I motif), Asp294 and Glu298 might interact with water molecules surrounding the magnesium ion in NLRP12 (Figure 3-5a). Thus, ATPase activity was expected to be reduced by mutation of these residues. Indeed, mutation of all three residues did result in decreased ATPase activity with the most prominent effect for the E298Q mutant (Figure 3-5b).

The role of the sensor I motif in ATP hydrolysis is not yet completely clarified and several studies rather suggest different functions in different proteins. This includes stabilization of the negative charge of the reaction intermediate, positioning of the attacking water molecule, and transmission of its movement upon engagement with the nucleotide to mediate conformational changes (Leipe et al., 2004; Wendler et al., 2012). Mutation of Arg343 to the polar but significantly shorter threonine (as in NLRC4 (Sandall et al., 2020)), did result in decreased ATPase activity of NLRP12 (Figure 3-5b), arguing that the sensor I motif in NLRP12 participates in ATP hydrolysis.

The conserved histidine in STAND ATPases is located at the end of the WHD and interacts with the  $\beta$ -phosphate of ADP, resulting in a ‘closed’ conformation where the WHD folds back towards the nucleotide binding site and renders the bound nucleotide inaccessible (Figure 3-5a, (Danot et al., 2009)). In line with the assumption that

aggregated NLRP12 adopts an artificial 'open' conformation, mutation of His514 to glutamate did not show any effect on the ATPase activity of NLRP12 (Figure 3-5b).

Overall, the mutation studies on NLRP12 show that changes in amino acids involved in ATP binding and hydrolysis result in decreased enzymatic activity, confirming that the measured ATPase activity is indeed dependent on NLRP12.

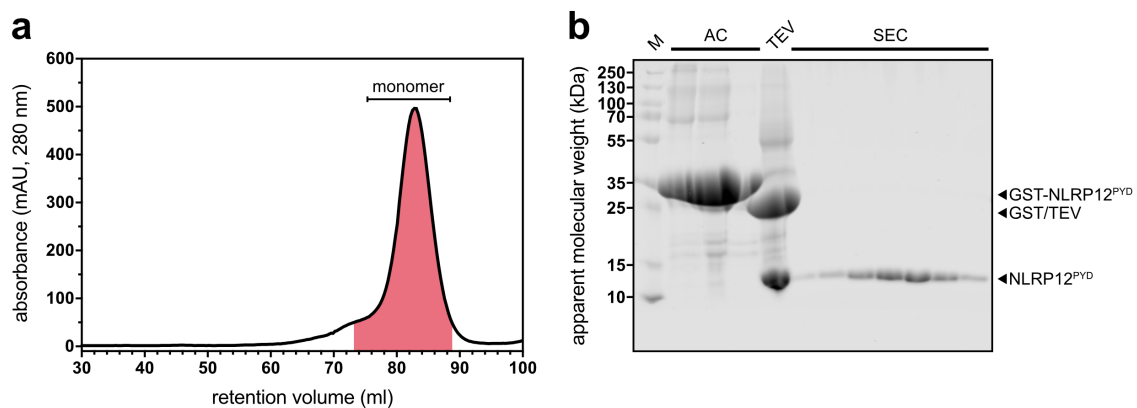
### **3.2 Functional investigation of the NLRP12 Pyrin domain**

In current opinion, polymerization of effector domains is required for the interaction with ASC and subsequent assembly into speck-like structures, which are a hallmark of ASC-dependent inflammasomes (Lu et al., 2014). Importantly, it was found that NLRP12 is capable to nucleate ASC speck formation, when overexpressed in HEK293T cells and the underlying interaction is dependent on its Pyrin domain (Figure 3-2, (Wang et al., 2002)). The structure of the NLRP12 Pyrin domain has been solved by NMR spectroscopy and X-ray crystallography in two independent studies, but its capability to form filaments has so far never been investigated (T. Jin et al., 2017; Pinheiro et al., 2011). In contrast, one of the studies even implied a role of NLRP12 in apoptosis rather than pyroptosis by showing direct interaction of its Pyrin domain and the UBA domain of the pro-apoptotic protein Fas-associated factor 1 (Pinheiro et al., 2011).

This part of the thesis presents an analysis on the capability of NLRP12<sup>PYD</sup> to self-polymerize into filaments and to interact with ASC *in vitro*. I found that recombinant human NLRP12<sup>PYD</sup> forms a stable monomer in solution and does not polymerize into filaments *in vitro* or in cells. Consequently, NLRP12<sup>PYD</sup> does also not directly interact with ASC under the conditions tested. Based on the crystal structure of human NLRP12<sup>PYD</sup> at 1.85 Å resolution (T. Jin et al., 2017), conformation and interfacing residues are studied. No significant differences between NLRP12<sup>PYD</sup> and filament-forming Pyrin domains is identified to explain its inability to self-polymerize. However, exchange of a tryptophan residue located in the type III interface with an arginine, does promote oligomerization of NLRP12<sup>PYD</sup>. It is speculated that the NACHT or LRR domains of NLRP12 orchestrate Pyrin domain polymerization by providing additional oligomerization interfaces. Finally, analysis of surface electrostatics in a model of the NLRP12<sup>PYD</sup> filament predicts charge matching surface patches with ASC, supporting the existence of a canonical NLRP12 inflammasome.

### 3.2.1 Purification of recombinant human NLRP12 Pyrin domain

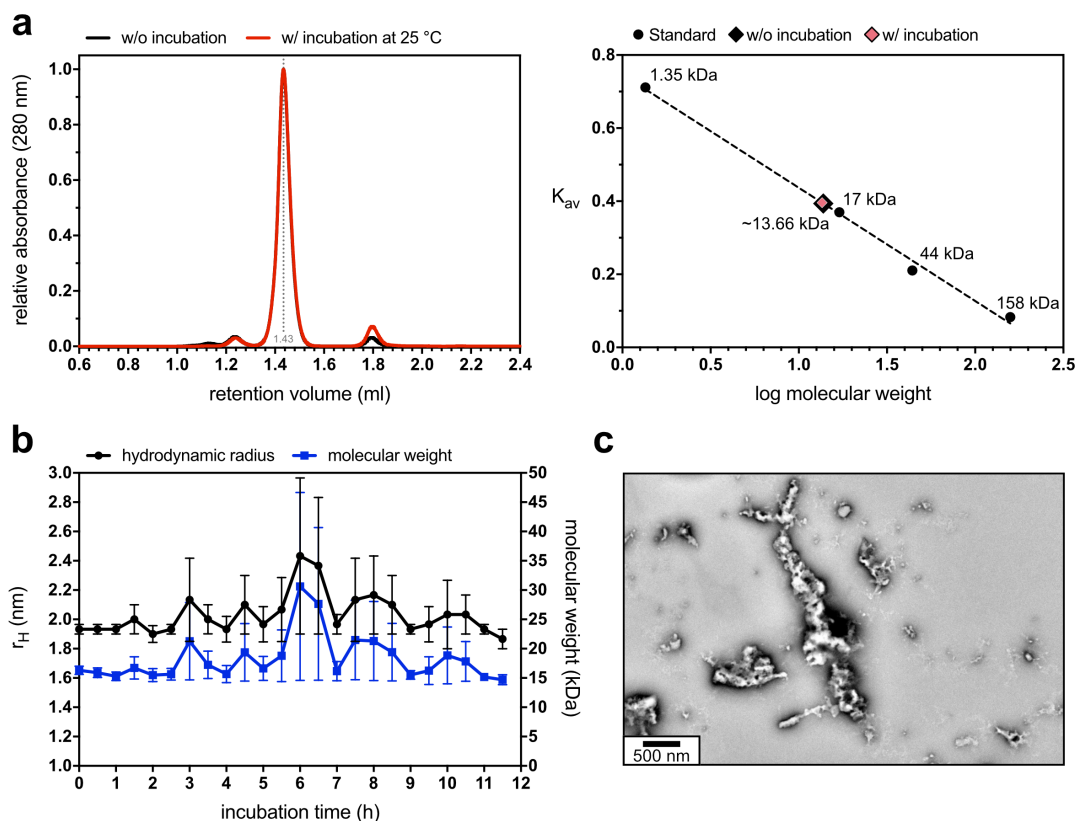
To investigate the polymerization of the NLRP12 Pyrin domain, human NLRP12<sup>PYD</sup> (aa 3-98) was expressed as N-terminal GST-fusion protein in *E. coli*. The protein was purified to homogeneity by affinity chromatography, subsequent tag cleavage, and size-exclusion chromatography. The chromatogram of a representative SEC run after AC and tag cleavage is given in Figure 3-6a. NLRP12<sup>PYD</sup> elutes as one major peak at around 84 ml and a small preceding shoulder. The retention volume is in accordance with a mainly monomeric species of NLRP12<sup>PYD</sup>. Thorough cleavage of the GST affinity tag as well as purity and integrity of the final protein sample was confirmed by SDS-PAGE analysis (Figure 3-6b). The SDS-gel shows one intense single band at an apparent molecular weight of ~35 kDa after affinity chromatography, corresponding to GST-NLRP12<sup>PYD</sup>. After cleavage using TEV protease, the band split up into one band for the GST affinity tag (MW = 27,105 Da) and another band for the sole NLRP12<sup>PYD</sup> (MW = 11,396 Da). The final SEC fractions display only one intense single band, corresponding to recombinant NLRP12<sup>PYD</sup> in crystallization-grade quality.



**Figure 3-6: Purification of human NLRP12<sup>PYD</sup>.** (a) Representative chromatogram of NLRP12<sup>PYD</sup> injected onto a Superdex 75 PG 16/600 size-exclusion column after affinity purification and tag cleavage. The column was connected to a tandem GStrap column for prolonged retention of the GST tag. Elution of protein was followed via the absorbance at 280 nm wavelength. The red area indicates pooled fractions of the monomeric peak. (b) Coomassie-stained samples from different steps of the purification process and fractions from (a) after reducing SDS-PAGE. M: marker, AC: affinity chromatography, TEV: tag cleavage using TEV protease, SEC: size-exclusion chromatography.

### 3.2.2 NLRP12<sup>PYD</sup> is monomeric and does not self-polymerize *in vitro*

To examine the self-polymerization capability of NLRP12<sup>PYD</sup>, the protein was analyzed using analytical gel filtration, dynamic light scattering, and electron microscopy as described above for NLRP9<sup>PYD</sup> (Figure 3-7). The protein was diluted to 2 mg·ml<sup>-1</sup> and incubated for 12 h at 25°C. Sequential analysis by analytical gel filtration revealed an average retention volume of 1.43 ml corresponding to an average molecular weight of 13.66 kDa independent of the incubation time (Figure 3-7a).

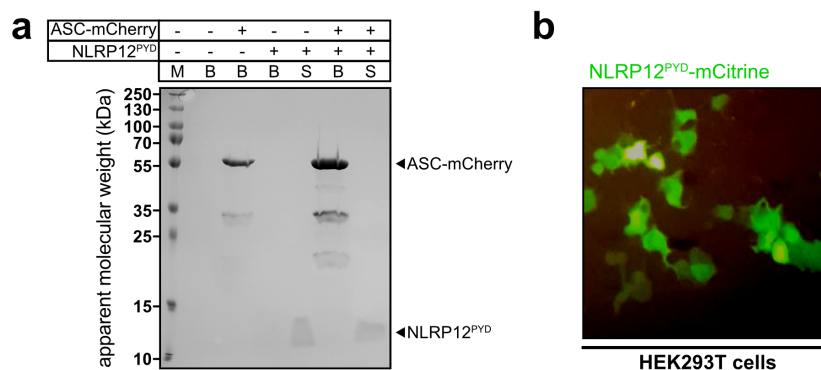


**Figure 3-7: Molecular dispersion of recombinant NLRP12<sup>PYD</sup>.** (a) Representative elution profile from analytical gel filtration of 50  $\mu$ g NLRP12<sup>PYD</sup> injected onto a Superdex 75 Increase 3.2/300 column and calculation of the molecular weight from the peak retention volume. Linear regression was used to fit the calibration curve to the partition coefficient ( $K_{av}$ ) versus the logarithm of the molecular weight of a standard ( $R^2 = 0.9951$ ). The molecular weight of NLRP12<sup>PYD</sup> was determined before and after 12 h of incubation time at 25°C. Data points are representative of three independent experiments.  $n = 3 \pm$  SEM. (b) Hydrodynamic radius and corresponding molecular weight of NLRP12<sup>PYD</sup> (2 mg·ml<sup>-1</sup>) as determined by DLS. Sample was measured every 30 min during 11.5 h of incubation at 25°C. Data points are representative of three independent experiments.  $n = 3 \pm$  SEM. (c) Negative stain EM image of 1.5 mg·ml<sup>-1</sup> NLRP12<sup>PYD</sup>, recorded by Inga Hochheiser (University of Bonn). Prior analysis, the sample was incubated overnight at 37°C. The depicted aggregates are representative of some minor spots on the otherwise completely 'empty' grid.

Instead, using dynamic light scattering, particles of NLRP12<sup>PYD</sup> showed an average hydrodynamic radius of 2.0 nm corresponding to a globular protein with a molecular weight of approximately 18.3 kDa (Figure 3-7b). However, the hydrodynamic radius of the particles raised between five and six hours of incubation time whereafter it declined again (Figure 3-7b), possibly indicating formation of aggregates that momentarily elevated the measured particle size. In fact, when NLRP12<sup>PYD</sup> was diluted to 1.5 mg·ml<sup>-1</sup> and incubated overnight at 37°C, analysis by negative stain EM revealed the presence of aggregates but not filaments in some minor spots of the otherwise ‘empty’ grid (Figure 3-7c). Because monomeric NLRP12<sup>PYD</sup> cannot be resolved by electron microscopy, it can be concluded that NLRP12<sup>PYD</sup> is largely monomeric in solution and does unexpectedly not readily self-polymerize under the conditions tested *in vitro*.

### 3.2.3 Monomeric NLRP12<sup>PYD</sup> does not interact with ASC nor self-polymerize in cells

To ensure that polymerization of NLRP12<sup>PYD</sup> is a requirement for the interaction with ASC, a pulldown experiment was performed. For this purpose, a hexahistidine tagged ASC-mCherry fusion protein was bound to Ni-NTA beads and afterwards incubated with monomeric NLRP12<sup>PYD</sup>. Subsequent analysis of the bound fraction and supernatant by reducing SDS-PAGE showed no binding between both proteins (Figure 3-8a).



**Figure 3-8: Analysis of ASC interaction and PYD polymerization in cells.** (a) Pulldown assay of human ASC and NLRP12<sup>PYD</sup>. ASC was purified by Dr. Rebecca Brinkschulte (University of Bonn) and harbored a C-terminal mCherry and an N-terminal hexahistidine tag that allowed for binding to Ni-NTA beads. After incubation with NLRP12<sup>PYD</sup> the bound fraction (B) and supernatant (S) was analyzed using reducing SDS-PAGE. The depicted pulldown experiment is representative of  $n = 2$  independent experiments. (b) Image of NLRP12<sup>PYD</sup>-mCitrine fusion protein overexpressed in HEK293T cells. Data is representative of  $n = 1$  independent experiment.



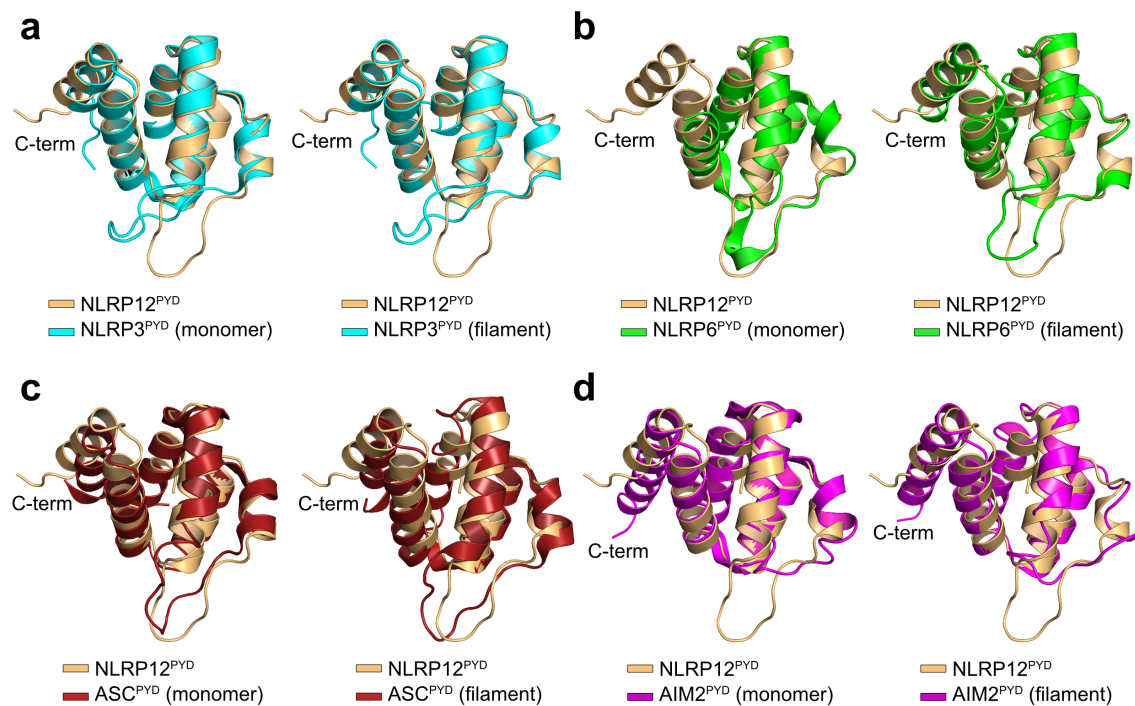
Additionally, filament formation was examined in the setting of HEK293T cells, which resembled a more physiological condition to investigate inflammasomes. To track filament formation, human NLRP12<sup>PYD</sup> was overexpressed as C-terminal mCitrine fusion protein. Similar to what was previously demonstrated for NLRP9<sup>PYD</sup> (Figure 2-9), fluorescent protein was found to diffusively locate within cells overexpressing human NLRP12<sup>PYD</sup>-mCitrine (Figure 3-8b). In line with the findings *in vitro*, it can be concluded that NLRP12<sup>PYD</sup> did not self-polymerize into filaments in the cellular system.

### 3.2.4 NLRP12<sup>PYD</sup> adopts a conformation with hallmarks of both, monomeric and filamentous Pyrin domains

Since NLRP12<sup>PYD</sup> was unable to form filaments, *in silico* analysis on conformational restraints that might prohibit self-polymerization was performed. To this end, the crystal structure of NLRP12<sup>PYD</sup> (PDB: 5H7N) was compared with structures of NLRP3<sup>PYD</sup>, NLRP6<sup>PYD</sup>, ASC<sup>PYD</sup>, and AIM2<sup>PYD</sup> obtained from monomeric and filamentous assemblies (Figure 3-9). As NLRP3 is the closest relative to NLRP12, monomeric and filamentous NLRP3<sup>PYD</sup> show a similar orientation of the six helical bundle with NLRP12<sup>PYD</sup> (Figure 3-9a). Indeed, both PYDs align with a RMSD value of 0.619 Å (monomer) and 0.665 Å (filament), respectively. However, the distinct orientation of the  $\alpha$ 2- $\alpha$ 3 loop is remarkable. Comparing NLRP12<sup>PYD</sup> with structures of NLRP6<sup>PYD</sup>, it can be observed that the  $\alpha$ 2- $\alpha$ 3 loop of NLRP12<sup>PYD</sup> follows the  $\alpha$ 2- $\alpha$ 3 loop of monomeric NLRP6<sup>PYD</sup>, whereas helix  $\alpha$ 3 and the following C-terminal region adopts a similar conformation as NLRP6<sup>PYD</sup> in the filament (Figure 3-9b). This is confirmed by a greater RMSD value of 1.708 Å for monomeric versus 1.370 Å for filamentous NLRP6<sup>PYD</sup>.

To assess these observations, NLRP12<sup>PYD</sup> was compared with PYDs of the less related proteins ASC and AIM2. NLRP12<sup>PYD</sup> and monomeric ASC<sup>PYD</sup> align with a RMSD value of 1.367 Å, whereas NLRP12<sup>PYD</sup> and filamentous ASC<sup>PYD</sup> align with a greater RMSD value of 1.749 Å (Figure 3-9c). Indeed, apart from the C-terminal region, NLRP12<sup>PYD</sup> closely resembles monomeric ASC<sup>PYD</sup>, including the  $\alpha$ 2- $\alpha$ 3 loop and the ensuing helix  $\alpha$ 3. In line, helix  $\alpha$ 3 of NLRP12<sup>PYD</sup> is positioned in a similar way as in filamentous AIM2<sup>PYD</sup>, but the overall structure aligns better with monomeric AIM2<sup>PYD</sup> (Figure 3-9d). This is substantiated by a RMSD value of 0.980 Å for monomeric and 1.569 Å for filamentous AIM2<sup>PYD</sup>. Recapitulating, NLRP12<sup>PYD</sup> adopts a conformation with hallmarks of both, monomeric and filamentous Pyrin domains.

To understand if the conformation of NLRP12<sup>PYD</sup> needs to change upon filament formation, a NLRP12<sup>PYD</sup> filament was modelled based on the filament structure of NLRP3<sup>PYD</sup> (PDB: 7PZD) and the contact region between subunits was analyzed for potential steric clashes. Importantly, no steric clash could be identified, indicating that the conformation of NLRP12<sup>PYD</sup> does not prohibit self-polymerization.

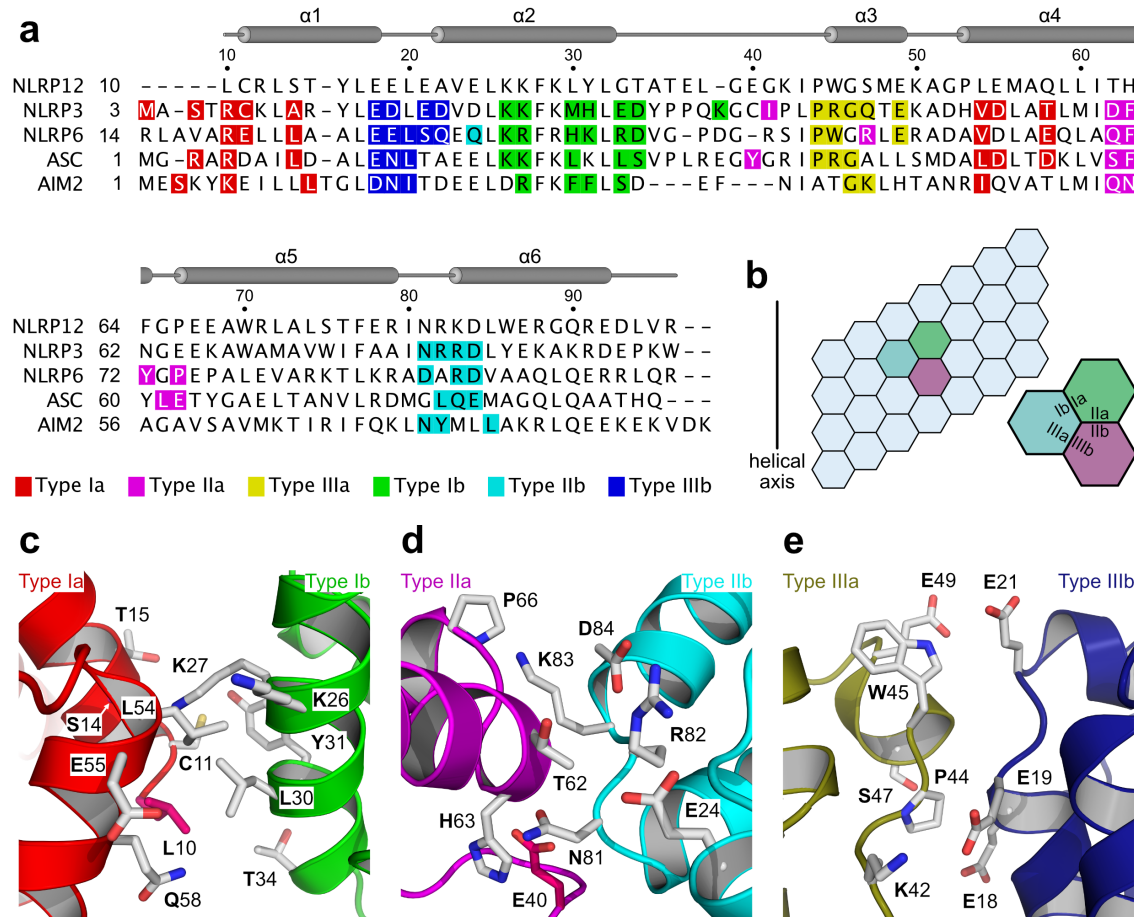


**Figure 3-9: Conformational analysis of NLRP12<sup>PYD</sup>.** Overlays of the MBP-NLRP12<sup>PYD</sup> crystal structure (PDB: 5H7N, chain B) with different structures of filament-forming PYDs. **(a)** Overlay with the NLRP3<sup>PYD</sup> crystal structure (PDB: 3QF2, chain A) and the NLRP3<sup>PYD</sup> filament structure (PDB: 7PZD). **(b)** Overlay with the MBP-NLRP6<sup>PYD</sup> crystal structure (PDB: 6NDJ, chain A) and the NLRP6<sup>PYD</sup> filament structure (PDB: 6NCV). **(c)** Overlay with the monomeric ASC<sup>PYD</sup> structure (PDB: 1UCP) and the ASC<sup>PYD</sup> filament structure (PDB: 3J63). **(d)** Overlay with the MBP-AIM2<sup>PYD</sup> crystal structure (PDB: 3VD8) and the GFP-AIM2<sup>PYD</sup> filament structure (PDB: 6MB2).

### 3.2.5 Amino acids important for filament formation match with NLRP12

The availability of high-resolution structural data of NLRP12<sup>PYD</sup> allowed to address its inability to self-polymerize at the molecular level. First, a structure-based sequence alignment of NLRP12<sup>PYD</sup> and the filament-forming PYDs of NLRP3, NLRP6, ASC, and AIM2 was performed (Figure 3-10a). NLRP12<sup>PYD</sup> (residues 10-96) displays sequence identities of 41.5%, 33.7%, 24.7%, and 23.5% with NLRP3<sup>PYD</sup>, NLRP6<sup>PYD</sup>, ASC<sup>PYD</sup>, and AIM2<sup>PYD</sup>, respectively (Figure 3-10a). Figure 3-10b shows the typical asymmetric interfaces mediating intra- and interstrand interactions in the Pyrin domain filament (Lu et al., 2015; Lu et al., 2014; Shen et al., 2019). Consequently, it was analyzed if residues

located in such interfaces and matching by charge or hydrophobicity in filament-forming Pyrin domains are mismatching in NLRP12<sup>PYD</sup>. Surprisingly, the majority of amino acids that participate in filament formation of NLRP3, NLRP6, ASC, or AIM2 were found to match with NLRP12 (Figure 3-10a). However, Leu10, Ser14, and Glu40 were identified to mismatch with their counterparts in filament-forming PYDs.



**Figure 3-10: Structural comparison of NLRP12<sup>PYD</sup> with filament-forming PYDs.** (a) Structure-based sequence alignment of the PYDs of NLRP12 and the filament-forming PYDs of NLRP3, NLRP6, ASC, and AIM2. For NLRP3, NLRP6, ASC, and AIM2, the filament structures are known (Hochheiser, Behrmann, et al., 2022; Lu et al., 2015; Lu et al., 2014; Shen et al., 2019) and the residues forming the asymmetric interfaces are highlighted with the indicated colors. Secondary structure elements of NLRP12<sup>PYD</sup> are plotted above the corresponding sequence. (b) Chart of three flanking subunits in a typical PYD filament. They form unified type I, type II, and type III interfaces with interface sides a and b, respectively. Subunits are labeled light blue, light green and light magenta. (c-e) Detailed view of the residues forming the (c) type I, (d) type II, and (e) type III interfaces in a modeled and hypothetical filament of NLRP12<sup>PYD</sup> that is based on the NLRP3<sup>PYD</sup> filament structure. Residues of NLRP12 not matching conserved properties of amino acids at equivalent positions in filament-forming Pyrin domains are highlighted as pink sticks.

To answer the question whether such mismatches could disrupt self-polymerization, interfaces in the aforementioned model of a hypothetical NLRP12<sup>PYD</sup> filament were analyzed in more detail. In the putative type I interface, hydrophobic patches on the ‘a’

and 'b' sides could establish substantial interactions (Figure 3-10c). Strikingly, Leu10 would match this interface and likely contribute in self-polymerization. While conserved to be hydrophobic in filament-forming Pyrin domains, Ser14 is polar but suited to form a hydrogen bond interaction with the primary amine of Lys27 (Figure 3-10c).

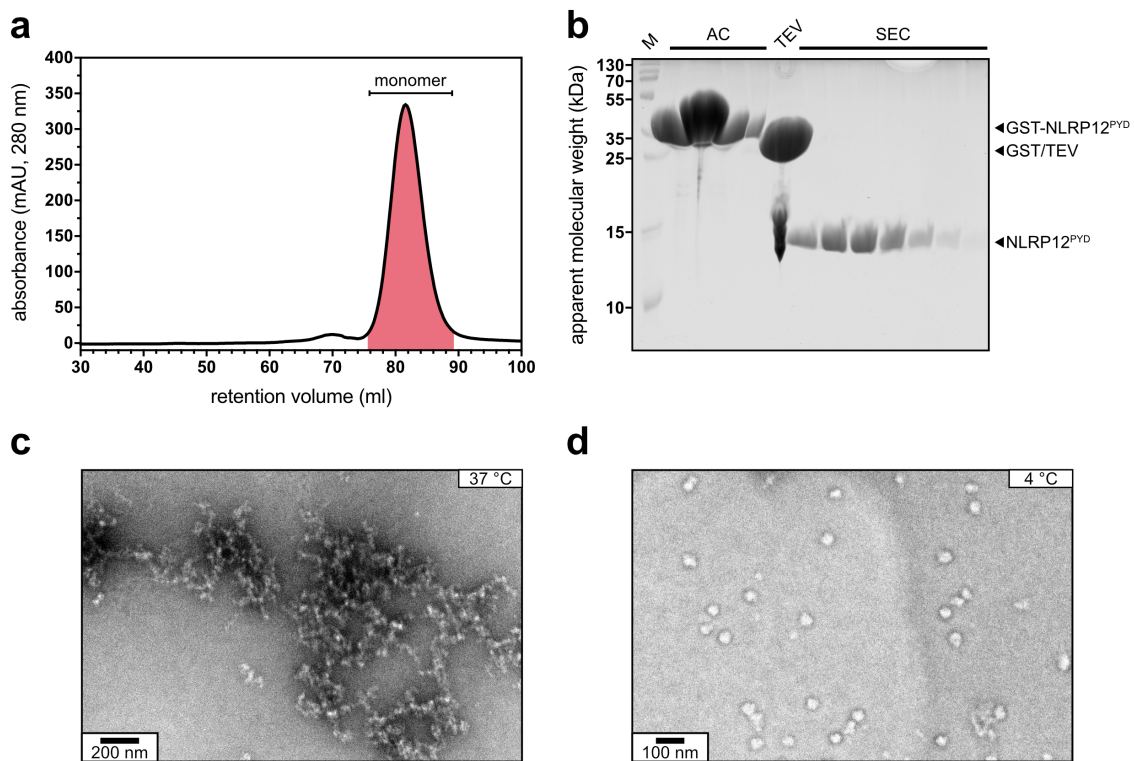
In the type II interface, the sidechain of Glu40 is located next to the sidechain of His63 (both 'a' side, Figure 3-10d). An interaction might fix the position and orientation of the  $\alpha$ 2- $\alpha$ 3 loop next to helix  $\alpha$ 4, which could change upon filament formation by substitution with higher affinity interactions. As such, Lys83 could change its conformation and reach out to form a salt bridge with Glu40. Additionally, Asn81 is close by His63 and might be able to establish a potential hydrogen bond interaction. Thr62 might participate in another polar interaction with the 'b' side formed by Glu24, Arg82, and Asp84 (Figure 3-10d).

While in the putative type III interface no mismatch could be identified by means of structure-based sequence alignment, the model reveals that Glu49 from the 'a' side and Glu21 from the 'b' side might create repulsive forces, which potentially destabilize the interface (Figure 3-10e). In NLRP3, which harbors both glutamate residues, an arginine that forms a salt bridge with the 'a' side glutamate and thereby compensates for the negative charge is found at the position of Trp45 (Figure 3-10a, (Hochheiser, Behrmann, et al., 2022)). In NLRP6, which shares the tryptophan and glutamate residue at the 'a' side, the glutamate found at the 'b' side in NLRP12 is substituted with a serine (Figure 3-10a, (Shen et al., 2019)). However, Glu18 and Ser47 as well as Glu19 and Lys42 might have the potential to overcome the repulsive forces by forming a hydrogen bond and salt bridge interaction, respectively (Figure 3-10e).

### 3.2.6 W54R mutation promotes oligomerization of the NLRP12 Pyrin domain

To test the hypothesis that Glu21 and Glu49 might destabilize the type III interface in a NLRP12<sup>PYD</sup> filament, Trp45 was exchanged to arginine using site-directed mutagenesis. In such variant the repulsive negative charge of the glutamate residues could crosslink with the now positively charged arginine by salt bridge formation. Identical to the wildtype protein, the mutant NLRP12<sup>PYD</sup> was expressed as an N-terminal GST-fusion protein in *E. coli* and purified to homogeneity by AC, TEV cleavage, and SEC. As previously seen for the wildtype protein, size-exclusion chromatography and SDS-PAGE analysis revealed that the W45R variant elutes as monomeric species in crystallization-grade quality (Figure 3-11a, b). To assay filament formation, the protein was diluted to

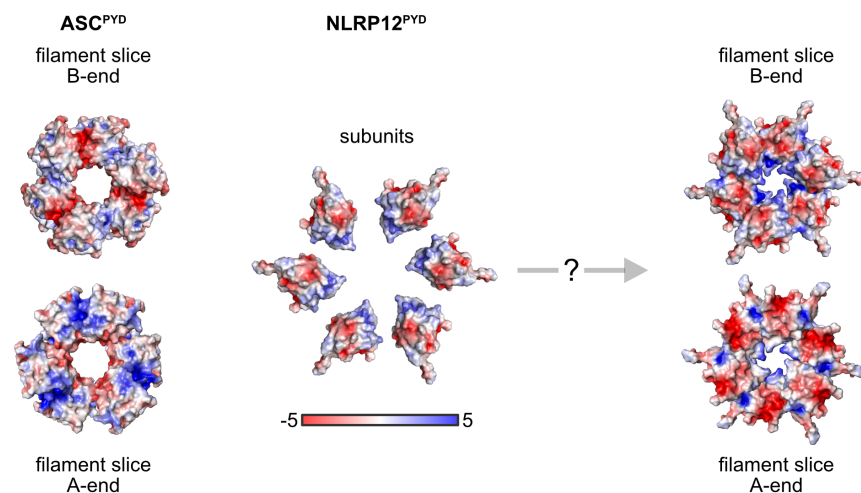
1.5 mg·ml<sup>-1</sup> and incubated overnight at 37°C. Subsequent analysis by negative stain EM showed that mutant NLRP12<sup>PYD</sup> formed net-like structures, which clearly differed from the aggregates seen with wildtype protein (Figure 3-11c and Figure 3-7c for comparison). However, these structures likewise differ significantly from the well-ordered filamentous structures of e.g., NLRP3<sup>PYD</sup> or NLRP6<sup>PYD</sup> (Hochheiser, Behrmann, et al., 2022; Shen et al., 2019). Interestingly, when incubation was performed at 4°C, mutant NLRP12<sup>PYD</sup> tend to form more roundish single particles with an average diameter of ~38 nm, corresponding to five times the diameter of a PYD filament (Figure 3-11d). In summary, the NLRP12 W45R mutation promotes the formation of oligomeric structures, but these structures differ significantly from well-ordered PYD filaments described in the literature.



**Figure 3-11: Purification and electron microscopy of the NLRP12<sup>PYD</sup> W45R mutant.** (a) Chromatogram of NLRP12<sup>PYD</sup> W45R mutant injected onto a Superdex 75 PG 16/600 size-exclusion column after affinity purification and tag cleavage. The column was connected to a tandem GStrap column for prolonged retention of the GST tag. Elution of protein was followed via the absorbance at 280 nm wavelength. The red area indicates pooled fractions of the monomeric peak. (b) Coomassie-stained samples from different steps of the purification process and fractions from (a) after reducing SDS-PAGE. M: marker, AC: affinity chromatography, TEV: tag cleavage using TEV protease, SEC: size-exclusion chromatography. (c-d) Negative stain EM image of 1.5 mg·ml<sup>-1</sup> NLRP12<sup>PYD</sup> W45R mutant, recorded by Inga Hochheiser (University of Bonn). Prior analysis, the sample was incubated overnight at (c) 37°C or (d) 4°C.

### 3.2.7 NLRP12<sup>PYD</sup> shows charge matching surface patches with ASC

To investigate the capability of NLRP12<sup>PYD</sup> to nucleate ASC speck formation, the aforementioned model of the hypothetical NLRP12<sup>PYD</sup> filament was further analyzed. One ring of the human ASC<sup>PYD</sup> (PDB: 3J63) filament structure and a slice of the hypothetical NLRP12<sup>PYD</sup> filament was used to calculate APBS-generated surface electrostatics (Jurrus et al., 2018) (Figure 3-12). As mentioned previously, it is known that the ‘B-end’ of the NLRP3<sup>PYD</sup> filament forms a seed for an interaction with the ‘A-end’ of ASC<sup>PYD</sup> to subsequently induce ASC polymerization (Hochheiser, Behrmann, et al., 2022). Importantly, similar as found for NLRP3, surface patches formed at the ‘B-end’ of the NLRP12<sup>PYD</sup> filament and the ‘A-end’ of the ASC<sup>PYD</sup> filament would be matching by charge complementarity (Figure 3-12). This highlights the plausibility of a resemblant PYD-mediated polymerization mechanism for nucleation of ASC specks in NLRP12 inflammasome formation.



**Figure 3-12: Molecular analysis of ASC nucleation capability of NLRP12<sup>PYD</sup>.** Color-coded (blue: positive, red: negative) electrostatic surface representation of subunits of NLRP12<sup>PYD</sup> and filament slices of ASC<sup>PYD</sup> and NLRP12<sup>PYD</sup> generated with APBS (Jurrus et al., 2018). The structure of NLRP12<sup>PYD</sup> subunits was adapted from the NLRP12<sup>PYD</sup> crystal structure (PDB: 5H7N, chain B). The filament slice of ASC<sup>PYD</sup> was adapted from the ASC<sup>PYD</sup> filament structure (PDB: 3J63). Based on the NLRP3<sup>PYD</sup> filament structure (PDB: 7PZD), the slice representation of a hypothetical NLRP12<sup>PYD</sup> filament was modeled using the crystal structure of the monomer. Bottom views (A-ends) represent a superjacent slice of the respective filament that was rotated by 180° about the y-axis and mirrored horizontally to show interfacing regions in the filament at the same x/y coordinates of top and bottom views. Electrostatic potentials are given in units of  $k_B T / e_c$  where  $k_B$  is the Boltzmann constant, T is the temperature and  $e_c$  is the charge of the electron.

### 3.3 Characterization of the NLRP12 NACHT domain

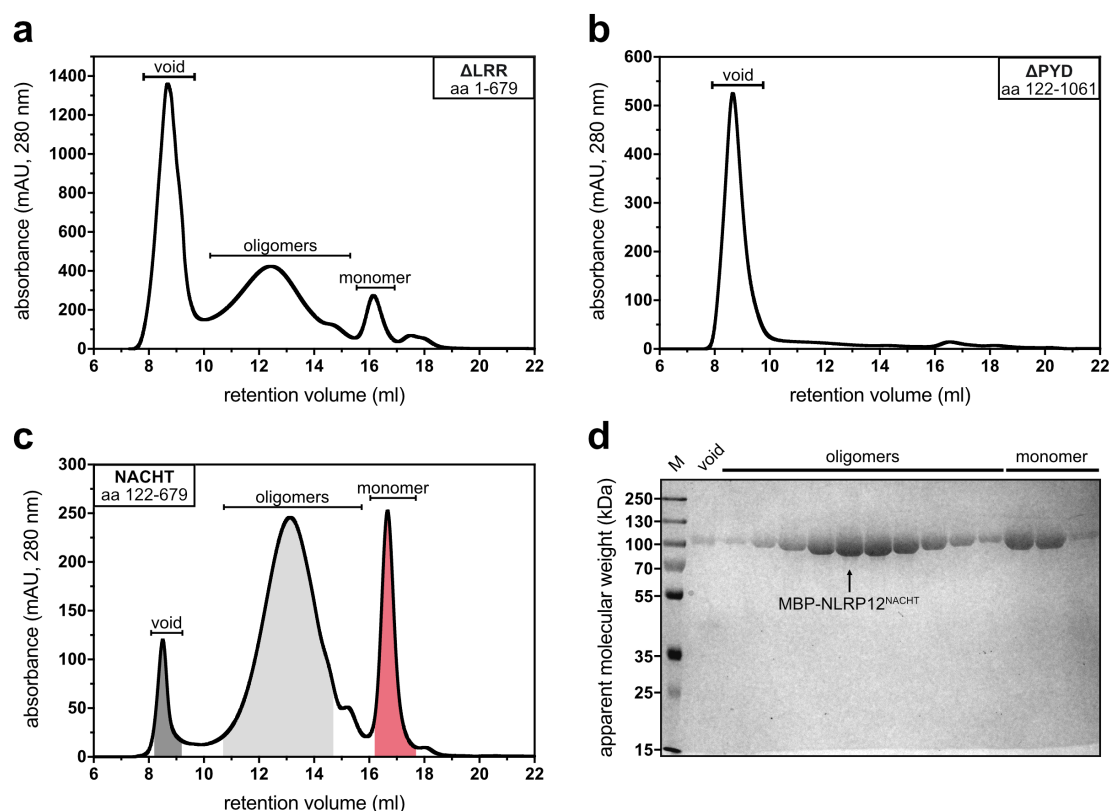
Previous experiments revealed that the NLRP12 PYD alone is not capable to self-polymerize *in vitro* and in cells, which entails its inability to interact with ASC. In contrast, the full-length protein did clearly show this competence when overexpressed in HEK293T cells (Figure 3-2). This conflict led to the hypothesis that the NACHT or LRR domains of NLRP12 must provide a scaffold for PYD oligomerization. Indeed, ATP-driven oligomerization of the NACHT domain is a widely accredited concept in the inflammasome field and especially documented by a structural study on activated NLRC4 $\Delta$ CARD, which assembles into wheel-like oligomeric structures (Schroder & Tschopp, 2010; Zhang et al., 2015). Thus, structural investigation of the NLRP12 NACHT domain might improve our mechanistic understanding in how this domain is regulated and facilitates oligomerization to drive inflammasome formation.

This part of the thesis summarizes the efforts being made to solve the structure of the NLRP12 NACHT domain and the insights that have been gained in this way. It is found that monomeric and oligomeric species of the NLRP12 NACHT domain are in dynamic equilibrium and oligomerization of monomers is widely independent from the presence of nucleotides. These findings are linked to the issue that crystals of suspected monomeric NLRP12 NACHT domain do not diffract, which initiated several attempts to inhibit oligomerization, stabilize the monomeric species, and optimize the protein construct. While the dynamic equilibrium could be effectively shifted towards the monomeric species, diffraction of crystals and subsequent structure determination of the NLRP12 NACHT domain has not yet been achieved.

#### 3.3.1 Construct design and purification

By screening different constructs of the human NLRP12 NACHT domain for good expression and yield of stable protein, one construct including the basic cluster of the FISNA domain and the polar cluster of the transition LRR (aa 122-679) was found to perform best. Based on this construct, two more constructs including the Pysin (aa 1-679) or LRR domain (aa 122-1061) have been designed. Experience has shown that, without extensive buffer optimization, a MBP tag is usually necessary to stabilize proteins of the NLRP family and prevent its precipitation. Bokhove et al. introduced an engineered MBP tag system, which combined mutations to increase solubility but also to provide crystal-packing interactions for increased crystallizability (Bokhove et al., 2016). Following their

example, the NACHT and  $\Delta$ PYD constructs were equipped with this mutant MBP tag using a short triple alanine linker, whereas the  $\Delta$ LRR construct was fused to a standard cleavable MBP tag (Figure 3-18a). All proteins were expressed as N-terminal MBP-fusion proteins in the *Sf9* insect cell system and purified to homogeneity by affinity purification and subsequent size-exclusion chromatography. While the SEC analysis of the  $\Delta$ LRR construct revealed probably aggregated (void), oligomeric, and monomeric species of the protein (Figure 3-13a), the  $\Delta$ PYD construct eluted as one major peak in the void volume (Figure 3-13b). This indicates that recombinantly expressed LRR domain of NLRP12 exhibits an intrinsic instability, which leads to aggregation and might similarly be responsible for aggregation of the recombinant full-length protein. However, also a great fraction of  $\Delta$ LRR protein eluted in the void volume, which differed significantly in case of the NACHT construct (Figure 3-13c). Indeed, the elution profile and subsequent SDS-PAGE analysis of NACHT protein revealed that the majority of the protein exists as oligomeric and monomeric species in crystallization-grade quality (Figure 3-13c, d).

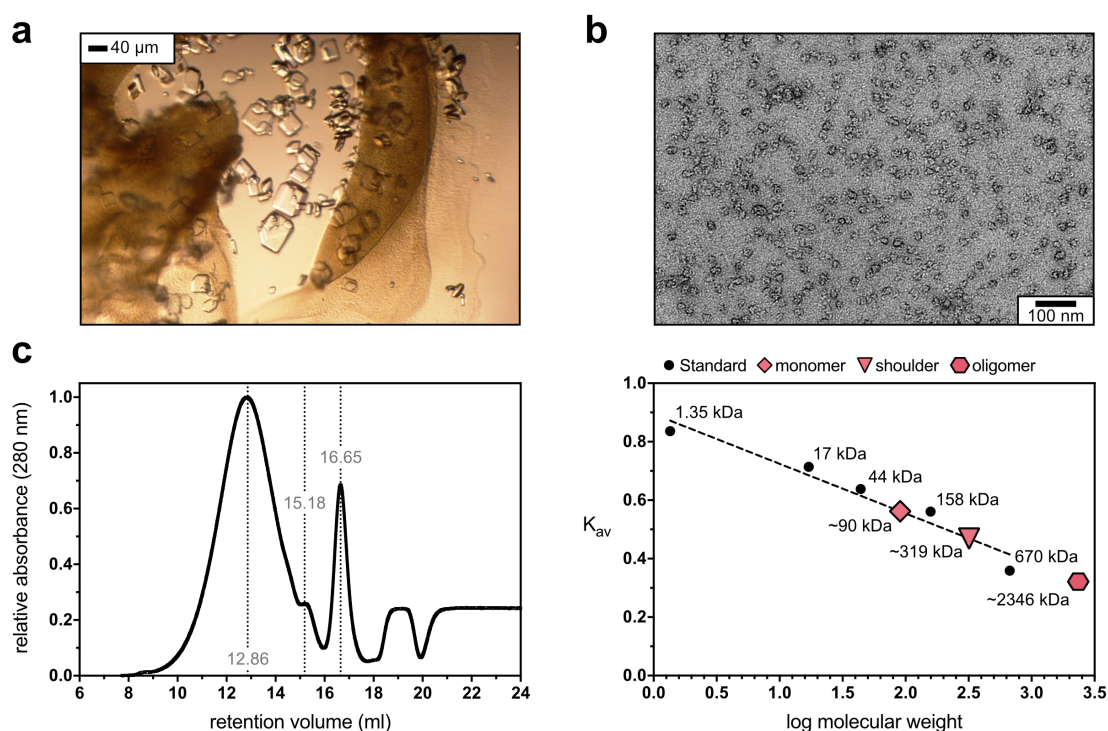


**Figure 3-13: Purification of NLRP12 constructs containing the NACHT domain.** (a-c) Representative chromatograms of different constructs of MBP-NLRP12 injected onto a Superose 6 Increase 10/300 GL size-exclusion column after affinity purification. Elution of protein was followed via the absorbance at 280 nm wavelength. The dark grey, light grey, and red areas indicate individually pooled fractions of the void, oligomeric, and monomeric peak, respectively. aa: amino acid. (d) Coomassie-stained samples from fractions from (c) after reducing SDS-PAGE. M: marker.



### 3.3.2 Monomeric and oligomeric NLRP12 species are in a dynamic equilibrium

Protein of the NLRP12 NACHT domain could be purified as monomeric species in crystallization-grade quality. Besides, peptide mass fingerprint analysis confirmed the identity of the protein sample. Consequently, MBP-NLRP12<sup>NACHT</sup> monomer was concentrated to 31 mg·ml<sup>-1</sup> and subjected to crystallization trials for the determination of a high-resolution X-ray crystal structure. Setup of crystallization screens did yield conditions to sufficiently grow crystals of the protein. Promising looking crystals appeared after 4-5 days at 15°C in 100 mM CAPS pH 10.5, 1.2 M NaCl, 200 mM LiSO<sub>4</sub> (Figure 3-14a) and protein content was confirmed by methylene blue staining, but unfortunately, the crystals did not diffract when measured at the synchrotron.



**Figure 3-14: Spontaneous oligomerization of monomeric NLRP12<sup>NACHT</sup>.** (a) Representative crystals of MBP-NLRP12<sup>NACHT</sup> protein that appeared in one of the optimization conditions but did not diffract at the synchrotron. Crystallization was performed by Dr. Kanchan Anand (University of Bonn). (b) Negative stain EM image of the oligomeric fraction of MBP-NLRP12<sup>NACHT</sup> after size-exclusion chromatography (0.04 mg·ml<sup>-1</sup>), recorded by Inga Hochheiser (University of Bonn). (c) Elution profile from analytical gel filtration of 100 μg monomeric MBP-NLRP12<sup>NACHT</sup> injected onto a Superose 6 Increase 10/300 GL column and calculation of the molecular weight from the peak retention volume. Linear regression was used to fit the calibration curve to the partition coefficient ( $K_{av}$ ) versus the logarithm of the molecular weight of a standard ( $R^2 = 0.9423$ ).

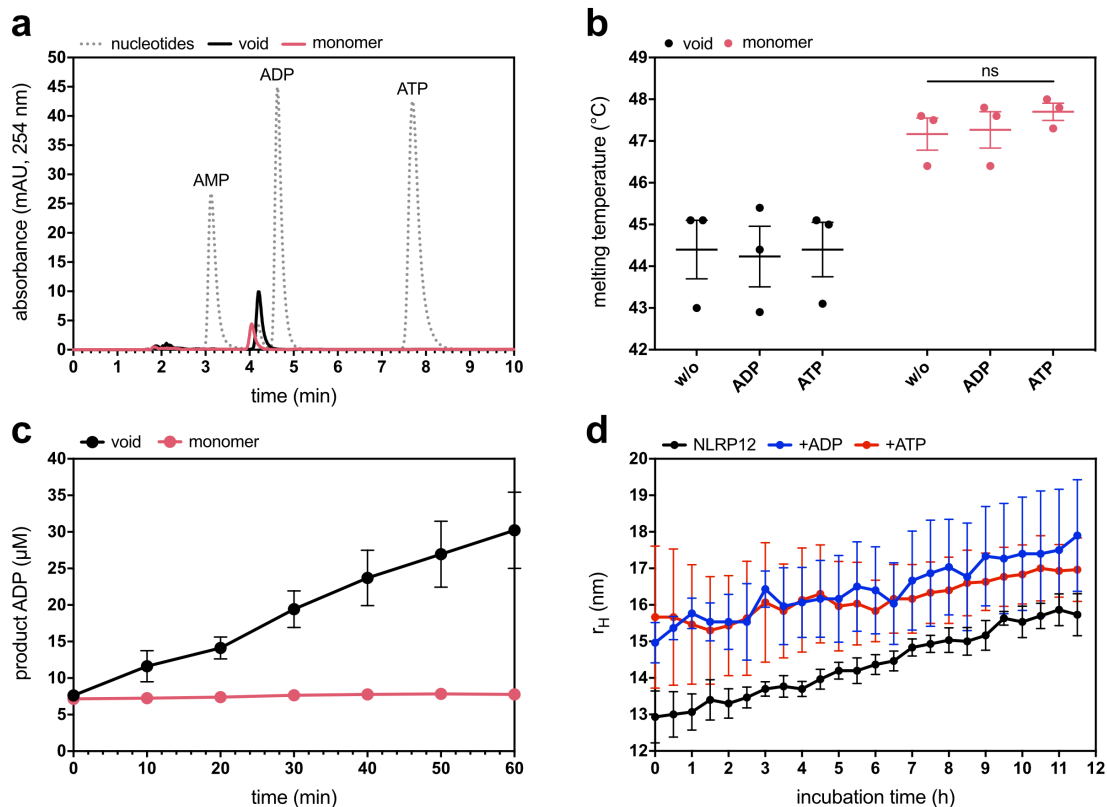
Interestingly, when oligomeric species of MBP-NLRP12<sup>NACHT</sup> were analyzed using negative stain EM, the particles displayed an inhomogeneous size and shape (Figure 3-14b). The average diameter of the particles varied between 16-34 nm, indicating a

plethora of different oligomers with an undefined number of subunits. Of note, MBP-NLRP12<sup>NACHT</sup> has an estimated diameter of 8-12 nm, suggesting the possibility that some particles may even represent oligomers dissociated into dimers. Vice versa, when the monomeric fraction of MBP-NLRP12<sup>NACHT</sup> was subjected to analytical gel filtration, again, oligomeric and monomeric species were identified (Figure 3-14c). The approximate molecular weight of the different species was determined to be > 670 kDa, 319 kDa, and 90 kDa, respectively (Figure 3-14c). Since the theoretical molecular weight of monomeric MBP-NLRP12<sup>NACHT</sup> is 105 kDa, the species represent monomers, tetramers, and a fraction of larger oligomers. In conclusion, it is likely that monomeric and oligomeric species of the NLRP12 NACHT domain are in a dynamic equilibrium, which might be the cause of not diffracting protein crystals.

### 3.3.3 Oligomerization of NLRP12<sup>NACHT</sup> is independent from nucleotides

To find out if the observed monomer  $\rightleftharpoons$  oligomer transition of the NLRP12 NACHT domain is dependent on incorporated nucleotide species and thus, regulated by ATP binding and hydrolysis, MBP-NLRP12<sup>NACHT</sup> was precipitated using perchloric acid and the released nucleotides were analyzed by ion-pairing reverse phase HPLC (Figure 3-15a). Surprisingly, MBP-NLRP12<sup>NACHT</sup> from both, the void and monomeric fraction, was free from nucleotides (Figure 3-15a). This result argues against a nucleotide-bound conformation of MBP-NLRP12<sup>NACHT</sup> and rather suggests an empty and thus ‘open’ conformation of aggregates, oligomers, and monomers prone to oligomerize.

Since nucleotide binding and hydrolysis are thought to play a pivotal role in the regulation of STAND ATPases by driving a conformational ‘binary switch’ mechanism (Danot et al., 2009), one idea was to shift the dynamic equilibrium towards the monomeric species. For this purpose, the proteins were incubated with high concentrations (1 mM) of ADP and ATP and subsequently analyzed by thermal shift assay to test for potential conformational changes. While incubation with nucleotides did not affect the thermal stability of MBP-NLRP12<sup>NACHT</sup> from the void fraction, presence of ATP slightly increased the apparent melting temperature of protein from the monomeric fraction ( $\Delta T_M = 0.53^\circ\text{C}$ , Figure 3-15b). Consequently, hydrolysis activity of MBP-NLRP12<sup>NACHT</sup> was analyzed in multi-cycle turnover ATP hydrolysis assays. Similar with full-length NLRP12, aggregated NLRP12<sup>NACHT</sup> protein was found to convert ATP to ADP but in contrast, protein from the monomeric fraction did not exhibit such activity (Figure 3-15c).



**Figure 3-15: Effect of nucleotides on NLRP12<sup>NACHT</sup> oligomerization.** (a) 50  $\mu\text{M}$  MBP-NLRP12<sup>NACHT</sup> protein from the void and the monomer fraction was precipitated using perchloric acid and the bound nucleotides have been analyzed using ion-pairing reverse phase HPLC. Elution of nucleotides was followed via the absorbance at 259 nm wavelength. Dashed line represents the elution profile of a 50  $\mu\text{M}$  nucleotide standard. Data is representative of  $n = 1$  independent experiment. (b) Thermal shift assay of 3  $\mu\text{M}$  MBP-NLRP12<sup>NACHT</sup> void or monomer and in the presence of 5 mM  $\text{MgCl}_2$  and 1 mM ADP or ATP. The measurement was setup with a temperature ramp ranging from 20-90°C, a slope of  $2^\circ\text{C}\cdot\text{min}^{-1}$ , and a 50-100% laser intensity. Data points are representative of three independent experiments.  $n = 3 \pm \text{SEM}$ ; ns  $P > 0.05$  (two-way ANOVA followed by the Dunnett's multiple comparisons test). (c) Hydrolysis assay based on ion-pairing reverse phase HPLC. 3  $\mu\text{M}$  of MBP-NLRP12<sup>NACHT</sup> void or monomer was incubated with 5 mM  $\text{MgCl}_2$  and 1 mM ATP at 25°C. Every 10 minutes a sample was injected onto a Chromolith Performance RP-18 HPLC column and elution of nucleotides was followed via the absorbance at 259 nm wavelength. The area under the curve was used to calculate the peak ratios and subsequently estimate the concentration of ADP as the product of the enzymatic reaction. Data points are representative of three independent experiments.  $n = 3 \pm \text{SEM}$ . (d) Hydrodynamic radius of 3  $\mu\text{M}$  MBP-NLRP12<sup>NACHT</sup> monomer as determined by DLS. Sample was supplemented with 5 mM  $\text{MgCl}_2 \pm 1$  mM nucleotides and measured every 30 min during 11.5 h of incubation at 25°C. Data points are representative of three independent experiments.  $n = 3 \pm \text{SEM}$ .

Finally, dynamic light scattering was used to follow the oligomerization of MBP-NLRP12<sup>NACHT</sup> in the absence or presence of nucleotides (Figure 3-15d). Already at the beginning of the measurement particles of the monomeric fraction were determined to have a relatively large hydrodynamic radius, indicating the presence of oligomers. However, the average size of these particles even increased over the course of the experiment, demonstrating further oligomerization. Importantly, the oligomerization rate did not differ significantly from the control when nucleotides were supplemented in the

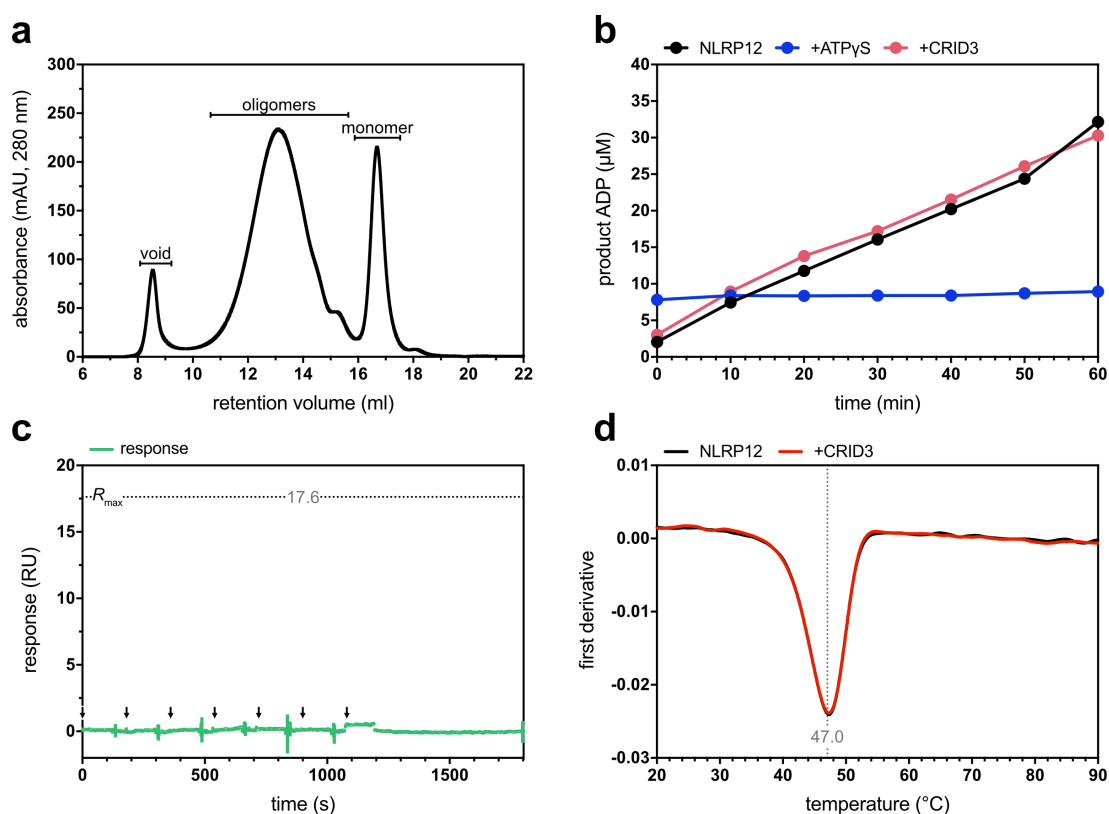
buffer. In the presence of ADP or ATP, the hydrodynamic radius of the particles was larger at the beginning of the measurement as if compared with the control. This difference might have technical reasons, since the control was measured first and interim oligomerization has likely increased the number of oligomers in the sample. Collectively, these results indicate that the observed oligomerization of the NLRP12 NACHT domain is largely independent from nucleotides.

### 3.3.4 The NLRP3-specific inhibitor CRID3 does not bind to NLRP12

In the following studies the aim was to stabilize the monomeric state of the NLRP12 NACHT domain or to inhibit its oligomerization. At the time, CRID3 (or MCC950) was already known as a potent NLRP3-specific inflammasome inhibitor that targets the NLRP3 NACHT domain (Coll et al., 2019). Mechanistically, Tapia-Abellan et al. proposed that CRID3 closes the active conformation of NLRP3 to an inactive state (Tapia-Abellan et al., 2019). Since NLRP12 (aa 120-631) shares 57.4% sequence identity with NLRP3 (aa 131-648; Figure 3-1), it was examined whether CRID3 could also bind to the NLRP12 NACHT domain and inhibit its oligomerization. In a first experiment, MBP-NLRP12<sup>NACHT</sup> was expressed and purified to homogeneity in the presence of CRID3 but otherwise identical conditions. SEC analysis revealed that presence of CRID3 did not influence the fraction of monomeric and oligomeric MBP-NLRP12<sup>NACHT</sup> and thus does not inhibit oligomerization of the NLRP12 NACHT domain (Figure 3-16a). Also, CRID3 was proposed to block ATP hydrolysis activity of NLRP3 (Coll et al., 2019). Consequently, the effect of CRID3 on the ATP hydrolysis activity of MBP-NLRP12<sup>NACHT</sup> from the void fraction was investigated (Figure 3-16b). In line with the previous result, CRID3 did not impair the ATPase function of NLRP12, whereas substitution of ATP with ATP $\gamma$ S, a commonly used nonhydrolyzable ATP analog (Lacabanne et al., 2020), did sufficiently prevent its hydrolysis (Figure 3-16b).

To confirm by orthogonal assay that CRID3 is unable to interact with NLRP12, the interaction was studied using surface plasmon resonance spectroscopy (SPR; Figure 3-16c). For this purpose, human NLRP12<sup>NACHT</sup> (aa 122-679) was expressed as N-terminal Avi- and Flag-tagged fusion protein in HEK293T cells. The protein was biotinylated intracellularly by co-transfection of the bacterial biotin-ligase BirA, purified via the Flag tag, and finally bound to a streptavidin-functionalized SPR sensor chip (methods section). Importantly, CRID3 showed no association with the NLRP12 NACHT domain up to

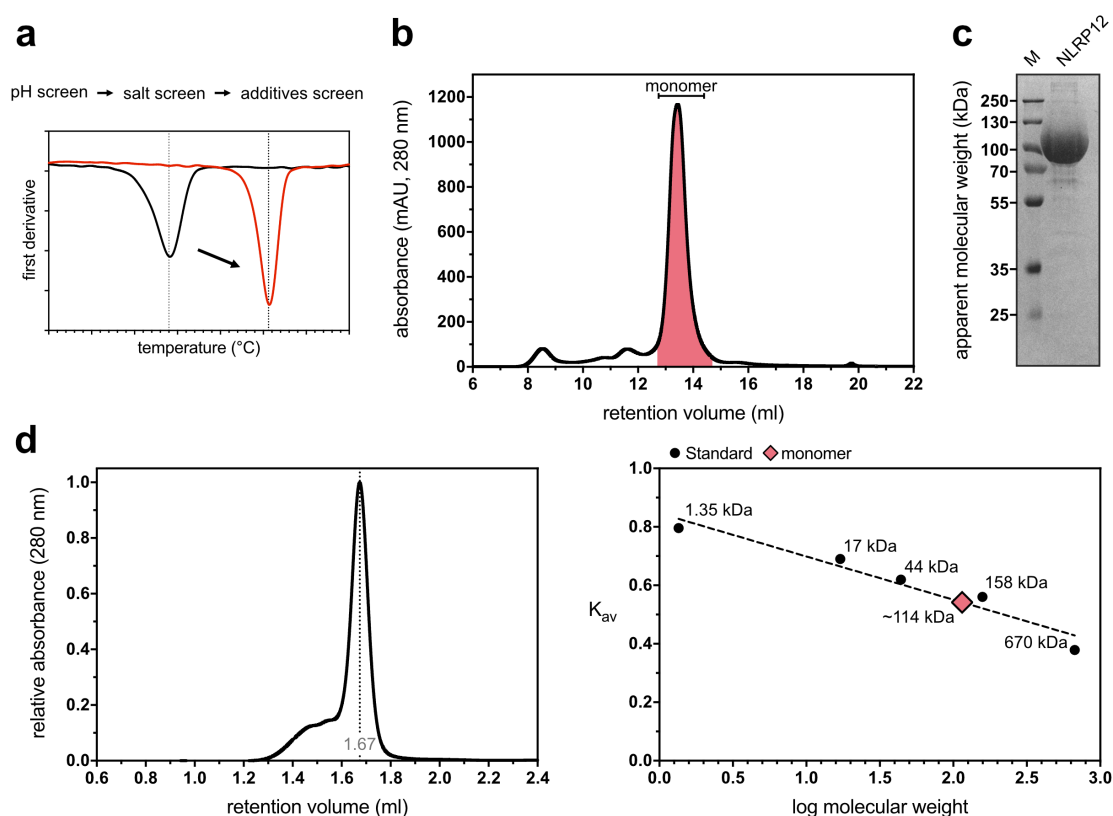
concentrations of 750 nM. However, injection of 3  $\mu\text{M}$  CRID3 did result in a slight response of  $\sim 0.6$  RU with a fast on and off rate (Figure 3-16c). In contrast, concentrations up to 60  $\mu\text{M}$  CRID3 did not change the thermal stability of MBP-NLRP12<sup>NACHT</sup> as evaluated in thermal shift assays (Figure 3-16d). Proposing that binding of CRID3 as an inhibitor does affect the conformation of its target, it is unlikely that CRID3 would bind to the NLRP12 NACHT domain without shifting its thermal stability. Thus, it can be concluded that CRID3 is a NLRP3-specific inhibitor that does not bind to NLRP12.



**Figure 3-16: Binding study of the NLRP3-specific inhibitor CRID3 on NLRP12.** (a) Chromatogram of MBP-NLRP12<sup>NACHT</sup> (aa 122-679) injected onto a Superose 6 Increase 10/300 GL size-exclusion column after affinity purification. Elution of protein was followed via the absorbance at 280 nm wavelength. The protein was expressed and purified in the presence of 5  $\mu\text{M}$  and 1  $\mu\text{M}$  CRID3, respectively. (b) Hydrolysis assay based on ion-pairing reverse phase HPLC. 3  $\mu\text{M}$  of MBP-NLRP12<sup>NACHT</sup> void was incubated with 5 mM MgCl<sub>2</sub> and 100  $\mu\text{M}$  ATP or ATP $\gamma$ S and in the presence of 2% DMSO or 100  $\mu\text{M}$  CRID3 at 25 $^{\circ}\text{C}$ . Every 10 minutes a sample was injected onto a Chromolith Performance RP-18 HPLC column and elution of nucleotides was followed via the absorbance at 259 nm wavelength. The area under the curve was used to calculate the peak ratios and subsequently estimate the concentration of ADP as the product of the enzymatic reaction. (c) Sensorgram following the binding of CRID3 to human NLRP12<sup>NACHT</sup> as measured by surface plasmon resonance spectroscopy (SPR). The measurement was performed in cooperation with Dr. Karl Gatterdam (University of Bonn). Arrows indicate injections of 0.7, 2.9, 11.7, 46.9, 187.5, 750, and 3000 nM CRID3, respectively.  $R_{\text{max}}$  indicates the theoretical maximum response of the interaction. (d) Thermal shift assay of 3  $\mu\text{M}$  MBP-NLRP12<sup>NACHT</sup> monomer in the presence of 2% DMSO or 60  $\mu\text{M}$  CRID3. The measurement was setup with a temperature ramp ranging from 15-95 $^{\circ}\text{C}$ , a slope of 2 $^{\circ}\text{C}\cdot\text{min}^{-1}$ , and a 40% laser intensity. Apparent melting temperatures ( $T_{\text{M}}$ ) of the samples are depicted as dashed lines.

### 3.3.5 Buffer optimization stabilizes the monomeric state

Since oligomerization of the NLRP12 NACHT domain was independent from nucleotides, it is possible that the underlying interactions are non-specific and therefore might be attenuated by an increased protein stability. Following a buffer optimization strategy that included sequential screening of pH, salt, and additives, thermal stability was used as a readout for conditions that potentially promote the monomeric state (Figure 3-17a). In this way, optimized buffer conditions could be found that not only markedly stabilized MBP-NLRP12<sup>NACHT</sup> but indeed also significantly increased the fraction of monomeric species (Figure 3-17a, b). Crystallization-grade quality of the sample was confirmed by SDS-PAGE analysis, which showed only one prominent band at a height corresponding to an apparent molecular weight of roughly 100 kDa (Figure 3-17c).



**Figure 3-17: Purification of NLRP12<sup>NACHT</sup> protein after buffer optimization.** (a) Schematic of the buffer optimization strategy. Increase in thermal stability of MBP-NLRP12<sup>NACHT</sup> was used as a readout for conditions that potentially promote the monomeric state. (b) Representative chromatogram of MBP-NLRP12<sup>NACHT</sup> injected onto a Superdex 200 Increase 10/300 GL size-exclusion column after affinity purification. The purification was performed under optimized buffer conditions. Elution of protein was followed via the absorbance at 280 nm wavelength. The red area indicates pooled fractions of the monomeric peak. (c) Coomassie-stained sample from the monomeric peak in (b) after reducing SDS-PAGE. M: marker. (d) Elution profile from analytical gel filtration of 76  $\mu$ g monomeric MBP-NLRP12<sup>NACHT</sup> injected onto a Superose 6 Increase 10/300 GL column and calculation of the molecular weight from the peak retention volume. Linear regression was used to fit the calibration curve to the partition coefficient ( $K_{av}$ ) versus the logarithm of the molecular weight of a standard ( $R^2 = 0.9394$ ).

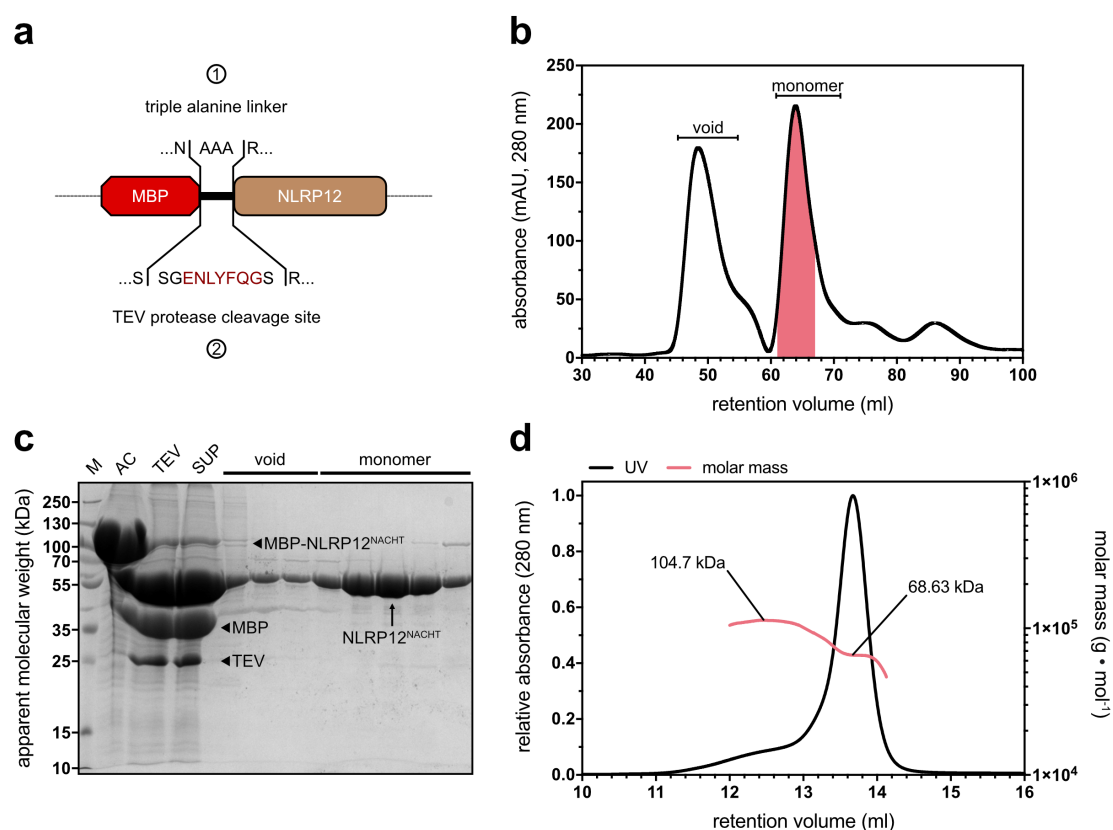
To analyze the oligomerization preference of the monomeric fraction, analytical gel filtration was conducted. Interestingly, it turned out that the majority of the protein did exist as a stable monomer and only a minor fraction did tend to oligomerize under these optimized conditions (Figure 3-17d). Hence, the sample was subjected to X-ray crystallography. Again, conditions to successfully grow crystals could be found but sufficient diffraction for structure determination was unfortunately not yet achieved.

### **3.3.6 Different purification strategy enables removal of the MBP affinity tag**

Since also crystals grown from most likely monomeric MBP-NLRP12<sup>NACHT</sup> did still not diffract at the synchrotron, one reasonable hypothesis was that the fused MBP tag might adopt different orientations relative to the NLRP12 NACHT domain and therefore cause perturbation and inequality of the crystal lattice. The previous construct design included a short triple alanine sequence between the MBP tag and the NLRP12 NACHT domain to establish a rigid helical linker and prevent such inequality (Figure 3-18a). However, rigidity relies on the continuation of this helix by the C-terminus of the MBP tag and the N-terminus of the NLRP12 NACHT domain, which might not be present. In consequence, imperfectly ordered crystals might result in X-ray diffraction at individual atoms that does not converge in constructive but destructive interference.

To enable removal of the MBP affinity tag, a new construct was designed with a cleavable linker sequence (Figure 3-18a) and the purification conditions were optimized to once again prevent aggregation. To increase the resolution between the NLRP12<sup>NACHT</sup> (MW = ~65 kDa) and the cleaved MBP tag (MW = ~42 kDa), the size-exclusion column was equipped with a tandem MBPTrap column for prolonged retention of MBP. The chromatogram of a representative SEC run after AC and tag cleavage is given in Figure 3-18b. NLRP12<sup>NACHT</sup> elutes as two major peaks – one close to the void volume and another at ~64 ml, corresponding to a monomeric fraction. Of note, the void fraction might contain aggregates and oligomers of NLRP12<sup>NACHT</sup>, since the used SEC column is not capable to separate both species. As indicated by a shift in SDS-PAGE analysis, the protein was sufficiently cleaved from the MBP affinity tag (AC versus TEV, Figure 3-18c) and finally obtained in crystallization-grade quality (monomer, Figure 3-18c). Next, NLRP12<sup>NACHT</sup> from the monomer fraction was characterized using online multiangle light scattering (SEC-MALS, Figure 3-18d). The protein eluted as one major peak with a slight shoulder to the left and the molecular weight of the species was

determined as 68.63 kDa and 104.7 kDa, respectively. Since NLRP12<sup>NACHT</sup> has a theoretical mass of 64.8 kDa, the identified species correspond to a monomer and dimer. Thus, the protein was concentrated to 10 mg·ml<sup>-1</sup> and subjected to crystallization trials. Suitable crystals were obtained after 3-4 days at 10-15 °C, but unfortunately, they did not sufficiently diffract for structure determination until now.



**Figure 3-18: Purification of NLRP12<sup>NACHT</sup> with cleaved MBP affinity tag.** (a) Schematic of the linker region between the MBP affinity tag and the NLRP12 NACHT domain. In the first approach, a short triple alanine linker was used, whereas the linker in the second approach contains a TEV protease cleavage site. (b) Representative chromatogram of NLRP12<sup>NACHT</sup> injected onto a Superdex 75 PG 16/600 size-exclusion column after affinity purification and tag cleavage. The purification was performed following a different strategy. Elution of protein was followed via the absorbance at 280 nm wavelength. The red area indicates pooled fractions of the monomeric peak. (c) Coomassie-stained samples from different steps of the purification process and fractions from (b) after reducing SDS-PAGE. M: marker, AC: affinity chromatography, TEV: tag cleavage using TEV protease, SUP: supernatant after centrifugation. (d) Elution profile from analytical gel filtration of 100 μg monomeric NLRP12<sup>NACHT</sup> injected onto a Superdex 200 Increase 10/300 GL column and corresponding molar mass as determined by multi angle light scattering (MALS).



### 3.4 Discussion and Conclusion

Since the discovery of NLRP12 and its first description in 2002, many controversial studies documented the likely dual role of NLRP12 in innate immunity and inflammation (Tuladhar & Kanneganti, 2020). Still, the picture that emerged about NLRP12 is rather puzzling and a matter of debate. Thus, it is important to gain more mechanistic understanding on its function and regulation, not least because NLRP12 has been linked with the development and progression of many human diseases (Tuladhar & Kanneganti, 2020). Especially due to its dual role in inflammation, NLRP12 might be a tempting drug target to modulate inflammatory response – a concept that was already proposed in context of multiple sclerosis (Gharagozloo et al., 2017). However, precisely because of its role in the central NF- $\kappa$ B signaling pathway, pharmacological intervention also carries the potential for severe side effects. Considering for example osteoclast differentiation, modulation of the NF- $\kappa$ B pathway via NLRP12 was shown to result in severe decline in bone mass by altering bone homeostasis and osteolytic responses (Krauss et al., 2015). Thus, specific interference with NLRP12-dependent inflammasome formation might be more beneficial. For that reason, this thesis does focus more on the NLRP12 inflammasome instead of its anti-inflammatory role in immunity.

During infection with strains of *Yersinia pestis* and *Plasmodium vivax*, NLRP12 has been shown to form an inflammasome with ASC and caspase-1 (Ataide et al., 2014; Vladimer et al., 2012). But interestingly, both studies revealed simultaneous activation of the NLRP3 inflammasome, which significantly contributes to host resistance (Ataide et al., 2014; Vladimer et al., 2012). Indeed, among other NLR family members, NLRP3 is most related with NLRP12 and shares essential sequence motifs important for its regulation ((Schroder & Tschopp, 2010), Figure 3-1). NLRP3 and NLRP12 might also share activation by specific stimuli and therefore compensate each other to ensure surveillance and protection against certain pathogens. Importantly, reconstitution of the NLRP12 inflammasome in HEK293T cells showed concentration-dependent and robust formation of ASC specks in the absence of NLRP3, confirming its ability to directly interact with ASC and nucleate polymerization, which in turn drives inflammasomal signaling ((Wang et al., 2002), Figure 3-2). However, recent reports on NLRP12 evidence a more complex composition of inflammasomes not only in infection but likewise in autoinflammatory disease. In acute glaucoma, NLRP12 was shown to collaborate with NLRP3 and NLRC4 in driving pyroptosis of ganglion cells (Chen et al., 2020). Also in Kawasaki syndrome, which has a yet unknown disease cause, NLRP12 and NLRC4 were

both found to be epigenetically upregulated and its expression levels do correlate with disease phenotype (Huang et al., 2018). Of note, TLR signaling is one important trigger for upregulation and priming of NLRP3 prior to inflammasome activation (Kelley et al., 2019). In contrast, NLRP12 is transcriptionally suppressed via the TLR-Blimp-1 axis (Lord et al., 2009; F. Shi et al., 2016). Hence, at least NLRP3 and NLRP12 might merely be expressed and activated simultaneously under very specific conditions. Conclusively, human NLRP12 is probably part of a delicately balanced multiprotein signaling platform that tightly regulates inflammation and collaborates with other NLR family members to facilitate host resistance and tissue homeostasis.

Such tight regulation might not be given when full-length NLRP12 is recombinantly expressed in baculovirus-infected *Sf9* insect cells, as the protein adopts no defined but most likely a constitutively ‘open’ conformation (Figure 3-3). In contrast, a fraction of recombinantly expressed human NLRP3 was found to adopt a ‘closed’ and autoinhibited state in a decameric assembly (Hochheiser, Pilsl, et al., 2022). However, the residues that establish intermolecular interactions in the NLRP3 decamer are not well conserved in NLRP12 (Figure 3-1), explaining why such oligomer could not be enriched even under optimized purification conditions that stabilized NLRP12 and allowed for cleavage of the affinity tag. Also, mass spectrometry analysis revealed that recombinant NLRP12 is phosphorylated at Ser192, which is in similar position as Ser198 of NLRP3 and could thus be an indication for a primed status ((Paik et al., 2021), Figure 3-1). In contrast, the NLRP3 decamer is not phosphorylated at Ser198 and therefore not primed for inflammasome activation (Hochheiser, Pilsl, et al., 2022). Interestingly, recombinant NLRP12 was also found to be phosphorylated at Ser755 within the LRR domain. While the relevance of such phosphorylation in NLRP12 is uncertain, a recent study identified that the phosphorylation status of the NLRP3 LRR domain is critical in regulating its association with NEK7 and subsequent inflammasome formation (Niu et al., 2021). It is known that NLRP3 interacts with NEK7 at the microtubule organizing center (MTOC), to where it localizes via microtubule retrograde transport (Li et al., 2017; Magupalli et al., 2020). Interestingly, recombinant NLRP12 co-purified with endogenous proteins of the tubulin superfamily (Figure 3-3e), suggesting that active NLRP12 is transported to the MTOC by a similar mechanism. Importantly, phosphorylation sites identified in the here presented study are purely based on mass spectrometry data obtained with recombinant protein. Due to differences in the kinome of insect and human cells, recombinant NLRP12 might be phosphorylated at artificial sites. Moreover, the

consequences of such modifications can only be interpreted based on knowledge about NLRP3, since the role of post-translational modifications in regulating NLRP12 has not yet been investigated. Thus, to validate that phosphorylation of the identified residues is important for the regulation of NLRP12, studies on endogenous protein should be conducted in a more physiological setting such as THP1 cells. Mutational studies on NLRP12 could then help to delineate its regulation by post-translational modifications.

Intrinsic ATPase activity has been shown to be important for the function of NLRP12 (MacDonald et al., 2013; Ye et al., 2008). Mechanistically, activated NLR family proteins are thought to couple ATP binding and hydrolysis with the generation of mechanochemical work to implement conformational changes that regulate the exposure of oligomerization interfaces (Danot et al., 2009; Sandall et al., 2020). Interestingly, purification of recombinant NLRP12 in the absence of the zwitterionic surfactant CHAPS resulted in protein that possesses ATPase activity, while presence of CHAPS during lysis rendered the protein inactive (Figure 3-4). While it is not yet clarified how CHAPS modifies NLRP12 activity, one hypothesis might be that it works as a detergent and solubilizes NLRP12, whereby interactions with cellular membranes are abrogated. In this context, it is important to review that, upon potassium ion efflux across the plasma membrane, the polybasic cluster in NLRP3 is thought to interact with negatively charged phosphatidylinositol-4-phosphate (PtdIns4P) on the dispersed *trans*-Golgi network (dTGNG), which was found to be an essential step for the assembly of the NLRP3 inflammasome (Chen & Chen, 2018; Tapia-Abellan et al., 2021). Also, in NLRP12 a basic region could be identified in the FISNA domain (Figure 3-1), which might equally couple NLRP12 inflammasome formation to localization on cellular membranes. Indeed, cigarette smoke extract was found to trigger recruitment of NLRP12 to membrane microdomains in A549 cells, where it interacts with caveolin-1 and is potentially activated for inflammasome formation (Singh et al., 2018). Interestingly, samples of purified NLRP12 comprised liposomes even though CHAPS was contained in the lysis buffer (Figure 3-3d). However, no direct interaction between liposomes and aggregates of NLRP12 could be observed under these conditions. Regarding ATP hydrolysis activity, it might also be possible that liposomes, which are co-purified in the absence of CHAPS, comprise small amounts of contaminating NTPases. In line, thermal shift denaturation assay as a readout for conformational change did not show alterations in thermal stability of NLRP12 upon incubation with ATP (Figure 3-4d). However, mutational analysis showed that measured ATPase activity was indeed dependent on

NLRP12 and not an artifact from contaminating proteins, since turnover was reduced when mutations were introduced in the Walker B or sensor I motif, respectively (Figure 3-5). To further conclude about the ATP hydrolysis mechanism in NLRP12, robust data for wildtype and mutant variants is needed. Therefore, the data needs repetition to ensure significance of the distinct hydrolysis activity.

When NLRP12 was incubated in the presence of ATP and magnesium chloride, not only ADP but also small amounts of AMP have been generated (Figure 3-4b). Notably, presence of NLRP12 did also catalyze the conversion of ADP to ATP and AMP (Figure 3-4c). Surprisingly, NLRP12 was thus found to harbor adenylate kinase activity. In theory, the consumption of two molecules ADP should result in one molecule AMP and ATP each. However, a lower amount of ATP was observed as if compared with AMP (Figure 3-4c). This can be explained by the coupled ATPase activity of NLRP12 that might cause rapid conversion of ATP back to ADP once it is generated. At the same time a favored affinity of NLRP12 towards ATP is likely, since ATP is consumed even when ADP is present in great excess. While adenylate kinase activity has already been proposed for NLRP3 (Brinkschulte, 2020), the underlying mechanism and its physiological role in NLRP12 are completely unknown. But interestingly, a coupled ATPase-adenylate kinase mechanism is not unique to NLR family proteins, as some members of the related AAA+ family of ABC transporters and also human adenylate kinase 6 have been shown to possess similar activity (Drakou et al., 2012; Kaur et al., 2018; Kaur et al., 2016). As proposed for the ABC transporter MsbA, this activity could involve the canonical and an additional nucleotide binding site in close proximity (Kaur et al., 2018).

Undoubtedly, only structural data of NLRP12 can ultimately reveal such secondary binding site and help to gain mechanistic understanding. Unfortunately, particles of human NLRP12 were not suitable to solve their structure using electron microscopy (Figure 3-3f). It is assumed that they are not well structured and inhomogeneous in conformation. To improve particle quality, the purification conditions have already been optimized for enhanced protein stability and cleavage of the MBP affinity tag. But potentially artificial post-translational modification might affect protein conformation. Thus, purification from a more physiological expression system such as HEK293T cells could be tested. Additionally, missing interaction partners that might be essential for proper conformation could be co-expressed with NLRP12. Interestingly, heat shock proteins (HSP)70 and 90 were described to associate with NLRP12 and to be required for its activity (Arthur et al., 2007; X. Li et al., 2021). Indeed, HSP70 and HSP90 are

molecular chaperones that assist in folding and maturation of proteins, thereby preventing misfolding and aggregation (Wegele et al., 2004).

The NLRP12 inflammasome has been demonstrated to form in a PYD-dependent manner (Wang et al., 2002). To be more precise, polymerization of the PYD is thought to be required for the interaction with ASC (Lu et al., 2014). To study NLRP12 inflammasome formation uncoupled from intricate regulatory mechanisms, the PYD of NLRP12 was investigated as its supposed effector domain. Similar with NLRP9, no self-polymerization of the NLRP12 PYD could be demonstrated *in vitro* or in HEK293T cells (Figure 3-7 and Figure 3-8). However, overexpression of full-length NLRP12 was found to trigger ASC speck formation in HEK293T cells whereas NLRP9 did not (Figure 2-2 and Figure 3-2). Importantly, this result argues for the capability of NLRP12 to nucleate ASC specks, although it does not explain its inability to form PYD filaments. *In silico* analysis based on the crystal structure of NLRP12<sup>PYD</sup> (T. Jin et al., 2017) revealed that the protein adopts a conformation with hallmarks of both, monomeric and filamentous PYDs (Figure 3-9). Still, no steric clash between two subunits in a potential filament could be identified, arguing against conformational restraints that might restrict self-polymerization. In line with this observation, detailed analysis of the putative interfaces formed in a NLRP12<sup>PYD</sup> filament did not reveal residues that would clearly interfere with its assembly (Figure 3-10). Au contraire, it was even found that charged surface patches formed by the ‘B-end’ of a putative NLRP12<sup>PYD</sup> filament would provide a proper interface for the nucleation of ASC (Figure 3-12). Only residues Glu21 and Glu49 might establish repulsive forces within the type III interface in the filament (Figure 3-10). In case of NLRP3, both glutamates are conserved but integrated in a salt bridge with an arginine in proximity (Hochheiser, Behrmann, et al., 2022). However, substitution of the corresponding tryptophan (Trp45) in NLRP12 with an arginine did not result in a protein that formed defined filaments under the conditions tested (Figure 3-11). Nevertheless, it would be worthwhile to test this mutation in HEK293T cells. Collectively, the molecular analysis did not reveal an explanation for the inability of NLRP12<sup>PYD</sup> to self-polymerize.

NLRP12 also plays a role in regulating the NF- $\kappa$ B pathway, although the function of its PYD in anti-inflammatory signaling remains to be elucidated. NLRP12 was demonstrated to interact with the pro-apoptotic protein FAF-1 (FAS-associated factor 1) via non-homotypic PYD interaction (Pinheiro et al., 2011). FAF-1 is not only a member of the FAS death-inducing signaling complex but can also regulate cell survival by directly suppressing NF- $\kappa$ B signaling, thus indicating a likely synergistic effect of FAF-1

and NLRP12 (Menges et al., 2009; Pinheiro et al., 2011). It can be postulated that the NLRP12<sup>PYD</sup> is regulated to switch between inflammatory and anti-inflammatory signaling by a yet unknown mechanism, which might well explain its inability to form filaments under the conditions tested. Intriguingly, interaction of NLRP12 with FAF-1 critically relies on the hydrophobic nature of Trp45 (Pinheiro et al., 2011), which is part of the previously discussed type III interface in the filament (Figure 3-10e). In conclusion, this suggests an important role of this interface for the effector function of the NLRP12 PYD. Still, it is possible that the NACHT and LRR domains of NLRP12 aid in oligomerization or that NLRP12<sup>PYD</sup> is able to trigger ASC polymerization regardless of filament formation. To test these hypotheses, ASC speck formation should be tested with different constructs of NLRP12 entailing the PYD, NACHT, or LRR domains as well as their respective subdomains. Likewise, oligomerization of NLRP3 via the NBD was initially assumed to be required for the interaction with ASC, since NLRP3<sup>PYD</sup> did not nucleate ASC<sup>PYD</sup> filament formation in fluorescence polarization assays (Lu et al., 2014). However, the here presented study and others unambiguously showed that NLRP3<sup>PYD</sup> can form filaments that are capable to nucleate ASC polymerization ((Hochheiser, Behrmann, et al., 2022; Marleaux et al., 2020; Stutz et al., 2017), Figure 2-9). Such discrepancy might reflect different construct design, post-translational modification or assay condition. Indeed, NLRP3<sup>PYD</sup> polymerization is regulated by a single phosphorylation at Ser5 (Stutz et al., 2017). While this particular serine residue is not conserved in the NLRP12 PYD (Figure 3-1), the recently described CAPS mutants G52S and A57S (Wang, 2022) may introduce SP and SQ phosphorylation motifs that potentially lead to charge-assisted activation of NLRP12. Moreover, Cys11 was previously shown to establish a disulfide bond in a crystallographic dimer of the NLRP12 PYD (Jin et al., 2018). Physiologically, high local levels of reactive oxygen species (ROS) were proposed to enable disulfide bond formation during infection or tissue damage (Jin et al., 2018). Thus, it is conceivable that disulfide bond formation stabilizes the formation of asymmetric interfaces in a NLRP12<sup>PYD</sup> filament. In contrast, reducing conditions during purification or in the cytoplasm of HEK293T cells might dissolve such linkage. In context of full-length NLRP12, the protein might translocate to a different cellular compartment, which potentially allows disulfide bond formation and oligomerization of the PYD.

In the process of trials to obtain diffracting crystals for structure determination, oligomerization of the NLRP12 NACHT domain has also been investigated. It was found that previously purified monomers tend to spontaneously form oligomers with an average

mass exceeding 670 kDa (Figure 3-14c). Conversely, analysis using negative stain EM revealed that the size of such oligomers was inhomogeneous and too small to correlate with the before determined mass (Figure 3-14b), indicating dissociation into smaller species including dimers. Thus, it was assumed that monomers and oligomers of MBP-NLRP12<sup>NACHT</sup> are in a dynamic equilibrium, which explains the phenomenon of not diffracting protein crystals because concomitant conformational change would likely disorder crystal packing. However, the ‘binary switch’ mechanism proposed for STAND ATPases includes the exchange of bound nucleotide prior to oligomerization (Danot et al., 2009; Lisa et al., 2019). In detail, the resting state is thought to be a long-lived, ‘closed’, and ADP-bound monomer. Binding of an inducer can trigger unmasking of oligomerization interfaces by isomerization of the protein into an ‘open’ form, which then enables the exchange of ADP with ATP and in turn promotes and stabilizes a multimeric assembly. Subsequent ATP hydrolysis is thought to dissolve such assembly and to return the protein back to the resting form (Danot et al., 2009). Importantly, the postulated ‘binary switch’ mechanism is particularly supported in NLR family proteins by structural studies on APAF-1 (apoptotic protease activating factor-1), NLRC4, and NLRP3 (Cheng et al., 2016; Hu et al., 2013; Reubold et al., 2011; Sandall et al., 2020; Sharif et al., 2019; Tenthorey et al., 2017; Zhang et al., 2015). In contrast, further characterization of MBP-NLRP12<sup>NACHT</sup> showed that the observed oligomerization process is largely independent from nucleotides. In summary, no nucleotide was bound to MBP-NLRP12<sup>NACHT</sup> protein, and although incubation with ATP did result in slightly increased thermal stability ( $\Delta T_M = 0.53^\circ\text{C}$ ), which might indicate binding capability, MBP-NLRP12<sup>NACHT</sup> purified as a monomer oligomerized similarly in the absence or presence of nucleotides and showed no ATPase activity (Figure 3-15). Of note, the effect on thermal stability was determined as not significant. This might suggest, that MBP-NLRP12<sup>NACHT</sup> protein is trapped in a ‘semi-open’ conformation that allows to form low affinity homotypic interactions but not ATP hydrolysis to adopt the resting form. Alternatively, deletion of the Pyrin and LRR domains could have generated artificial interfaces that drive rather unspecific oligomerization of MBP-NLRP12<sup>NACHT</sup> protein.

Interestingly, the observed oligomerization behavior of the NLRP12 NACHT domain resembles a report on oligomerization of the bacterial AAA+ ATPase ClpB. In the absence of nucleotides, monomers of ClpB have been shown to undergo reversible self-association into heptamers and intermediate-size oligomers (Akoiev et al., 2004). However, presence of ATP $\gamma$ S or ADP and conditions of low ionic strength stabilized the

hexameric and heptameric species, respectively (Akoev et al., 2004). Indeed, purification of MBP-NLRP12<sup>NACHT</sup> under optimized conditions including low ionic strength (methods section) did significantly influence oligomerization, but in contrast to ClpB stabilized the monomer (Figure 3-17). Despite further optimization of the purification conditions that did not only stabilize the monomer but also allowed for cleavage of the MBP affinity tag (Figure 3-18), generated crystals of the NLRP12 NACHT domain did still not diffract. Low resolution and poor-quality diffraction can be a consequence of loose crystal packing or large solvent channels (Heras & Martin, 2005), since such conditions would still allow NLRP12<sup>NACHT</sup> to adopt different conformational states also in the crystal. To improve diffraction quality, different post-crystallization treatments such as dehydration could be applied (Heras & Martin, 2005). Moreover, surface methylation prior to crystallization might be an option to obtain different crystal packing (Walter et al., 2006). Furthermore, precise mutations or NLRP12-specific drugs that force the monomeric protein in the ‘closed’ conformation could be applied to improve conformational homogeneity and reduce disorder in the crystal. NLRP12-specific drugs have not been developed at the time but interestingly, the inhibitor CRID3 is well known to prohibit oligomerization of its target NLRP3 (Ismael et al., 2018). Since NLRP3 and NLRP12 are highly related proteins, CRID3 binding to NLRP12 was tested using different methods. Importantly, CRID3 did not show binding to NLRP12, confirming its specificity for NLRP3 (Figure 3-16). This result is supported by a study from Coll et al., who showed that a NLRP3-NLRP12 chimera with exchange of the NACHT domains is no longer protected in a drug affinity responsive target stability (DARTS) assay (Coll et al., 2019). However, high-resolution structural data of the NLRP3-CRID3 inhibitor complex would pave the way for the development of novel NLRP12-specific drugs or mutational studies that could render NLRP12 susceptible to inhibition by CRID3.



## Chapter 4: Investigating NLRP3-specific small molecule inhibitors

Some work presented in this chapter was accomplished in cooperation with Julia Hockling, Dr. Gregor Hagelüken, Dr. Jonas Möcking, Dr. Anemarie Steiner, Tim Keuler, and Dr. Karl Gatterdam (University of Bonn). As a technical assistant Julia Hockling was involved in the expression and purification of human NLRP3 protein. Dr. Gregor Hagelüken supervised the crystallographic data collection and processing for structure determination. Dr. Jonas Möcking and Dr. Anemarie Steiner performed the flow cytometry analysis of mutant NLRP3 depicted in Figure 4-8c. Tim Keuler performed the synthesis of compounds shown in Figure 4-11 that have been investigated using SPR spectroscopy. Dr. Karl Gatterdam performed SPR measurements with CRID3-containing probes (Figure 4-12a-f), excluding the competitive assays (Figure 4-12g-h).

Part of this chapter is published in:

Hochheiser, I. V., Pils, M., Hagelueken, G., Moecking, J., **Marleaux, M.**, Brinkschulte, R., Latz, E., Engel, C., & Geyer, M. Structure of the NLRP3 decamer bound to the cytokine release inhibitor CRID3. *Nature* **604**, 184-189 (2022). DOI: 10.1038/s41586-022-04467-w

Keuler, T., Ferber, D., **Marleaux, M.**, Geyer, M., & Gutschow, M. Structure-Stability Relationship of NLRP3 Inflammasome-Inhibiting Sulfonyleureas. *ACS Omega* **7**, 8158-8162 (2022). DOI: 10.1021/acsomega.2c00125

Keuler, T., Gatterdam, K., Akbal, A., Lovotti, M., **Marleaux, M.**, Geyer, M., Latz, E., & Gutschow, M. Development of Fluorescent and Biotin Probes Targeting NLRP3. *Front Chem* **9**, 642273 (2021). DOI: 10.3389/fchem.2021.642273

#### 4.1 Molecular study of the NLRP3 inhibitor CRID3

NLRP3 is today the best studied member of the NLR family and serves as a prototypical model for canonical inflammasome activation (Swanson et al., 2019). Importantly, its dysregulation in sterile conditions can contribute to a variety of complex and often autoinflammatory diseases, including cryopyrin-associated periodic syndrome (CAPS), nonalcoholic steatohepatitis (NASH), gout, multiple sclerosis, type 2 diabetes, Alzheimer's disease, Parkinson's disease, atherosclerosis, and cancer (Conforti-Andreoni et al., 2011; Guo et al., 2015; Kim et al., 2016; Schwaid & Spencer, 2021; Strowig et al., 2012). Today, anti-inflammatory drugs that have been approved in the clinic comprise diverse kinase or IL-1 pathway inhibitors. However, these rather indirect compounds were not originally invented with the aim of targeting inflammasomes and thus can lead to diverse outcomes (Schwaid & Spencer, 2021). For that reason, NLRP3 has attracted great attention as a direct therapeutic target.

The small molecule compound glyburide (494 Da) is well known as a potent sulfonylurea-containing antidiabetic drug that specifically blocks the ATP-sensitive potassium channel in pancreatic  $\beta$ -cells (Ashcroft & Ashcroft, 1992). In 2001, when inflammasomes had not yet been discovered, Pfizer found that glyburide, independent of its antidiabetic properties, also inhibited the maturation and release of IL-1 $\beta$  (Perregaux et al., 2001). Based on this finding, Pfizer developed a novel class of diarylsulfonylurea compounds with pharmacological anti-inflammatory properties, which they termed cytokine release inhibitory drugs (CRIDs) (Laliberte et al., 2003; Perregaux et al., 2001). Initially, CRIDs were speculated to target glutathione *S*-transferase  $\omega$ -1 by modifying the catalytic center cysteine (Laliberte et al., 2003). Only twelve years later and after glyburide was found to inhibit the assembly of the NLRP3 inflammasome (Lamkanfi et al., 2009), Coll and colleagues identified CRID3 (sometimes also referred to as CP-456, 773 or MCC950) to target NLRP3 with an IC<sub>50</sub> value of 8.1 nM in human monocytes (Coll et al., 2015). After four more years, independent studies demonstrated an interaction of CRID3 with the NACHT domain of NLRP3, but structural data to clearly identify the binding site and a detailed understanding of the mode of action were lacking (Coll et al., 2019; Tapia-Abellan et al., 2019; Vande Walle et al., 2019). Since then, CRID3 developed as an important tool to manipulate and investigate the NLRP3 inflammasome that was used in an extensive number of studies and preclinical models (Corcoran et al., 2021; Mangan et al., 2018). Clinical development of CRID3 stopped after phase Ib testing due to increased risk of hepatotoxicity, but many advanced sulfonylurea-containing

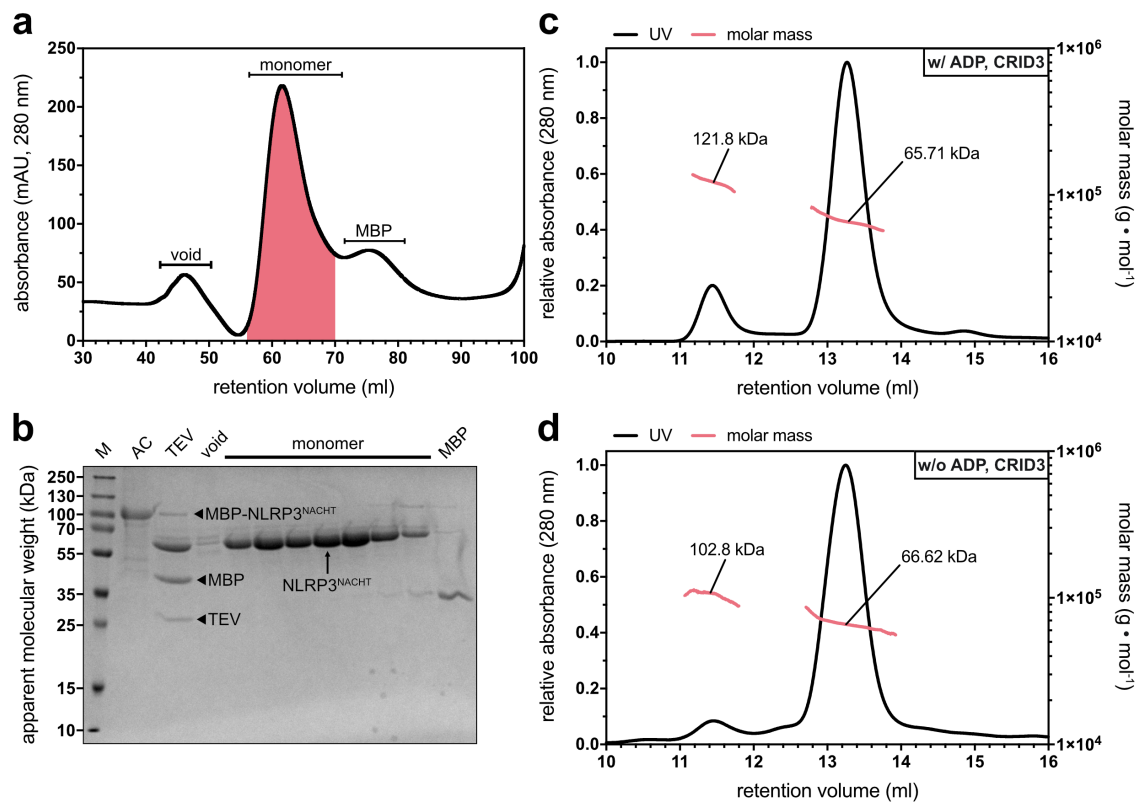
compounds inspired by CRID3 have recently progressed into clinical trials as bona fide NLRP3 inhibiting drugs (El-Sharkawy et al., 2020; Schwaid & Spencer, 2021).

This part of the thesis provides biochemical and structural data about the mode of action of the NLRP3-specific inhibitor CRID3. I show that CRID3 binds the NLRP3 NACHT domain with high affinity, thereby stabilizing a ‘closed’ conformation, which inhibits ATP hydrolysis and inflammasome activation. Determination of a high-resolution crystal structure of the NLRP3-CRID3 complex allows for detailed analysis of the CRID3 binding site and inhibition specificity. The hexahydro-*s*-indacene moiety of CRID3 is incorporated in a hydrophobic cluster formed by four subdomains of the NLRP3 NACHT domain and the transition LRR. Additionally, the central sulfonylurea group of CRID3 interacts with the Walker A motif of the NLRP3 NBD and is sandwiched between two opposing arginines from the NBD and HD2, respectively. Finally, the tertiary alcohol group forms hydrogen bond interactions with a water molecule and residues of HD2. In this way, CRID3 acts like a doorstop that is glued between four subdomains of the NLRP3 NACHT domain and the transition LRR, thereby locking NLRP3 in the inactive conformation. These findings show a prototypic example for direct inflammasome inhibition, which paves the way for the development of more advanced inhibitors not only of NLRP3 but also of related family members that share a similar mode of activation.

#### **4.1.1 Purification of recombinant human NLRP3<sup>NACHT</sup> protein**

For structural studies, recombinant human NLRP3 (aa 131-694, referred to as NLRP3<sup>NACHT</sup>) was expressed as MBP-fusion protein in the *Sf9* insect cell system. The protein was purified to homogeneity by affinity chromatography, subsequent tag cleavage, and size-exclusion chromatography in the presence of CRID3 but otherwise identical conditions as described above for cleaved NLRP12<sup>NACHT</sup> protein. A representative chromatogram of the SEC run after AC and tag cleavage is shown in Figure 4-1a. The majority of the protein eluted as one peak at around 62 ml, corresponding to a retention volume expected for an approximately 65 kDa protein on this particular type of column. Other fractions contained oligomeric or aggregated species (void) and unbound MBP. Using SDS-PAGE analysis, the identity of the central peak could be confirmed as tag-cleaved NLRP3<sup>NACHT</sup> and the purity of the protein was determined to be of crystallization-grade quality (Figure 4-1b). To validate the monomeric state of NLRP3<sup>NACHT</sup>, the protein was concentrated to ~10 mg·ml<sup>-1</sup> and subsequently

characterized using SEC-MALS analysis (Figure 4-1c). Similar with NLRP12<sup>NACHT</sup> (Figure 3-18d), the protein eluted as one major peak with a smaller second peak to the left and the molecular weight of the species was determined as 65.71 kDa and 121.8 kDa, respectively. Since NLRP3<sup>NACHT</sup> has a theoretical mass of 65.9 kDa, the identified species correspond well to a monomer and dimer. To enable also biochemical characterization of CRID3 binding, NLRP3<sup>NACHT</sup> was purified in the absence of ADP and CRID3. Interestingly, peak fractions could only be concentrated to  $\sim 1 \text{ mg} \cdot \text{ml}^{-1}$ , indicating reduced protein stability and solubility, compared to the much better behaved NLRP3<sup>NACHT</sup> that was purified in the presence of ADP and CRID3. However, SEC-MALS experiments showed that monomers of both proteins are equally stable (Figure 4-1d).

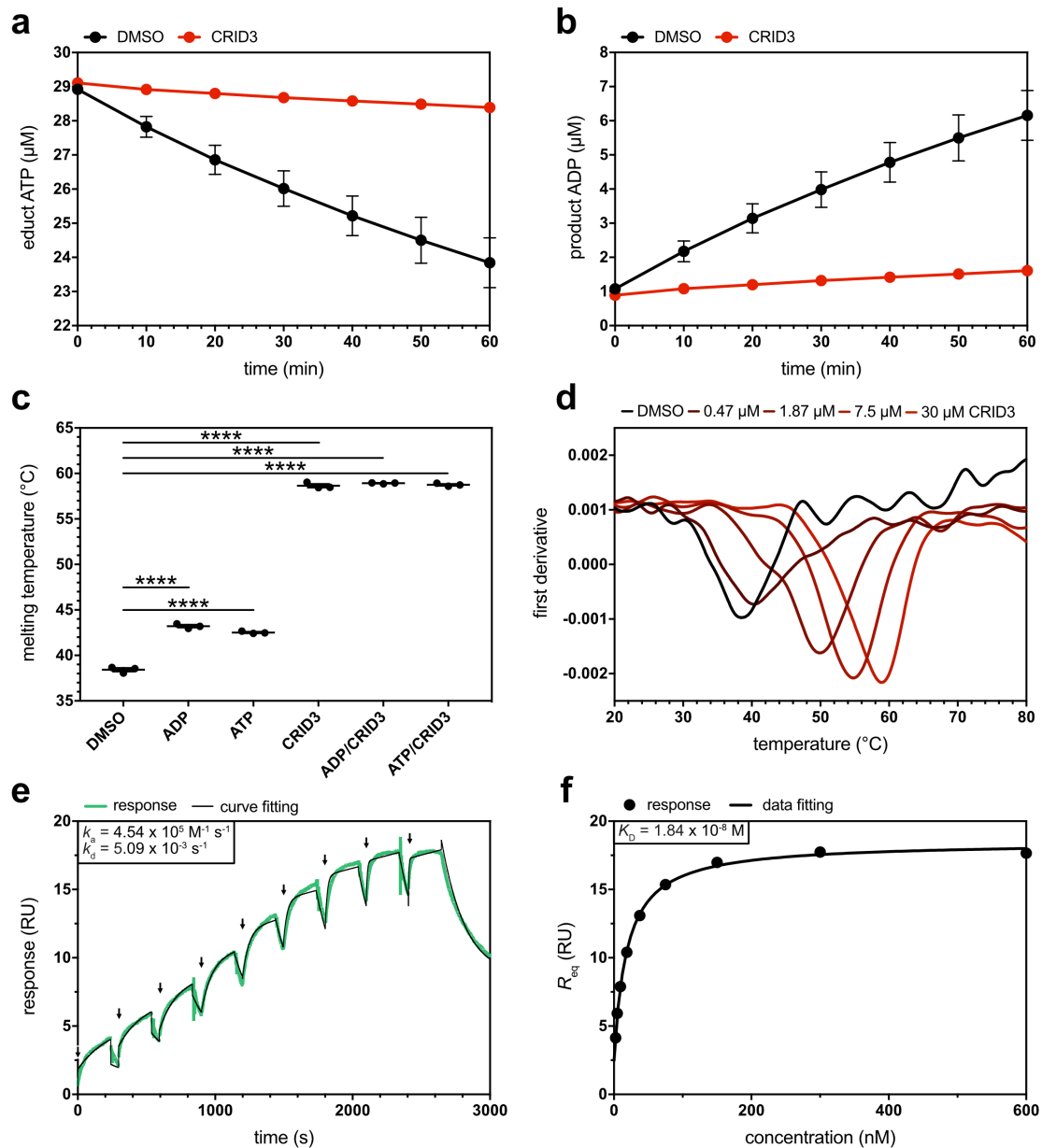


**Figure 4-1: Purification of NLRP3<sup>NACHT</sup>.** (a) Representative chromatogram of NLRP3<sup>NACHT</sup> injected onto a Superdex 75 PG 16/600 size-exclusion column after affinity purification and tag cleavage. Elution of protein was followed via the absorbance at 280 nm wavelength. The red area indicates pooled fractions of the monomeric peak. (b) Coomassie-stained samples from different steps of the purification process and fractions from (a) after reducing SDS-PAGE. M: marker, AC: affinity chromatography, TEV: tag cleavage using TEV protease. The technical assistant Julia Hockling was involved in the expression and purification of NLRP3 protein. (c, d) Elution profile from analytical gel filtration of 50  $\mu\text{g}$  monomeric NLRP3<sup>NACHT</sup> injected onto a Superdex 200 Increase 10/300 GL column and corresponding molar mass as determined by multi angle light scattering (MALS). NLRP3<sup>NACHT</sup> was purified in the (c) presence or (d) absence of the ADP and CRID3 ligands prior to MALS analysis.

#### 4.1.2 Biochemical characterization of CRID3 binding

To find out whether the NLRP3<sup>NACHT</sup> construct is capable of interacting with CRID3, different binding experiments have been performed. It has already been proposed that CRID3 might block enzymatic activity of NLRP3 (Coll et al., 2019). Thus, ATPase activity of monomeric NLRP3<sup>NACHT</sup> protein was investigated as a potential readout for CRID3 binding. NLRP3<sup>NACHT</sup> was found to hydrolyze ATP with a turnover rate of  $\sim 0.03 \text{ min}^{-1}$  and this activity was indeed almost abrogated in the presence of CRID3 (Figure 4-2a, b). Also, thermal stability of NLRP3<sup>NACHT</sup> in the presence of nucleotides and CRID3 was analyzed. As depicted in Figure 4-2c, the presence of CRID3 resulted in a tremendous stabilization of NLRP3<sup>NACHT</sup> protein ( $\Delta T_M = 20.2^\circ\text{C}$ ). Importantly, this effect was found to be dose-dependent and therefore likely specific for the protein-compound interaction (Figure 4-2d). NLRP3 is also significantly stabilized in the presence of the nucleotides ADP ( $\Delta T_M = 4.8^\circ\text{C}$ ) or ATP ( $\Delta T_M = 4.1^\circ\text{C}$ ) but interestingly, presence of both CRID3 and nucleotides did not result in additive stabilization ( $\Delta T_M = 20.5^\circ\text{C}$  and  $20.3^\circ\text{C}$ , Figure 4-2c). This suggests that CRID3 binding might lock NLRP3 in an inactive conformation that is not affected by nucleotide binding or even renders the nucleotide binding site as inaccessible.

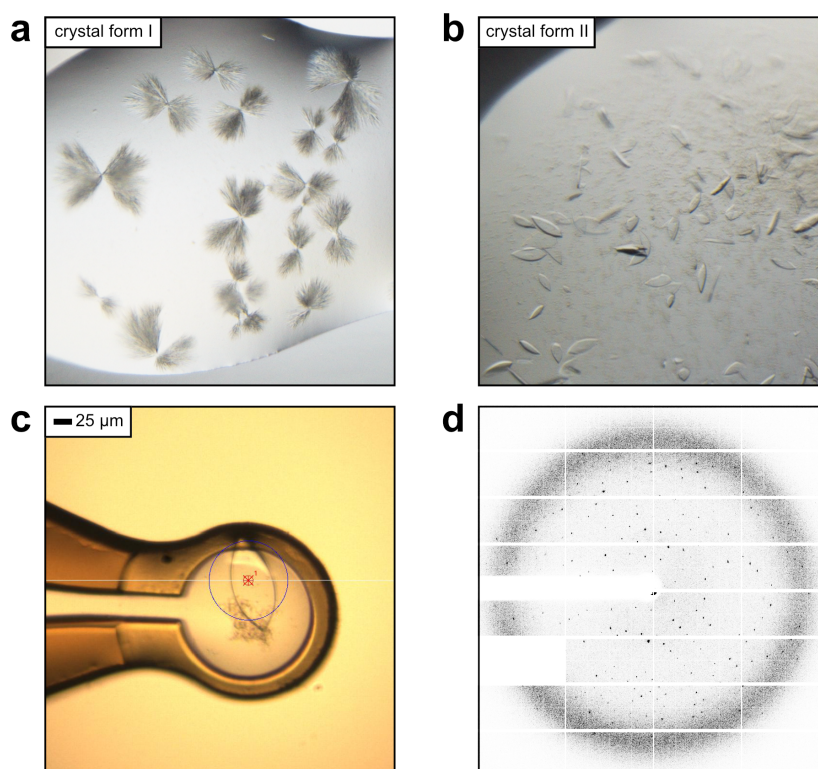
To finally determine the kinetics and affinity of CRID3 binding, the interaction was studied using SPR spectroscopy (Figure 4-2e, f). For this purpose, human NLRP3<sup>NACHT</sup> (aa 131-694) was expressed as N-terminal Avi- and Flag-tagged fusion protein in HEK293T cells. The protein was biotinylated intracellularly by co-transfection of BirA, purified via the Flag tag, and finally bound to a streptavidin-functionalized SPR sensor chip (methods section). Importantly, CRID3 specifically bound to NLRP3<sup>NACHT</sup> with rather slow kinetics and high affinity in the nanomolar range. Using a 1:1 binding model, the second-order association constant ( $k_a$ ), the first-order dissociation constant ( $k_d$ ), and the equilibrium dissociation constant ( $K_D$ ) were determined to be  $4.54 \times 10^5 \text{ M}^{-1} \text{ s}^{-1}$ ,  $5.09 \times 10^{-3} \text{ s}^{-1}$ , and  $1.84 \times 10^{-8} \text{ M}$ , respectively. Saturation of the available CRID3 binding sites was reached with concentrations  $>150 \text{ nM}$ , resulting in a reasonable response unit level of  $\sim 17 \text{ RU}$  (Figure 4-2e). Importantly, this rules out the chance of unspecific binding of CRID3 and therefore confirms its specificity. Taken together, CRID3 specifically binds to and stabilizes a monomer of the NLRP3 NACHT domain, which prevents its hydrolysis activity and activation into a signaling competent state.



**Figure 4-2: Binding study of the inhibitor CRID3 to NLRP3.** (a, b) Hydrolysis assay based on ion-pairing reverse phase HPLC. 3  $\mu\text{M}$  of NLRP3<sup>NACHT</sup> was incubated with 30  $\mu\text{M}$  ATP in the presence of 2% DMSO or 30  $\mu\text{M}$  CRID3 at 25°C. MgCl<sub>2</sub> was already included in the purification buffer. Every 10 minutes a sample was injected onto a Chromolith Performance RP-18 HPLC column and elution of nucleotides was followed via the absorbance at 259 nm wavelength. The area under the curve was used to calculate the peak ratios and subsequently estimate the concentration of (a) ATP and (b) ADP as the educt and product of the enzymatic reaction. Data points are mean  $\pm$  SEM of three independent experiments. (c) Thermal shift assay of 3  $\mu\text{M}$  NLRP3<sup>NACHT</sup> in the presence of 2% DMSO or 30  $\mu\text{M}$  ligands ADP, ATP, and CRID3. The measurement was setup with a temperature ramp ranging from 15-95°C, a slope of 1.5°C·min<sup>-1</sup>, and a 90% laser intensity. Data points are representative of three independent experiments.  $n = 3 \pm \text{SEM}$ ; \*\*\*\*  $P \leq 0.0001$  (two-way ANOVA followed by the Dunnett's multiple comparisons test). (d) Thermal shift assay of 3  $\mu\text{M}$  NLRP3<sup>NACHT</sup> in the presence of 2% DMSO or different concentrations of CRID3. NLRP3 is stabilized in a dose-dependent manner. Data is representative of three independent experiments. (e) Sensorgram following the specific binding of CRID3 to NLRP3<sup>NACHT</sup> as measured by SPR. Arrows indicate injections of 2.34, 4.68, 9.37, 18.75, 37.5, 75, 150, 300, and 600 nM CRID3, respectively. The second-order association constant ( $k_a$ ) and first-order dissociation constant ( $k_d$ ) were calculated from a 1:1 binding model. (f) For steady state analysis, the response in equilibrium ( $R_{\text{eq}}$ ) was determined from (e) and plotted versus the analyte concentration. The equilibrium dissociation constant ( $K_D$ ) was calculated from a binding model.

#### 4.1.3 Determination of an X-ray crystal structure of NLRP3 in complex with CRID3

To investigate the NLRP3-CRID3 complex at the molecular level, the recombinant protein that was purified in the presence of CRID3 was subjected to crystallization trials for the determination of a high-resolution X-ray crystal structure. Interestingly, intensive screening for successful crystallization conditions revealed two different crystal forms of the NLRP3-CRID3 complex. The first crystal form represents needle clusters that could be optimized in size by specific concentration of sodium ions (Figure 4-3a). But however, these crystals showed only poor diffraction. In contrast, a second crystal form representing plates with scalpel-like morphology showed high-resolution diffraction (Figure 4-3b). After optimization of the crystallization conditions, the final crystal appeared in 0.1 M MES pH 6.5, 0.19 M calcium chloride, 28% (w/v) PEG400 and was measured using the P13 beamline of the Deutsches Elektronen Synchrotron (DESY) located in Hamburg (Figure 4-3c).



**Figure 4-3: Crystal forms and diffraction image of human NLRP3<sup>NACHT</sup> protein.** (a, b) Representative crystals of NLRP3<sup>NACHT</sup> in the presence of CRID3 appeared in two different sets of optimization conditions. Crystal form I represents needle clusters with poor diffraction. Crystal form II represents scalpel-formed single crystals with high-resolution diffraction. (c) Final crystal of NLRP3<sup>NACHT</sup> just before measurement at the synchrotron. The red cross and blue circle represent the beam position and its approximate diameter, respectively. (d) Diffraction image of NLRP3<sup>NACHT</sup> with single spots that diffracted higher than 2.48 Å resolution. Data collection and processing was supervised by Dr. Gregor Hagelüken (University of Bonn).

The recorded diffraction images revealed single spots with a resolution higher than 2.48 Å and a diffraction pattern clearly evidencing protein crystals (Figure 4-3d). Consequently, the dataset could be successfully processed in space group C 1 2 1 at a final resolution of 2.48 Å (Table 4-1). Initial phases were obtained by molecular replacement using the coordinates of NLRP3 from the NLRP3-NEK7 cryo-EM structure (PDB: 6NPY, aa 134-694) as a search model. As the C-terminal section of the cryo-EM structure showed clear discrepancy with the calculated electron density map, model building of this part of NLRP3 was guided by the AlphaFold2 structure prediction (Jumper et al., 2021). Finally, the model of NLRP3 could be built as a continuous chain spanning residues 134-679 with the exception of seven disordered loop regions (151-164, 177-200, 213-218, 452-462, 513-515, 540-553, 620-622) and was refined to  $R_{\text{work}}$  of 20.96% and  $R_{\text{free}}$  of 23.68% with excellent stereochemistry (Table 4-1, Figure 4-4). Additional details of the data collection, quality, and refinement statistics are shown in Table 4-1.

The central NLRP3 NOD module classifies in the NACHT clade within the STAND ATPase family (Danot et al., 2009; Leipe et al., 2004). As such it contains a P-loop nucleotide binding domain (NBD, aa 218-371) that is extended by a helical lid domain (HD1, aa 372-433) and the regulatory winged helix domain (WHD, aa 434-540). The NOD module is followed by a structural spacer element (HD2, aa 541-648) and the C-terminal LRR domain, which can be divided in a transition (trLRR) and a canonical (cnLRR) segment (Figure 4-4a). In NLRP3, the NBD is made from the classical five-stranded  $\alpha$ - $\beta$ - $\alpha$  Rossmann-like fold with the exception of two antiparallel beta strands formed by residues 269-271 and 325-327 (Figure 4-4b). In contrast to other STAND ATPases, the NLRP3 NBD does not contain the conserved hhGRExE motif that is typically found in a region that precedes the first beta strand (roughly 25-30 residues upstream of Walker A) and interacts with the adenine moiety of the nucleotide (Danot et al., 2009; Leipe et al., 2004). Instead, NLRP3 contains an N-terminal FISNA domain (aa 131-217) that docks on the last beta strand of the NBD by forming an antiparallel beta sheet with residues 172-175 (Figure 4-4b). Additionally, a solvent exposed polybasic cluster is included in a helix (aa 136-147) that is stabilized on the NBD by multiple hydrophobic interactions (Figure 4-4a, b, Figure 4-9a). The activation loop that harbors the tandem SP<sub>198</sub>-SP<sub>201</sub> phosphorylation motif, which is an essential regulatory element during priming (Paik et al., 2021), is intrinsically disordered and therefore not resolved in the structure (Figure 4-4b).



**Table 4-1: Crystallographic data collection and refinement statistics of NLRP3<sup>NACHT</sup>**

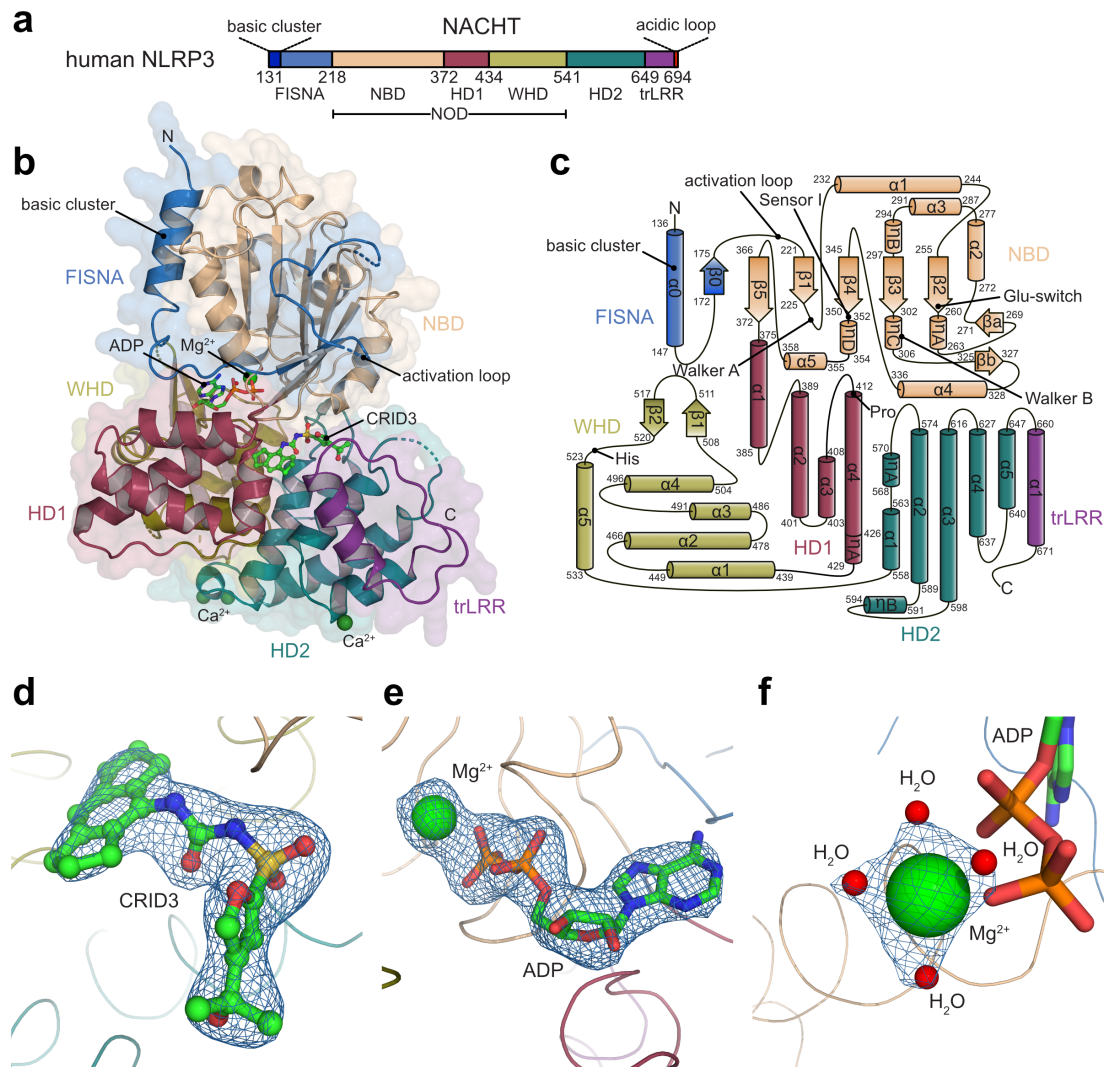
Data collection	
Space group	C 1 2 1
<i>a</i> , <i>b</i> , <i>c</i> (Å)	107.09, 100.25, 62.66
$\alpha$ , $\beta$ , $\gamma$ (°)	90.00, 105.25, 90.00
Resolution (Å) <sup>a</sup>	42.60-2.48 (2.57-2.48)
<i>R</i> <sub>merge</sub> (%)	9.76 (168.50)
<i>I</i> / $\sigma$ ( <i>I</i> )	9.96 (0.89)
Completeness (%)	99.65 (98.63)
CC <sub>1/2</sub>	0.998 (0.568)
CC*	1.000 (0.851)
Redundancy	6.8 (6.8)
Refinement	
Resolution (Å)	42.60-2.48
Number of reflections	22 625
<i>R</i> <sub>work</sub> / <i>R</i> <sub>free</sub> <sup>b</sup>	0.210/0.237
Number of atoms	
Protein	3895
Ligands	59
Water	30
<i>B</i> factors	
Protein	100.90
Ligands	77.34
Water	74.23
RMSD	
Bond lengths (Å)	0.003
Bond angles (°)	0.61
Residues in Ramachandran	
Favored regions (%)	98.24
Allowed regions (%)	1.76
More quality parameters	
Rotamer outliers (%)	0.23
Clashscore	5.70
MolProbity Score	1.31
PDB	
Accession number	unpublished

<sup>a</sup> Values in parentheses are for the highest resolution shell.

<sup>b</sup> *R*<sub>free</sub> value is equivalent to the *R* value but is calculated for 7.81% of the reflections chosen at random and omitted from the refinement process.

Ensuing the NBD, HD1 is packed as a four helical bundle, whereas the WHD is packed as five winged helices and two short antiparallel beta strands (aa 508-511 and aa 517-520) that form a beta sheet between the second and third helix (Figure 4-4b). Resembling a ‘crab claw’ (Danot et al., 2009), the WHD folds back towards the nucleotide binding site (Figure 4-4b). As a consequence, NLRP3 adopts a conformation where the nucleotide is deeply buried within the protein and likely nonexchangeable. Finally, HD2 forms a seven

helical bundle that contains three crystallographic calcium ion binding sites and connects the NOD module with the C-terminal LRR domain (Figure 4-4b). A detailed topology map of human NLRP3 (aa 134-679) is given in Figure 4-4c.

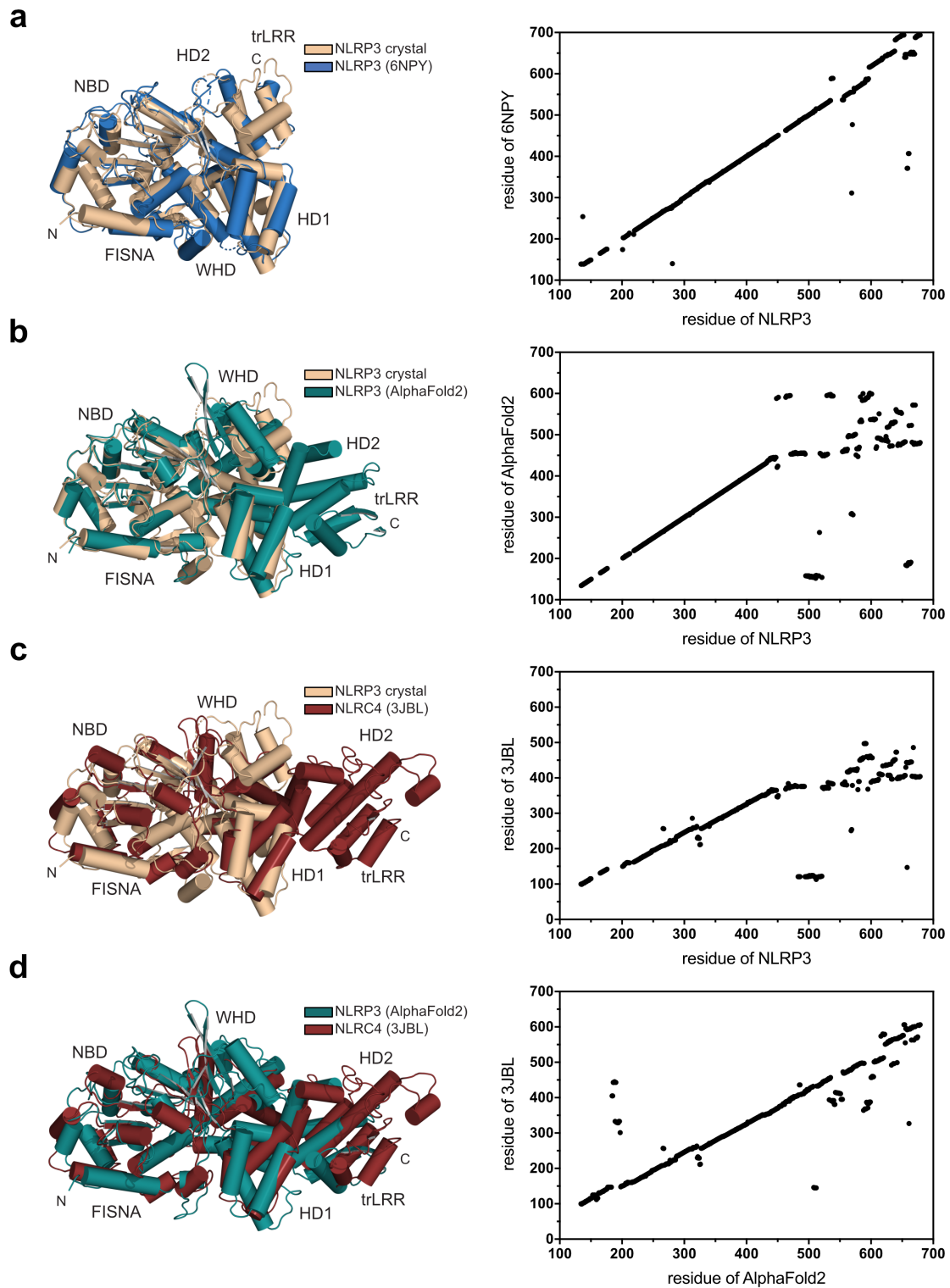


**Figure 4-4: High-resolution crystal structure of the NLRP3-CRID3 complex.** (a) Domain composition of human NLRP3 (aa 131-694) with domain boundaries indicated. The basic cluster (aa 131-147) and the acidic loop (aa 689-702) are drawn as blue and red bars, respectively. (b) Cartoon and transparent surface representation of the NLRP3-CRID3 complex as determined from the crystal structure at 2.48 Å resolution. Disordered regions are shown as dashed lines. ADP is shown in stick representation and with carbons colored green. CRID3 is shown in stick-and-balls representation and with carbons colored green. Ions are shown as green spheres. Water molecules are shown as red spheres. Different domains are color-coded as in (a) and labelled accordingly. The basic cluster and the activation loop are additionally labelled. (c) Topology map of human NLRP3 (aa 134-679) color-coded as in (a) and labelled accordingly. Positions of the basic cluster, the activation loop, the Walker A and Walker B sites, the glutamate switch, the sensor I, and the conserved proline and histidine residues of NLRP3 are additionally labelled.  $\alpha$ : alpha-helix,  $\eta$ :  $3_{10}$ -helix,  $\beta$ : beta-strand. (d-f) Differential electron density ( $F_o - F_c$ , simulated annealing-omit map) of (d) CRID3, (e) ADP·Mg<sup>2+</sup>, and (f) water molecules complexing the magnesium ion displayed at  $\pm 4\sigma$  contour level.

Importantly, the ligand binding sites for CRID3 and ADP·Mg<sup>2+</sup> were well resolved by the high-resolution structural data and could be unambiguously identified in the difference electron density map (Figure 4-4d, e). Moreover, even four coordinated water molecules could be identified after the placement of the magnesium ion (Figure 4-4f). Apart from the relevance of the CRID3 binding site, this is to my knowledge the first study of an NLR family protein to include structural data on the catalytic magnesium ion, which will provide detailed insights for advanced mechanistic understanding of the ATPase function in inflammasomes and future development of better pharmacological inhibitors.

#### **4.1.4 The NLRP3 NACHT domain adopts a ‘closed’ and inactive state**

To determine whether NLRP3 is in the active or inactive state, the overall conformation of the subdomains was investigated. For this purpose, the model was first compared with the cryo-EM structure of inactive NLRP3 (PDB: 6NPY) that was used for the initial molecular replacement (Figure 4-5a). Both structures follow the same overall arrangement of secondary structure elements but with slightly different assignment of the amino acid register especially in the C-terminal section. As already stated before, the C-terminal section of the cryo-EM structure did not match with the electron density map that was calculated from the diffraction data and thus this part of the model had to be rebuilt. It is likely that due to the lower resolution of the cryo-EM structure some loops have been assigned incorrectly, which explains the observed shifts in the amino acid register. The NLRP3 crystal structure was also compared with a prediction performed by the recently released AlphaFold2 server (Jumper et al., 2021). Interestingly, AlphaFold2 predicted a different conformation of NLRP3 with a ~90 ° rotation between the HD1 and WHD domains relative to the crystal structure (Figure 4-5b). This conformational difference is in line with the transition of STAND ATPases from an inactive to an active state (Danot et al., 2009; Sandall et al., 2020). Indeed, subunits of an active mouse NLRC4 oligomer (PDB: 3JBL, (Zhang et al., 2015)) show a similar ‘open’ conformation as the AlphaFold2 prediction of NLRP3 (Figure 4-5c, d). Overall, this leads to the conclusion that the crystal structure of NLRP3 represents a ‘closed’ and most likely inactive state.



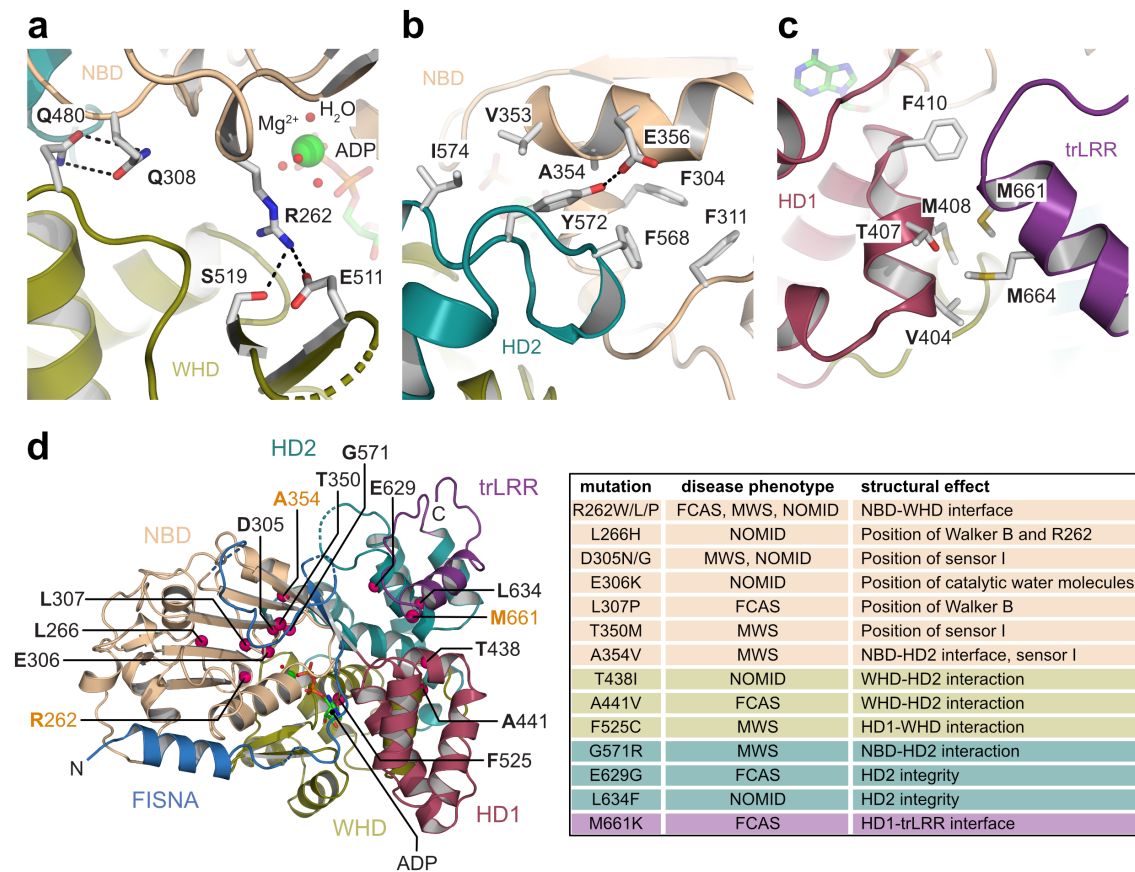
**Figure 4-5: Conformation of the NLRP3-CRID3 complex.** The left panels show overlaid cartoon representations of the NLRP3 crystal structure (residues 134-679), the cryo-electron microscopy structure of inactive NLRP3 (PDB: 6NPY, residues 139-694), one subunit from the cryo-electron microscopy structure of an active NLRC4 inflammasome (PDB: 3JBL, residues 99-612) and a prediction of NLRP3 (residues 134-679) performed by the AlphaFold2 server (Jumper et al., 2021). The respective FISNA-NBD-HD1 regions have been aligned. Helices are shown as cylinders. In the right panels each residue in the reference molecule (x-axis) is plotted versus the nearest residue of the aligned molecule (y-axis). A straight line with a 45° angle indicates overall conformational similarity, whereas spreading indicates for a distinct conformation. Shifts in the line correspond to differences in the amino acid register, which indicate e.g., shorter or longer loop regions.

#### 4.1.5 CAPS mutants disrupt interdomain interactions that stabilize the inactive state

Knowing that the NLRP3 crystal structure represents a ‘closed’ conformation, the cryo-EM structure of active mouse NLRC4 (PDB: 3JBL) and the NLRP3 structure prediction from AlphaFold2 can be used to model the transition from the ‘closed’ and inactive to the ‘open’ and active conformation. Such transition model then allows to determine intramolecular interdomain interactions that stabilize both states. In this way, three interfaces could be identified in NLRP3 that are established in the inactive state and need to be resolved during activation (Figure 4-6a-c). The first interface is formed between the NBD and the WHD of NLRP3 (Figure 4-6a). Unfortunately, the sidechain of Glu511 (WHD) is not well resolved in the electron density map but its position fits well to form a salt bridge with the adjacent Arg262 (NBD). Alternatively, the oxygen atom of Ser519 (WHD) could serve as a hydrogen bond acceptor for the arginine residue. Furthermore, residues Gln308 and Gln480 (Figure 4-6a), as well as the conserved His522 and the  $\beta$ -phosphate of ADP, form additional hydrogen bonds interconnecting the WHD with the NBD and the HD1 (Figure 4-9c). A second interface is predominantly formed by hydrophobic and van der Waals interactions between Phe304, Phe311, Val353, Ala354, and Glu356 of the NBD and Phe568, Tyr572, and Ile574 of the HD2. Residues Glu356 and Tyr572 form an additional hydrogen bond interaction that further stabilizes this interface (Figure 4-6b). The third interface is established between the NACHT and the LRR domain and is composed of hydrophobic interactions between Val404, Thr407, Met408, and Phe410 of the HD1 and Met661 and Met664 of the transition LRR segment (Figure 4-6c).

Over the past decade, numerous gain-of-function mutations in NLRP3 have been identified in patients with cryopyrin-associated periodic syndromes (CAPS), which subsume a spectrum of autoinflammatory phenotypes and clinical features (Booshehri & Hoffman, 2019). While the mechanisms leading to CAPS are not completely understood, it is well established that NLRP3 becomes hyperactive and participates in inflammasome formation that is independent from ligand sensing (signal II), which in turn results in elevated levels of pro-inflammatory cytokines together with systemic and tissue inflammation (Booshehri & Hoffman, 2019). Interestingly, by mapping all verified and pathogenic mutations on the NLRP3 crystal structure it becomes apparent that almost all mutation sites cluster at least close to one of the three interdomain interfaces or the nucleotide binding site, thus likely destabilizing the autoinhibited conformation (Figure 4-6d). Indeed, three mutation sites – Arg262, Ala354, and Met661 – are even directly

involved in interface formation, thereby validating their importance for stabilizing the subdomain assembly in the inactive state. A list of all validated and pathogenic mutation sites in the NLRP3 NACHT domain as well as their potential effects is given in the right panel of Figure 4-6d.

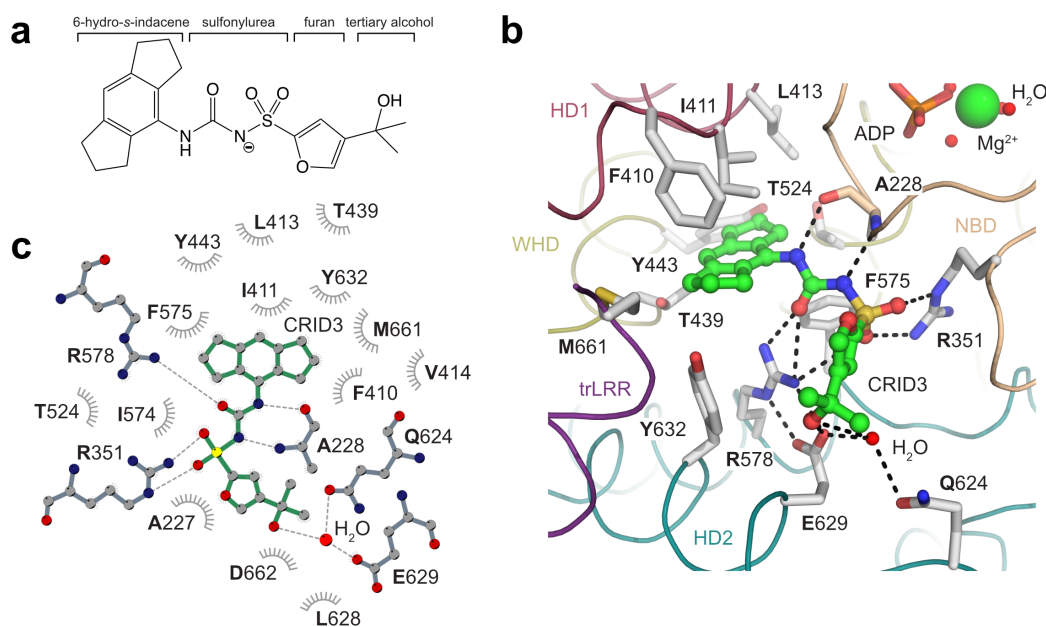


**Figure 4-6: Interdomain interactions and CAPS mutants in the NLRP3 NACHT domain.** (a-c) Detailed view on the molecular interactions that stabilize the inactive state of NLRP3. Hydrogen bond interactions are shown as dashed black lines. (d) Cartoon representation of NLRP3 as determined from the crystal structure (left panel). Domains are color-coded as in Figure 4-4a and residues that have been verified to be mutated in patients with CAPS are depicted as pink spheres and labelled accordingly. Residues that are also essential for interdomain interactions are highlighted in orange letters. The table (right panel) summarizes pathogenic mutations and their potential structural effects based on the NLRP3 structure. Mutation sites are taken from the Infervers database (Van Gijn et al., 2018). CAPS: cryopyrin-associated periodic syndrome, CINCA: chronic infantile neurological cutaneous articular syndrome, FCAS: familial cold autoinflammatory syndrome, NOMID: neonatal-onset multisystem inflammatory disorder, MWS: Muckle-Wells syndrome.

#### 4.1.6 Molecular analysis of the CRID3 binding site

In line with its high affinity and tremendous stabilizing effect (Figure 4-2), CRID3 was found to bind into a cleft in NLRP3 located on the backside of the Walker A motif and formed by four subdomains of the NACHT domain and the transition LRR (Figure 4-4b). Importantly, high resolution structural data allowed for unambiguous identification of the

CRID3 binding pose (Figure 4-4d), which enabled detailed molecular analysis of the binding interface with a buried surface area of 552 Å<sup>2</sup> as determined by PDBePISA (Krissinel & Henrick, 2007) (Figure 4-7a, b). It was found that the hexahydro-*s*-indacene moiety interacts with the sidechain of the superjacent Ile411 and thereby integrates into a surrounding hydrophobic cluster that is formed by residues Met408, Phe410, Ile411, and Leu413 of the HD1, Thr439, Tyr443, and Thr525 of the WHD, Phe575 and Tyr632 of the HD2, and Met661 of the trLRR domain. The central sulfonylurea group is sandwiched between Ala228 (mainchain) and Arg351 of the NBD and Arg578 of the HD2 by forming hydrogen bond interactions. Residue Arg578 is further stabilized by a salt bridge with Glu629. Finally, residues Gln624 and Glu629 of the NLRP3 HD2 domain were identified to participate in hydrogen bonding with a water molecule and the tertiary alcohol group of CRID3, resulting in a specific configuration of Pro625. It is noteworthy that no polar interaction with the oxygen atom of the furan moiety in CRID3 was identified within a distance shell of 4.2 Å, but Ala227 of Walker A could be involved in hydrophobic interactions since no solvent molecules are present in between. A simplified view on the molecular interactions of CRID3 with NLRP3 is given in Figure 4-7c.



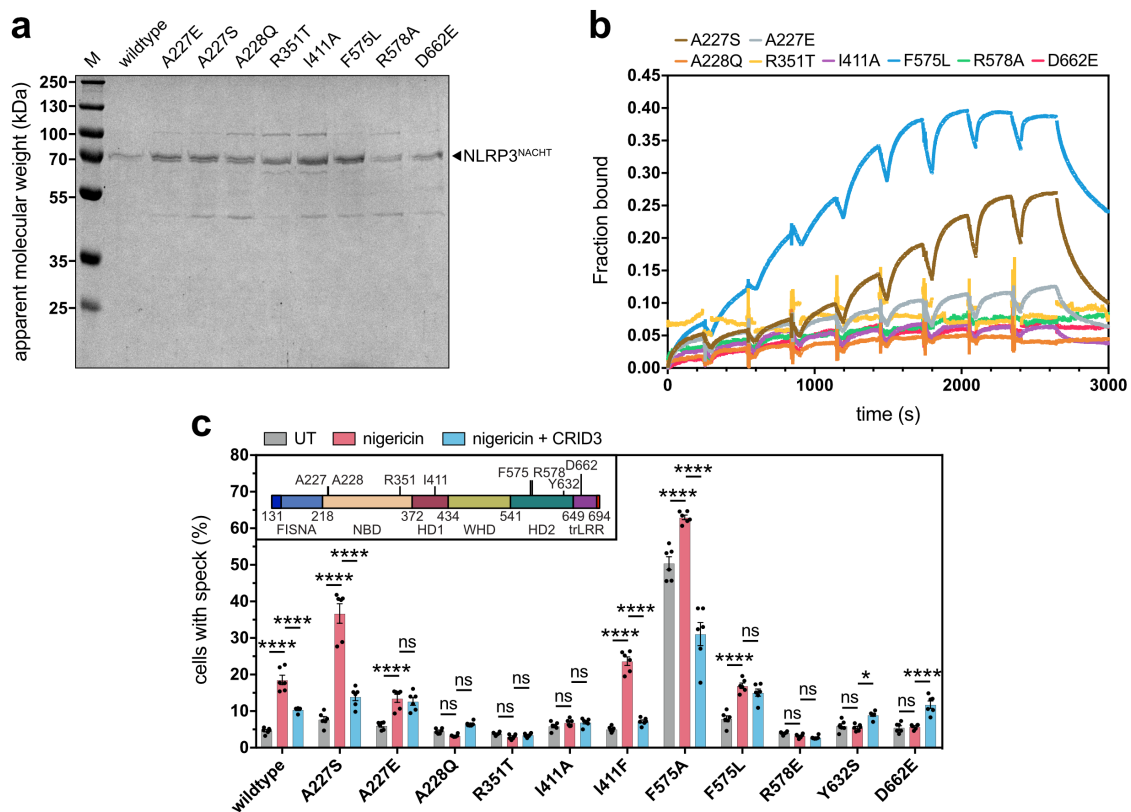
**Figure 4-7: The CRID3 binding site in NLRP3.** (a) Structural formula of CRID3 with deprotonated nitrogen (at neutral pH; pK<sub>a</sub> value of 4.74) and depiction of the different moieties. (b) Detailed view on important molecular interactions of NLRP3 with CRID3. Important mainchains and sidechains are shown as sticks. CRID3 is shown in stick-and-balls representation and with carbons colored green. The magnesium ion is shown as a green sphere. Water molecules are shown as red spheres. Hydrogen bond interactions are shown as dashed black lines. (c) Simplified view on the molecular interactions of NLRP3 with CRID3 generated with LigPlot+ (Laskowski & Swindells, 2011).

To confirm these findings, variants of NLRP3 with an exchange of key residues in the CRID3 binding site have been generated by site-directed mutagenesis. Mutants of human NLRP3<sup>NACHT</sup> (aa 131-694) were expressed as N-terminal Avi- and Flag-tagged fusion protein in HEK293T cells. Similar with wildtype protein, the NLRP3 mutants were biotinylated intracellularly by co-transfection of BirA, purified via the Flag tag, and finally bound to a streptavidin-functionalized SPR sensor chip (methods section, Figure 4-8a). Using SPR spectroscopy, it was found that CRID3 binds to wildtype NLRP3 with high affinity (Figure 4-2e, f), whereas binding to variants affecting hydrogen bonding with the sulfonyleurea group (A228Q, R351T, and R578A) or the CH- $\pi$  interaction with the hexahydro-*s*-indacene moiety (I411A) was completely abrogated (Figure 4-8b). Mutations A227E and D662E did also significantly decrease the affinity to CRID3 (Figure 4-8b). This is most likely due to steric occupation of the binding site and the CRID3 entry vector in NLRP3. However, mild substitutions, such as A227S or F575L, did not decrease binding of CRID3 to NLRP3 (Figure 4-8b), thereby being proof for the ability to generate non-destructive variants of the CRID3 binding interface.

Next, the capability of CRID3 to inhibit NLRP3 activation and inflammasome formation has been determined in cells. For this purpose, HEK293T cells stably expressing low levels of ASC-BFP have been transfected with variants of full-length NLRP3, treated with the ionophore nigericin plus-minus CRID3, and subsequently analyzed using the time-of-flight inflammasome activation method (TOFIE, (Sester et al., 2015)). As a control, cells have been transfected with wildtype NLRP3 and probed for its activation and inhibition capabilities. A basal fraction of specking cells could already be detected in the absence of an inducer but nigericin treatment resulted in a significant increase in this fraction, whereas presence of CRID3 prevented NLRP3 inflammasome activation (Figure 4-8c). Similar results were obtained when the NLRP3 variants A227S or I411F have been transfected, demonstrating that these mutants do not disrupt the CRID3 binding site in NLRP3 (Figure 4-8c). Besides, treatment of the A227S variant with nigericin induced the formation of a larger fraction of specking cells as if compared with the I411F variant or the wildtype control, suggesting that this mutation renders NLRP3 to be activated more easily (Figure 4-8c). Importantly, transfection of the A227E and F575L variants also resulted in cells responding to nigericin treatment, but NLRP3 activation could no longer be inhibited by CRID3 (Figure 4-8c). This result indicates that the integrity of residues A227 and F575 in NLRP3 is essential for the ability of CRID3 to bind to its target site and inhibit NLRP3 activation. However, inability of CRID3 to



inhibit the F575L variant is puzzling, since high affinity binding could clearly be observed in the SPR approach (Figure 4-8b). In contrast to the F575L mutant, transfection of another variant, F575A, did result in autoactivation of NLRP3. But still, the fraction of active NLRP3 was enlarged with nigericin treatment and well responsive to inhibition with CRID3 (Figure 4-8c), which is more in line with the SPR data (Figure 4-8b). An explanation for the discrepancy between the data obtained with the F575L variant in the SPR approach and in the cellular assay is pending at the time of writing. Interestingly, most other variants tested were insensitive to activation with nigericin or even activated in the presence of CRID3 (Figure 4-8c), which leads to the conclusion that the integrity of this cleft in NLRP3 is essential not only for CRID3 binding but also for the mode of action of NLRP3 and inflammasome activation.

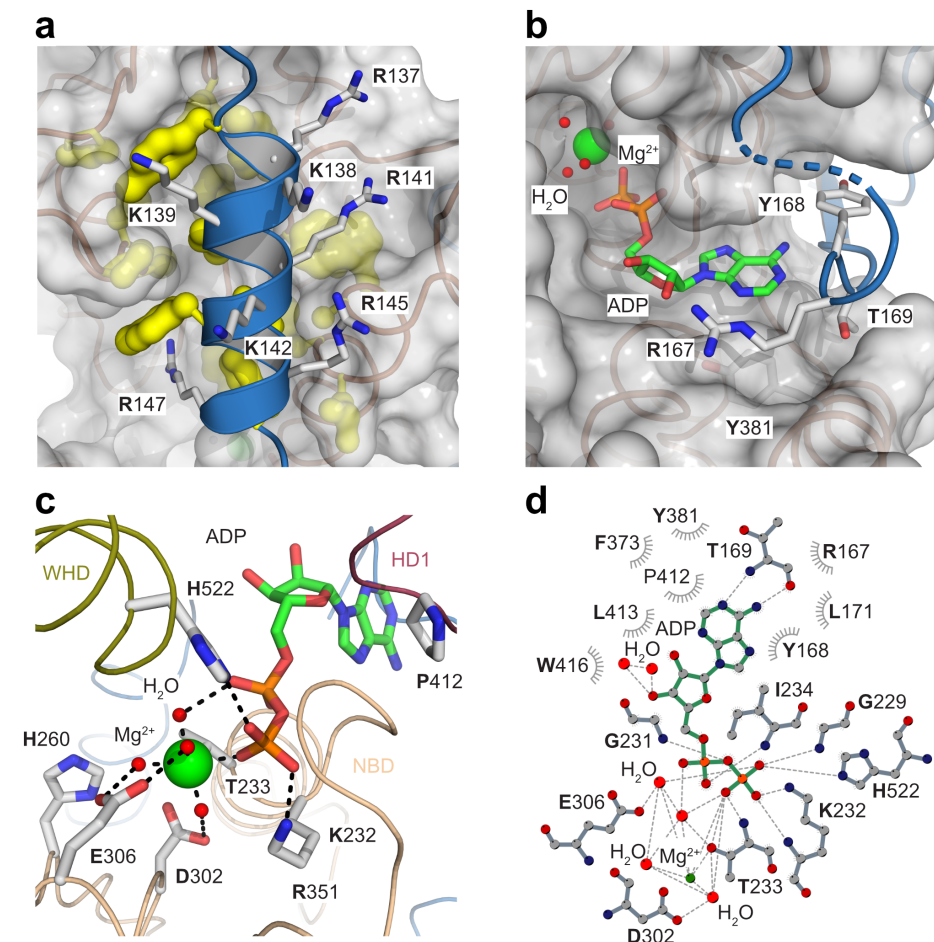


**Figure 4-8: Mutational study on the CRID3 binding site in NLRP3.** (a) Coomassie-stained samples of wildtype and mutant NLRP3<sup>NACHT</sup> protein after reducing SDS-PAGE. The protein samples were used for the SPR spectroscopy approach. M: marker. (b) Sensorgrams following the specific binding of CRID3 to site-directed mutants of NLRP3<sup>NACHT</sup> as measured by SPR. The bound fraction corresponds to the ratio between actual response and theoretical maximal response. (c) Mutational analysis of the CRID3 binding interface in context of full-length NLRP3. Residues of NLRP3 that have been targeted by site-directed mutagenesis are depicted in the box. ASC speck formation and inhibition by CRID3 was measured in HEK293T cells using an inducible NLRP3 expression system. The experiments have been performed by Dr. Jonas Möcking and Dr. Annemarie Steiner (University of Bonn). Data points are representative of at least three independent experiments.  $n \geq 3 \pm \text{SEM}$ ; ns  $P > 0.05$ , \*  $P \leq 0.05$ , \*\*\*\*  $P \leq 0.0001$  (two-way ANOVA followed by the Tukey's multiple comparisons test). UT: untreated.

#### 4.1.7 Effects of CRID3 on the NLRP3 ATPase active center

Intrinsic ATPase activity is associated with all functions of NLRP3, suggesting that ATP binding and hydrolysis plays a central role in regulation (Duncan et al., 2007; MacDonald et al., 2013; Sandall et al., 2020). Importantly, presence of CRID3 did clearly interfere with ATP hydrolysis activity of the NLRP3 NACHT domain *in vitro* (Figure 4-2a, b). To gain insights into the CRID3 mode of action, the NLRP3 ATPase active center and the effects of CRID3 binding were investigated at the molecular level. During potassium efflux, NLRP3 is thought to be recruited to membranes of the dTGN where it interacts with negatively charged PtdIns4P and becomes eventually activated (Chen & Chen, 2018; Tapia-Abellan et al., 2021). This interaction is thought to be established by a polybasic cluster that is part of a helix stabilized by multiple hydrophobic interactions on the NBD (Figure 4-9a). Interaction of the polybasic cluster with phospholipids plus antecedent phosphorylation of the succeeding activation loop during priming might in combination destabilize an interjacent loop that contains residues Arg167, Tyr168, and Thr169. Interestingly, during the resting state, these residues seal the bound nucleotide by interacting with the adenine and sugar moieties to potentially prevent its dissociation (Figure 4-9b). Still, it is a matter of debate whether dissociation of the bound nucleotide drives a conformational change to the ‘open’ and active form or if, on the contrary, such conformational change is prerequisite for nucleotide exchange. However, CRID3 binding seems not to directly influence the position of this particular loop in NLRP3.

Within the classical Walker A motif (consensus GxxxxGKS/T), residue Lys232 was expectedly found to interact with the  $\beta$ -phosphate of ADP and Thr233 to participate in the coordination of the magnesium ion (Figure 4-9c, d). The extended Walker B motif hhhhhD<sub>302</sub>GhDE contains three acidic residues. Asp302 and the catalytic Glu306 positioned 4 residues upstream of the Walker B box coordinate three water molecules around the magnesium ion that might be essential for the nucleophilic attack on ATP and consequent hydrolysis between the  $\beta$ - and  $\gamma$ -phosphates (Figure 4-9c). The  $\alpha$ -phosphate of the nucleotide coordinates a fourth water molecule, whereas the  $\beta$ -phosphate directly interacts with the magnesium ion resulting in an ideal six-coordinate octahedral geometry (Case et al., 2020) (Figure 4-9c).



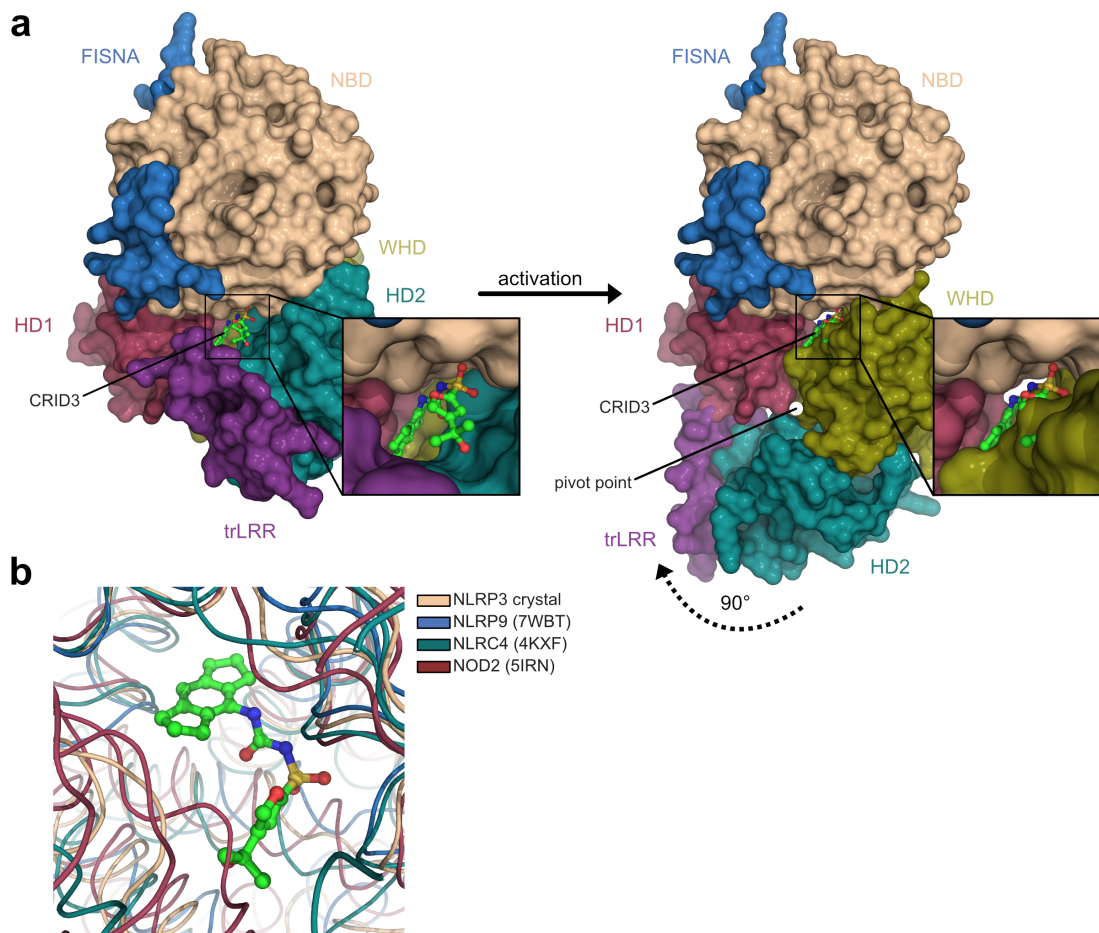
**Figure 4-9: The polybasic cluster and nucleotide binding site of NLRP3.** (a) Surface representation of NLRP3 with the helix containing the polybasic cluster (blue) shown in cartoon representation. Solvent exposed basic residues are shown as sticks and hydrophobic residues that stabilize the cluster on the NBD are shown with yellow gaussian surfaced sidechains. (b) Surface representation of the nucleotide binding site. A loop (blue) that follows the polybasic cluster and seals ADP from being released is shown in cartoon representation with depicted amino acids shown as sticks. (c) Detailed view on important molecular interactions of NLRP3 with ADP·Mg<sup>2+</sup>. Hydrogen bond interactions are shown as dashed black lines. (d) Simplified view on the molecular interactions of NLRP3 with ADP·Mg<sup>2+</sup> generated with LigPlot+ (Laskowski & Swindells, 2011).

The observation that four of six direct contacts with the magnesium ion in NLRP3 are made by water molecules may indicate weak coordination and may be the reason for the lack of electron density for the divalent ion in other structural data. Asp305 points in direction of Arg351, which was determined as sensor I. While in the crystal structure Arg351 forms a hydrogen bond with CRID3 (Figure 4-7b, c), it is plausible that in an active apo state this residue interacts with both, the  $\gamma$ -phosphate of ATP and the negatively charged Asp305, thereby repositioning the Walker B motif for the hydrolysis reaction. Interestingly, His260 is in the position expected to be a ‘glutamate switch’ motif in NLRP3 (Figure 3-1) and related AAA+ ATPases (Wendler et al., 2012). However, in the crystal structure the residue adopts a conformation where the sidechain is too far away

from the Walker B motif to directly influence hydrolysis (Figure 4-9c). This might be due to the extended Walker B motif of NLRP3, which results in positioning of the catalytic Glu306 one level apart from Asp302 (Figure 4-9c). As a consequence, not His260 but the downstream Arg262 that interacts with the WHD (Figure 4-6a) might be the ‘glutamate switch’ motif in NLRP3. Furthermore, it is known that a proline residue of HD1 and a histidine residue of WHD are essential for the interaction with the nucleotide, since they are distinctive features of NLR family proteins and other STAND ATPases (Danot et al., 2009; Hu et al., 2013; Sandall et al., 2020). In NLRP3, Pro412 interacts with the adenine moiety of ADP, whereas His522 forms a hydrogen bond with the  $\beta$ -phosphate, which significantly adds to the intramolecular interdomain interactions that stabilize the inactive state (Figure 4-9c, d). Importantly, the preceding Ile411 is superjacent of the hexahydro-s-indacene moiety of CRID3 (Figure 4-7b). Further interaction of CRID3 with the Walker A motif (Ala228) and sensor I (Arg351) might rigidify the nucleotide binding site in NLRP3 and thus explain its ability to inhibit ATPase activity.

#### **4.1.8 CRID3 locks NLRP3 in the inactive state**

Since many mutations within the CRID3 interface rendered NLRP3 as none-responsive to nigericin (Figure 4-8c), it is proposed that the integrity of the CRID3 binding site in NLRP3 is also essential for inflammasome activation. Consequently, it is hypothesized that the available space is needed to allow for the rotation of the WHD upon activation of NLRP3. Mechanistically, such conformational change might be sterically prevented by different mutations and similarly by binding of CRID3. To test this hypothesis, a model of active NLRP3 was generated based on the structure of active mouse NLRC4 (Zhang et al., 2015) and the AlphaFold2 prediction of human NLRP3 (Jumper et al., 2021). By analyzing the CRID3 binding site, it was found that the cleft was indeed no longer present in the active conformation and CRID3 would clash with the WHD of NLRP3 (Figure 4-10a). This suggests that CRID3 acts like a doorstop glued between four subdomains of the NLRP3 NACHT domain and the transition LRR, thereby locking NLRP3 in the inactive conformation. Importantly, other members of the NLR family may have a similar cleft to NLRP3 (Figure 4-10b), making them potential targets for future drugs engaging the same binding site as CRID3. Therefore, the mode of action of CRID3 represents a prototypical example of direct inhibition of inflammasomes.

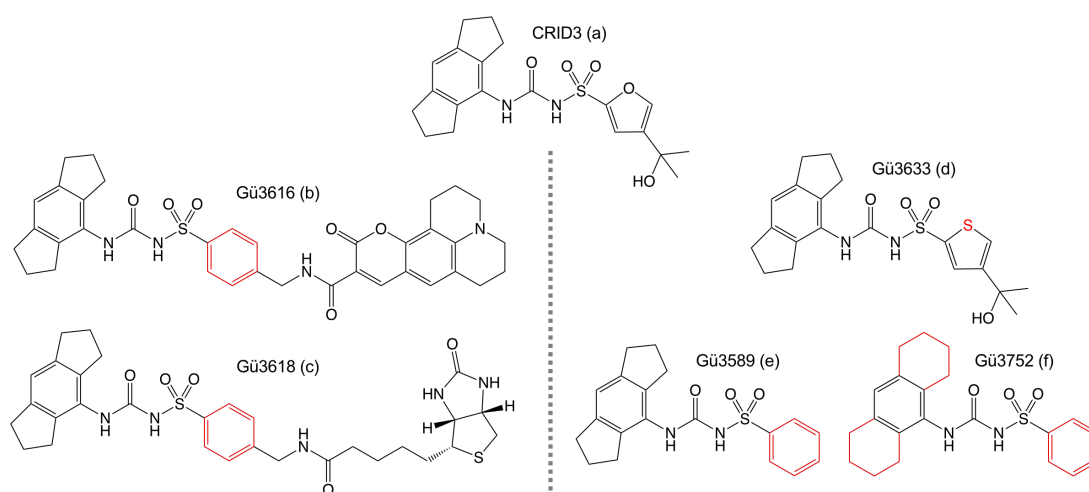


**Figure 4-10: CRID3 binding site in the active state and comparison with NLR family members.** (a) Surface representation of NLRP3 as determined from the crystal structure and close up of the CRID3 binding site. CRID3 is shown as sticks-and-balls and interacts with five subdomains (NBD, HD1, WHD, HD2, and trLRR) of NLRP3. Upon activation, NLRP3 is thought to adopt an ‘open’ conformation following a 90° rotation of the WHD-HD2-LRR module away from HD1 (Danot et al., 2009). Such conformation is modeled based on the structure of active NLRC4 (Zhang et al., 2015) and the AlphaFold2 prediction of NLRP3 (Jumper et al., 2021). The pivot point (Thr438) is highlighted as a white circle. In the ‘open’ conformation, CRID3 would clash with the WHD of NLRP3. (b) Overlaid ribbon representations of the CRID3 binding site in NLRP3 with structures of inactive bovine NLRP9 (PDB: 7WBT), mouse NLRC4 (PDB: 4KXF), and rabbit NOD2 (PDB: 5IRN).

## 4.2 Biochemical study of CRID3-containing probes and CRID3 analogs

In cooperation with the group of Prof. Dr. Michael Gütschow (Pharmaceutical Institute, University of Bonn), we aimed to develop novel CRID3-containing fluorescent and biotin-tagged probes that can be used e.g., for competition assays, pulldown experiments, or confocal microscopy. For this purpose, probes that contain a CRID3-related NLRP3 binding unit and a coumarin 343 fluorophore or biotin have been synthesized and their affinity for NLRP3 has been analyzed using SPR spectroscopy. We also found that no systematic study on the chemical stability of CRID3 is yet publicly available, although

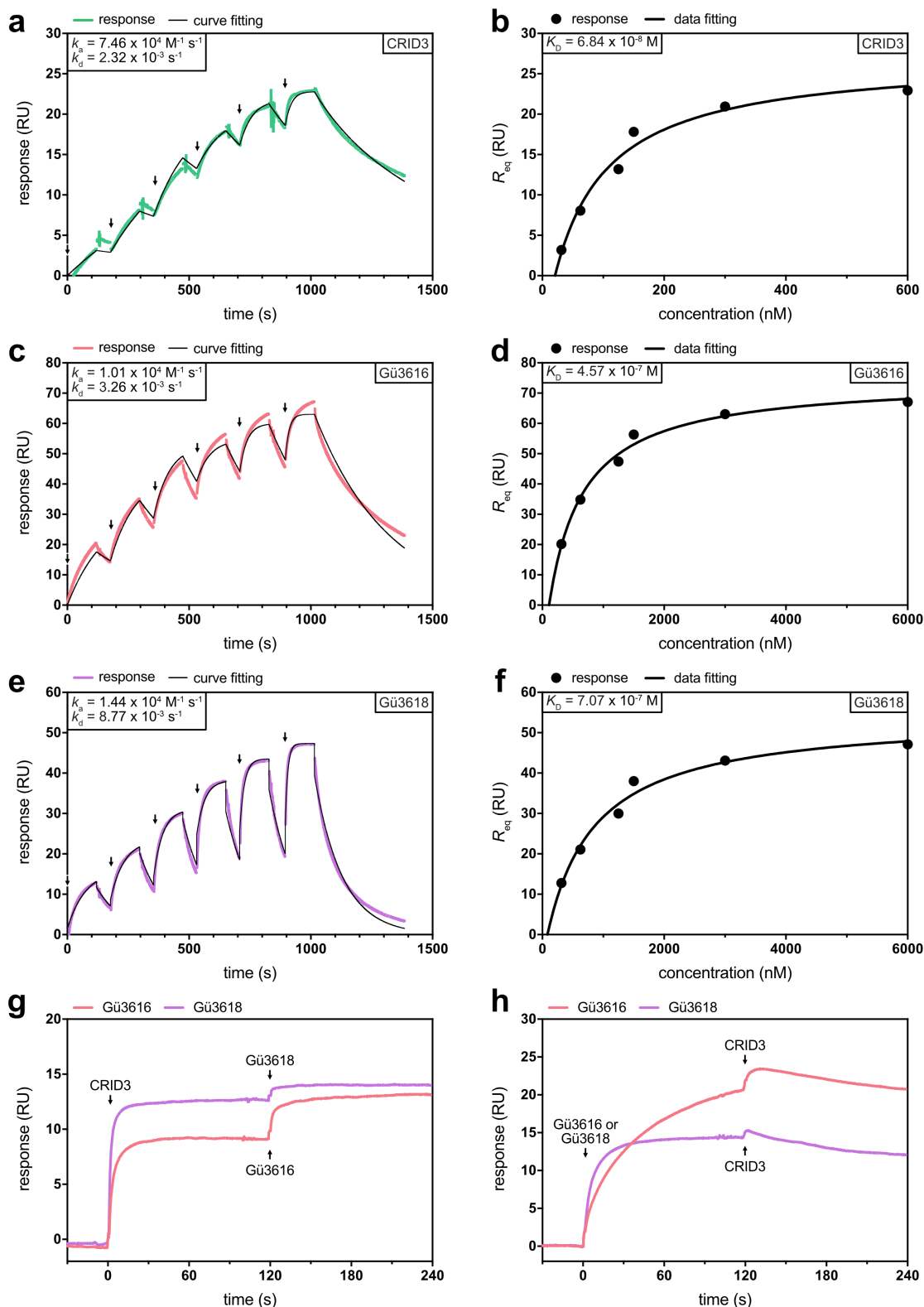
its pharmacokinetic and toxicokinetic properties limited its therapeutic development in the clinic (Corcoran et al., 2021). Therefore, we performed a positional scanning with respect to the substituents at the sulfur and the terminal nitrogen of the central sulfonamide core. The synthesized CRID3 analogs were evaluated for their chemical stability and affinity for NLRP3 using an HPLC or SPR approach, respectively. While data about the chemical stability of the CRID3 analogs is not subject of this thesis, fundamental structure-affinity relationships for CRID3 shall be provided. Selected fluorescent or biotin-tagged probes and CRID3 analogs that have been measured using SPR spectroscopy are shown in Figure 4-11.



**Figure 4-11: CRID3-containing probes and CRID3 analogs.** Structural formula of CRID3, a CRID3-based fluorescent (Gü3616) and biotin probe (Gü3618), and three CRID3 analogs with exchange of the ring oxygen by sulfur (Gü3633), introduction of an unsubstituted aromatic *S*-substituent (Gü3589), and exchange of the hexahydro-*s*-indacene moiety with an octahydroanthracene moiety (Gü3752), respectively. Differences from the original CRID3 molecule are highlighted in red. All compounds were synthesized by Tim Keuler from the group of Prof. Dr. Michael Gütschow (Pharmaceutical Institute, University of Bonn).

#### 4.2.1 SPR binding studies with CRID3-based fluorescent and biotin probes

In line with the crystal structure of the NLRP3-CRID3 complex (Figure 4-10a), previous studies suggested the eastern sulfonamide part of CRID3 as an appropriate exit vector to connect a functional moiety (Agarwal, Pethani, et al., 2020; Hill et al., 2017). Thus, we followed a similar structural design as introduced by Vande Walle et al., who developed a CRID3-derived probe for photoaffinity labeling (Vande Walle et al., 2019) and used a benzylamine moiety as a flexible exit vector to connect a coumarin 343 fluorophore or biotin, respectively (Figure 4-11).



**Figure 4-12: Binding study of CRID3-containing probes.** (a, c, e) SPR sensorgram following the specific binding of (a) CRID3, (c) Gü3616, or (e) Gü3618 to NLRP3<sup>NACHT</sup> protein from HEK293T cells. Arrows indicate injections of different concentrations of CRID3 (31.25, 62.5, 125, 150, 300, 600 nM) or CRID3-based probes (312.5, 625, 1250, 1500, 3000, 6000 nM). The second-order association constant ( $k_a$ ) and first-order dissociation constant ( $k_d$ ) were calculated from a 1:1 binding model. (b, d, f) For steady state analysis the response in equilibrium ( $R_{eq}$ ) was determined from (a, c, e) and plotted versus the analyte concentration. The equilibrium dissociation constant ( $K_D$ ) was calculated from a binding model. Measurements were performed by Dr. Karl Gatterdam (University of Bonn). (g, h) Displacement assays to

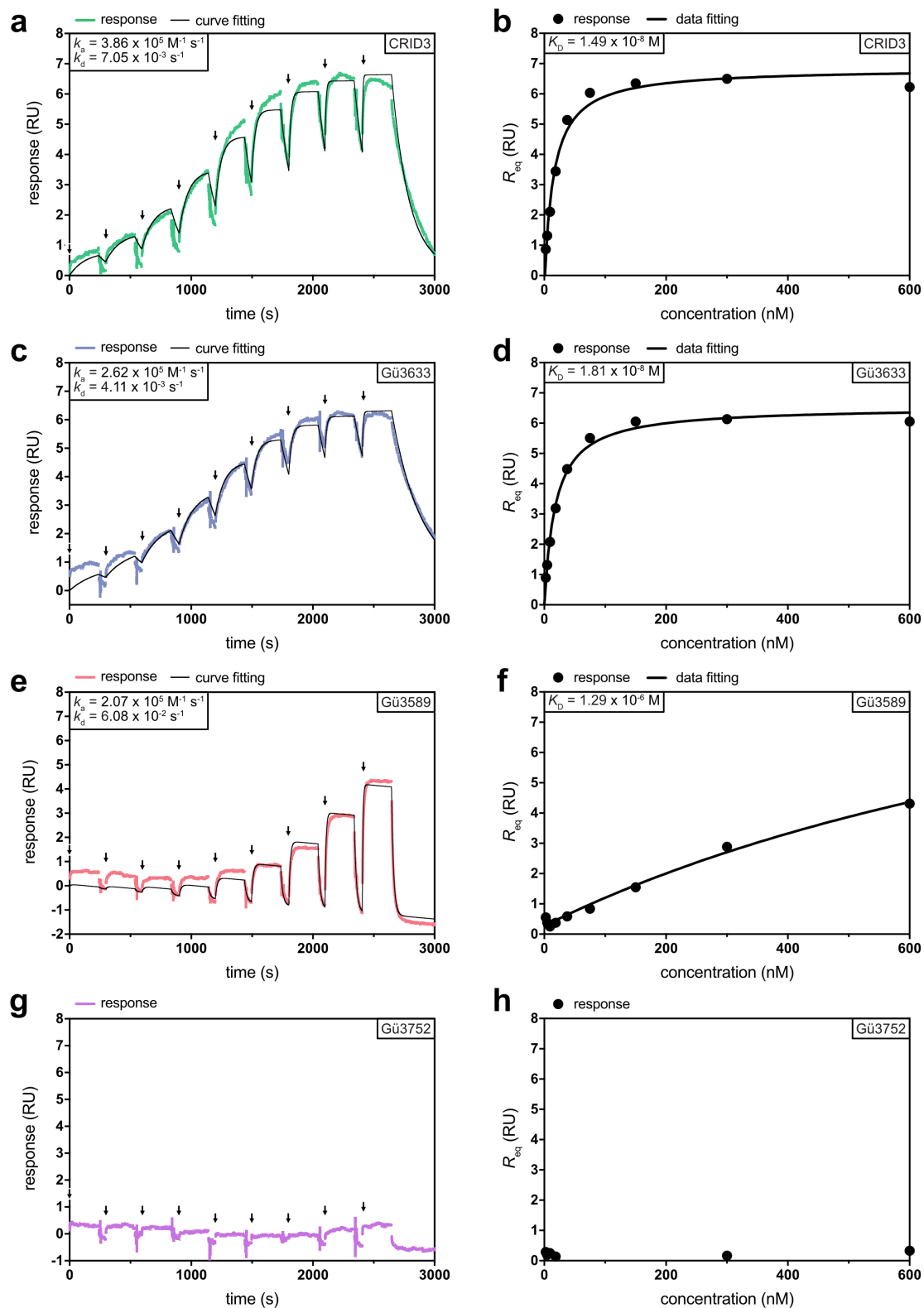
confirm that CRID3 and the CRID3-containing probes engage the same binding pocket on the target protein NLRP3. The sensorgrams follow the specific and competitive binding of CRID3, Gü3616, and Gü3618 to NLRP3<sup>NACHT</sup> protein as measured by SPR spectroscopy. In the first injection step either (**g**) CRID3 or (**h**) CRID3-based probes were provided. Following, equimolar concentrations of the second compound were injected in the presence of the first compound (second arrow).

SPR analysis revealed specific binding of these compounds to recombinant NLRP3<sup>NACHT</sup> protein but with somehow faster dissociation rate and concomitant 7-10-fold lower affinity as if compared with CRID3 (457 nM and 707 nM versus 68 nM; Figure 4-12a-f). Of note, the affinity of the probes towards NLRP3 further decreased when the length of the linker unit was extended (data not shown). To confirm that the fluorescent and biotin probes share the same binding site with CRID3, binding experiments were performed under competitive conditions. For this purpose, probes were injected in the presence of CRID3 and after preceding saturation of the CRID3 binding site on NLRP3 (Figure 4-12g). For further confirmation, the system was also tested the other way around, meaning NLRP3 was saturated with the individual probe whereafter CRID3 binding was assayed (Figure 4-12h). Importantly, no significant change in response, indicative of a second binding site, could be observed, thus arguing for the assumption that CRID3 and both compounds engage the same binding pocket on the target protein NLRP3.

#### 4.2.2 Structure-affinity relationship of CRID3

To determine the fundamental structure-affinity relationships of CRID3 for NLRP3, binding affinity of three different analogs has been analyzed using SPR spectroscopy. As predicted from the structural data, an exchange of the ring oxygen by sulfur might not significantly influence the affinity towards NLRP3<sup>NACHT</sup> protein because the furan moiety is not much involved in the interaction. Similar with CRID3, such analog indeed showed high affinity binding (Figure 4-13a-d). Thus, thiophene chemistry becomes a new synthetic option to develop advanced NLRP3 inhibitors (Keuler et al., 2022). Interestingly, this is already reflected in some CRID3-inspired compounds that recently progressed into clinical trials (Schwaid & Spencer, 2021). In contrast, an unsubstituted aromatic *S*-substituent strongly decreased the affinity towards NLRP3, which validates that the tertiary alcohol group significantly contributes to the NLRP3-CRID3 interaction (Figure 4-13e, f). Further replacement of the hexahydro-*s*-indacene moiety with an octahydroanthracene moiety completely abolished the ability to bind to NLRP3, most likely indicating steric hindrance (Figure 4-13g, h).





**Figure 4-13: Binding study of CRID3 analogs.** (a, c, e, g) SPR sensorgram following the specific binding of (a) CRID3, (c) Gü3633, (e) Gü3589, and (g) Gü3752 to NLRP3<sup>NACHT</sup> protein from HEK293T cells. Arrows indicate injections of 2.34, 4.68, 9.37, 18.75, 37.5, 75, 150, 300, and 600 nM compounds, respectively. The second-order association constant ( $k_a$ ) and first-order dissociation constant ( $k_d$ ) were calculated from a 1:1 binding model. (b, d, f, h) For steady state analysis the response in equilibrium ( $R_{eq}$ ) was determined from (a, c, e, g) and plotted versus the analyte concentration. The equilibrium dissociation constant ( $K_D$ ) was calculated from a binding model.

### 4.3 Discussion and Conclusion

Since the discovery of CRID3 as an NLRP3 inflammasome pathway inhibitor, many studies investigated its specificity and mode of action. But determination of direct binding on NLRP3 turned out to be difficult. For that reason, drug discovery efforts have been constrained by the lack of knowledge about the molecular target of CRID3 and the mechanism by which it inhibits inflammasome formation. It was not until 2019 that the direct interaction of CRID3 with recombinant NLRP3 was reported for the first time (Coll et al., 2019). Using an SPR approach, it could be shown that CRID3 binds to NLRP3 with high affinity ( $K_D \approx 10\text{-}224$  nM), whereas binding to a Walker B mutant was abrogated. Based on these findings the authors proposed that CRID3 directly targets the NLRP3 Walker B motif to inhibit ATP hydrolysis and inflammasome activation (Coll et al., 2019). Four months later, Vande Walle and colleagues reported a selective photoaffinity labelling assay that also revealed the NLRP3 NACHT domain as the molecular target of diarylsulfonylurea inhibitors (Vande Walle et al., 2019). While the CRID3 binding site and its mode of action seemed to be elucidated, structural data clearly confirming these results were lacking. Only recently, our group reported a cryo-EM structure of an NLRP3 decamer in complex with CRID3 (Hochheiser, Pilsl, et al., 2022). In combination with the crystal structure presented here, the binding site of CRID3 is unambiguously identified and the long-standing question about the mode of action of this exciting anti-inflammatory agent is resolved. Strikingly, CRID3 does not target the NLRP3 Walker B motif but binds to a cleft located on the backside of the Walker A motif, whereby it ties together five subdomains of NLRP3 (Figure 4-7). Hydrophobic interactions with the western hexahydro-*s*-indacene moiety and multiple hydrogen bond interactions with the central sulfonylurea and the eastern tertiary alcohol group explain its high specificity and affinity for NLRP3 as well as the remarkable stabilizing effect (Figure 4-2). While mutational studies on NLRP3 are solely valid and confirmed the CRID3 binding site (Figure 4-8), two recent cryo-EM structures of full-length NLRP3 oligomers bound to CRID3 and a crystal structure of NLRP3 in complex with the CRID3 derivative NP3-146 essentially determined the same binding site and thus further confirm the here presented results (Dekker et al., 2021; Hochheiser, Pilsl, et al., 2022; Ohto et al., 2022).

Mechanistically, CRID3 interferes with the NLRP3 inflammasome in three ways:

- 1) Inhibition of nucleotide exchange and ATP hydrolysis
- 2) Establishment of tight interdomain interactions stabilizing an inactive conformer
- 3) Prevention of structural rearrangements necessary to form an active state

One important interaction is established via the sensor I motif in NLRP3 (Arg351), whose conformation of the sidechain is fixed by the binding of CRID3 (Figure 4-7b). Interestingly, the crystal structure suggests that in an ATP-bound conformation and in the absence of CRID3, Arg351 is not only capable of interacting with the  $\gamma$ -phosphate of ATP as a sensor, but also with Asp305 to potentially reposition the Walker B motif for hydrolysis. Such rather important function would explain why not only the two other acidic residues (Asp302 and Glu306) that coordinate the magnesium ion are regularly found in the Walker B motif of NLR family proteins but indeed Asp305 is also widely conserved (Sandall et al., 2020). Importantly, CRID3 binding clearly interferes with all functions of the sensor I motif, including the potential interaction with Asp305. Additional interaction of CRID3 with the Walker A site and residues proximal to the conserved Pro412 might rigidify the nucleotide binding pocket to collectively inhibit nucleotide exchange, ATP sensing, and structural rearrangements that are prerequisite for or consequence of the hydrolysis reaction. Importantly, these ideas are reflected by the finding that presence of CRID3 inhibits ATP hydrolysis activity of NLRP3 and the thermal stability data, which showed that presence of nucleotides failed to further stabilize the CRID3-bound form (Figure 4-2a-c). Interestingly, Dekker and colleagues suggested that in the absence of compound, Arg351 would likely be able to form a salt bridge with Glu527 of the WHD (Dekker et al., 2021). This would imply that the sensor I motif is also involved in interdomain organization (Dekker et al., 2021). Indeed, in the structure of inactive rabbit NOD2 (PDB: 5IRN) the Arg351-equivalent Arg398 shows the same conformation without presence of an inhibitor and forms a hydrogen bond interaction with Asn643 (Maekawa et al., 2016). Therefore, it is plausible that the  $\gamma$ -phosphate could substitute for the electrostatic interaction with Glu527 when ADP is exchanged for ATP to weaken the interdomain interactions that stabilize the inactive state. To confirm this hypothesis, determination of a high-resolution structure of NLRP3 in the apo state would be valuable. While CRID3 binding might disrupt the interdomain interaction between Arg351 and Glu527, it is fairly compensated by the integration of Arg351 into a number of new interactions across the WHD and other subdomains of the NLRP3 NACHT and LRR domains.

Establishment of tight interdomain interactions is essentially the mechanism how CRID3 stabilizes the monomeric state of NLRP3. The crystal structure suggests that three intramolecular interdomain interfaces between subdomains of the NACHT and LRR domains stabilize the inactive monomeric state (Figure 4-6a-c). Interestingly, the

potential salt bridge between Arg262 and Glu511 in the interface between the NBD and the WHD was also highlighted by Dekker and colleagues (Dekker et al., 2021). But unfortunately, their structural data did as well not provide density for the sidechain of Glu511, indicating flexibility of this part of the protein in both structures. However, similar interactions can be found in the structures of inactive NOD2 and NLRC4, where the Arg262-equivalents Arg314 and Arg206 form salt bridge interactions with Glu580 and Asp407, respectively (Dekker et al., 2021; Hu et al., 2013; Maekawa et al., 2016). Interestingly, in case no magnesium ion is bound to NLRP3, Arg262 forms a salt bridge with the catalytic Glu306 from the Walker B motif, whereby it moves away from the interdomain interface (Dekker et al., 2021). While this interaction might be an artifact in structures of ADP-bound NLRP3 that miss the magnesium ion, it could be relevant during nucleotide exchange. In this way, the release of ADP together with the dissociation of the magnesium ion could mechanistically cause the destabilization of the NBD-WHD interface to trigger conformational changes. In addition, and consistent with the concept of a ‘glutamate switch’ motif (Zhang & Wigley, 2008), the formation of the NBD-WHD interaction directly affects the position of Arg262 and thus its interaction with the catalytic Glu306, which could subsequently regulate hydrolysis activity in NLRP3.

In an oligomeric state, additional intermolecular interactions can be found that further stabilize the resting state of NLRP3 (Andreeva et al., 2021; Hochheiser, Pils, et al., 2022; Ohto et al., 2022). But disease-relevant mutations that likely interfere with the inactive state (Figure 4-6d) are each capable to drive hyperactivation and CAPS (Booshehri & Hoffman, 2019). This might indicate that all of these interactions are rather loose and only collectively able to regulate the delicate balance between inactive and active NLRP3. In contrast, binding of CRID3 caused an impressive 20°C shift in thermal stability of NLRP3<sup>NACHT</sup> protein (Figure 4-2c, d), which suggests a very potent stabilization of the ‘closed’ and inactive conformation. Indeed, the ability of CRID3 to close the conformation of CAPS mutants D305N and T350M (Tapia-Abellan et al., 2019), which likely affect nucleotide binding and hydrolysis, demonstrates its capability to even modify the internal energetic profile of mutant and hyperactive NLRP3 to favor the ‘closed’ and inactive state. CRID3 can also bind to and inhibit the hyperactive mouse NLRP3 A350V variant (corresponding to A354V in human, NBD-HD2 interface), whereas the likely pathogenic L351P mutation in mice (L355P in human) abolishes binding (Vande Walle et al., 2019). This difference can be explained by the large structural effects that potentially come with the L355P mutation. Leu355 is positioned at the center of a helix

following the sensor I motif (Figure 4-4c). Mutation to proline disrupts this helix, which might have consequences for the fold of the NBD and also for the nearby CRID3 binding site.

Examining a model of active NLRP3, it was found that the CRID3 binding site was no longer present and CRID3 would sterically clash with the WHD (Figure 4-10a), leading to the conclusion that CRID3 must also prevent the structural rearrangements necessary to adopt the active conformation. This concept was basically proven by the finding that diverse variants of NLRP3 with mutations in the CRID3 interface could no longer be activated by treatment of cells with nigericin (Figure 4-8c). While such mutations did probably not interfere with hydrolysis activity or stabilized interdomain interactions, they obviously modified the cleft in NLRP3 that is formed by these residues. Since integrity of this cleft is directly coupled with the capability to activate NLRP3, intercalation via CRID3 seems to be an effective concept of inhibition. Importantly, this concept also suggests that active NLRP3 cannot be bound by CRID3, since the binding site is no longer present. However, using an assay based on bioluminescence resonance energy transfer (BRET), Tapia-Abellán and colleagues could demonstrate that CRID3 also interacts with the ‘open’ conformation of NLRP3 (Tapia-Abellan et al., 2019). But careful inspection of their results revealed that the BRET signal after incubation with CRID3 differs significantly if cells have been treated with CRID3 before or after activation with nigericin, indicating different conformations. Thus, the mechanism how CRID3 binds to and inhibits the active NLRP3 conformer remains to be determined. Notably, the structural rearrangements that lead to the ‘open’ and active conformation are thought to be shared among STAND ATPases (Danot et al., 2009). Hence, it is well conceivable that more NLR family members can be inhibited by specific compounds with the same mode of action as CRID3.

A number of inhibitors with a mode of action distinct from CRID3 have also been identified. This includes diverse ATPase activity inhibitors, such as CY-09, Bay-11-7082, Parthenolide, BOT-4-one, MNS, Dapansutrile (OLT1177), INF39, and HS-203873, but also the NLRP3 oligomerization blocker Tranilast, the cysteine-modifying agents Oridonin and RRx-001, which attenuate NEK7 interaction, and JC-171, which probably attenuates the NLRP3-ASC interaction (Coll et al., 2022; El-Sharkawy et al., 2020). Noteworthy, the sulfonamide analog JC-171 and its derivatives JC121 and JC124 might have the same binding site and mode of action as glyburide, since they are based on this structural entity (Fulp et al., 2018). However, most of these proposed ATPase and protein-

protein interaction inhibitors have an unknown binding site with low potency and specificity, which implicates a number of off-target effects (Coll et al., 2022). In contrast, CRID3 shows high affinity binding to its specific target NLRP3 with a half maximal inhibitory concentration ( $IC_{50}$ ) of 7.5 nM and only modest binding ( $IC_{50} = 11 \mu\text{M}$ ) to its only known off-target carbonic anhydrase 2 (Coll et al., 2015; Coll et al., 2022; Kennedy et al., 2021). Thus, interference via CRID3 is a prototypical example of selective and direct inflammasome inhibition. This is as well reflected by the endeavors of multiple companies to move advanced CRID3-inspired compounds into the clinic as bona fide NLRP3-inhibiting drugs (Schwaid & Spencer, 2021).

High level of excitement for CRID3 is further fueled by numerous indications in treating common diseases for which curative treatment is limited, including arthritis, gout, fibrosis, coronary artery disease, and Crohn's disease (Schwaid & Spencer, 2021). Consequently, many patented next generation compounds are structurally similar to CRID3 but comprise directed improvements that might come with better pharmacology and toxicity. In line with the here presented biochemical and structural data (Figure 4-7b, c, Figure 4-12, Figure 4-13) and previously determined structure-activity relationships of CRID3 (Harrison et al., 2020; Hill et al., 2017), most compounds that are exemplified in the patents from IFM, Inflazom, Nodthera, or Jecure and reported to have good potency and pharmacokinetics show the highest degree of modification on the eastern isopropyl furan moiety (Schwaid & Spencer, 2021). Since the metabolically reactive furan moiety is a known cause of drug-induced liver damage (Tian et al., 2022), it is often exchanged with a variety of bioisosteric aromatic heterocycles such as thiophenes, thiazoles, and diazoles (Schwaid & Spencer, 2021). Interestingly, while other companies retained the central sulfonylurea linked to a tricyclic moiety, IFM standardly replaced the urea with an acetamide that was linked to substituted phenyl (Schwaid & Spencer, 2021). But importantly, all CRID3-like compounds reviewed by Schwaid and Spencer contain a hydrophobic western moiety and three central oxygen atoms that, in case of CRID3, form the critical interactions with the hydrophobic cluster and two arginine residues of NLRP3 (Figure 4-7b), suggesting the same mode of action for these novel compounds (Schwaid & Spencer, 2021). However, *N*-cyano sulfoximineurea analogs have also been reported as equipotent derivatives of CRID3 (Agarwal, Sasane, et al., 2020), which might suggest that interaction of Arg351 with one oxygen atom is sufficient or even induces a distinct but equipotent binding pose. One rational idea might be that the *N*-cyano sulfoximine is able to reach the position of the water molecule that establishes hydrogen bond

interactions with residues Gln624 and Glu629 of NLRP3 and the tertiary alcohol group of CRID3 (Figure 4-7b, c). This would indeed explain why an *N*-cyano sulfoximineurea analog has the same potency as CRID3, even though it contains a toluene rather than the isopropyl furan moiety (Agarwal, Sasane, et al., 2020).

Along with modifications, compounds can be equipped with restricted distribution profiles to prevent interference with NLRP3 function in compartments that are not involved in disease (Schwaid & Spencer, 2021). On the other hand, with indications in neurological diseases such as Parkinson's disease, Alzheimer's disease, multiple sclerosis, Huntington's disease and stroke (Chen et al., 2022; Corcoran et al., 2021; Lunemann et al., 2021), the penetration of the blood brain barrier (BBB) has become a major goal. Importantly, CRID3 shows only poor brain uptake and rapid washout in positron emission tomography studies because it might be a ligand of efflux transporters (Hill et al., 2020). This information along with the different requirements on physicochemical properties such as molecular weight, lipophilicity, and number of hydrogen bond donors and acceptors should be considered when developing next generation NLRP3 inhibitors for the treatment of neurological diseases (Banks, 2009; Pajouhesh & Lenz, 2005).

Based on the high-resolution structural data presented in this thesis and the structures of already published NLRP3-inhibitor complexes (Dekker et al., 2021; Hochheiser, Pils, et al., 2022; Ohto et al., 2022), it can be anticipated that new structure-guided drug design will fasten the development of next-generation highly specific NLRP3 inhibitors with designated properties and mode of action. As an example, identification of the water molecule that bridges the interaction between the tertiary alcohol group of CRID3 and residues Gln624 and Glu629 of NLRP3 (Figure 4-7b, c) enables rational drug design to replace the water molecule with hydrogen bond donors or acceptors, thereby increasing compound specificity.





## 5 Summary and Conclusion

In the first part of this thesis, human NLRP9 was investigated. The primary aim was to confirm the existence of an ASC-dependent NLRP9 inflammasome and to gain insights into its mechanistic regulation and assembly. Interestingly, a sequence-based alignment with NLRP3 revealed several differences. In brief, NLRP9 does not harbor a polybasic cluster at the beginning of the FISNA domain nor an acidic loop in the LRR region. In addition, no activation loop containing SP phosphorylation sites or a sensor I motif could be identified. Furthermore, the Walker B motif significantly differs from the consensus sequence conserved in other NLR family members. For that reason, it is hypothesized that the NLRP9 NACHT domain possesses only low ATPase activity and might be regulated in a different way compared to NLRP3. While inactive full-length NLRP3 was recently found to form a decamer, full-length NLRP9 was purified as a stable monomer that can dimerize upon incubation in the presence of ATP. Particles visualized by negative stain EM showed similarities with a model predicted by AlphaFold2 and a crystal structure of bovine full-length NLRP9. It is hypothesized that monomeric NLRP9 adopts a similar ADP-bound conformation that would likely represent the inactive state, which should be assessed in future structural studies.

In line with different regulation and function of NLRP9, overexpression of full-length protein was unable to trigger spontaneous ASC speck formation in cells. Bypassing interdomain regulatory mechanisms, the NLRP9 PYD was expressed as a single domain construct and investigated as the respective protein effector domain facilitating signal transduction. Strikingly, the PYD was purified as a monomer and did not polymerize into filaments nor nucleate ASC speck formation *in vitro* or in cells. Based on a high-resolution crystal structure of the NLRP9 PYD that was determined in this work, the molecular characteristics were investigated. It was found, that no conformational restraints prevent the formation of an NLRP9 PYD filament but the presence of several mismatches in the hypothetical filament interfaces abrogate polymerization. In addition, it was found that no electrostatic interface for the nucleation of ASC PYD exists on the surface of NLRP9. Taken together, the first part of this thesis contradicts the existence of a potential NLRP9 inflammasome. However, the regulation by PTMs or the synergistic activation with e.g., NLRP6 are still possible scenarios in which the NLRP9 inflammasome might form. Thus, further investigation is needed to unravel its function.

In the second part of this thesis, human NLRP12 was investigated. Similar with NLRP9, the existence of an ASC-dependent NLRP12 inflammasome is under debate and the primary aim was to gain insights into its potential assembly and mechanistic regulation. In line with the high sequence identity between human NLRP3 and NLRP12, important sequence motifs were found to be well conserved between both proteins. Using optimized buffer conditions and sucrose density gradient centrifugation, a protocol to purify full-length human NLRP12 cleaved from its affinity tag could be established. Negative stain EM revealed single particles that looked promising but turned out to be too inhomogeneous for structure determination. Interestingly, NLRP12 was co-purified with endogenous proteins of the tubulin superfamily, indicating association with microtubules in cells. Similarly, NLRP3 is known to be transported to the MTOC to form an inflammasome with ASC. In line, overexpression of NLRP12 triggered robust ASC speck formation in HEK293T cells, confirming its ability to form an inflammasome.

To gain mechanistic understanding, a NLRP12 PYD single domain construct was investigated. Unexpectedly, NLRP12 PYD was purified as a monomer and did not polymerize into filaments *in vitro* or in cells. In addition, a direct interaction with ASC could not be confirmed using an *in vitro* pulldown assay. Based on a previously determined high-resolution crystal structure of the NLRP12 PYD, the molecular characteristics were investigated. It was found that the NLRP12 PYD adopts a conformation with hallmarks of both monomeric and filamentous PYDs but importantly, no steric restraints nor significant mismatches in the hypothetical filament interfaces preventing polymerization could be identified. Strikingly, it was even found that the electrostatic surface of NLRP12 PYD filaments would likely provide an interface to nucleate the polymerization of ASC PYD. To approach this discrepancy, a variant of the NLRP12 PYD was tested. The variant contained a mutation (W45R) that was aimed to compensate repulsive forces between two glutamate residues in the potential filament and thus to increase the affinity between individual subunits. The mutant did tend to oligomerize more easily but not to form defined filaments under the conditions tested. In conclusion, this work provides distinct evidence for the existence of an ASC-dependent NLRP12 inflammasome but the assembly must be tightly regulated. It is well possible that the regulatory NACHT domain of NLRP12 acts as a scaffold for polymerization, which should be investigated in future cellular assays. In this work, the NLRP12 NACHT domain was investigated using biochemical and structural methods.

The successful design of an NLRP12 NACHT expression construct and the establishment of a sufficient purification strategy did result in monomeric protein of good yield and crystallization-grade quality. However, the monomeric species was found to be in dynamic equilibrium with an oligomeric conformer. Interestingly, oligomerization appeared to be independent of a bound nucleotide or hydrolysis reaction. Indeed, monomeric NLRP12 NACHT protein did not hydrolyze ATP, whereas the void volume protein or full-length NLRP12 was active. In addition, full-length NLRP12 did also possess adenylate kinase activity, the physiological relevance of which remains to be elucidated. The ATPase activity of NLRP12 was confirmed by introducing specific mutations that did affect hydrolysis function. Interestingly, presence of detergent during lysis completely abrogated ATP hydrolysis activity of wildtype NLRP12, suggesting a potential role of lipid membranes during activation similar to NLRP3. The monomeric NLRP12 NACHT protein does likely represent an inactive conformation, which was investigated using structural methods. To this end, optimized purification conditions were screened to stabilize and consequently enrich the monomeric species, cleave the affinity tag, and generate protein crystals. However, the crystals did not yet diffract at the synchrotron, indicating insufficient order of the crystal lattice presumably due to slightly different conformation of the individual protein molecules.

In the third part of this thesis, ways of potent and direct pharmacological interference with the inflammasome pathway were studied on the prototypic example of the NLRP3-specific small molecule inhibitor CRID3. Importantly, the concrete binding site and the mode of action of CRID3 was previously unknown and thus the aim was to investigate the NLRP3-CRID3 complex via biochemical and structural methods. For this purpose, a sufficient purification strategy was developed and allowed the expression and purification of monomeric human NLRP3 NACHT protein in good yield and crystallization-grade quality. Using diverse biochemical assays, it could be shown that CRID3 directly binds to the NLRP3 NACHT domain with high affinity ( $K_D \approx 20$  nM), which results in significant thermal stabilization of the protein and inhibition of the ATPase function. Importantly, in the second part of this thesis, CRID3 binding to the closely related NLRP12 NACHT domain was excluded, confirming its high specificity for NLRP3.

Successful determination of a high-resolution crystal structure of the NLRP3 NACHT domain in complex with the inhibitor CRID3 and  $ADP \cdot Mg^{2+}$  provided detailed molecular insights into NLRP3 function and inhibition by CRID3. Comparison with previously

determined or predicted structures revealed that the NLRP3 NACHT domain adopts an ADP-bound and ‘closed’ conformation, which is proposed to be the inactive state. In line, the conformation of NLRP3 was found to be stabilized by three intramolecular interdomain interfaces, each harboring a disease-relevant residue known to trigger CAPS when mutated. It is assumed that such mutation destabilizes the inactive state and leads to hyperactive NLRP3 that drives aberrant inflammation.

The CRID3 binding site was identified within a cleft located on the backside of the Walker A motif and formed by four subdomains of the NACHT domain and the transition LRR. The central sulfonylurea is sandwiched between two opposing arginines and the Walker A motif of NLRP3, whereas the western hexahydro-*s*-indacene moiety is included in a hydrophobic cluster. The eastern tertiary alcohol group interacts with the protein via a water molecule by forming hydrogen bonds. The CRID3 binding site was confirmed by mutational studies in two independent assays including NLRP3 NACHT domain and full-length constructs. In contrast to wildtype NLRP3, the majority of the mutants were unable to form an inflammasome upon treatment with nigericin, suggesting that the integrity of the CRID3 binding pocket is also essential for NLRP3 activation.

Structural investigation of the ATPase active center revealed residues and motifs that are mechanistically or regulatory important for nucleotide binding and hydrolysis. Worth mentioning here is Arg351, which was identified as the sensor I motif in NLRP3 and found to participate in the interaction with the sulfonylurea moiety of CRID3. As a result, the residue adopts a conformation in which it is unlikely to be functional. CRID3 is additionally supposed to rigidify the nucleotide binding site by interacting with the Walker A region and Ile411, which is only one residue upstream of the conserved Pro412. Collectively, these findings provide an explanation for how CRID3 abrogates NLRP3 hydrolysis activity. To further study the effect of CRID3, a model of the NLRP3 NACHT domain in the active conformation was investigated and revealed a steric clash of CRID3 with the WHD. Thus, it is assumed that CRID3 locks NLRP3 in the inactive state and thereby prevents its activation. However, the data also suggests that CRID3 can only bind to the inactive conformer, making conformation an important issue to consider in future drug development. Strikingly, the fold and conformation of the CRID3 binding pocket in NLRP3 is consistent with other members of the NLR family, providing the opportunity to develop compounds that specifically target these proteins for inhibition by the same mode of action. Moreover, with the here determined structure from the NLRP3-CRID3 complex, structure-guided drug design comes within reach.

In addition, binding of CRID3-based fluorescent and biotin probes as well as different CRID3 analogs were tested on the NLRP3 NACHT protein. Using SPR, the different probes were shown to engage the same binding site as CRID3 and to bind NLRP3 with barely reduced affinity. In accordance with the structural data, this confirms that CRID3 can be extended at the eastern side without loss of interaction. Likewise, substitution of sulfur for the ring oxygen of the furan moiety did not result in significant decrease in affinity. Thus, thiophene chemistry becomes a new synthetic option for the development of advanced NLRP3 inhibitors. Considering the known metabolic reactivity of furans, which is often the cause of drug-induced liver damage, this finding is of great value. Interestingly, the importance of this finding is already reflected in several CRID3-inspired compounds that recently progressed into clinical trials. In contrast, removal of the tertiary alcohol group from CRID3 resulted in significantly lower affinity, and substitution of the hexahydro-*s*-indacene moiety with an octahydroanthracene moiety completely abolished binding, confirming the structural data and revealing a basic structure-affinity relationship of CRID3.



## 6 Methods

### 6.1 Molecular genetics

#### 6.1.1 Polymerase chain reaction

Polymerase chain reaction (PCR) was used to amplify the protein-coding sequence from template DNA in the preparation of expression vectors. To this end, primer pairs with overhangs containing recognition sites for two selected restriction enzymes were designed, allowing targeted ligation of the generated amplicon into the multiple cloning site (MCS) of an expression vector. A list of primers for subcloning is given in Table 7-1.

Amplification was conducted in a thermocycler using a two-step protocol with a number of alternating cycles of denaturation, annealing, and elongation. In the first step, the annealing temperature was set at two degrees below the lowest melting temperature of the respective primer pair calculated without the overhangs. In the second step, the overhangs were included in the calculation. Melting temperatures were calculated using the NEB  $T_M$  Calculator online tool (<https://tmcalculator.neb.com>). The standard PCR reaction mix and protocol is shown in Table 6-1 and Table 6-2, respectively.

**Table 6-1: Reaction mix for standard and mutagenesis PCR**

Component	Final concentration
DNA template	100-500 ng
Primer forward	0.3 $\mu$ M
Primer reverse	0.3 $\mu$ M
dNTPs	200 $\mu$ M
Q5 reaction buffer (5x)	1x
Q5 high GC enhancer (5x)	1x
Q5 polymerase	0.02 U/ $\mu$ l
H <sub>2</sub> O	Fill up to 50 $\mu$ l

**Table 6-2: Protocol for standard PCR**

Step	Temperature ( $^{\circ}$ C)	Time (s)	Number of cycles
Initial denaturation	98	180	1
Denaturation	98	30	5
Annealing	$T_M-2$	20	
Elongation	72	30/kb	
Denaturation	98	30	37
Annealing	$T_{M, \text{+overhangs}}-2$	20	
Elongation	72	30/kb	
Final elongation	72	60/kb	1

### 6.1.2 Restriction enzyme digestion

Restriction enzymes are a class of bacterial or archaeal endonucleases that recognize specific and mostly palindromic double-stranded DNA sequences for cleavage. Depending on the enzyme, cleavage can produce 5' or 3' protruding ends (sticky ends) or blunt ends. Restriction enzymes were primarily used to cleave PCR amplicons and to linearize target vectors to generate ligation-compatible overhangs. Another application was the digestion of template DNA in site-directed mutagenesis (see section 6.1.5) or the testing of generated expression vectors for the presence of the ligated protein-coding sequence (see section 6.1.9) prior to Sanger sequencing.

Digestions were setup as shown in Table 6-3 and performed at 37°C for 1-2 h. For the testing of generated expression vectors, the concentration of restriction enzyme was reduced to 0.2 U/ $\mu$ l. If the digested DNA was not purified via agarose gel electrophoresis, the ExtractMe DNA Clean-Up Kit was used according to the manufacturer's instructions.

**Table 6-3: Reaction mix for restriction enzyme digestion**

Component	Final concentration
DNA sample	variable
Cut Smart buffer (10x)	1x
Restriction enzymes	1 U/ $\mu$ l
H <sub>2</sub> O	Fill up to 20 $\mu$ l

### 6.1.3 Agarose gel electrophoresis

Agarose gel electrophoresis was used to separate DNA samples by size. For this purpose, 1% agarose was dissolved in TAE buffer and boiled until the agarose was completely dissolved. For later detection of DNA bands in the gel, the UV-excitable DNA-binding dye peqGREEN was added according to the manufacturer's instructions. The mixture was transferred into a chamber containing a comb and cooled down to form a gel. The comb was removed to create sample wells. Subsequently, the gel was transferred into an electrophoresis chamber filled with TAE buffer. The DNA samples were prepared by adding 6x DNA gel loading dye and loaded onto the gel. A molecular weight size marker was loaded for comparison. The gel was run for 40 min at a constant voltage of 100 V.

After electrophoresis, the DNA bands were documented using a bench-top UV light table or the ChemiDoc™ XRS+ imaging system. DNA needed for downstream cloning applications was extracted from the gel using a clean scalpel and purified using the ExtractMe DNA Clean-up & Gel-Out Kit according to the manufacturer's instructions.



### 6.1.4 Ligation of DNA

After restriction enzyme digestion and purification by agarose gel electrophoresis, the PCR amplicon containing the protein-coding sequence was ligated into a linearized destination vector to obtain the desired expression vector. For this purpose, a T4 DNA ligase from bacteriophage T4 was utilized for the formation of a phosphodiester bond between compatible sticky ends. The reaction was carried out at 16°C or room temperature (RT) overnight, whereafter the ligase was inactivated by incubation at 68°C for 10 min. Finally, the ligated vector was transformed into competent bacteria for amplification and positive selection. The reaction mixture for the ligation of DNA is given in Table 6-4.

**Table 6-4: Reaction mix for ligation of DNA**

Component	Amount
DNA – vector	1 µl (~50 ng)
DNA – insert	10-15 µl (variable)
T4 ligation buffer (10x)	2 µl (1x)
T4 DNA ligase	1 µl (20 U/µl)
H <sub>2</sub> O	Fill up to 20 µl

### 6.1.5 Site-directed mutagenesis

Mutagenesis PCR was conducted to generate expression vectors encoding for mutant protein investigated in functional studies. For this purpose, a variant of the QuickChange mutagenesis protocol described by Liu and Naismith (Liu & Naismith, 2008) was applied. The protocol for the mutagenesis PCR and a list of primers used for site-directed mutagenesis is shown in Table 6-5 and Table 7-2, respectively.

After amplification by PCR, the template DNA was digested utilizing the methylation-sensitive restriction enzyme DpnI. DpnI cleaves the palindromic recognition sequence 5'-GATC-3' only when the adenine nucleotide is methylated. Thus, the PCR amplified DNA containing the mutation is protected while the methylated template plasmid purified from bacteria is digested. Finally, enzymes were inactivated for 10 min at 68°C and the amplicon was transformed into competent bacteria for amplification and positive selection.

**Table 6-5: Protocol for mutagenesis PCR**

Step	Temperature (°C)	Time (s)	Number of cycles
Initial denaturation	98	180	1
Denaturation	98	30-50	37
Annealing	$T_M-2$	20-50	
Elongation	72	30/kb	
Final elongation	72	60/kb	1

### 6.1.6 Bacterial transformation

Plasmid DNA was transformed into heat-shock-competent *Escherichia coli* NEB $\beta$ 10 or DH5 $\alpha$  cells for vector amplification or in electro-competent *E. coli* DH10 *MultiBac*<sup>Turbo</sup> cells for the generation of a bacmid shuttle vector. For bacterial expression of recombinant protein, the expression vector was transformed into heat-shock-competent *E. coli* BL21 (DE3) cells. Standard protocols based on glycerol or CaCl<sub>2</sub> were used to prepare transformation-competent cells, which were thereafter stored at -80°C.

Before transformation, 60  $\mu$ l of competent bacteria were thawed on ice and mixed with 50-150 ng plasmid DNA. After 10 min of incubation, the cells were transformed either by heat-shock or by electroporation. For transformation by heat-shock, the bacteria-DNA mixture was incubated at 42°C for 42 sec and then immediately cooled on ice. For transformation by electroporation, the reaction mixture was transferred into an electroporation cuvette and applied to an electroporator set to 1.7 kV.

After transformation, 800  $\mu$ l LB medium was added and the bacteria were allowed to recover at 37°C and 800 revolutions per minute (rpm) for 60 min to establish the expression of antibiotics resistance genes encoded on the transformed plasmid. In case of bacmid generation, the bacteria were incubated for another 120 min. Afterwards, bacteria were pelleted at 4,000 x g for 5 min and the supernatant was decanted. A residual 50-100  $\mu$ l were retained to resuspend the cells and finally streak them out on LB agar plates containing antibiotics for positive selection of transformed cells. A list of antibiotics and the concentrations used to prepare selection medium or agar plates is shown in Table 6-6.

**Table 6-6: Usage of antibiotics**

Antibiotic	Final concentration
Ampicillin	100 $\mu$ g/ml
Kanamycin	50 $\mu$ g/ml
Gentamycin	7-10 $\mu$ g/ml
Tetracycline	10 $\mu$ g/ml

### **6.1.7 Preparation of plasmid DNA from bacteria**

Single colonies of bacteria were picked from LB agar plates and inoculated in LB medium containing the respective antibiotics. Depending on the scale of the plasmid preparation, the culture volume was adjusted and the bacteria were grown at 37°C in a shaking incubator overnight. At the next day, the bacteria were spun down at 4,000 x g for 5-20 min and the supernatant was removed. Depending on the scale of the bacterial culture, the following DNA purification was performed using the ExtractMe Plasmid Mini Kit, the ExtractMe Plasmid Midi Kit, or the PureLink™ HiPure Plasmid Maxiprep Kit according to the manufacturer's instructions.

### **6.1.8 Determination of DNA concentration**

The concentration and purity of DNA samples was determined using a NanoDrop spectrophotometer. The concentration was measured at 260 nm absorbance ( $A_{260}$  of 1.0 = 50 µg/ml pure dsDNA) and adjusted by bichromatic absorbance correction (measured at 340 nm absorbance). The purity was estimated by evaluating the 260/280 nm and 260/230 nm ratios.

### **6.1.9 Testing of generated expression vectors**

Prior to Sanger sequencing, a newly generated expression vector was tested for the presence of the ligated insert containing the protein-coding sequence. For this purpose, approximately 500 ng of plasmid DNA was digested with appropriate restriction enzymes to excise the insert and linearize the vector. Subsequently, the digested DNA was analyzed by agarose gel electrophoresis to confirm the presence of the respective insert.

### **6.1.10 Sequencing of DNA samples**

To confirm the overall correctness of the expression vector and especially the correct amplification and insertion of the protein-coding sequence after PCR and ligation, Sanger sequencing was performed by external service providers (GATC Biotech AG, Ebersberg, Germany or MicroSynth AG, Göttingen, Germany) using adequate sequencing primers that are listed in Table 7-3. The sequencing results were provided by electronic services and analyzed using ApE software.

### 6.1.11 Preparation of expression vectors for recombinant protein production

The expression vectors for recombinant protein production were generated following the subcloning strategies depicted in Table 6-7. In brief, the protein-coding sequence was amplified using PCR or synthesized at Eurofins Scientific (Luxemburg) and digested using the depicted restriction enzymes. Similarly, the destination vectors were digested with the same set of restriction enzymes to generate compatible overhangs for directed ligation. Prior to ligation, the cleaved amplicons and destination vectors were purified using agarose gel electrophoresis. After ligation, the newly subcloned expression vectors were transformed into competent bacteria and streaked out on LB agar plates containing antibiotics for positive selection. Single colonies were grown to amplify the plasmid DNA, which was subsequently tested for presence of the expression vector containing the respective ligated insert. The sequence was finally confirmed by Sanger sequencing.

A variation of the protocol was performed for subcloning the MBP-NLRP12 (1-1061) expression vector. Because the NLRP12 protein-coding sequence contained the recognition sites for BamHI and EcoRI, three amplicons were generated by performing different PCR reactions on the DNA template vector 2 (Table 7-4). Using specific primer pairs, the BamHI and EcoRI restriction sites were deleted by introducing silent mutations in the protein-coding sequence. The generated amplicons were then used as PCR templates following the depicted subcloning strategy (Table 6-7).

**Table 6-7: Subcloning strategies for the preparation of expression vectors**

Expression vector	Template	Primer	Restriction	Destination
MBP-NLRP9 (1-991)	Vector 1	NLRP9_1+, NLRP9_991-	BamHI, HindIII	Vector 1
GST-NLRP9-PYD (1-97)	Vector 1	NLRP9_1+, NLRP9_97-	NcoI, EcoRI	Vector 3
NLRP9-PYD (1-91)- NLRP3 (91-99)-Linker- mCitrine-HEK	Synthesized at Eurofins Scientific (Luxemburg)		AscI, NotI	Vector 4
NLRP9b-PYD (1-88)- NLRP3 (91-99)-Linker- mCitrine-HEK	Synthesized at Eurofins Scientific (Luxemburg)		AscI, NotI	Vector 4
MBP-NLRP12 (1-1061)	Amplicons	NLRP12_1+, NLRP12_1061-	BamHI, EcoRI	Vector 1
GST-NLRP12-PYD (3-98)	MBP-NLRP12 (1-1061)	NLRP12_3+, NLRP12_98-	NcoI, EcoRI	Vector 3
NLRP12-PYD (1-101)-HEK	MBP-NLRP12 (1-1061)	NLRP12_1+, NLRP12_101-	AscI, NotI	Vector 4
mMBP-NLRP12-NACHT (122-679)	MBP-NLRP12 (1-1061)	NLRP12_122+, NLRP12_679-	NotI, XhoI	Vector 2

MBP-NLRP12-NACHT (122-679)	MBP-NLRP12 (1-1061)	NLRP12_122+, NLRP12_679-	BamHI, EcoRI	Vector 1
Avi-Flag-NLRP12-NACHT (122-679)-HEK-SPR	MBP-NLRP12 (1-1061)	NLRP12_122+, NLRP12_679-	AscI, NotI	Vector 5
MBP-NLRP3-NACHT (131-694)	Vector 3	NLRP3_131+, NLRP3_694-	BamHI, EcoRI	Vector 1
TetO6-NLRP3 (1-1036)- coexpress-mCherry-HEK	Kind gift from Rainer Stahl (Institute of Innate Immunity, University Clinics Bonn, Germany)			
pRP-CMV-NLRP3 (1-1036)-IRES-ATG- mCitrine-HA-HEK	Kind gift from Rainer Stahl (Institute of Innate Immunity, University Clinics Bonn, Germany)			
NLRP3-PYD (1-99)- mCitrine-HEK	Kind gift from Rainer Stahl (Institute of Innate Immunity, University Clinics Bonn, Germany)			
Avi-Flag-NLRP3-NACHT (131-694)-HEK-SPR	Subcloned at IFM Therapeutics (Boston, USA)			
BirA-HEK-SPR	Kind gift from IFM Therapeutics (Boston, USA)			

### 6.1.12 Preparation of the bacmid shuttle vector

The DH10 *MultiBac*<sup>Turbo</sup> strain is transformed with the *MultiBac*<sup>Turbo</sup> bacmid, which consists of a modified baculoviral genome. The bacmid harbors a Tn7 attachment site located within a *lacZa* reporter gene, while all generated *Sf9* expression vectors are based on the pACEBac1 transfer vector containing Tn7 transposition elements. Thus, transformation of an expression vector eventually leads to insertion of Tn7 elements (together with the protein-coding sequence) into the baculoviral genome and disruption of the *lacZa* gene, which can be monitored by blue/white screening using the chromogenic substrate X-Gal (5-bromo-4-chloro-3-indolyl  $\beta$ -D-galactopyranoside). For this purpose, transformed bacteria were streaked out on LB agar plates containing ampicillin, kanamycin, gentamycin, tetracycline (at the concentrations indicated in Table 6-6), X-Gal (100  $\mu$ g/ml), and IPTG (isopropyl- $\beta$ -D-thiogalactopyranoside, 40  $\mu$ g/ml) and grown at 37°C for 48 h or until distinct blue/white selection was possible.

Single white colonies were picked and inoculated in 4 ml LB medium containing antibiotics. The bacteria were grown at 37°C in a shaking incubator overnight and subsequently harvested by centrifugation at 4,000 x g for 5 min. The bacmid shuttle vector was extracted from the cells using the ExtractMe Plasmid Mini Kit. In brief, the pellet was resuspended and the bacteria were lysed by alkaline lysis. After neutralization, the solution was cleared by centrifugation at 20,000 x g for 10 min. The supernatant (~700  $\mu$ l) was transferred into a fresh tube and the bacmid DNA was precipitated by addition of 800  $\mu$ l ice-cold isopropanol. Then, the precipitated DNA was collected by centrifugation at 20,000 x g and 4°C for 30 min. The isopropanol was removed and the DNA pellet was

carefully washed with 800  $\mu$ l ice-cold 70% ethanol. Before the ethanol was removed, the DNA was spun down at 20,000 x g and 4°C for 10 min. The washing step was repeated and the tube was transferred to a sterile tissue culture hood before the ethanol was removed and the DNA pellet was dried by leaving the tube opened. Finally, the bacmid DNA was solubilized in 100  $\mu$ l *Sf9* insect cell medium for subsequent transfection.

## 6.2 Expression of recombinant protein

### 6.2.1 Cultivation of HEK293 cells and *Sf9* insect cells

All work with eucaryotic cell cultures was performed in a sterile tissue culture hood. Consumables that were used during this work were sterilized with 80% ethanol before placing them in the tissue culture hood. Cells were cultured in single-use plasticware (adherent culture) or appropriately sterilized glassware (suspension culture).

*Sf9* insect cells were grown as suspension cultures in SF900™ SFM III medium at 27°C and 80 rpm. The cell density was monitored every 3 days and adjusted to not exceed 5 x 10<sup>6</sup> cells/ml. For this purpose, 10  $\mu$ l of the cell suspension was mixed 1:1 (v/v) with 0.4% trypan blue solution to stain dead cells and subsequently counted using the EVE™ automatic cell counter. If necessary, the cells were split to achieve a lower density.

FreeStyle™ HEK293-F cells were grown as suspension cultures in FreeStyle™ 293 expression medium at 37°C, 5% CO<sub>2</sub> and 135 rpm. The cell density was monitored every 3 days and the cells were split to maintain a cell density below 1 x 10<sup>6</sup> cells/ml. To count the cells, 10  $\mu$ l of the cell suspension was mixed 1:1 (v/v) with 0.4% trypan blue solution and analyzed using a Neubauer counting chamber.

HEK293T cells were grown as adherent cultures in DMEM (Dulbecco's modified eagle's medium) containing high glucose and supplemented with 100 U/ml penicillin, 0.1% (w/v) streptomycin, 2 mM L-glutamine, and 10% FBS (fetal bovine serum) at 37°C and 5% CO<sub>2</sub>. The cell density was monitored every 3 days and the cells were passaged at 80-90% confluency. To this end, the growth medium was removed and the cells were washed with 10 ml DPBS (Dulbecco's phosphate-buffered saline). Next, the cells were incubated for 5 min at 37°C and in the presence of 10 ml Trypsin/EDTA (ethylenediaminetetraacetic acid). Then, the cells were carefully rinsed with 5 ml growth medium before they were collected by centrifugation at 400 x g for 5 min. The cells were resuspended in 1 ml growth medium and eventually counted using a Neubauer counting chamber. For passaging, 100  $\mu$ l of the cells was transferred to a new culture.

### 6.2.2 Preparation and propagation of recombinant baculovirus

Generated bacmid shuttle vectors were transfected into *Sf9* insect cells for the production of recombinant baculovirus particles that can be subsequently used to infect a larger *Sf9* insect cell culture for heterologous expression of recombinant protein.

700,000 cells per well (3 ml) were seeded into 6-well culture plates and allowed to adhere at 27°C for 30 min. In the meanwhile, 8 µl of Cellfectin™ or 5 µl TransIT™-Insect transfection reagent was diluted in 100 µl *Sf9* insect cell medium and then mixed with the prepared bacmid DNA (see section 6.1.12). To form DNA-lipid complexes, the solution was incubated at RT for 20 min. For transfection, the solution was transferred to a respective well and incubated with the cells at 27°C. After 3-4 h, the medium was replaced and the cells were further incubated for 72 h to produce viral particles ( $V_0$ ).

For propagation, a 50 ml suspension culture of *Sf9* insect cells ( $0.5 \times 10^6$  cells/ml) was infected with 3% (v/v) of  $V_0$  supernatant and cultured for 72 h. Successful infection of *Sf9* insect cells was monitored by a stop of cell division and an increase in cell size. After incubation, the cells were pelleted by centrifugation at 500 x g for 20 min and the supernatant ( $V_1$ ) was collected and filtered (0.45 µm pore size). To further propagate the viral particles, the procedure was repeated with a 200 ml suspension culture of *Sf9* insect cells ( $1 \times 10^6$  cells/ml) infected with 3% (v/v) of  $V_1$  to produce a  $V_2$  viral stock. All viral stocks were stored at 4°C until use.

### 6.2.3 Recombinant protein expression in *Sf9* insect cells

For recombinant protein expression, a suspension culture of *Sf9* insect cells ( $1.5 \times 10^6$  cells/ml) was infected with 3% (v/v) of  $V_2$  and cultured for 72 h. The cells were collected by centrifugation at 1,000 x g and 4°C for 20 min and washed with cold PBS. Finally, the cell pellet was snap-frozen in liquid nitrogen and stored at -80°C until purification.

### 6.2.4 Recombinant protein expression in FreeStyle™ HEK293-F cells

For each transfection, a 150 ml suspension culture ( $0.25 \times 10^6$  cells/ml) was prepared and grown for 48 h or until the cell density reached  $1 \times 10^6$  cells/ml. 150 µg of plasmid DNA and 600 µg PEI (polyethylenimine) transfection reagent was diluted in 7.5 ml OptiMEM (improved serum-free minimal essential medium), respectively. Both solutions were vortexed, incubated for 5 min, mixed, incubated for 20 min, and then transferred to the cells. The cells were cultured for 24 h before they were harvested. For this purpose, the

cells were collected by centrifugation at 1,300 x g and 4°C for 20 min. Finally, the pellet was washed with cold PBS, snap-frozen in liquid nitrogen, and stored at -80°C until purification.

### **6.2.5 Recombinant protein expression in HEK293T cells**

HEK293T cells were seeded in T175 cell culture flasks and grown until confluency reached 60-70%. Then, the culture medium was exchanged and the transfection was started. For each flask, 30 µg of plasmid DNA and 160 µl of Transporter 5 transfection reagent was diluted in 1 ml OptiMEM, respectively. The solutions were vortexed, incubated for 5 min, mixed, incubated for 20 min, and then transferred to the cells. The cells were cultured for 24 h before they were harvested. For this purpose, the medium was removed and the cells were carefully washed before they were scraped into cold DPBS. Finally, the cells were collected by centrifugation at 1,300 x g and 4 °C for 15 min, snap-frozen in liquid nitrogen, and stored at -80°C until purification.

### **6.2.6 Recombinant protein expression in *Escherichia coli***

The expression vector was transformed into *E. coli* BL21 (DE3) cells as described above (see section 6.1.6) and streaked out on LB agar plates containing the appropriate antibiotics. Bacteria were picked from single colonies and inoculated in 50-100 ml LB medium containing antibiotics to grow a starter culture at 37°C in a shaking incubator overnight. The starter culture was used to inoculate a 1 L expression culture to obtain an optical density (OD)<sub>600</sub> value of 0.1. The expression culture was grown at 37°C in a shaking incubator until OD<sub>600</sub> reached a value greater than 0.8. Then, the cells were cooled to 16°C and the expression was induced by addition of 0.5-0.55 mM IPTG. The bacteria were further grown at 16°C in a shaking incubator overnight and harvested by centrifugation at 4,000 x g and 4°C for 20 min. The cell pellet was washed with cold PBS, snap-frozen in liquid nitrogen, and stored at -80°C until purification.

## **6.3 Protein purification**

### **6.3.1 Cell lysis**

The frozen cells were resuspended in 5 ml lysis buffer per gram of cell pellet and thawed on ice using a magnetic stirrer. In case of *Sf9* insect cells or bacteria, the lysis buffer was supplemented with 1 mM PMSF (phenylmethylsulfonylfluoride) and 1 µg/ml DNase I to



prevent the degradation by cellular proteases and to reduce the viscosity of the lysate, respectively. In case of bacteria, the lysis buffer was further supplemented with a spatula tip of lysozyme. In case of HEK293 cells, 50 ml lysis buffer was supplemented with one tablet of cOmplete™ ULTRA, EDTA free protease inhibitor cocktail. *Sf9* insect cells and bacteria were lysed by sonication with continuous cooling on ice (*Sf9*: 6 s on-time, 5 s off-time for 4-6 min at 40% intensity; bacteria: 50 s on-time, 50 s off-time at 70, 80, and 90% intensity). HEK293 cells were lysed by solubilization of cell membranes using Triton X-100 contained in the lysis buffer. For this purpose, HEK293 cells were incubated in lysis buffer for 30 min on ice. Crude cell lysates were cleared by centrifugation at 10°C and appropriate g-force before the supernatant was filtered (0.45 µm pore size).

### **6.3.2 Affinity chromatography**

Affinity chromatography was used as the first purification step. Specific binding properties of the recombinant protein towards an immobilized ligand was utilized to reversibly capture the protein of interest on a stationary phase, while endogenous proteins and other cell components did flow through. For this purpose, the expression constructs were designed to harbor an N-terminal affinity tag with well-known binding properties towards their ligand molecules. In this study, recombinant proteins were fused to GST (glutathione-S-transferase)-, MBP (maltose-binding protein)-, or Flag-affinity tags and purified via GSTrap or MBPTrap columns connected to a fast protein liquid chromatography (FPLC) system (Äkta Prime Plus or Äkta Start) or via specific affinity resins packed into Econo-Pac™ columns for gravity-flow chromatography. At a final step and after washing, the bound protein was eluted by application of a binding-competitive molecule, such as glutathione, maltose, or soluble Flag peptide. All purification steps were performed on ice or in a cooling cabinet set to 4°C.

### **6.3.3 Determination of protein concentration**

The concentration and purity of protein samples was determined using a NanoDrop spectrophotometer. The absorbance at 280 nm wavelength was measured and adjusted by bichromatic absorbance correction (measured at 340 nm absorbance) to calculate the protein concentration according to the Beer-Lambert law:  $A = \epsilon lc$ , where A is the absorbance,  $\epsilon$  is the extinction coefficient at 280 nm, l is the optical path length and c is the concentration in mol/L. The purity was estimated by evaluating the 260/280 nm ratio.

### 6.3.4 Affinity tag cleavage

Most expression constructs were designed to contain a sequence coding for a tobacco etch virus (TEV) protease cleavage site (amino acid sequence: ENLYFQGS) directly upstream of the protein of interest. Thus, the N-terminal affinity tag could be cleaved off the protein after affinity chromatography to reconstitute a more native state. TEV cleavage was performed at 4°C overnight by addition of TEV protease to the affinity-purified protein. TEV protease was prepared in house using established protocols.

### 6.3.5 Dialysis

In certain cases, affinity tag cleavage was performed in combination with a buffer exchange by dialysis. The protein solution (~5 ml) was transferred into a SnakeSkin™ dialysis tubing (3.5 kDa MWCO) and dialyzed against 200 ml dialysis buffer at 4°C overnight. The dialysis buffer was constantly stirred at low speed using a magnetic stirrer.

### 6.3.6 Preparative size-exclusion chromatography

Preparative size-exclusion chromatography (SEC) was applied as the final purification or polishing step to remove residual contaminants, such as the supplemented TEV protease. In addition, monomeric and defined oligomeric species could be separated and individually collected. This separation is achieved by a porous gel matrix that allows proteins of small hydrodynamic radius to diffuse into the material and be retained, while proteins of larger hydrodynamic radius pass through the matrix faster and therefore elute first. A list of gel filtration columns used for preparative size-exclusion chromatography is given in Table 7-7. If necessary, a tandem affinity chromatography column was connected to the gel filtration column to increase retention and thus separation of the cleaved affinity tag from the protein of interest. Gel filtration columns were operated in combination with an appropriate FPLC system (Äkta Prime Plus or Äkta Pure) located in a cooling cabinet set to 4°C. After equilibration of the column with at least one column volume (CV) of the respective SEC buffer, the protein sample was injected from a sample loop connected to the FPLC system and the flow-through was fractionated by an automated fraction collector. After SDS-PAGE analysis, fractions containing the protein of interest were pooled, concentrated, snap-frozen in liquid nitrogen and stored at -80°C. Detailed purification protocols are supplied in section 6.3.9.

### 6.3.7 Sucrose density gradient centrifugation

Sucrose density gradient centrifugation was applied as an alternative method to size-exclusion chromatography. Using a custom-built tool, a 10-40% sucrose gradient was prepared in an ultracentrifugation tube. The protein sample was carefully pipetted on top of the gradient and separated by centrifugation for 14 h at 35,500 rpm and 4°C in a SW60 Ti swinging bucket rotor.

### 6.3.8 Concentration of protein samples

Protein samples were concentrated by centrifugation at 4°C in an Amicon™ Ultra Centrifugal Filter Unit according to the manufacturer's instructions. The filter unit features a regenerated cellulose membrane with a defined pore size. Proteins with larger size are retained while buffer passes the membrane and sample volume decreases.

### 6.3.9 Protein purification protocols

#### Human NLRP9 full-length (1-991)

Buffers			
Lysis buffer		SEC buffer	
HEPES pH 7.2	50 mM	HEPES pH 7.2	20 mM
NaCl	500 mM	NaCl	500 mM
DTT	1 mM	TCEP	1 mM
MgCl <sub>2</sub>	5 mM	MgCl <sub>2</sub>	5 mM
Glycerol	10%	Glycerol	10%

Elution buffer is prepared by supplementing lysis buffer with 10 mM maltose.

#### Protocol

NLRP9 (1-991) was expressed as MBP-fusion protein in *Sf9* insect cells as described and the harvested cells were stored at -80°C. For purification, the frozen cell pellet was resuspended in lysis buffer and thawed on ice, whereafter PMSF and DNase I was added. Subsequently, the cells were lysed by sonication and the crude lysate was cleared by centrifugation at 70,000 x g and 10°C for 50 min. After filtration, the lysate was applied to an MBPTrap column equilibrated with lysis buffer for affinity purification. The flow rate was set to 1 ml/min and the presence of protein was followed via the absorbance at 280 nm wavelength. The column was washed with lysis buffer until A<sub>280</sub> reached baseline levels (~20 CV), before the protein was eluted in 1 ml fractions. The peak fractions were pooled and supplemented with 1:25 (w/w) TEV protease for cleavage of the affinity tag. The sample was incubated at 4°C overnight, centrifuged at 10,000 x g and 4°C for 10 min and then loaded onto a Superose 6 PG XK 16/70 column equilibrated with SEC buffer. The flow-through was collected in 2 ml fractions and analyzed by SDS-PAGE. The void and monomeric peak fractions containing NLRP9 (1-991) were pooled and concentrated, respectively. The protein was snap-frozen in liquid nitrogen and stored at -80°C.

Human NLRP9 PYD (1-97)

<b>Buffers</b>					
<b>Lysis buffer</b>		<b>Wash buffer</b>		<b>SEC buffer</b>	
HEPES pH 7.5	50 mM	HEPES pH 7.5	50 mM	HEPES pH 7.5	50 mM
NaCl	150 mM	NaCl	300 mM	NaCl	150 mM
$\beta$ ME	10 mM	$\beta$ ME	10 mM	TCEP	1 mM

Elution buffer is prepared by supplementing lysis buffer with 10 mM reduced glutathione.

<b>Protocol</b>
<p>NLRP9 PYD (1-97) was expressed as GST-fusion protein in <i>E. coli</i> cells as described and the harvested cells were stored at -80°C. For purification, the frozen cell pellet was resuspended in lysis buffer and thawed on ice, whereafter PMSF and DNase I was added. Subsequently, the cells were lysed by the addition of lysozyme and further sonication. The crude lysate was cleared by centrifugation at 70,000 x g and 10°C for 30 min. After filtration, the lysate was applied to a GSTrap column equilibrated with lysis buffer for affinity purification. The flow rate was set to 1 ml/min and the presence of protein was followed via the absorbance at 280 nm wavelength. The column was washed with wash buffer until <math>A_{280}</math> reached baseline levels (~20 CV). Then, the column was washed with 3 CV lysis buffer, before the protein was eluted in 1 ml fractions. The peak fractions were pooled and supplemented with 1:100 (w/w) TEV protease for cleavage of the affinity tag. The sample was incubated at 4°C overnight, centrifuged at 10,000 x g and 4°C for 10 min and then loaded onto a HiLoad 16/600 Superdex 75 PG column connected to a tandem GSTrap column for prolonged retention of the cleaved GST tag. Before loading, both columns were equilibrated with SEC buffer. The flow-through was collected in 2 ml fractions and analyzed by SDS-PAGE. The monomeric peak fractions containing NLRP9 PYD (1-97) were pooled and concentrated to 31.7 mg/ml. The protein was snap-frozen in liquid nitrogen and stored at -80°C.</p>

Human NLRP12 full-length (1-1061)

The following protocol was applied to purify protein shown in Figure 3-3b-d. Protein used in ATPase assays and nanoDSF (Figure 3-4) was purified using a variation of the purification buffers (lysis buffer II and SEC buffer II) and the affinity tag was not cleaved. Data shown in Figure 3-4b, c was generated with protein purified in the absence of CHAPS.

<b>Buffers</b>					
<b>Lysis buffer</b>		<b>Lysis buffer II</b>		<b>SEC buffer</b>	
Tris pH 8.5	50 mM	Tris pH 8.0	20 mM	Tris pH 8.5	50 mM
NaCl	10 mM	NaCl	150 mM	NaCl	10 mM
KCl	150 mM	$\beta$ ME	15 mM	KCl	150 mM
EDTA	2 mM	CHAPS	0.25%	TCEP	1 mM
$\beta$ ME	15 mM	Sucrose	10%		
CHAPS	0.25%				
Sucrose	10%				
<b>SEC buffer II</b>		Elution buffer is prepared by supplementing lysis buffer with 10 mM maltose.			
HEPES pH 8.0	20 mM				
NaCl	150 mM				
TCEP	1 mM				
Sucrose	10%				
<b>Protocol</b>					
<p>NLRP12 (1-1061) was expressed as MBP-fusion protein in <i>Sf9</i> insect cells as described and the harvested cells were stored at -80°C. For purification, the frozen cell pellet was resuspended in lysis buffer and thawed on ice, whereafter DNase I was added. Subsequently, the cells were lysed by sonication (10-20 s on-time, 20 s off-time for 4 min at 80% intensity) and the crude lysate was cleared by centrifugation at 10,000 x g and 4°C for 30 min. After filtration, the lysate was applied to an MBPTrap column equilibrated with lysis buffer for affinity purification. The flow rate was set to 0.5 or 1 ml/min and the presence of protein was followed via the absorbance at 280 nm wavelength. The column was washed with lysis buffer until <math>A_{280}</math> reached baseline levels (~20 CV), before the protein was eluted in 1 ml fractions. The peak fractions were pooled and supplemented with 1:100 (w/w) TEV protease for cleavage of the affinity tag. The sample was incubated at 4°C overnight, centrifuged at 10,000 x g and 4°C for 10 min and then loaded onto a Superose 6 PG XK 16/70 column equilibrated with SEC buffer. The flow-through was collected in 2 ml fractions and analyzed by SDS-PAGE. The void peak fractions containing NLRP12 (1-1061) were pooled and concentrated. The protein was snap-frozen in liquid nitrogen and stored at -80°C.</p>					

The following protocol was applied to purify human NLRP12 full-length (1-1061) protein using sucrose density gradient centrifugation (Figure 3-3e).

<b>Buffers</b>					
<b>Lysis buffer</b>		<b>Wash buffer</b>		<b>Sucrose buffer</b>	
Tris pH 8.5	50 mM	Tris pH 8.5	50 mM	Tris pH 8.5	20 mM
NaCl	10 mM	NaCl	10 mM	NaCl	10 mM
KCl	150 mM	KCl	150 mM	KCl	150 mM
EDTA	2 mM	TCEP	1 mM	TCEP	1 mM
βME	15 mM			Sucrose	10%, 40%
CHAPS	0.25%				
Sucrose	10%				

Elution buffer is prepared by supplementing wash buffer with 10 mM maltose.

<b>Protocol</b>
<p>NLRP12 (1-1061) was expressed as MBP-fusion protein in <i>Sf9</i> insect cells as described and the harvested cells were stored at -80°C. For purification, the frozen cell pellet was resuspended in lysis buffer and thawed on ice, whereafter PMSF and DNase I was added. Subsequently, the cells were lysed by sonication (10 s on-time, 20 s off-time for 4 min at 80% intensity) and the crude lysate was cleared by centrifugation at 10,000 x g and 4°C for 30 min. After filtration, the lysate was applied to amylose resin (1.5 ml bead slurry per 500 ml culture) equilibrated with lysis buffer for affinity purification. The resin was packed into an Econo-Pac™ column. The resin was washed with 30 CV lysis buffer and 15 CV wash buffer, before the protein was eluted in 1 ml fractions. The protein concentration of the individual fractions was measured to supplement 1:100 (w/w) TEV protease for cleavage of the affinity tag. The samples were incubated at 4°C overnight and subsequently 2 nmol of the protein was loaded onto a 10-40% sucrose gradient. Sucrose density gradient centrifugation was applied as described above. After centrifugation, the sucrose gradient was fractionated in 200 µl fractions, which were analyzed by SDS-PAGE and negative stain electron microscopy. The residual protein was snap-frozen in liquid nitrogen and stored at -80°C.</p>

The following protocol was applied to purify wildtype and mutant human NLRP12 full length (1-1061) protein that was analyzed in ATPase assays (Figure 3-5b).

<b>Buffers</b>					
<b>Lysis buffer</b>		<b>Elution buffer</b>		<b>SEC buffer</b>	
HEPES pH 7.5	100 mM	HEPES pH 7.5	50 mM	HEPES pH 7.5	25 mM
NaCl	50 mM	NaCl	50 mM	NaCl	50 mM
Glycerol	20%	Maltose	10 mM	Maltose	2 mM
		Glycerol	20%	Glycerol	20%

The SEC buffer was supplemented with 2 mM maltose for improved protein stability.

#### **Protocol**

Wildtype or mutant NLRP12 (1-1061) was expressed as MBP-fusion protein in *Sf9* insect cells as described and the harvested cells were stored at -80°C. For purification, the frozen cell pellet was resuspended in lysis buffer and thawed on ice, whereafter PMSF and DNase I was added. Subsequently, the cells were lysed by sonication as described and the crude lysate was cleared by centrifugation at 70,000 x g and 10°C for 30 min. After filtration, the lysate was applied to an MBPTrap column equilibrated with lysis buffer for affinity purification. The flow rate was set to 1 ml/min and the presence of protein was followed via the absorbance at 280 nm wavelength. The column was washed with lysis buffer until A<sub>280</sub> reached baseline levels (~20 CV), before the protein was eluted in 1 ml fractions. The peak fractions were pooled, concentrated, and centrifuged at 10,000 x g and 4°C for 10 min. Then, the protein was loaded onto a Superose 6 Increase 10/300 GL column equilibrated with SEC buffer. The flow-through was collected in 0.5 ml fractions and analyzed by SDS-PAGE. The void peak fractions containing NLRP12 (1-1061) were pooled and concentrated. The protein was snap-frozen in liquid nitrogen and stored at -80°C.

Human NLRP12 PYD (3-98, wildtype and W45R mutant)

<b>Buffers</b>					
<b>Lysis buffer</b>		<b>Wash buffer</b>		<b>SEC buffer</b>	
HEPES pH 7.5	50 mM	HEPES pH 7.5	50 mM	HEPES pH 7.5	50 mM
NaCl	150 mM	NaCl	300 mM	NaCl	150 mM
$\beta$ ME	10 mM	$\beta$ ME	10 mM	TCEP	1 mM

Elution buffer is prepared by supplementing lysis buffer with 10 mM reduced glutathione.

<b>Protocol</b>
<p>NLRP12 PYD (3-98) was expressed as GST-fusion protein in <i>E. coli</i> cells as described and the harvested cells were stored at -80°C. For purification, the frozen cell pellet was resuspended in lysis buffer and thawed on ice, whereafter PMSF and DNase I was added. Subsequently, the cells were lysed by the addition of lysozyme and further sonication. The crude lysate was cleared by centrifugation at 70,000 x g and 10°C for 30 min. After filtration, the lysate was applied to a GSTrap column equilibrated with lysis buffer for affinity purification. The flow rate was set to 1 ml/min and the presence of protein was followed via the absorbance at 280 nm wavelength. The column was washed with wash buffer until <math>A_{280}</math> reached baseline levels (~20 CV). Then, the column was washed with 3 CV lysis buffer, before the protein was eluted in 2 ml fractions. The peak fractions were pooled and supplemented with 1:100 (w/w) TEV protease for cleavage of the affinity tag. The sample was incubated at 4°C overnight, centrifuged at 10,000 x g and 4°C for 10 min and then loaded onto a HiLoad 16/600 Superdex 75 PG column connected to a tandem GSTrap column for prolonged retention of the cleaved GST tag. Before loading, both columns were equilibrated with SEC buffer. The flow-through was collected in 2 ml fractions and analyzed by SDS-PAGE. The monomeric peak fractions containing NLRP12 PYD (3-97) were pooled and concentrated. The protein was snap-frozen in liquid nitrogen and stored at -80°C.</p>



Human NLRP12 $\Delta$ PYD (122-1061)**Buffers**

<b>Lysis buffer</b>		<b>SEC buffer</b>	
Tris pH 7.4	50 mM	HEPES pH 7.4	20 mM
NaCl	200 mM	NaCl	150 mM
TCEP	0.5 mM	TCEP	0.5 mM
Glycerol	10%		

Elution buffer is prepared by supplementing lysis buffer with 10 mM maltose.

**Protocol**

NLRP12 (122-1061) was expressed as MBP-fusion protein in *Sf9* insect cells as described and the harvested cells were stored at -80°C. For purification, the frozen cell pellet was resuspended in lysis buffer and thawed on ice, whereafter PMSF and DNase I was added. Subsequently, the cells were lysed by sonication as described and the crude lysate was cleared by centrifugation at 70,000 x g and 10°C for 50 min. After filtration, the lysate was applied to an MBPTrap column equilibrated with lysis buffer for affinity purification. The flow rate was set to 1 ml/min and the presence of protein was followed via the absorbance at 280 nm wavelength. The column was washed with lysis buffer until A<sub>280</sub> reached baseline levels (~20 CV), before the protein was eluted in 1 ml fractions. The peak fractions were pooled, concentrated, and centrifuged at 10,000 x g and 4°C for 10 min. Then, the protein was loaded onto a Superose 6 Increase 10/300 GL column equilibrated with SEC buffer. The flow-through was collected in 0.5 ml fractions and analyzed by SDS-PAGE. The void peak fractions containing NLRP12 (122-1061) were pooled and concentrated. The protein was snap-frozen in liquid nitrogen and stored at -80°C.

Human NLRP12 $\Delta$ LRR (1-679) and NLRP12 NACHT (122-679)**Buffers**

<b>Lysis buffer</b>		<b>SEC buffer</b>	
Tris pH 8.0	20 mM	HEPES pH 8.0	20 mM
NaCl	150 mM	NaCl	150 mM
$\beta$ ME	5 mM	TCEP	1 mM

Elution buffer is prepared by supplementing lysis buffer with 10 mM maltose. In case the CRID3 effect was investigated (Figure 3-16a), the buffers were each supplemented with 1  $\mu$ M CRID3.

**Protocol**

NLRP12 (1-679 or 122-679) was expressed as MBP-fusion protein in *Sf9* insect cells as described and the harvested cells were stored at  $-80^{\circ}\text{C}$ . In case the CRID3 effect was investigated (Figure 3-16a), protein expression was performed in the presence of 5  $\mu$ M CRID3 added to the culture medium. For purification, the frozen cell pellet was resuspended in lysis buffer and thawed on ice, whereafter PMSF and DNase I was added. Subsequently, the cells were lysed by sonication as described and the crude lysate was cleared by centrifugation at 70,000 x g and  $10^{\circ}\text{C}$  for 50 min. After filtration, the lysate was applied to an MBPTrap column equilibrated with lysis buffer for affinity purification. The flow rate was set to 1 ml/min and the presence of protein was followed via the absorbance at 280 nm wavelength. The column was washed with lysis buffer until  $A_{280}$  reached baseline levels ( $\sim 20$  CV), before the protein was eluted in 1 ml fractions. The peak fractions were pooled, concentrated, and centrifuged at 10,000 x g and  $4^{\circ}\text{C}$  for 10 min. Then, the protein was loaded onto a Superose 6 Increase 10/300 GL column equilibrated with SEC buffer. The flow-through was collected in 0.5 ml fractions and analyzed by SDS-PAGE. The void, oligomeric, and monomeric peak fractions containing NLRP12 (1-679 or 122-679) were pooled and concentrated, respectively. The protein was snap-frozen in liquid nitrogen and stored at  $-80^{\circ}\text{C}$ .

The following protocol was applied to purify NLRP12 NACHT (122-679) protein after optimization of the buffer conditions using nanoDSF (Figure 3-17).

<b>Buffers</b>					
<b>Lysis buffer</b>		<b>Elution buffer</b>		<b>SEC buffer</b>	
HEPES pH 7.5	100 mM	HEPES pH 7.5	50 mM	HEPES pH 7.5	25 mM
NaCl	50 mM	NaCl	50 mM	NaCl	50 mM
Glycerol	20%	Maltose	10 mM	Maltose	2 mM
		Glycerol	20%	Glycerol	20%

The SEC buffer was supplemented with 2 mM maltose for improved protein stability.

#### **Protocol**

NLRP12 (122-679) was expressed as MBP-fusion protein in *Sf9* insect cells as described and the harvested cells were stored at -80°C. For purification, the frozen cell pellet was resuspended in lysis buffer and thawed on ice, whereafter PMSF and DNase I was added. Subsequently, the cells were lysed by sonication as described and the crude lysate was cleared by centrifugation at 70,000 x g and 10°C for 50 min. After filtration, the lysate was applied to an MBPTrap column equilibrated with lysis buffer for affinity purification. The flow rate was set to 1 ml/min and the presence of protein was followed via the absorbance at 280 nm wavelength. The column was washed with lysis buffer until A<sub>280</sub> reached baseline levels (~20 CV), before the protein was eluted in 1 ml fractions. The peak fractions were pooled, concentrated, and centrifuged at 10,000 x g and 4°C for 10 min. Then, the protein was loaded onto a Superdex 200 Increase 10/300 GL column equilibrated with SEC buffer. The flow-through was collected in 0.5 ml fractions and analyzed by SDS-PAGE. The monomeric peak fractions containing NLRP12 (122-679) were pooled and concentrated. The protein was snap-frozen in liquid nitrogen and stored at -80°C.

The following protocol was applied to purify NLRP12 NACHT (122-679) with cleaved MBP affinity tag (Figure 3-18).

<b>Buffers</b>					
<b>Lysis buffer</b>		<b>Dialysis buffer</b>		<b>SEC buffer</b>	
Tris pH 7.8	20 mM	HEPES pH 7.8	20 mM	HEPES pH 7.8	20 mM
NaCl	150 mM	NaCl	150 mM	NaCl	150 mM
MgCl <sub>2</sub>	10 mM	MgCl <sub>2</sub>	10 mM	MgCl <sub>2</sub>	10 mM
ADP	1 mM	ADP	1 mM	ADP	1 mM
βME	5 mM	TCEP	1 mM	TCEP	1 mM
		L-arginine	500 mM	L-arginine	150 mM

Elution buffer is prepared by supplementing lysis buffer with 10 mM maltose.

<b>Protocol</b>
<p>NLRP12 (122-679) was expressed as MBP-fusion protein in <i>Sf9</i> insect cells as described and the harvested cells were stored at -80°C. For purification, the frozen cell pellet was resuspended in lysis buffer and thawed on ice, whereafter PMSF and DNase I was added. Subsequently, the cells were lysed by sonication as described and the crude lysate was cleared by centrifugation at 70,000 x g and 10°C for 40 min. After filtration, the lysate was applied to an MBPTrap column equilibrated with lysis buffer for affinity purification. The flow rate was set to 1 ml/min and the presence of protein was followed via the absorbance at 280 nm wavelength. The column was washed with lysis buffer until A<sub>280</sub> reached baseline levels (~20 CV), before the protein was eluted in 1 ml fractions. The peak fractions were pooled and supplemented with 1:50 (w/w) TEV protease for cleavage of the affinity tag. The sample (~5 ml) was incubated at 4°C overnight while dialyzed against 200 ml dialysis buffer. After dialysis, the sample was collected, centrifuged at 10,000 x g and 4°C for 10 min, and then loaded onto a HiLoad 16/600 Superdex 75 PG column connected to a tandem MBPTrap column for prolonged retention of the cleaved MBP tag. Before loading, both columns were equilibrated with SEC buffer. The flow-through was collected in 2 ml fractions and analyzed by SDS-PAGE. The monomeric peak fractions containing NLRP12 (122-679) were pooled and concentrated. The protein was snap-frozen in liquid nitrogen and stored at -80°C.</p>

The following protocol was applied to purify NLRP12 NACHT (122-679) protein for SPR spectroscopy (Figure 3-16c).

<b>Buffers</b>			
<b>Lysis buffer</b>		<b>Elution buffer</b>	
HEPES pH 7.5	20 mM	HEPES pH 7.5	20 mM
NaCl	150 mM	NaCl	150 mM
MgCl <sub>2</sub>	2 mM	MgCl <sub>2</sub>	2 mM
ADP	0.5 mM	ADP	0.5 mM
TCEP	1 mM	TCEP	1 mM
Triton X-100	1%	Glycerol	10%
Glycerol	10%	3x Flag peptide	100 µg/ml

<b>Protocol</b>
<p>NLRP12 (122-679) used for SPR spectroscopy was expressed as Avi-Flag-His<sub>10</sub>-fusion protein in HEK293T cells as described in section 6.2.5. The N-terminal Avi tag was biotinylated in cells by co-transfection of the BirA expression vector (Table 6-7) at a ratio of 1:6 (i.e., 5 of 30 µg plasmid DNA). In addition, cells were supplemented with 10 µM CRID3 four hours after transfection to potentially stabilize an inactive conformation of the recombinant protein produced. For purification, the frozen cell pellet was resuspended in lysis buffer supplemented with cOmplete™ ULTRA, EDTA free protease inhibitor cocktail and thawed on ice. Subsequently, the cells were lysed by incubation on ice for 30 min and the crude lysate was cleared by centrifugation at 12,000 x g and 4°C for 10 min. The lysate was applied to anti-Flag M2 affinity gel (1.5 ml bead slurry per 5 x T175 culture flask) equilibrated with 3 CV glycine pH 3.5 and 10 CV lysis buffer for affinity purification. The protein-resin solution was transferred into a 50 ml falcon tube and the protein was allowed to bind to the resin at 4°C and under constant rotation for at least 1 h. The protein-bound resin was packed into an Econo-Pac™ column and the unbound fraction was allowed to flow-through by gravity flow. The resin was washed with 20 CV lysis buffer, before the protein was eluted with 2 CV elution buffer. The protein was analyzed by SDS-PAGE, snap-frozen in liquid nitrogen, and stored at -80°C.</p>

Human NLRP3 NACHT (131-694)

<b>Buffers</b>					
<b>Lysis buffer</b>		<b>Dialysis buffer</b>		<b>SEC buffer</b>	
Tris pH 7.8	20 mM	HEPES pH 7.8	20 mM	HEPES pH 7.8	20 mM
NaCl	150 mM	NaCl	150 mM	NaCl	150 mM
MgCl <sub>2</sub>	10 mM	MgCl <sub>2</sub>	10 mM	MgCl <sub>2</sub>	10 mM
ADP	1 mM	ADP	1 mM	ADP	1 mM
βME	5 mM	TCEP	1 mM	TCEP	1 mM
CRID3	10 μM	L-arginine	500 mM	L-arginine	150 mM
		CRID3	10 μM	CRID3	10 μM

Elution buffer is prepared by supplementing lysis buffer with 10 mM maltose. For some biochemical analyses, the protein was purified in the absence of ADP and CRID3.

<b>Protocol</b>
<p>NLRP3 (131-694) was expressed as MBP-fusion protein in <i>Sf9</i> insect cells as described and the harvested cells were stored at -80°C. For purification, the frozen cell pellet was resuspended in lysis buffer and thawed on ice, whereafter PMSF and DNase I was added. Subsequently, the cells were lysed by sonication as described and the crude lysate was cleared by centrifugation at 70,000 x g and 10°C for at least 30 min. After filtration, the lysate was applied to an MBPTrap column equilibrated with lysis buffer for affinity purification. The flow rate was set to 1 ml/min and the presence of protein was followed via the absorbance at 280 nm wavelength. The column was washed with lysis buffer until A<sub>280</sub> reached baseline levels (~20 CV), before the protein was eluted in 1 ml fractions. The peak fractions were pooled and supplemented with 1:50 (w/w) TEV protease for cleavage of the affinity tag. The sample (~5 ml) was incubated at 4°C overnight while dialyzed against 200 ml dialysis buffer. After dialysis, the sample was collected, centrifuged at 10,000 x g and 4°C for 10 min, and then loaded onto a HiLoad 16/600 Superdex 75 PG column connected to a tandem MBPTrap column for prolonged retention of the cleaved MBP tag. Before loading, both columns were equilibrated with SEC buffer. The flow-through was collected in 2 ml fractions and analyzed by SDS-PAGE. The monomeric peak fractions containing NLRP3 (131-694) were pooled and concentrated to 9 mg/ml. The protein was snap-frozen in liquid nitrogen and stored at -80°C. For some biochemical analyses, the protein was purified in the absence of ADP and CRID3. Due to lower solubility of the protein, the concentration was adjusted to 1 mg/ml.</p>

The following protocol was applied to purify NLRP3 NACHT (131-694, wildtype and mutants) protein for SPR spectroscopy.

<b>Buffers</b>			
<b>Lysis buffer</b>		<b>Elution buffer</b>	
HEPES pH 7.5	20 mM	HEPES pH 7.5	20 mM
NaCl	150 mM	NaCl	150 mM
MgCl <sub>2</sub>	2 mM	MgCl <sub>2</sub>	2 mM
ADP	0.5 mM	ADP	0.5 mM
TCEP	1 mM	TCEP	1 mM
Triton X-100	1%	Glycerol	10%
Glycerol	10%	3x Flag peptide	100 µg/ml

<b>Protocol</b>
<p>NLRP3 (131-694) used for SPR spectroscopy was expressed as Avi-Flag-His<sub>10</sub>-fusion protein in FreeStyle™ HEK293-F cells as described in section 6.2.4. The N-terminal Avi tag was biotinylated in cells by co-transfection of the BirA expression vector (Table 6-7) at a ratio of 1:6 (i.e., 25 of 150 µg plasmid DNA). In addition, cells were supplemented with 10 µM CRID3 four hours after transfection to potentially stabilize an inactive conformation of the recombinant protein produced. For purification, the frozen cell pellet was resuspended in lysis buffer supplemented with cOmplete™ ULTRA, EDTA free protease inhibitor cocktail and thawed on ice. Subsequently, the cells were lysed by incubation on ice for 30 min and the crude lysate was cleared by centrifugation at 12,000 x g and 4°C for 10 min. The lysate was applied to anti-Flag M2 affinity gel (1.5 ml bead slurry per 150 ml culture) equilibrated with 3 CV glycine pH 3.5 and 10 CV lysis buffer for affinity purification. The protein-resin solution was transferred into a 50 ml falcon tube and the protein was allowed to bind to the resin at 4°C and under constant rotation for at least 1 h. The protein-bound resin was packed into an Econo-Pac™ column and the unbound fraction was allowed to flow-through by gravity flow. The resin was washed with 20 CV lysis buffer, before the protein was eluted with 2 CV elution buffer. The protein was analyzed by SDS-PAGE, snap-frozen in liquid nitrogen, and stored at -80°C.</p>

## 6.4 Analytical methods

### 6.4.1 SDS-PAGE analysis

Sodium dodecyl sulfate (SDS) polyacrylamide gel electrophoresis (PAGE) was performed to separate proteins by their size and therefore to assess their presence, purity, and integrity. Proteins in a sample were denatured by addition of SDS sample buffer and incubation at 96°C for 5-10 min. The SDS sample buffer contains a reducing agent to dissolve cysteine bridges and the negatively charged detergent SDS, which uniformly binds to the protein, resulting in denaturation and masking of the intrinsic charge. Discontinuous polyacrylamide gels were prepared in house using the recipe shown in Table 6-8 and the Mini-Protean Tetra Cell casting system.

**Table 6-8: Recipe for the preparation of polyacrylamide gels**

<b>4 stacking gels</b>	<b>4%</b>	<b>4 separation gels</b>	<b>12%</b>	<b>15%</b>	<b>18%</b>
30% acrylamide	0.9 ml	30% acrylamide	8.4 ml	10.5 ml	13.5 ml
stacking gel buffer	0.7 ml	separation gel buffer	5.85 ml	5.85 ml	5.85 ml
10% APS	53 µl	10% APS	235.5 µl	235.5 µl	235.5 µl
TEMED	5.3 µl	TEMED	7.05 µl	7.05 µl	7.05 µl
H <sub>2</sub> O	3.6 ml	H <sub>2</sub> O	6.75 ml	4.65 ml	1.65 ml

Ammonium persulfate (APS) initiates the polymerization of acrylamide and the crosslinker bis-acrylamide into gels, which is catalyzed in the presence of tetramethyl ethylenediamine (TEMED). The pore size is adjusted by the percentage of the polymer. A stacking gel was prepared on top of the separation gel to concentrate the proteins into a sharp band before they are resolved during electrophoresis. During polymerization, a comb was used to create sample wells. The gels were mounted in the Mini-Protean Tetra Cell electrophoresis system filled with SDS running buffer and then loaded with the protein samples. Application of an electric current (35 mA per gel at RT for 45 min) generates an electric field leading to the migration of the SDS-coated proteins through the gel. In this method, the migration distance is only dependent on the molecular weight, which can thus be estimated using a molecular weight standard. To stain and visualize protein bands, the gels were incubated for 10-30 min with Coomassie staining solution followed by Coomassie destain solution boiled in a microwave. For downstream analysis by mass spectrometry, the staining and destaining solutions were not heated and incubation at RT was extended overnight. Finally, protein gels were documented using the ChemiDoc™ XRS+ imaging system.



#### 6.4.2 Mass spectrometry

Protein identification and determination of post-translational modifications (PTMs) was performed by peptide mass fingerprint analysis. For this purpose, protein samples were separated in SDS-PAGE and stained as described. Subsequently, protein bands were cut from the gel using a clean scalpel and analyzed by the group of Prof. Dr. Henning Urlaub at the Max Planck Institute for Multidisciplinary Sciences (Göttingen, Germany). In brief, the protein was purified from the gel, proteolytically digested into peptides, and subjected to a mass spectrometer. The obtained peptide masses were compared to a database to identify the corresponding proteins and their PTMs. The final evaluation of the results was done using Scaffold software.

#### 6.4.3 Pulldown assay

In this study, a pulldown assay was performed to investigate the physical interaction between two proteins, ASC and NLRP12<sup>PYD</sup>. Hexahistidine-tagged ASC-mCherry was purified and provided by Dr. Rebecca Brinkschulte (University of Bonn, Germany). To this end, 20  $\mu$ l bead slurry (Ni-NTA agarose) was equilibrated with pulldown buffer (20 mM Tris pH 8.0, 150 mM NaCl, 5 mM  $\beta$ ME) and subsequently bound with 50  $\mu$ g ASC-mCherry at 4°C overnight. The beads were washed five times by centrifugation at 400 x g and 4°C for 5 min before they were used in the experiment. For one pulldown approach, 5  $\mu$ l of ASC-bound beads were mixed with 20  $\mu$ l unbound beads and 146  $\mu$ l NLRP12<sup>PYD</sup> (0.1 mg/ml) to yield a molar ratio of 2:1 (NLRP12<sup>PYD</sup>:ASC). The sample was filled up to 300  $\mu$ l using pulldown buffer and incubated at RT for 2 h. The beads were washed five times and resuspended in 7  $\mu$ l SDS sample buffer. Finally, the samples were analyzed by SDS-PAGE analysis.

#### 6.4.4 ATP hydrolysis assay

To analyze the amount of nucleotide converted by a protein of interest, a multi-cycle turnover ATP hydrolysis assay based on ion-pairing reversed phase high performance liquid chromatography (HPLC) was established in the laboratory. HPLC is a technically optimized liquid chromatographic method for the separation and quantitative analysis of substance mixtures. In this process, the eluent (mobile phase) is continuously pumped through the chromatography column, which is filled with the solid stationary phase, at a pressure of 50-400 bar. The separation is based on the polarity differences between the

mobile and stationary phases. In reversed phase HPLC, a nonpolar stationary phase and a polar mobile phase is used. Depending on the number of negative charges, the hydrophobicity of AMP (2<sup>-</sup>), ADP (3<sup>-</sup>), and ATP (4<sup>-</sup>) can be gradually increased using the ion-pairing reagent tetrabutylammonium bromide (TBA-Br), leading to a retention difference at the stationary phase that is related to the number of phosphate groups. In this way, distinct nucleotide species can be separated on a C18 silica column, eluted using low concentrations of acetonitrile, and detected by absorbance at 259 nm wavelength.

Nucleotides were dissolved in the purification buffer of the proteins analyzed. Using a NanoDrop spectrophotometer, the concentration of the nucleotides was measured at 259 nm absorbance and adjusted to 1 mM. In addition, a 50 mM MgCl<sub>2</sub> stock solution was prepared using the protein purification buffer. The reaction mix was prepared as stated in the respective figure legends. In case the CRID3 effect was investigated, the protein was preincubated in the presence of DMSO or CRID3 for 30 min on ice, before magnesium and nucleotides were added. The reaction mix was incubated at 25°C for 60 min and a 10 µl sample was injected every 10 minutes onto a 1260 Infinity II LC system equipped with an autosampler and connected to a Chromolith Performance RP-18e 100-4.6 column equilibrated with the eluent (30 mM K<sub>2</sub>HPO<sub>4</sub>, 70 mM KH<sub>2</sub>PO<sub>4</sub>, 10 mM TBA-Br, 4% acetonitrile; pH 6.5). The detected nucleotide peaks were integrated using OpenLab Analysis software and the ratios were calculated to determine the molar concentrations of educt and product.

#### **6.4.5 Analysis of protein-bound nucleotides**

To analyze nucleotide species that are bound to a purified protein, a precipitation assay based on perchloric acid was used. A sample with 50 µM protein or nucleotides (control) was prepared and ice-cold perchloric acid (4 M stock) was added to a final concentration of 1 M. The sample was mixed, incubated for 5 min on ice, and cleared from the precipitated protein by centrifugation at 16,000 x g and 4°C for 2 min. The supernatant was transferred to a new tube and neutralized using 34% (v/v) 2 M ice-cold potassium hydroxide (incubated with lid opened). The pH was checked using a pH indicator paper and further adjusted to 6.5-8.0 using 0.1 M perchloric acid or potassium hydroxide. The solution was cleared by centrifugation at 16,000 x g and 4°C for 15 min before a 10 µl sample of the supernatant was analyzed for nucleotide content by ion-pairing reversed phase HPLC.

#### 6.4.6 Thermal shift assay

For stability characterization, protein was analyzed using nano-format differential scanning fluorimetry (nanoDSF). The method is based on thermal unfolding of a protein by application of a linear temperature gradient and simultaneous measurement of its intrinsic fluorescence at 350 and 330 nm wavelength. The fluorescence of tryptophan and tyrosine residues changes when the amino acids become solvent exposed. Thus, an unfolding event can be monitored. The stability of a protein is given by the melting temperature  $T_M$ , which is defined as the temperature where half of the protein is unfolded. Protein stability can be enhanced e.g., upon conformational change, optimized buffer conditions, or binding of a specific ligand molecule, which was investigated in this work.

Protein samples were prepared with the appropriate protein purification buffer in a final volume of 30  $\mu$ l and incubated for 30 min on ice before loading into standard nanoDSF capillaries. Capillaries were prepared in technical duplicates and thermal unfolding was monitored in a Prometheus NT.48 device. The melting temperature was automatically determined as the inflection point of the first derivative of the 350/330 nm ratio using software provided by the manufacturer.

#### 6.4.7 Analytical gel filtration

Analytical gel filtration was performed to investigate the degree of oligomerization of a protein sample in solution and to estimate the molar mass of protein species based on their retention on a column using an appropriate standard. For this purpose, proteins were prepared as indicated and incubated, if necessary, before loading onto an analytical gel filtration column (Table 7-7, 10/300 or 3.2/300 format) equilibrated with the respective SEC buffer and connected to an Äkta Micro FPLC system or a 1260 Infinity II LC system. For sample preparation, the protein purification buffer was used. The protein standard was prepared and measured according to the manufacturer's instructions.

The peak retention volume of an analyte ( $V_e$ ), the total column volume ( $V_c$ ), and the void volume of a column ( $V_0$ ) can be used to calculate the partition coefficient ( $K_{av}$ ) of a molecular species using the following formula:

$$K_{av} = \frac{V_e - V_0}{V_c - V_0}$$

Linear regression was used to fit a calibration curve to the partition coefficient ( $K_{av}$ ) versus the logarithm of the molecular weight of a standard. Finally, the calibration curve was used to calculate the molecular weight estimate of an analyte.

#### 6.4.8 SEC-MALS

Size exclusion chromatography (SEC) combined with multi-angle light scattering (MALS) was used to investigate the degree of oligomerization of a protein sample and to directly measure the absolute molar mass of protein species independent of their retention on a column. In a MALS experiment, light that is scattered from a polarized particle in solution is measured simultaneously at various different angles. The amount of scattered light at each angle is directly proportional to the product of the molar mass and concentration of the investigated molecule. The concentration is determined via an online refractive index (RI) or UV detector. Thus, a regression analysis can be used to obtain the scattering at  $0^\circ$  scattering angle, which is related to the molecular weight. For large particles that show anisotropic scattering, the radius of gyration can also be calculated.

Proteins were prepared in SEC buffer and centrifugated at  $10,000 \times g$  and  $4^\circ\text{C}$  for 10 min. The supernatant was loaded onto an equilibrated column for analytical gel filtration (Table 7-7, 10/300 format) that was connected to a 1260 Bioinert Infinity LC system equipped with a miniDawn 3141MD3 and an Optilab rEX 650 device for online MALS (661 nm) and RI detection (658 nm), respectively. Elution of the protein was followed at 280 nm absorbance. The molar mass calculation was performed using Astra 8 software.

#### 6.4.9 Dynamic light scattering

Dynamic light scattering (DLS) was used to determine the particle size of a protein sample in solution. Due to Brownian motion of dispersed particles, light from an incident laser beam is scattered at a specific angle with varying intensity, which is measured over time. In general, smaller particles move with higher speed and thus show faster fluctuations than larger particles. Using an intensity autocorrelation function and cumulant fitting algorithms, the translational diffusion coefficient is determined and the hydrodynamic radius of a particle is obtained from the Stokes-Einstein equation.

For DLS, the protein sample was prepared as depicted and spun at  $18,000 \times g$  and  $4^\circ\text{C}$  for 10 min. The supernatant was incubated in a DLS cuvette at  $25^\circ\text{C}$  for 11.5 h and every 30 min the size distribution was automatically measured using a DynaPro NanoStar (660.5 nm wavelength) setup with 3 s of acquisition time. Each data point corresponds to the average of 20 DLS acquisitions. Data processing and analysis to determine the hydrodynamic radius and molecular weight of the protein sample was performed automatically by the analysis software supplied with the instrument.

#### 6.4.10 SPR spectroscopy

Surface plasmon resonance (SPR) spectroscopy was used to investigate the interaction between proteins and small molecule inhibitors. An SPR experiment provides vital information about the kinetics, specificity, and affinity of a respective binding event. In SPR spectroscopy, a plane-polarized light is reflected at a metal-dielectric interface (often gold) under conditions of total internal reflection. Incident light photons with a specific momentum are absorbed by free outer shell and conduction-band electrons in the metal surface, causing them to resonate and turn into electron density waves called plasmons. Since photons are absorbed, the reflected light intensity is minimal at a certain angle, called the resonance angle, which is measured by a detector and converted into resonance units (RU). Due to an evanescent wave generated by the plasmons and the reflected photons on the opposite side of the interface, the momentum of the plasmons is sensitively affected by the composition of the external medium. Therefore, a change in refractive index or mass results in a proportional change in resonance angle that can be tracked.

SPR experiments were performed on a Biacore™ 8K instrument equipped with a streptavidin-functionalized sensor chip (Series S sensor chip SA). The chip contains 8 channels with two flow cells (Fc) each for referencing. The system was set to 25°C and flushed with running buffer (10 mM HEPES pH 7.4, 200 mM NaCl, 0.5 mM ADP, 0.5 mM TCEP (tris[2-carboxyethyl]phosphine) or dithiothreitol (DTT), 2 mM MgCl<sub>2</sub>, 1 g/L carboxymethyl dextran (CMD) 0.05% Tween20, 2% DMSO) before the sensor chip was inserted into the instrument and normalized according to the manufacturer's instructions. Next, the chip was conditioned with three consecutive injections of 1 M NaCl in 50 mM NaOH at a flow rate of 10 µl/min for 1 min and the protein (ligand) was immobilized on Fc2 at 1-2 µl/min for 900-3600 s. The flow system was washed using 50% isopropanol in 1 M NaCl and 50 mM NaOH. Free streptavidin binding sites on both flow cells were saturated by four consecutive injections of biotin-PEG (1 µM, Mn = 2,300 Da) at 10 µl/min for 2 min. Since NLRPs do not tolerate regeneration, binding was measured in single-cycle kinetics mode. For this purpose, increasing concentrations of the compounds (analytes) under investigation were injected over both flow cells at 30 µl/min (association: 120-240 s, dissociation: 60/360-600 s). Data were collected at a rate of 10 Hz and double referenced by reference flow cell and blank cycle subtraction. To correct for the different volume exclusion at the active and reference flow cells, a 4-point solvent correction was applied. Binding parameters were obtained from the processed data by fitting a 1:1 interaction model using Biacore Insight Evaluation software supplied with the device.

For better comparability of the NLRP3 variants studied and to account for different degrees of immobilization, the measured response level was normalized to the theoretical maximum response ( $R_{max}$ ), yielding the bound fraction. The  $R_{max}$  value was calculated using the following formula (MW: molecular weight):

$$R_{max} = \frac{MW_{analyte}}{MW_{ligand}} \times \text{immobilized ligand (RU)} \times \text{stoichiometry}$$

For the displacement assay, a variant of the described protocol was used. Compounds were not measured in single-cycle kinetics mode but injected in a two-step cycle. First, compounds were injected at a concentration 10-times the equilibrium dissociation constant ( $K_D$ ) of Gü3616 or Gü3618, respectively. In a second step, equimolar concentration of a competitive compound was injected in the presence of the first compound. Both injections were applied at a flow rate of 30  $\mu$ l/min for 120 s.

#### 6.4.11 Electron microscopy

Negative stain electron microscopy (EM) was primarily used to assess the degree of aggregation, heterogeneity, and overall quality of a protein sample before further steps were taken to determine a three-dimensional structure. In this method, the protein is adsorbed on an electron-transparent sample support (EM grid) and the specimen is stained with an amorphous film of heavy metal salts for increased electron scattering and thus contrast. The sample is then imaged using a transmission electron microscope (TEM), where electrons are diffracted by interacting with the sample to produce an image that is eventually recorded by a detector.

For negative stain EM, a carbon-coated copper grid was glow-discharged for hydrophilization and incubated for 1 min with 5  $\mu$ l of a protein sample. The excess protein was removed using a blotting paper and the grid was further washed by dipping in three individual 20  $\mu$ l drops of the respective protein purification buffer. The buffer was blotted away using a blotting paper. The sample was then stained with 2% uranyl formate and incubated for 30 s before carefully removing the staining solution with a blotting paper and air drying the grid. Stained samples were imaged using a JEOL JEM-2200FS TEM operating at 200 kV and equipped with a CMOS (complementary metal-oxide semiconductor) camera (TemCam-F416). The images were recorded at a magnification range of 20,000-50,000.

#### 6.4.12 X-ray crystallography

X-ray crystallography was applied to determine the molecular structure of proteins. For this purpose, protein crystals were prepared by using the hanging- or sitting-drop vapor diffusion methods. In these methods, a small volume of protein of crystallization-grade quality is mixed with a crystallization solution often containing a buffer system, salts, or a precipitant and incubated in a sealed chamber. A reservoir at the bottom of the chamber is filled with the crystallization solution only, leading to steady evaporation of solvent molecules from the protein drop and subsequent vapor diffusion across the concentration gradient. If conditions are right, the protein eventually becomes supersaturated and the spontaneous formation of crystals is nucleated. In the crystal, a regular array of individual molecules is stabilized by a number of repetitive intermolecular interactions (crystal contacts). Importantly, good diffraction quality can only be achieved if the crystal lattice is sufficiently ordered. However, the formation of crystal contacts depends, among other parameters, on the composition of amino acids, which determine the polarity, charge, and shape of a protein surface. For this reason, the appropriate crystallization conditions are not yet predictable and must be screened individually for each protein and conformation.

To determine the structure, a protein crystal is irradiated from different angles with an X-ray beam of monochromatic wavelength. If the crystal is sufficiently ordered, the X-rays are scattered by the electrons encountered, and constructive interference at the periodic lattice planes leads to peaks of scattered intensity that can be observed in a distinctive diffraction pattern. The condition for coherent scattering of X-rays from a crystal lattice is described by the Bragg's law  $n\lambda = 2d \sin(\theta)$ , where  $n$  is the diffraction order,  $\lambda$  is the wavelength,  $d$  is the spacing of the Bragg planes, and  $\theta$  is the glancing angle. Therefore, the diffraction pattern contains information about the unit cell, space group, and the reciprocal vectors of the crystal lattice. Mathematically, the diffraction pattern is the Fourier transform of the electron density distribution, which can be reconstructed theoretically. However, detectors measure the spot intensities and thus the structure factor amplitudes but not the phases of the diffracted X-rays, which are both required for the reverse Fourier transform operation. This is known as the phase problem in X-ray crystallography and solved by different approaches. In this work, molecular replacement was used to obtain initial phases from a known protein structure homologous or identical to that of the protein under study. Finally, a model of the protein was built into the determined electron density map and refined in accordance with different quality markers until the experimental diffraction data were explained in the best possible way.

### Crystallization of proteins and diffraction data collection

For an initial screening of sufficient crystallization conditions, a set of commercially available (section 7.6) and in house protein crystallization screens were tested at different temperatures (4°C, 10°C, 15°C, and 20°C). Crystallization plates were prepared as sitting-drops in 96 MRC-well plates using a Crystal Gryphon LCP or Mosquito crystal robotic device. In general, the protein drop was prepared with 1:1 ratio (v/v; 0.1-0.2 µl) of protein and crystallization solution and the reservoir was filled with 50-70 µl. Immediately after preparation, the plate was sealed with an adhesive film, incubated at the chosen temperature, and regularly checked for the appearance of crystals.

In case crystals were monitored, the condition was tried to be optimized in different ways. One possibility was the testing of an additive screen. For this purpose, the crystallization plate was pipetted by hand and as sitting-drops in 96 MRC-well plates. The protein drop was prepared with 1:1 ratio (v/v, 1 µl) of protein and crystallization solution and supplemented with 0.1 µl of an additive solution. Another option was crystallization in homemade optimization screens. Here, the concentration of individual ingredients was varied together with the pH value. Optimization screens were designed with a software available at the Institute of Structural Biology and based on the initial hit conditions. Stock solutions were prepared freshly and filtered (0.2 µm pore size) before they were used to prepare the optimized crystallization solutions with an epMotion 5073m robotic device or by hand. Crystallization plates with optimization screens were prepared as sitting-drops as described above or as hanging-drops in 24-well format. Hanging drops were prepared with 1:1 ratio (v/v, 0.5-0.6 µl) of protein and crystallization solution and pipetted onto glass coverslips. Each well was filled with 300-500 µl crystallization solution and a cover slip with a hanging drop was sealed on top using silicon paste.

Promising crystals to be analyzed in diffraction experiments were transferred to a cryo-loop, cryoprotected with 15% ethylene glycol (NLRP9<sup>PYD</sup> or NLRP12<sup>NACHT</sup>) or 33% PEG400 (NLRP3<sup>NACHT</sup>) in the respective crystallization solution and flash-cooled in liquid nitrogen. For all further steps, the crystals were kept under cryogenic conditions. Data collection was performed at the synchrotron beamlines PX1 of the Swiss Light Source (SLS) in Villigen, Switzerland or P13 of the Deutsches Elektronen-Synchrotron (DESY) in Hamburg, Germany. In brief, the crystals were mounted on a goniometer in the X-ray beam using a robotic device, aligned in the beam path, and datasets were collected with 360° of crystal rotation (0.1° rotation per image). Diffraction data were collected with an EIGER 16M or PILATUS 6M detector at SLS or DESY, respectively.



### Data processing, structure determination, and refinement

In case of NLRP9<sup>PYD</sup> the dataset was processed using the XDS program package, which includes different automatically performed routines to identify diffraction spots in the data images, determine parameters of the crystal lattice (unit cell and space group), scale the spot intensities, calculate the structure factor amplitudes, and prepare the output data for subsequent structure determination. The structure factor phases needed to reconstruct the electron density map were obtained with PHASER (Read, 2001), as implemented in the PHENIX software suite, using the molecular replacement method (Rossmann, 1990) and the coordinates of the known structure of NLRP4<sup>PYD</sup> (PDB: 4EWI, (Eibl et al., 2012)) as a search model. The electron density map was calculated and used to build an initial model of NLRP9<sup>PYD</sup>, which was examined and manually modified according to the electron density map and common stereochemical restraints using COOT software. The model was improved by alternating cycles of automatic refinement using PHENIX.refine (Afonine et al., 2012) and manual model building in COOT. The agreement between the crystallographic model and the fitted experimental X-ray diffraction data is represented by the residual (*R*)-factor, where  $F_{obs}$  are the observed structure factor amplitudes,  $F_{calc}$  are the structure factor amplitudes calculated from the model, and  $k$  is a scale factor:

$$R_{work} = \frac{\sum |F_{obs(work)} - kF_{calc}|}{\sum F_{obs(work)}}$$

However, the *R*-factor is biased because after each refinement process, the new electron density map is calculated using the diffraction pattern along with the atomic model, which was previously refined to better fit the experimental data and improve the *R*-factor itself. To evaluate the phase accuracy and thus the model quality with less bias and to avoid overparameterization, only 90-95% of the experimental diffraction data is refined as the working dataset. For cross-validation, the other part of the data is excluded from all refinements and the agreement between the model and the original, so-called free dataset is calculated separately. The resulting  $R_{free}$  value is related to the mean phase error:

$$R_{free} = \frac{\sum |F_{obs(free \neq work)} - kF_{calc}|}{\sum F_{obs(free \neq work)}}$$

During the final phase of the refinement process, the geometry of the model was continuously analyzed using the Ramachandran plot (Ramachandran et al., 1963) and the MolProbity online tool (Williams et al., 2018) and adjusted accordingly.

In case of the NLRP3-CRID3 complex, an initial dataset at a resolution of 2.88 Å was obtained and processed as described above. Initial phases were determined by molecular replacement using the coordinates of NLRP3 from the NLRP3-NEK7 structure (PDB: 6NPY, (Sharif et al., 2019)) as a search model. Model building and refinement were performed as described. During this process, an improved dataset with a final resolution of 2.48 Å could be obtained and the last crystallographic model of NLRP3 was used as a search model in molecular replacement. Again, the model was built and refined as described. During the final phase of the refinement process, CRID3 was added to the model. For this purpose, the molecule was drawn in ChemDraw software and exported as a SMILES string. The SMILES string was used for ligand building and optimization in PHENIX.eLBOW (Moriarty et al., 2009) before the atomic coordinates and ligand restraints were imported in COOT and refined along with the protein model.

#### **6.4.13 PYD filament assay**

To probe NLRP9 and NLRP12 PYDs for their capability to assemble into filaments and to induce ASC speck formation in cells, a PYD filament assay was performed. For this purpose, HEK293T cells or HEK293T cells stably expressing ASC-TagBFP under the CMV promoter (HEK293T<sup>ASC-BFP</sup>) were seeded into 96-well plates and grown for 48 h. HEK293T<sup>ASC-BFP</sup> cells were a kind gift from the laboratory of Prof. Dr. Eicke Latz (University of Bonn). Per well, 200 ng of transfection grade plasmid DNA coding for human NLRP3<sup>PYD</sup>-mCitrine, human NLRP9<sup>PYD</sup>-mCitrine, mouse NLRP9b<sup>PYD</sup>-mCitrine, human NLRP12<sup>PYD</sup>-mCitrine, or the mCitrine vector control was transfected with Lipofectamine 2000 according to the manufacturer's instructions. The cells were cultured for 24 h before the medium was removed to fixate the cells with 4% formaldehyde and stain the nuclei with 10 µM Draq5 diluted in PBS. Subsequently, the cells were imaged using an Observer.Z1 epifluorescence microscope equipped with a 20x objective (dry, Plan Aplanachromat, NA 0.8), an Axiocam 506 mono, and ZEN Pro software. Due to lower expression of the mCitrine control (via internal ribosomal entry site), transfected cells had to be imaged with higher exposure time. If necessary, brightness and contrast were adjusted for visualization.

For quantitative analysis, PYD filament or ASC speck formation was analyzed in six images per experiment and condition using Cellprofiler software. In brief, cells were identified by their nuclei (Draq5 signal) and saved as objects. The objects were expanded by 10 pixels to include the cell's cytoplasm and subsequently measure the intensity of the mCitrine signal in the respective regions of the image. Objects positive for mCitrine were saved as new objects. In this way, 3338, 938, 2398, and 2794 HEK293T cells and 4549, 1628, 3593, and 5350 HEK392T<sup>ASC-BFP</sup> cells positive for the expression of either human NLRP3<sup>PYD</sup>-mCitrine, human NLRP9<sup>PYD</sup>-mCitrine, mouse NLRP9b<sup>PYD</sup>-mCitrine, or the mCitrine vector control, respectively, were identified and further analyzed. Filamentous structures were enhanced in the mCitrine channel and subsequently identified as objects. Filamentous objects were filtered for a minimum major axis length value of 10 and a minimum compactness value of 1.7. Similarly, ASC specks were enhanced in the BFP channel and subsequently identified as objects. Finally, mCitrine-positive cells with filaments or specks were determined as mCitrine positive objects that overlap with filament or speck objects, respectively. The determined cell numbers were exported in spreadsheet format and further analyzed using *Excel* software.

#### **6.4.14 ASC speck formation assay**

The ASC speck formation assay was used to test NLRP family proteins for their capability to form an inflammasome with the adaptor protein ASC or to study inflammasome formation in the presence of the NLRP3-specific inhibitor CRID3. To this end, the assay was performed in two different setups. In the first setup, the protein under investigation (full-length NLRP3, NLRP9, or NLRP12) was overexpressed in HEK293T cells and spontaneous activation and concomitant inflammasome assembly was monitored by the formation of ASC specks. In the second setup, the protein under investigation (full-length NLRP3 wildtype and mutants) was expressed under a doxycycline-inducible promoter. For this purpose, the transactivator TetON3G is encoded on the same plasmid as NLRP3 and constitutively expressed under a PGK promoter. Doxycycline binds to TetON3G, which in turn associates with the Tet-responsive element (TetO6) to induce protein expression (Kang et al., 2019). The latter setup allowed for low expression levels leading to protein in an inactive conformation. Thus, specific activation with nigericin and inhibition with the small molecule inhibitor CRID3 could be studied. In this setup, inflammasome formation was also monitored by ASC speck formation.

### Overexpression system

HEK293T<sup>ASC-BFP</sup> cells were seeded in 96-well plates and grown for 24 h. For transfection, 10, 50, 100, or 200 ng transfection grade plasmid DNA coding for human NLRP3, NLRP9, or NLRP12 was prepared. The plasmids also encode for IRES-dependent co-expression of mCitrine that was later used to identify transfected cells. Thus, an IRES-mCitrine vector control was also prepared for transfection. To ensure that ASC speck formation is only dependent on the investigated proteins and not the transfected DNA itself, the prepared plasmid DNA sample was filled up to 200 ng with the mCitrine vector control and finally transfected with Lipofectamine 2000 according to the manufacturer's instructions. The cells were cultured for 24 h, harvested by adding trypsin, washed with DPBS, and finally resuspended in 100  $\mu$ l flow cytometry buffer (DPBS with 2 mM EDTA and 0.5% BSA). The samples were analyzed in an LSRFortessa II flow cytometer operating at a medium flow rate. Transfected cells were gated according to the expression of mCitrine and checked for the presence of ASC specks by analyzing the area and width of the BFP signal.

### Doxycycline-inducible system

HEK293T<sup>ASC-BFP</sup> cells were seeded in 24 well plates and grown for 24 h. Per well, 100 ng transfection grade plasmid DNA coding for NLRP3 (wildtype and mutants) was transfected with Lipofectamine 2000 according to the manufacturer's instructions. Cells were cultured for 18 h and NLRP3 expression was induced with 10 ng/ml doxycycline. To investigate NLRP3 inhibition with CRID3, doxycycline was applied in combination with 20  $\mu$ M of the compound. After 6 h of incubation, nigericin was added at a final concentration of 10  $\mu$ M to specifically activate NLRP3 in the according samples. The cells were incubated for another hour, harvested by adding trypsin, washed with DPBS, and finally resuspended in 100  $\mu$ l flow cytometry buffer. The samples were analyzed in an LSRFortessa II flow cytometer operating at a medium flow rate. Transfected cells were gated according to the presence of mCherry, which was co-expressed from the NLRP3 encoding plasmid. According to a nontransfected control (mCherry-negative), the gate for mCherry-positive cells was set to low expression levels and adjusted between experiments to obtain similar numbers of mCherry-positive cells and low baseline levels of ASC specks in the NLRP3 wildtype samples. Finally, the mCherry-positive population was checked for the presence of ASC specks as previously described (Sester et al., 2015).

## **6.5 *In silico* methods**

### **6.5.1 Determination of protein parameters**

Gene and DNA sequences coding for the proteins studied were taken from the Ensembl database (Howe et al., 2021). The primary structure of a protein was taken from the Uniprot database (UniProt, 2021). Protein parameters, such as the molecular weight, the theoretical pI value, and the extinction coefficient at 280 nm wavelength were calculated using the ExPASy ProtParam online tool (Gasteiger et al., 2003).

### **6.5.2 Sequence alignments**

Sequence alignments of amino acids were performed using Clustal Omega (Madeira et al., 2019) and secondary structure assignments were prepared using Esprout 3.0 (Robert & Gouet, 2014). For structure-based sequence alignments, the structures of the investigated proteins were aligned in PyMOL and the residues were examined regarding their three-dimensional location. If necessary, sequence alignments previously performed with Clustal Omega were adjusted.

### **6.5.3 Calculation of a *B* factor distribution**

To calculate individual *B* factors for backbones and sidechains of single protein residues, a script was used that was coded by myself. A PDB file is chosen from the computer and the script extracts the information provided for each atom. For each residue, the *B* factors of the backbone and sidechain atoms is averaged, respectively. Atoms with an occupancy value of zero were excluded from the calculation. Finally, the average *B* factor of the backbone and sidechain atoms for each residue is output in spreadsheet format.

### **6.5.4 Determination of residues that are nearest in their three-dimensional position**

To determine the residue of an analyzed protein that is nearest to a specific residue of a reference protein, a script was used that was coded by myself. First, PyMOL software is used to align two protein structures under study and the PDB files are exported. The generated PDB files are chosen from the computer and the script extracts the information provided for each atom. For each residue of the reference molecule, the residue of the analyzed molecule with a minimum distance is determined based on the three-dimensional position of their C $\alpha$  atoms. Finally, the residue pairs are output in spreadsheet format.

### **6.5.5 Graphs and statistical analysis**

Molecular diagrams were drawn using the PyMOL molecular graphics suite. Preparation of data graphs, linear regression, and statistical analysis were performed using Prism software. Figures were prepared using Affinity Designer graphical software.

Unless otherwise stated, the technical and methodological principles described in this methods section can be found in the following references: (<https://www.sprpages.nl>, 09.2022), (Rupp, 2009), (Miller, 2008), or in the user manuals and technical notes of the respective equipment manufacturers.

## 7 Materials

### 7.1 Chemicals

The chemicals used in the presented work were purchased from the following suppliers: Carl Roth (Karlsruhe, Germany), Sigma-Aldrich (St Louis, USA), Applichem (Darmstadt, Germany), Thermo Fisher Scientific (Waltham, USA), Merck Millipore (Burlington, USA), VWR (Darmstadt, Germany), Jena Bioscience (Jena, Germany), Serva (Heidelberg, Germany), MedChemtronica (Sollentuna, Sweden), and Linde plc (Dublin, Ireland).

### 7.2 Consumables

Consumable	Supplier
Pipette tips (20 $\mu$ l, 200 $\mu$ l, 1000 $\mu$ l)	VWR (Darmstadt, Germany)
Serological pipettes (5 ml, 10 ml, 25 ml, 50 ml)	Sarstedt (Nürnberg, Germany)
Petri dishes for agar plates	Labomedic (Bonn, Germany)
EVE™ cell counting slides	NanoEntek (Seoul, South Korea)
Econo-Pac™ chromatography column	Bio-Rad Laboratories, Inc (Hercules, USA)
Amicon™ ultracentrifugal filters	Merck Millipore (Burlington, USA)
Cell scraper 23 cm	Thermo Fisher Scientific (Waltham, USA)
6-well tissue culture plates	Sarstedt (Nürnberg, Germany)
24-well tissue culture plates	Sarstedt (Nürnberg, Germany)
96-well tissue culture plates, clear	Greiner (Kremsmünster, Austria)
96-well tissue culture plates, black	Greiner (Kremsmünster, Austria)
96-MRC well plates	Jena Bioscience (Jena, Germany)
96-well microplates, round bottom	Greiner (Kremsmünster, Austria)
96-deep well blocks (1 ml)	Eppendorf (Hamburg, Germany)
96-deep well blocks (2 ml)	VWR (Darmstadt, Germany)
Adhesive foil	Molecular Dimensions (Newmarket, England)
Microplate foils	Cytiva (Marlborough, USA)
96-well septa	Cytiva (Marlborough, USA)
Coverslips	VWR (Darmstadt, Germany)
Korasilon™ silicon paste	Carl Roth (Karlsruhe, Germany)
Cell culture flasks (T25, T75, T175)	Sarstedt (Nürnberg, Germany)
Cuvette, PE (1 cm path length)	Sarstedt (Nürnberg, Germany)
Cuvette for electroporation	Eppendorf (Hamburg, Germany)
Microcuvette kit for the NanoStar, disposable	Wyatt Technologies (Santa Barbara, USA)
Reaction tubes (0.5 ml, 1 ml, and 2 ml)	Eppendorf (Hamburg, Germany)
PCR tubes	Sarstedt (Nürnberg, Germany)
Falcon tubes (15 ml, 50 ml)	Greiner (Kremsmünster, Austria)
Syringes (5 ml, 10 ml, 20 ml)	Carl Roth (Karlsruhe, Germany)
Syringe filters (0.22 $\mu$ m and 0.45 $\mu$ m)	Carl Roth (Karlsruhe, Germany)
Filter paper (0.22 $\mu$ m)	Merck Millipore (Burlington, USA)

Consumable	Supplier
Blotting paper	Whatman plc (Maidstone, England)
pH indicator paper	Carl Roth (Karlsruhe, Germany)
SnakeSkin™ dialysis tubing (3.5kDa MWCO)	Thermo Fisher Scientific (Waltham, USA)
Prometheus standard capillaries	NanoTemper Technologies (München, Germany)
Flow cytometry tubes	Sarstedt (Nürnberg, Germany)
Carbon-coated EM grids	Plano (Wetzlar, Germany)
peqGreen DNA stain	VWR (Darmstadt, Germany)
Draq5 fluorescent probe solution (5 mM)	Thermo Fisher Scientific (Waltham, USA)
DNA gel loading dye	New England Biolabs (Ipswich, USA)
BIAdesorb solutions	Cytiva (Marlborough, USA)
BIAnormalization solution (70%)	Cytiva (Marlborough, USA)
Series S sensor chip SA	Cytiva (Marlborough, USA)
Biotin-PEG (Mn = 2,300 Da)	Sigma-Aldrich (St Louis, USA)
3x-Flag peptide	Sigma-Aldrich (St Louis, USA)
cOmplete ULTRA, EDTA-free protease inhibitor	Roche (Basel, Switzerland)

### 7.3 Marker

Marker	Supplier
PageRuler plus prestained protein ladder	Thermo Fisher Scientific (Waltham, USA)
1 kbp DNA ladder	Carl Roth (Karlsruhe, Germany)
100 bp DNA ladder	Carl Roth (Karlsruhe, Germany)
Gel filtration standard	Bio-Rad (Munich, Germany)

### 7.4 Enzymes

Enzyme	Supplier
Q5 High Fidelity DNA Polymerase, GC enhancer, Q5 polymerase buffer	New England Biolabs (Ipswich, USA)
Restriction endonucleases, CutSmart buffer	New England Biolabs (Ipswich, USA)
T4 DNA ligase, T4 ligase buffer	New England Biolabs (Ipswich, USA)
DNase I	Applichem (Darmstadt, Germany)
TEV protease	Institute of Structural Biology (Bonn, Germany)
Lysozyme	Carl Roth (Karlsruhe, Germany)

### 7.5 Kits

Kit	Supplier
ExtractMe DNA Clean-Up Kit	Blrt (Gdansk, Poland)
ExtractMe DNA Clean-Up & Gel-Out Kit	Blrt (Gdansk, Poland)
ExtractMe Plasmid Mini Kit	Blrt (Gdansk, Poland)
ExtractMe Plasmid Midi Kit	Blrt (Gdansk, Poland)
PureLink™ HiPure Plasmid Maxiprep Kit	Invitrogen (Waltham, USA)



## 7.6 Crystallization screens

Crystallization screen	Supplier, Reference
JCSG Plus	Jena Bioscience (Jena, Germany), (Page et al., 2003)
Morpheus	Molecular Dimensions (Newmarket, England), (Gorrec, 2009)
ProPlex	Molecular Dimensions (Newmarket, England), (Radaev et al., 2006)
PACT premier	Molecular Dimensions (Newmarket, England), (Newman et al., 2005)
LMB	Molecular Dimensions (Newmarket, England), (Gorrec, 2016)
The ligand friendly	Molecular Dimensions (Newmarket, England), (Ng et al., 2016)
MemGold	Molecular Dimensions (Newmarket, England), (Newstead et al., 2008)
Additives Screen	Hampton Research (Aliso Viejo, USA)

## 7.7 Buffer and solutions

Buffers for protein purification or analysis were prepared with ultrapure water, filtered (0.22  $\mu\text{m}$  pore size), degassed under vacuum in an ultrasonic water bath, and stored at 4°C until use. Purification buffers are listed with the corresponding protocols in section 6.3.9. The buffers and solutions listed in the following table are intended for general use. They have usually been prepared with ultrapure water and filtered only when necessary.

Buffer/Solution	Ingredients
TAE buffer	40 mM Tris pH 8.0, 20 mM acetic acid, 1 mM EDTA
SDS sample buffer (4x)	240 mM Tris pH 6.8, 8% SDS, 5% $\beta$ ME, 0.04% bromophenol blue, 40% glycerol
Stacking gel buffer	0.5 M Tris pH 6.8, 10 mM SDS
Separation gel buffer	1.5 M Tris pH 8.8, 10 mM SDS
APS solution	10% APS in ddH <sub>2</sub> O
SDS running buffer	25 mM Tris pH 8.3, 194 mM glycine, 0.1% (w/v) SDS
Coomassie staining solution	40% (v/v) ethanol, 10% (v/v) acetic acid, 0.1% (w/v) Coomassie brilliant blue R250
Coomassie destain solution	10% (v/v) ethanol, 5% (v/v) acetic acid
PMSF solution	100 mM PMSF in isopropanol
PBS	20 mM Na <sub>2</sub> HPO <sub>4</sub> , 4.6 mM NaH <sub>2</sub> PO <sub>4</sub> , 150 mM NaCl; pH 7.5

## 7.8 Bacterial strains and cell lines

Strain or cell line	Supplier
<i>Escherichia coli</i> ( <i>E. coli</i> ) DH5 $\alpha$	Thermo Fisher Scientific (Waltham, USA)
<i>E. coli</i> NEB $\beta$ 10	New England Biolabs (Ipswich, USA)
<i>E. coli</i> BL21 (DE3)	Thermo Fisher Scientific (Waltham, USA)
<i>E. coli</i> DH10 <i>MultiBac</i> <sup>Turbo</sup>	Geneva Biotech (Pregny-Chambésy, Switzerland)
<i>Sf9</i> insect cells (clonal isolate of <i>Spodoptera frugiperda Sf21</i> cells [IPLB- <i>Sf21</i> -AE])	Thermo Fisher Scientific (Waltham, USA)
Human embryonic kidney (HEK) 293T cells	ATCC (Manassas, USA)
HEK293T <sup>ASC-BFP</sup> cells	Institute of Innate Immunity (Bonn, Germany)
FreeStyle <sup>TM</sup> HEK293-F cells	Thermo Fisher Scientific (Waltham, USA)

### 7.8.1 Bacterial growth media

Bacterial growth media were prepared in house, sterilized by autoclavation, and stored at room temperature until use. Antibiotics were added after autoclavation and cooling.

Media	Ingredients
Lysogeny broth (LB) medium	10 g/L tryptone, 5 g/L yeast extract, 5 g/L NaCl; pH 7.0
LB Agar plates	20 g/L agar in LB medium

### 7.8.2 Cell culture media and transfection reagents

Media	Supplier
Gibco <sup>TM</sup> DMEM	Thermo Fisher Scientific (Waltham, USA)
FBS	Sigma-Aldrich (St Louis, USA)
Gibco <sup>TM</sup> DPBS	Thermo Fisher Scientific (Waltham, USA)
Gibco <sup>TM</sup> OptiMEM <sup>TM</sup>	Thermo Fisher Scientific (Waltham, USA)
FreeStyle <sup>TM</sup> 293 Expression Medium	Thermo Fisher Scientific (Waltham, USA)
Sf-900 <sup>TM</sup> III SFM	Invitrogen (Waltham, USA)
Trypsin-EDTA	Thermo Fisher Scientific (Waltham, USA)
Cellfectin <sup>TM</sup> insect cell transfection reagent	Thermo Fisher Scientific (Waltham, USA)
<i>TransIT</i> <sup>TM</sup> insect cell transfection reagent	Mirus Bio (Madison, USA)
Transporter <sup>TM</sup> 5 transfection reagent	Polysciences (Warrington, USA)
Lipofectamine 2000	Thermo Fisher Scientific (Waltham, USA)

## 7.9 Nucleic acids

### 7.9.1 Nucleotides

Nucleotide	Supplier
AMP	Jena Bioscience (Jena, Germany)
ADP	Jena Bioscience (Jena, Germany) or Sigma-Aldrich (St Louis, USA)
ATP	Jena Bioscience (Jena, Germany) or Sigma-Aldrich (St Louis, USA)

Nucleotide	Supplier
ATP $\gamma$ S	Biolog Life Science Institute (Bremen, Germany)
dNTPs	Roche (Mannheim, Germany)

All nucleotides were purchased in HPLC grade quality (purity  $\geq$  95%).

### 7.9.2 Primers

Primers were purchased from Metabion International AG (Bonn, Germany) or provided by external sequencing service providers. The purchased primers were dissolved in ultrapure water, adjusted to a concentration of 10  $\mu$ M, and stored at -20°C until use.

**Table 7-1: Amplification primers for subcloning**

Primer	strand	Restriction site	Sequence (5'→3')
NLRP9_1+	forward	NcoI	ttcagggatccatggcagaatcttttttc
NLRP9_97-	reverse	EcoRI	cggaattcctagttagcttatttctcatctcttc
NLRP9_991-	reverse	HindIII	cgacaagcttcagaggagcacaccctg
NLRP12_Out1	forward	BamHI	cgcgatccatgctacgaaccgcaggcaggacggcctctgtcgcctgtccacctacttgaagaactggaggct
NLRP12_Out2	reverse	-	agtacatagctgcaagaactcctggaaac
NLRP12_Out3	forward	-	atccacttgagttccaggagtctttgca
NLRP12_Out4	reverse	-	gtcgctctgagctttgctttgaatccactg
NLRP12_Out5	forward	-	gatggacctgttgactgattcaagcaa
NLRP12_1+	forward	BamHI	cgcgatccatgctacgaaccgcaggcaggacggc
NLRP12_1061-	reverse	EcoRI	cggaattcagcagcaatgtccaataaggtttgtt
NLRP12_3+	forward	NcoI	catgccatggtacgaaccgcaggcagg
NLRP12_98-	reverse	EcoRI	cggaattcaggtatccctaccaggctctctct
NLRP12_1+	forward	AscI	ttggcgcgccgatgctacgaaccgcaggcagg
NLRP12_101-	reverse	NotI	tttcttttggcgccgctggcagcaccaggtggggtatccctacc
NLRP12_122+	forward	NotI	aaggaaaaagcggccgagaaaagatccccaggaaacctacaggac
NLRP12_122+	forward	BamHI	cgcgatccagaaaagatccccaggaaacctacaggac
NLRP12_122+	forward	AscI	ttggcgcgccgagaaaagatccccaggaaacctac
NLRP12_679-	reverse	XhoI	ggatgctcaggtaccgcgcggcttccccgtccgcgctgtaggt
NLRP12_679-	reverse	EcoRI	ccggaattctaccgcgcggcttccccgtccgcgctgtaggt
NLRP12_679-	reverse	NotI	aaggaaaaagcggccgcttaccgcgcggcttccccgtcc
NLRP3_131+	forward	BamHI	atacgggatccaagatgaagaaggactaccgcaagaagtac
NLRP3_694-	reverse	EcoRI	ctacggaattcattcttctcttcttcttggcatgtt

**Table 7-2: Primers for site-directed mutagenesis**

Primer	strand	Mutation	Sequence (5'→3')
NLRP12_W45R	forward	W45R	gagaaggcaagatccccggggaagcatggagaag
NLRP12_K223A	forward	K223A	gataggcgcgtccatgctggcacacaaggtgatg
NLRP12_K223A	reverse	K223A	atggacgcgctatccctgccgcgcttgc
NLRP12_R253W	forward	R253W	caactgctgggagatgaaccagagtccacggaatg
NLRP12_R253W	reverse	R253W	tcatctcccagcagttgatgtagaagagataatcaaatctgcc
NLRP12_D294N	forward	D294N	catcatcaacggcttcgatgagctcaagcctcttcc

Primer	strand	Mutation	Sequence (5'→3')
NLRP12_D294N	reverse	D294N	gaagccgtgatgatgaaaaggaggcgctcggg
NLRP12_D297N	forward	D297N	cggcttcaatgagctcaagccttcttccacgatcctc
NLRP12_D297N	reverse	D297N	tgagctcattgaagccgtcgtgatgatgaaaaggaggcgc
NLRP12_E298Q	forward	E298Q	cttcgatcagctcaagccttcttccacgatcctcagg
NLRP12_E298Q	reverse	E298Q	gcttgagctgatcgaagccgtcgtgatgatgaaaaggagg
NLRP12_R343T	forward	R343T	accacaacgccccacggccttggagaagctcc
NLRP12_R343T	reverse	R343T	gtggcgcttggtgatgagcaagatagctcag
NLRP12_H514E	forward	H514E	cttcacgagttgagttccaggagttctttgcagcta
NLRP12_H514E	reverse	H514E	aaactcaactcgtatgaagctgtagtacctctcacagttg
NLRP3_A227S	forward	A227S	gtggtgtccaggggtcggcaggattggaaaacaatc
NLRP3_A227S	reverse	A227S	gttttccaatccctgccacccctggaacaccacgggtg
NLRP3_A227E	forward	A227E	gtggtgtccagggggaggcaggattggaaaacaatc
NLRP3_A227E	reverse	A227E	gttttccaatccctgctcccccctggaacaccacgggtg
NLRP3_A228Q	forward	A228Q	gtgtccagggggcgaaggattggaaaacaatcctg
NLRP3_A228Q	reverse	A228Q	gttttccaatccctgcccctggaacaccacgggtg
NLRP3_R351T	forward	R351T	ctgctcaccacgacacctgtggccctggagaactg
NLRP3_R351T	reverse	R351T	ctccagggccacaggtgtcgtggtgatgacagagaggc
NLRP3_I411A	forward	I411A	cttcaccatgtgcttcccccctggtctgctggatcgtg
NLRP3_I411A	reverse	I411A	ccagcagaccagggggcgaagcacatggtgaagaggac
NLRP3_I411F	forward	I411F	cttcaccatgtgcttctccccctggtctgctggatcgtg
NLRP3_I411F	reverse	I411F	ccagcagaccagggggaagaagcacatggtgaagaggac
NLRP3_F575A	forward	F575A	ggggattttgattgctgtgtacgttctctttggc
NLRP3_F575A	reverse	F575A	gaggaaacgtacaacagcaatcaaatccccttttcg
NLRP3_F575L	forward	F575L	ggggattttgatttgggtgtacgttctctttggc
NLRP3_F575L	reverse	F575L	gaggaaacgtacaacaaaatcaaatccccttttcg
NLRP3_R578A	forward	R578A	gattttgtgtagcttctctttggcctggtaac
NLRP3_R578A	reverse	R578A	caggccaaagaggaaagctacaacaaaatcaaatccc
NLRP3_R578E	forward	R578E	gttgtagagttctctttggcctggtaacaggag
NLRP3_R578E	reverse	R578E	gaggaaactctacaacaaaatcaaatccccttttcg
NLRP3_Y632S	forward	Y632S	cagctggaattgtctctgtttgtacgagatgcaggag
NLRP3_Y632S	reverse	Y632S	catctctacaacaggagaacaattccagctggctggg
NLRP3_D662E	forward	D662E	ctctccaccagaatggagcacatggttctcttttcg
NLRP3_D662E	reverse	D662E	ggaagaaacctgtgctccattctggtggagagattgatc

Table 7-3: Primers used in Sanger sequencing

Primer	strand	Sequence (5'→3')
NLRP9_1	forward	ctttgagcaactgaagttaac
NLRP9_2	forward	ctgtgtatccaagagttttgtc
NLRP9_3	forward	cgaaaactcatatttactctg
NLRP9_4	forward	cagcttgcagcatcctcactg
NLRP12_Out2	reverse	agtacatagctgcaagaactcctggaac
NLRP12_Out3	forward	atccactgagttccaggagttctttgca
NLRP12_Out4	reverse	gtcgtctgagcttcttgaatccactg
NLRP12_Out5	forward	gatggacctgttcagtgattcaaagcaa
NLRP3_1	forward	ctcatcaaggagcaccggagccagc
NLRP3_2	forward	ttcaggagaacagggtcctcttcac
NLRP3_3	forward	gcaaatcaggctggagctgctgaaatg
NLRP3_4	forward	tgtgtgcaatcgaagaagctctg

Primer	strand	Sequence (5'→3')
MBPfw	forward	atgccgaacatcccgcagatgtcc
pEGFP_C2-RP	reverse	tttaaagcaagtaaacctc
pGEX5-FP	forward	aacgtattgaagctatccc
pEGFP-RP	reverse	aacagctcctcgcccttg
pEGFP_N	reverse	ccgtccagctcgaccag
pQE-FP	forward	cggataacaatttcacacag
T7	forward	taatacgactcactataggg
pIRES-RP	reverse	tatagacaaacgcacaccg
CMV-for	forward	cgcaaatgggcggtaggcgtg
IRES-R-359	reverse	acccaacagctggccctcg
IRES-for	forward	taggegtgtacggtggg

### 7.9.3 Vectors

Table 7-4: DNA template vectors

Number	Name	Reference
1	pRP-CMV-NLRP9-IRES-ATG-mCitrine-HA	Kind gift from Rainer Stahl (Institute of Innate Immunity, University Clinics Bonn, Germany)
2	pRP-CMV-NLRP12-IRES-ATG-mCitrine-HA	Kind gift from Rainer Stahl (Institute of Innate Immunity, University Clinics Bonn, Germany)
3	pACEBAC1-MBP-tev-NLRP3	Geyer lab; protein-coding sequence of human NLRP3 is codon-optimized for expression in <i>Spodoptera frugiperda</i>

All DNA template vectors contain an Amp<sup>R</sup> resistance gene for positive selection during plasmid DNA amplification in bacteria.

Table 7-5: Destination vectors

Number	Name	Resistance	Reference
1	pACEBac1-MBP-tev	Gent <sup>R</sup>	Geyer lab, modified from pACEBac1
2	pACEBac1-mMBP	Gent <sup>R</sup>	Geyer lab, modified from pACEBac1
3	pGex4T1-GST-tev	Amp <sup>R</sup>	GE Healthcare (Freiburg, Germany)
4	pR 5'LTR-mCitrine	Amp <sup>R</sup>	Kind gift from Rainer Stahl (Institute of Innate Immunity, University Clinics Bonn, Germany)
5	IFM5-55-pIRESpuo3-N-Avi-tag	Amp <sup>R</sup>	Kind gift from IFM Therapeutics (Boston, USA)

### 7.10 Columns and affinity resins

Table 7-6: Columns and resins used for affinity chromatography

Column	Supplier
MBPTrap HP	GE Healthcare Europe (Freiburg, Germany)
GSTrap FF	GE Healthcare Europe (Freiburg, Germany)

Resin	Supplier
Amylose resin	New England Biolabs (Ipswich, USA)
Anti-Flag M2 affinity gel	Sigma-Aldrich (St Louis, USA)
Ni-NTA agarose	Qiagen, Hilden, Germany

Table 7-7: Gel filtration and reversed phase columns

Column	Supplier
HiLoad 16/600 Superdex 75 PG	GE Healthcare Europe (Freiburg, Germany)
Superdex 75 Increase 10/300 GL	GE Healthcare Europe (Freiburg, Germany)
Superdex 75 Increase 3.2/300	GE Healthcare Europe (Freiburg, Germany)
HiLoad 16/600 Superdex 200 PG	GE Healthcare Europe (Freiburg, Germany)
Superdex 200 Increase 10/300 GL	GE Healthcare Europe (Freiburg, Germany)
Superdex 200 Increase 3.2/300	GE Healthcare Europe (Freiburg, Germany)
Superose 6 PG XK 16/70	GE Healthcare Europe (Freiburg, Germany)
Superose 6 Increase 10/300 GL	GE Healthcare Europe (Freiburg, Germany)
Superose 6 Increase 3.2/300	GE Healthcare Europe (Freiburg, Germany)
Chromolith Performance RP-18e 100-4.6	Merck Millipore (Burlington, USA)

## 7.11 Devices

Device	Name/Type	Manufacturer
Scale	PCB-6000-1	Kern & Sohn (Balingen-Frommern, Germany)
Scale	PCB-2500-2	Kern & Sohn (Balingen-Frommern, Germany)
Scale	Secura 324-1S	Sartorius (Göttingen, Germany)
Thermomixer	Thermomixer comfort	Eppendorf (Hamburg, Germany)
Electroporator	Eporator	Eppendorf (Hamburg, Germany)
Water bath	ED-5	Julabo (Seelbach, Germany)
Water bath	WNB22	Memmert (Schwabach, Germany)
Ultrasonic bath	Sonorex Digitec	Bandelin (Berlin, Germany)
Ultrasonic homogenizer	Sonopuls HD3100	Bandelin (Berlin, Germany)
pH meter	Lab855	SI Analytics (Mainz, Germany)
Stirrer	Magnetic stirrer	VWR (Darmstadt, Germany)
Stirrer	MR3002	Heidolph Instruments (Schwabach, Germany)
Vacuum pump	VNC2/PC600 Lan NT	Vacuubrand (Wertheim, Germany)
Circle shaker	Vortex Genie 2	Scientific Industries (Bohemia, USA)
Pipettes	Research Plus	Eppendorf (Hamburg, Germany)
Pipette helper	accu-jet	Brand (Wertheim, Germany)
Gel casting and PAGE system	Mini-Protean Tetra Cell	Bio-Rad (Hercules, USA)
Power supply	PowerPac Basic and HC	Bio-Rad (Hercules, USA)
Microwave	HMT75M451	Bosch (Gerlingen, Germany)

<b>Device</b>	<b>Name/Type</b>	<b>Manufacturer</b>
Ultrapure water system	Micropure UV/UF	Thermo Fisher Scientific (Waltham, USA)
Dry Bath	Accublock digital dry bath	Labnet International (Edison, USA)
Circle shaker	KS 260 basic	IKA (Staufen, Germany)
Benchtop transilluminator	Visi-White	Analytik Jena (Jena, Germany)
Benchtop UV transilluminator	2UV	UVP (Upland, USA)
Imaging system	ChemiDoc XRS+	Bio-Rad (Hercules, USA)
Water bath	VWB6	VWR (Darmstadt, Germany)
DNA electrophoresis chambers	Sub-Cell GT	Bio-Rad (Hercules, USA)
Spectrophotometer	NanoDrop 2000c	Thermo Fisher Scientific (Waltham, USA)
PCR Thermocycler	Mastercycler nexus SX1, X2	Eppendorf (Hamburg, Germany)
UV-VIS photometer	Biophotometer D30	Eppendorf (Hamburg, Germany)
Mini centrifuge	Sprout Plus	Biozym Scientific (Hessisch Oldendorf, Germany)
Centrifuge	5427R, 5804R, 5810, 5425, 5424R	Eppendorf (Hamburg, Germany)
Centrifuge	Megastar 1.6R	VWR (Darmstadt, Germany)
Centrifuge	Avanti Jxn-26, Optima XPN-100	Beckman Coulter (Brea, USA)
Rotor	JLA 8.1000, JA 25.50, SW 60 Ti	Beckman Coulter (Brea, USA)
-80°C freezer	VIP Eco	Panasonic (Kadoma, Japan)
Dewar	26B	KGW-Isotherm (Karlsruhe, Germany)
Refrigerator, Freezer	different	Liebherr (Bulle, Switzerland)
FPLC systems	Äkta Start, Prime Plus, Pure, Micro	GE Healthcare (Freiburg, Germany)
HPLC systems	Bioinert 1260 Infinity, 1260 Infinity II	Agilent Technologies (Santa Clara, USA)
Roller mixer	RS-TR 05	Phoenix Instrument (Garbsen, Germany)
Cooling cabinet	Unichromat 1500	Uniequip (Planegg, Germany)
Thermostat cabinet	TC 445 S	Lovibond (Dortmund, Germany)
Autoclave	VX150	Systec (Linden, Germany)
Drying cabinet	Kelvitron t	Heraeus (Hanau, Germany)
Laboratory dishwasher	GG05 PG 8583 CD	Miele (Gütersloh, Germany)
Ice machine	CoolNat	Ziegra (Isernhagen, Germany)
Flow cytometer	LSRFortessa II	Becton Dickinson (Franklin Lakes, USA)
Pipetting robot	Crystal Gryphon LCP	Art Robins Instruments (Sunnyvale, USA)
Pipetting robot	Mosquito Crystal	SPT labtech (Melbourn, England)
Pipetting robot	EPMotion 5073	Eppendorf (Hamburg, Germany)

Device	Name/Type	Manufacturer
Protein crystallization imager	RI-1000	Formulatrix (Bedford, USA)
Cryo-loops	none	MiTIGen (Ithaca, USA)
Microscope	SMZ18	Nikon (Minato, Japan)
Microscope	Axio Vert.A1, Axiocam208	ZEISS (Jena, Germany)
Microscope	CKX53	Olympus (Shinjuku, Japan)
Epifluorescence microscope	Observer.Z1, 20x objective, Axiocam 506 mono	ZEISS (Jena, Germany)
Electron microscope	JEM-2200FS	Jeol (Akishima, Japan)
CMOS camera	TemCam-F416	TVIPS (Gauting, Germany)
Cell counting chamber	Neubauer chamber	Paul Marienfeld (Lauda-Königshofen, Germany)
Automatic cell counter	EVE	NanoEntek (Seoul, South Korea)
Class II biological safety cabinet	MSC-Advantage 1.8	Thermo Fisher Scientific (Waltham, USA)
Class II biological safety cabinet	Scanlaf Mars	Labogene (Lillerød, Denmark)
CO <sub>2</sub> incubator	MCO-20AIC	Sanyo (Ōsaka, Japan)
Incubator	Mini incubator	Labnet (Edison, USA)
Incubation shaker	Minitron, Multitron, Multitron Pro	Infors HT (Bottmingen, Switzerland)
MALS detector	miniDawn 3141-MD3	Wyatt Technologies (Santa Barbara, USA)
RI detector	Optilab rEX 650	Wyatt Technologies (Santa Barbara, USA)
DLS instrument	Dynapro NanoStar 672	Wyatt Technologies (Santa Barbara, USA)
nanoDSF instrument	Prometheus NT.48	NanoTemper Technologies (München, Germany)
SPR system	Biacore 8K	GE Healthcare (Freiburg, Germany)

## 7.12 Software

Software	Developer/Distributor
ApE 2.0	(Davis & Jorgensen, 2022)
Prism 7	GraphPad Software (San Diego, USA)
Affinity Designer 1.10.5	Serif (West Bridgford, England)
PyMOL 2.2.0	Schrödinger (New York City, USA)
Biacore Insight Evaluation 3.0.12.15655	Cytiva (Marlborough, USA)
ChemDraw 20.1	PerkinElmer (Waltham, USA)
LigPlot Plus 2.2.4	(Laskowski & Swindells, 2011)
Scaffold 5	Proteome Software (Portland, USA)
COOT 0.9.5	(Emsley & Cowtan, 2004)
PHENIX 1.19.2-4158	(Adams et al., 2002)
XDS package version January 31, 2020	(Kabsch, 1993)
OpenLab 2.2 and 3.4	Agilent Technologies (Santa Clara, USA)
Astra 8.0.0.19	Wyatt Technologies (Santa Barbara, USA)
DYNAMICS 7.8.2.18	Wyatt Technologies (Santa Barbara, USA)



<b>Software</b>	<b>Developer/Distributor</b>
PR.ThermControl 2.1.5	NanoTemper Technologies (München, Germany)
NetBeans 8.2	Apache Software Foundation (Forest Hill, USA), Oracle Corporation (Austin, USA)
XAMPP 7.2.4-0	Apache Friends (Volunteer team)
CLC Sequence Viewer 7	Qiagen (Hilden, Germany)
ImageLab 6.0.1	Bio-Rad (Hercules, USA)
OpenChrom 1.4.0	Lablicate (Hamburg, Germany)
ZEN 3.0	ZEISS (Jena, Germany)
CellProfiler 3.1.9	(McQuin et al., 2018)
Office for Mac 16.16.27	Microsoft (Redmond, USA)
EndNote 20.4	Clarivate Analytics (London, England)



## References

- Adams, P. D., Grosse-Kunstleve, R. W., Hung, L. W., Ioerger, T. R., McCoy, A. J., Moriarty, N. W., Read, R. J., Sacchettini, J. C., Sauter, N. K., & Terwilliger, T. C. PHENIX: building new software for automated crystallographic structure determination. *Acta Crystallogr D Biol Crystallogr* **58**, 1948-1954 (2002).
- Ade, J., DeYoung, B. J., Golstein, C., & Innes, R. W. Indirect activation of a plant nucleotide binding site-leucine-rich repeat protein by a bacterial protease. *Proc Natl Acad Sci U S A* **104**, 2531-2536 (2007).
- Afonine, P. V., Grosse-Kunstleve, R. W., Echols, N., Headd, J. J., Moriarty, N. W., Mustyakimov, M., Terwilliger, T. C., Urzhumtsev, A., Zwart, P. H., & Adams, P. D. Towards automated crystallographic structure refinement with phenix.refine. *Acta Crystallogr D Biol Crystallogr* **68**, 352-367 (2012).
- Agarwal, S., Pethani, J. P., Shah, H. A., Vyas, V., Sasane, S., Bhavsar, H., Bandyopadhyay, D., Giri, P., Viswanathan, K., Jain, M. R., & Sharma, R. Identification of a novel orally bioavailable NLRP3 inflammasome inhibitor. *Bioorg Med Chem Lett* **30**, 127571 (2020).
- Agarwal, S., Sasane, S., Shah, H. A., Pethani, J. P., Deshmukh, P., Vyas, V., Iyer, P., Bhavsar, H., Viswanathan, K., Bandyopadhyay, D., Giri, P., Mahapatra, J., Chatterjee, A., Jain, M. R., & Sharma, R. Discovery of N-Cyano-sulfoximineurea Derivatives as Potent and Orally Bioavailable NLRP3 Inflammasome Inhibitors. *ACS Med Chem Lett* **11**, 414-418 (2020).
- Akoev, V., Gogol, E. P., Barnett, M. E., & Zolkiewski, M. Nucleotide-induced switch in oligomerization of the AAA+ ATPase ClpB. *Protein Sci* **13**, 567-574 (2004).
- Allen, I. C., Wilson, J. E., Schneider, M., Lich, J. D., Roberts, R. A., Arthur, J. C., Woodford, R. M., Davis, B. K., Uronis, J. M., Herfarth, H. H., Jobin, C., Rogers, A. B., & Ting, J. P. NLRP12 suppresses colon inflammation and tumorigenesis through the negative regulation of noncanonical NF-kappaB signaling. *Immunity* **36**, 742-754 (2012).
- Ammelburg, M., Frickey, T., & Lupas, A. N. Classification of AAA+ proteins. *J Struct Biol* **156**, 2-11 (2006).
- Anand, P. K., Malireddi, R. K., Lukens, J. R., Vogel, P., Bertin, J., Lamkanfi, M., & Kanneganti, T. D. NLRP6 negatively regulates innate immunity and host defence against bacterial pathogens. *Nature* **488**, 389-393 (2012).
- Andreeva, L., David, L., Rawson, S., Shen, C., Pasricha, T., Pelegrin, P., & Wu, H. NLRP3 cages revealed by full-length mouse NLRP3 structure control pathway activation. *Cell* **184**, 6299-6312 e6222 (2021).
- Arthur, J. C., Lich, J. D., Aziz, R. K., Kotb, M., & Ting, J. P. Heat shock protein 90 associates with monarch-1 and regulates its ability to promote degradation of NF-kappaB-inducing kinase. *J Immunol* **179**, 6291-6296 (2007).
- Arthur, J. C., Lich, J. D., Ye, Z., Allen, I. C., Gris, D., Wilson, J. E., Schneider, M., Roney, K. E., O'Connor, B. P., Moore, C. B., Morrison, A., Sutterwala, F. S., Bertin, J., Koller, B. H., Liu, Z., & Ting, J. P. Cutting edge: NLRP12 controls dendritic and myeloid cell migration to affect contact hypersensitivity. *J Immunol* **185**, 4515-4519 (2010).
- Arya, P., & Acharya, V. Plant STAND P-loop NTPases: a current perspective of genome distribution, evolution, and function : Plant STAND P-loop NTPases: genomic organization, evolution, and molecular mechanism models contribute broadly to plant pathogen defense. *Mol Genet Genomics* **293**, 17-31 (2018).

- Ashcroft, S. J., & Ashcroft, F. M. The sulfonylurea receptor. *Biochim Biophys Acta* **1175**, 45-59 (1992).
- Ataide, M. A., Andrade, W. A., Zamboni, D. S., Wang, D., Souza Mdo, C., Franklin, B. S., Elian, S., Martins, F. S., Pereira, D., Reed, G., Fitzgerald, K. A., Golenbock, D. T., & Gazzinelli, R. T. Malaria-induced NLRP12/NLRP3-dependent caspase-1 activation mediates inflammation and hypersensitivity to bacterial superinfection. *PLoS Pathog* **10**, e1003885 (2014).
- Bae, J. Y., & Park, H. H. Crystal structure of NALP3 protein pyrin domain (PYD) and its implications in inflammasome assembly. *J Biol Chem* **286**, 39528-39536 (2011).
- Baker, P. J., Boucher, D., Bierschenk, D., Tebartz, C., Whitney, P. G., D'Silva, D. B., Tanzer, M. C., Monteleone, M., Robertson, A. A., Cooper, M. A., Alvarez-Diaz, S., Herold, M. J., Bedoui, S., Schroder, K., & Masters, S. L. NLRP3 inflammasome activation downstream of cytoplasmic LPS recognition by both caspase-4 and caspase-5. *Eur J Immunol* **45**, 2918-2926 (2015).
- Banks, W. A. Characteristics of compounds that cross the blood-brain barrier. *BMC Neurol* **9 Suppl 1**, S3 (2009).
- Bardoel, B. W., & Strijp, J. A. Molecular battle between host and bacterium: recognition in innate immunity. *J Mol Recognit* **24**, 1077-1086 (2011).
- Barnett, K. C., Coronas-Serna, J. M., Zhou, W., Ernandes, M. J., Cao, A., Kranzusch, P. J., & Kagan, J. C. Phosphoinositide Interactions Position cGAS at the Plasma Membrane to Ensure Efficient Distinction between Self- and Viral DNA. *Cell* **176**, 1432-1446 e1411 (2019).
- Baroja-Mazo, A., Compan, V., Martin-Sanchez, F., Tapia-Abellan, A., Couillin, I., & Pelegrin, P. Early endosome autoantigen 1 regulates IL-1beta release upon caspase-1 activation independently of gasdermin D membrane permeabilization. *Sci Rep* **9**, 5788 (2019).
- Baroja-Mazo, A., Martin-Sanchez, F., Gomez, A. I., Martinez, C. M., Amores-Iniesta, J., Compan, V., Barbera-Cremades, M., Yague, J., Ruiz-Ortiz, E., Anton, J., Bujan, S., Couillin, I., Brough, D., Arostegui, J. I., & Pelegrin, P. The NLRP3 inflammasome is released as a particulate danger signal that amplifies the inflammatory response. *Nat Immunol* **15**, 738-748 (2014).
- Barry, R., John, S. W., Liccardi, G., Tenev, T., Jaco, I., Chen, C. H., Choi, J., Kasperkiewicz, P., Fernandes-Alnemri, T., Alnemri, E., Drag, M., Chen, Y., & Meier, P. SUMO-mediated regulation of NLRP3 modulates inflammasome activity. *Nat Commun* **9**, 3001 (2018).
- Basak, C., Pathak, S. K., Bhattacharyya, A., Mandal, D., Pathak, S., & Kundu, M. NF-kappaB- and C/EBPbeta-driven interleukin-1beta gene expression and PAK1-mediated caspase-1 activation play essential roles in interleukin-1beta release from Helicobacter pylori lipopolysaccharide-stimulated macrophages. *J Biol Chem* **280**, 4279-4288 (2005).
- Bauernfeind, F. G., Horvath, G., Stutz, A., Alnemri, E. S., MacDonald, K., Speert, D., Fernandes-Alnemri, T., Wu, J., Monks, B. G., Fitzgerald, K. A., Hornung, V., & Latz, E. Cutting edge: NF-kappaB activating pattern recognition and cytokine receptors license NLRP3 inflammasome activation by regulating NLRP3 expression. *J Immunol* **183**, 787-791 (2009).
- Bauernfried, S., Scherr, M. J., Pichlmair, A., Duderstadt, K. E., & Hornung, V. Human NLRP1 is a sensor for double-stranded RNA. *Science* **371** (2021).
- Bertheloot, D., Latz, E., & Franklin, B. S. Necroptosis, pyroptosis and apoptosis: an intricate game of cell death. *Cell Mol Immunol* **18**, 1106-1121 (2021).
- Bokhove, M., Sadat Al Hosseini, H., Saito, T., Dioguardi, E., Gegenschatz-Schmid, K., Nishimura, K., Raj, I., de Sanctis, D., Han, L., & Jovine, L. Easy mammalian expression and crystallography of maltose-binding protein-fused human proteins. *J Struct Biol* **194**, 1-7 (2016).
- Booshehri, L. M., & Hoffman, H. M. CAPS and NLRP3. *J Clin Immunol* **39**, 277-286 (2019).

## References

---

- Boucher, D., Monteleone, M., Coll, R. C., Chen, K. W., Ross, C. M., Teo, J. L., Gomez, G. A., Holley, C. L., Bierschenk, D., Stacey, K. J., Yap, A. S., Bezbradica, J. S., & Schroder, K. Caspase-1 self-cleavage is an intrinsic mechanism to terminate inflammasome activity. *J Exp Med* **215**, 827-840 (2018).
- Boyden, E. D., & Dietrich, W. F. Nalp1b controls mouse macrophage susceptibility to anthrax lethal toxin. *Nat Genet* **38**, 240-244 (2006).
- Brinkschulte, H. M. R. Biochemical and structural characterization of the NLRP3 inflammasome. *Rheinische Friedrich-Wilhelms-Universität Bonn* (2020).
- Broz, P., & Dixit, V. M. Inflammasomes: mechanism of assembly, regulation and signalling. *Nat Rev Immunol* **16**, 407-420 (2016).
- Broz, P., Pelegrin, P., & Shao, F. The gasdermins, a protein family executing cell death and inflammation. *Nat Rev Immunol* **20**, 143-157 (2020).
- Bulau, A. M., Nold, M. F., Li, S., Nold-Petry, C. A., Fink, M., Mansell, A., Schwerd, T., Hong, J., Rubartelli, A., Dinarello, C. A., & Bufler, P. Role of caspase-1 in nuclear translocation of IL-37, release of the cytokine, and IL-37 inhibition of innate immune responses. *Proc Natl Acad Sci U S A* **111**, 2650-2655 (2014).
- Burdette, B. E., Esparza, A. N., Zhu, H., & Wang, S. Gasdermin D in pyroptosis. *Acta Pharm Sin B* **11**, 2768-2782 (2021).
- Cai, S., Batra, S., Del Piero, F., & Jeyaseelan, S. NLRP12 modulates host defense through IL-17A-CXCL1 axis. *Mucosal Immunol* **9**, 503-514 (2016).
- Carrillo, J. L. M., Rodríguez, F. P. C., Coronado, O. G., García, M. A. M., & Cordero, J. F. C. Physiology and Pathology of Innate Immune Response Against Pathogens. In *Physiology and Pathology of Immunology* (2017).
- Caruso, R., Warner, N., Inohara, N., & Nunez, G. NOD1 and NOD2: signaling, host defense, and inflammatory disease. *Immunity* **41**, 898-908 (2014).
- Case, D. R., Zubieta, J., & R, P. D. The Coordination Chemistry of Bio-Relevant Ligands and Their Magnesium Complexes. *Molecules* **25** (2020).
- Castano-Rodriguez, N., Kaakoush, N. O., Goh, K. L., Fock, K. M., & Mitchell, H. M. The NOD-like receptor signalling pathway in *Helicobacter pylori* infection and related gastric cancer: a case-control study and gene expression analyses. *PLoS One* **9**, e98899 (2014).
- Chae, J. J., Wood, G., Masters, S. L., Richard, K., Park, G., Smith, B. J., & Kastner, D. L. The B30.2 domain of pyrin, the familial Mediterranean fever protein, interacts directly with caspase-1 to modulate IL-1 $\beta$  production. *Proc Natl Acad Sci U S A* **103**, 9982-9987 (2006).
- Chae, J. J., Wood, G., Richard, K., Jaffe, H., Colburn, N. T., Masters, S. L., Gumucio, D. L., Shoham, N. G., & Kastner, D. L. The familial Mediterranean fever protein, pyrin, is cleaved by caspase-1 and activates NF- $\kappa$ B through its N-terminal fragment. *Blood* **112**, 1794-1803 (2008).
- Chan, A. H., & Schroder, K. Inflammasome signaling and regulation of interleukin-1 family cytokines. *J Exp Med* **217** (2020).
- Chandler, C. E., & Ernst, R. K. Bacterial lipids: powerful modifiers of the innate immune response. *F1000Res* **6** (2017).
- Chen, H., Deng, Y., Gan, X., Li, Y., Huang, W., Lu, L., Wei, L., Su, L., Luo, J., Zou, B., Hong, Y., Cao, Y., Liu, Y., & Chi, W. NLRP12 collaborates with NLRP3 and NLRC4 to promote pyroptosis inducing ganglion cell death of acute glaucoma. *Mol Neurodegener* **15**, 26 (2020).

- Chen, J., & Chen, Z. J. PtdIns4P on dispersed trans-Golgi network mediates NLRP3 inflammasome activation. *Nature* **564**, 71-76 (2018).
- Chen, K. P., Hua, K. F., Tsai, F. T., Lin, T. Y., Cheng, C. Y., Yang, D. I., Hsu, H. T., & Ju, T. C. A selective inhibitor of the NLRP3 inflammasome as a potential therapeutic approach for neuroprotection in a transgenic mouse model of Huntington's disease. *J Neuroinflammation* **19**, 56 (2022).
- Chen, L., Wilson, J. E., Koenigsnecht, M. J., Chou, W. C., Montgomery, S. A., Truax, A. D., Brickey, W. J., Packey, C. D., Maharshak, N., Matsushima, G. K., Plevy, S. E., Young, V. B., Sartor, R. B., & Ting, J. P. NLRP12 attenuates colon inflammation by maintaining colonic microbial diversity and promoting protective commensal bacterial growth. *Nat Immunol* **18**, 541-551 (2017).
- Chen, S. T., Chen, L., Lin, D. S., Chen, S. Y., Tsao, Y. P., Guo, H., Li, F. J., Tseng, W. T., Tam, J. W., Chao, C. W., Brickey, W. J., Dzhagalov, I., Song, M. J., Kang, H. R., Jung, J. U., & Ting, J. P. NLRP12 Regulates Anti-viral RIG-I Activation via Interaction with TRIM25. *Cell Host Microbe* **25**, 602-616 e607 (2019).
- Cheng, J., Waite, A. L., Tkaczyk, E. R., Ke, K., Richards, N., Hunt, A. J., & Gumucio, D. L. Kinetic properties of ASC protein aggregation in epithelial cells. *J Cell Physiol* **222**, 738-747 (2010).
- Cheng, T. C., Akey, I. V., Yuan, S., Yu, Z., Ludtke, S. J., & Akey, C. W. A Near-Atomic Structure of the Dark Apoptosome Provides Insight into Assembly and Activation. *Structure* **25**, 40-52 (2017).
- Cheng, T. C., Hong, C., Akey, I. V., Yuan, S., & Akey, C. W. A near atomic structure of the active human apoptosome. *Elife* **5** (2016).
- Christgen, S., & Kanneganti, T. D. Inflammasomes and the fine line between defense and disease. *Curr Opin Immunol* **62**, 39-44 (2020).
- Chung, I. C., OuYang, C. N., Yuan, S. N., Li, H. P., Chen, J. T., Shieh, H. R., Chen, Y. J., Ojcius, D. M., Chu, C. L., Yu, J. S., Chang, Y. S., & Chen, L. C. Pyk2 activates the NLRP3 inflammasome by directly phosphorylating ASC and contributes to inflammasome-dependent peritonitis. *Sci Rep* **6**, 36214 (2016).
- Ciechanover, A. The ubiquitin-proteasome proteolytic pathway. *Cell* **79**, 13-21 (1994).
- Civril, F., Deimling, T., de Oliveira Mann, C. C., Ablasser, A., Moldt, M., Witte, G., Hornung, V., & Hopfner, K. P. Structural mechanism of cytosolic DNA sensing by cGAS. *Nature* **498**, 332-337 (2013).
- Cohen, S., Tuckwell, K., Katsumoto, T. R., Zhao, R., Galanter, J., Lee, C., Rae, J., Toth, B., Ramamoorthi, N., Hackney, J. A., Berman, A., Damjanov, N., Fedkov, D., Jeka, S., Chinn, L. W., Townsend, M. J., Morimoto, A. M., & Genovese, M. C. Fenebrutinib versus Placebo or Adalimumab in Rheumatoid Arthritis: A Randomized, Double-Blind, Phase II Trial (ANDES Study). *Arthritis Rheumatol* (2020).
- Coll, R. C., Hill, J. R., Day, C. J., Zamoshnikova, A., Boucher, D., Massey, N. L., Chitty, J. L., Fraser, J. A., Jennings, M. P., Robertson, A. A. B., & Schroder, K. MCC950 directly targets the NLRP3 ATP-hydrolysis motif for inflammasome inhibition. *Nat Chem Biol* **15**, 556-559 (2019).
- Coll, R. C., Robertson, A. A., Chae, J. J., Higgins, S. C., Munoz-Planillo, R., Inserra, M. C., Vetter, I., Dungan, L. S., Monks, B. G., Stutz, A., Croker, D. E., Butler, M. S., Haneklaus, M., Sutton, C. E., Nunez, G., Latz, E., Kastner, D. L., Mills, K. H., Masters, S. L., . . . O'Neill, L. A. A small-molecule inhibitor of the NLRP3 inflammasome for the treatment of inflammatory diseases. *Nat Med* **21**, 248-255 (2015).
- Coll, R. C., Schroder, K., & Pelegrin, P. NLRP3 and pyroptosis blockers for treating inflammatory diseases. *Trends Pharmacol Sci* (2022).

## References

---

- Conforti-Andreoni, C., Ricciardi-Castagnoli, P., & Mortellaro, A. The inflammasomes in health and disease: from genetics to molecular mechanisms of autoinflammation and beyond. *Cell Mol Immunol* **8**, 135-145 (2011).
- Corcoran, S. E., Halai, R., & Cooper, M. A. Pharmacological Inhibition of the Nod-Like Receptor Family Pyrin Domain Containing 3 Inflammasome with MCC950. *Pharmacol Rev* **73**, 968-1000 (2021).
- Crawford, S. E., Ramani, S., Tate, J. E., Parashar, U. D., Svensson, L., Hagbom, M., Franco, M. A., Greenberg, H. B., O'Ryan, M., Kang, G., Desselberger, U., & Estes, M. K. Rotavirus infection. *Nat Rev Dis Primers* **3**, 17083 (2017).
- Cullen, S. P., Kearney, C. J., Clancy, D. M., & Martin, S. J. Diverse Activators of the NLRP3 Inflammasome Promote IL-1 $\beta$  Secretion by Triggering Necrosis. *Cell Rep* **11**, 1535-1548 (2015).
- Danot, O., Marquenet, E., Vidal-Ingigliardi, D., & Richet, E. Wheel of Life, Wheel of Death: A Mechanistic Insight into Signaling by STAND Proteins. *Structure* **17**, 172-182 (2009).
- Davis, M. W., & Jorgensen, E. M. ApE, A Plasmid Editor: A Freely Available DNA Manipulation and Visualization Program. *Frontiers in Bioinformatics* **2** (2022).
- Deddouche, S., Goubau, D., Rehwinkel, J., Chakravarty, P., Begum, S., Maillard, P. V., Borg, A., Matthews, N., Feng, Q., van Kuppeveld, F. J., & Reis e Sousa, C. Identification of an LGP2-associated MDA5 agonist in picornavirus-infected cells. *Elife* **3**, e01535 (2014).
- Dekker, C., Mattes, H., Wright, M., Boettcher, A., Hinniger, A., Hughes, N., Kapps-Fouthier, S., Eder, J., Erbel, P., Stiefl, N., Mackay, A., & Farady, C. J. Crystal Structure of NLRP3 NACHT Domain With an Inhibitor Defines Mechanism of Inflammasome Inhibition. *J Mol Biol* **433**, 167309 (2021).
- Dennehy, P. H. Rotavirus Infection: A Disease of the Past? *Infect Dis Clin North Am* **29**, 617-635 (2015).
- Dick, M. S., Sborgi, L., Ruhl, S., Hiller, S., & Broz, P. ASC filament formation serves as a signal amplification mechanism for inflammasomes. *Nat Commun* **7**, 11929 (2016).
- Diebolder, C. A., Halff, E. F., Koster, A. J., Huizinga, E. G., & Koning, R. I. Cryoelectron Tomography of the NAIP5/NLRC4 Inflammasome: Implications for NLR Activation. *Structure* **23**, 2349-2357 (2015).
- Dinarello, C. A. Immunological and inflammatory functions of the interleukin-1 family. *Annu Rev Immunol* **27**, 519-550 (2009).
- Dinarello, C. A. Overview of the IL-1 family in innate inflammation and acquired immunity. *Immunol Rev* **281**, 8-27 (2018).
- Dinarello, C. A., Novick, D., Kim, S., & Kaplanski, G. Interleukin-18 and IL-18 binding protein. *Front Immunol* **4**, 289 (2013).
- Ding, J., Wang, K., Liu, W., She, Y., Sun, Q., Shi, J., Sun, H., Wang, D. C., & Shao, F. Pore-forming activity and structural autoinhibition of the gasdermin family. *Nature* **535**, 111-116 (2016).
- Douglas, T., & Saleh, M. Cross-regulation between LUBAC and caspase-1 modulates cell death and inflammation. *J Biol Chem* **295**, 5216-5228 (2020).
- Drakou, C. E., Malekkou, A., Hayes, J. M., Lederer, C. W., Leonidas, D. D., Oikonomakos, N. G., Lamond, A. I., Santama, N., & Zographos, S. E. hCINAP is an atypical mammalian nuclear adenylate kinase with an ATPase motif: structural and functional studies. *Proteins* **80**, 206-220 (2012).
- Du, M., & Chen, Z. J. DNA-induced liquid phase condensation of cGAS activates innate immune signaling. *Science* **361**, 704-709 (2018).

- Duncan, J. A., Bergstralh, D. T., Wang, Y., Willingham, S. B., Ye, Z., Zimmermann, A. G., & Ting, J. P. Cryopyrin/NALP3 binds ATP/dATP, is an ATPase, and requires ATP binding to mediate inflammatory signaling. *Proc Natl Acad Sci U S A* **104**, 8041-8046 (2007).
- Duong, B. H., Onizawa, M., Oses-Prieto, J. A., Advincula, R., Burlingame, A., Malynn, B. A., & Ma, A. A20 restricts ubiquitination of pro-interleukin-1beta protein complexes and suppresses NLRP3 inflammasome activity. *Immunity* **42**, 55-67 (2015).
- Dzeja, P., & Terzic, A. Adenylate kinase and AMP signaling networks: metabolic monitoring, signal communication and body energy sensing. *Int J Mol Sci* **10**, 1729-1772 (2009).
- Eibl, C., Grigoriu, S., Hessenberger, M., Wenger, J., Puehringer, S., Pinheiro, A. S., Wagner, R. N., Proell, M., Reed, J. C., Page, R., Diederichs, K., & Peti, W. Structural and functional analysis of the NLRP4 pyrin domain. *Biochemistry* **51**, 7330-7341 (2012).
- Eibl, C., Hessenberger, M., Wenger, J., & Brandstetter, H. Structures of the NLRP14 pyrin domain reveal a conformational switch mechanism regulating its molecular interactions. *Acta Crystallogr D Biol Crystallogr* **70**, 2007-2018 (2014).
- El-Sharkawy, L. Y., Brough, D., & Freeman, S. Inhibiting the NLRP3 Inflammasome. *Molecules* **25** (2020).
- Ellwanger, K., Becker, E., Kienes, I., Sowa, A., Postma, Y., Cardona Gloria, Y., Weber, A. N. R., & Kufer, T. A. The NLR family pyrin domain-containing 11 protein contributes to the regulation of inflammatory signaling. *J Biol Chem* **293**, 2701-2710 (2018).
- Emsley, P., & Cowtan, K. Coot: model-building tools for molecular graphics. *Acta Crystallogr D Biol Crystallogr* **60**, 2126-2132 (2004).
- Enkhbayar, P., Kamiya, M., Osaki, M., Matsumoto, T., & Matsushima, N. Structural principles of leucine-rich repeat (LRR) proteins. *Proteins* **54**, 394-403 (2004).
- Erzberger, J. P., & Berger, J. M. Evolutionary relationships and structural mechanisms of AAA+ proteins. *Annu Rev Biophys Biomol Struct* **35**, 93-114 (2006).
- Evavold, C. L., Ruan, J., Tan, Y., Xia, S., Wu, H., & Kagan, J. C. The Pore-Forming Protein Gasdermin D Regulates Interleukin-1 Secretion from Living Macrophages. *Immunity* **48**, 35-44 e36 (2018).
- Faustin, B., Lartigue, L., Bruey, J. M., Luciano, F., Sergienko, E., Bailly-Maitre, B., Volkmann, N., Hanein, D., Rouiller, I., & Reed, J. C. Reconstituted NALP1 inflammasome reveals two-step mechanism of caspase-1 activation. *Mol Cell* **25**, 713-724 (2007).
- Fenini, G., Karakaya, T., Hennig, P., Di Filippo, M., Slaufova, M., & Beer, H. D. NLRP1 Inflammasome Activation in Keratinocytes: Increasing Evidence of Important Roles in Inflammatory Skin Diseases and Immunity. *J Invest Dermatol* (2022).
- Fernandes-Alnemri, T., Kang, S., Anderson, C., Sagara, J., Fitzgerald, K. A., & Alnemri, E. S. Cutting edge: TLR signaling licenses IRAK1 for rapid activation of the NLRP3 inflammasome. *J Immunol* **191**, 3995-3999 (2013).
- Fernandez, M. V., Budde, J., Del-Aguila, J. L., Ibanez, L., Deming, Y., Harari, O., Norton, J., Morris, J. C., Goate, A. M., group, N.-L. f. s., Ncrad, & Cruchaga, C. Evaluation of Gene-Based Family-Based Methods to Detect Novel Genes Associated With Familial Late Onset Alzheimer Disease. *Front Neurosci* **12**, 209 (2018).
- Ferrao, R., & Wu, H. Helical assembly in the death domain (DD) superfamily. *Curr Opin Struct Biol* **22**, 241-247 (2012).



## References

---

- Finger, J. N., Lich, J. D., Dare, L. C., Cook, M. N., Brown, K. K., Duraiswami, C., Bertin, J., & Gough, P. J. Autolytic proteolysis within the function to find domain (FIIND) is required for NLRP1 inflammasome activity. *J Biol Chem* **287**, 25030-25037 (2012).
- Fitzgerald, K. A., & Kagan, J. C. Toll-like Receptors and the Control of Immunity. *Cell* **180**, 1044-1066 (2020).
- Franklin, B. S., Bossaller, L., De Nardo, D., Ratter, J. M., Stutz, A., Engels, G., Brenker, C., Nordhoff, M., Mirandola, S. R., Al-Amoudi, A., Mangan, M. S., Zimmer, S., Monks, B. G., Fricke, M., Schmidt, R. E., Espevik, T., Jones, B., Jarnicki, A. G., Hansbro, P. M., . . . Latz, E. The adaptor ASC has extracellular and 'prionoid' activities that propagate inflammation. *Nat Immunol* **15**, 727-737 (2014).
- Fulp, J., He, L., Toldo, S., Jiang, Y., Boice, A., Guo, C., Li, X., Rolfe, A., Sun, D., Abbate, A., Wang, X. Y., & Zhang, S. Structural Insights of Benzenesulfonamide Analogues as NLRP3 Inflammasome Inhibitors: Design, Synthesis, and Biological Characterization. *J Med Chem* **61**, 5412-5423 (2018).
- Gallo, R. L. Human Skin Is the Largest Epithelial Surface for Interaction with Microbes. *J Invest Dermatol* **137**, 1213-1214 (2017).
- Gao, W., Yang, J., Liu, W., Wang, Y., & Shao, F. Site-specific phosphorylation and microtubule dynamics control Pyrin inflammasome activation. *Proc Natl Acad Sci U S A* **113**, E4857-4866 (2016).
- Garlanda, C., Dinarello, C. A., & Mantovani, A. The interleukin-1 family: back to the future. *Immunity* **39**, 1003-1018 (2013).
- Gasteiger, E., Gattiker, A., Hoogland, C., Ivanyi, I., Appel, R. D., & Bairoch, A. ExpPASy: The proteomics server for in-depth protein knowledge and analysis. *Nucleic Acids Res* **31**, 3784-3788 (2003).
- Geijtenbeek, T. B., & Gringhuis, S. I. Signalling through C-type lectin receptors: shaping immune responses. *Nat Rev Immunol* **9**, 465-479 (2009).
- Gharagozloo, M., Gris, K. V., Mahvelati, T., Amrani, A., Lukens, J. R., & Gris, D. NLR-Dependent Regulation of Inflammation in Multiple Sclerosis. *Front Immunol* **8**, 2012 (2017).
- Gharagozloo, M., Mahmoud, S., Simard, C., Mahvelati, T. M., Amrani, A., & Gris, D. The Dual Immunoregulatory function of Nlrp12 in T Cell-Mediated Immune Response: Lessons from Experimental Autoimmune Encephalomyelitis. *Cells* **7** (2018).
- Gil-Varea, E., Urcelay, E., Vilarino-Guell, C., Costa, C., Midaglia, L., Matesanz, F., Rodriguez-Antiguedad, A., Oksenberg, J., Espino-Paisan, L., Dessa Sadovnick, A., Saiz, A., Villar, L. M., Garcia-Merino, J. A., Ramio-Torrenta, L., Trivino, J. C., Quintana, E., Robles, R., Sanchez-Lopez, A., Arroyo, R., . . . Comabella, M. Exome sequencing study in patients with multiple sclerosis reveals variants associated with disease course. *J Neuroinflammation* **15**, 265 (2018).
- Gioannini, T. L., Teghanemt, A., Zhang, D., Coussens, N. P., Dockstader, W., Ramaswamy, S., & Weiss, J. P. Isolation of an endotoxin-MD-2 complex that produces Toll-like receptor 4-dependent cell activation at picomolar concentrations. *Proc Natl Acad Sci U S A* **101**, 4186-4191 (2004).
- Gong, Q., Robinson, K., Xu, C., Huynh, P. T., Chong, K. H. C., Tan, E. Y. J., Zhang, J., Boo, Z. Z., Teo, D. E. T., Lay, K., Zhang, Y., Lim, J. S. Y., Goh, W. I., Wright, G., Zhong, F. L., Reversade, B., & Wu, B. Structural basis for distinct inflammasome complex assembly by human NLRP1 and CARD8. *Nat Commun* **12**, 188 (2021).
- Gong, T., Liu, L., Jiang, W., & Zhou, R. DAMP-sensing receptors in sterile inflammation and inflammatory diseases. *Nat Rev Immunol* **20**, 95-112 (2020).
- Goodridge, H. S., Simmons, R. M., & Underhill, D. M. Dectin-1 stimulation by *Candida albicans* yeast or zymosan triggers NFAT activation in macrophages and dendritic cells. *J Immunol* **178**, 3107-3115 (2007).

- Gorrec, F. The MORPHEUS protein crystallization screen. *J Appl Crystallogr* **42**, 1035-1042 (2009).
- Gorrec, F. Protein crystallization screens developed at the MRC Laboratory of Molecular Biology. *Drug Discov Today* **21**, 819-825 (2016).
- Goubau, D., Schlee, M., Deddouche, S., Puijssers, A. J., Zillinger, T., Goldeck, M., Schuberth, C., Van der Veen, A. G., Fujimura, T., Rehwinkel, J., Iskarpatyoti, J. A., Barchet, W., Ludwig, J., Dermody, T. S., Hartmann, G., & Reis e Sousa, C. Antiviral immunity via RIG-I-mediated recognition of RNA bearing 5'-diphosphates. *Nature* **514**, 372-375 (2014).
- Gray, E. E., Winship, D., Snyder, J. M., Child, S. J., Geballe, A. P., & Stetson, D. B. The AIM2-like Receptors Are Dispensable for the Interferon Response to Intracellular DNA. *Immunity* **45**, 255-266 (2016).
- Gringhuis, S. I., den Dunnen, J., Litjens, M., van Het Hof, B., van Kooyk, Y., & Geijtenbeek, T. B. C-type lectin DC-SIGN modulates Toll-like receptor signaling via Raf-1 kinase-dependent acetylation of transcription factor NF-kappaB. *Immunity* **26**, 605-616 (2007).
- Gritsenko, A., Yu, S., Martin-Sanchez, F., Diaz-Del-Olmo, I., Nichols, E. M., Davis, D. M., Brough, D., & Lopez-Castejon, G. Priming Is Dispensable for NLRP3 Inflammasome Activation in Human Monocytes In Vitro. *Front Immunol* **11**, 565924 (2020).
- Guan, K., Wei, C., Zheng, Z., Song, T., Wu, F., Zhang, Y., Cao, Y., Ma, S., Chen, W., Xu, Q., Xia, W., Gu, J., He, X., & Zhong, H. MAVS Promotes Inflammasome Activation by Targeting ASC for K63-Linked Ubiquitination via the E3 Ligase TRAF3. *J Immunol* **194**, 4880-4890 (2015).
- Guo, H., Callaway, J. B., & Ting, J. P. Inflammasomes: mechanism of action, role in disease, and therapeutics. *Nat Med* **21**, 677-687 (2015).
- Ha, H. J., & Park, H. H. Crystal structure of the human NLRP9 pyrin domain reveals a bent N-terminal loop that may regulate inflammasome assembly. *FEBS Lett* **594**, 2396-2405 (2020).
- Hafner-Bratkovic, I., Susjan, P., Lainscek, D., Tapia-Abellan, A., Cerovic, K., Kadunc, L., Angosto-Bazarra, D., Pelegrin, P., & Jerala, R. NLRP3 lacking the leucine-rich repeat domain can be fully activated via the canonical inflammasome pathway. *Nat Commun* **9**, 5182 (2018).
- Hagar, J. A., Powell, D. A., Aachoui, Y., Ernst, R. K., & Miao, E. A. Cytoplasmic LPS activates caspase-11: implications in TLR4-independent endotoxic shock. *Science* **341**, 1250-1253 (2013).
- Half, E. F., Diebolder, C. A., Versteeg, M., Schouten, A., Brondijk, T. H., & Huizinga, E. G. Formation and structure of a NAIP5-NLRC4 inflammasome induced by direct interactions with conserved N- and C-terminal regions of flagellin. *J Biol Chem* **287**, 38460-38472 (2012).
- Han, S., Lear, T. B., Jerome, J. A., Rajbhandari, S., Snively, C. A., Gulick, D. L., Gibson, K. F., Zou, C., Chen, B. B., & Mallampalli, R. K. Lipopolysaccharide Primes the NALP3 Inflammasome by Inhibiting Its Ubiquitination and Degradation Mediated by the SCFFBXL2 E3 Ligase. *J Biol Chem* **290**, 18124-18133 (2015).
- Hara, H., Seregin, S. S., Yang, D., Fukase, K., Chamailard, M., Alnemri, E. S., Inohara, N., Chen, G. Y., & Nunez, G. The NLRP6 Inflammasome Recognizes Lipoteichoic Acid and Regulates Gram-Positive Pathogen Infection. *Cell* **175**, 1651-1664 e1614 (2018).
- Hara, H., Tsuchiya, K., Kawamura, I., Fang, R., Hernandez-Cuellar, E., Shen, Y., Mizuguchi, J., Schweighoffer, E., Tybulewicz, V., & Mitsuyama, M. Phosphorylation of the adaptor ASC acts as a molecular switch that controls the formation of speck-like aggregates and inflammasome activity. *Nat Immunol* **14**, 1247-1255 (2013).
- Harrison, D., Boutard, N., Brzozka, K., Bugaj, M., Chmielewski, S., Cierpich, A., Doedens, J. R., Fabritius, C. R. Y., Gabel, C. A., Galezowski, M., Kowalczyk, P., Levenets, O., Mroczkowska, M., Palica, K., Porter, R. A., Schultz, D., Sowinska, M., Topolnicki, G., Urbanski, P., . . . Watt, A. P.

- Discovery of a series of ester-substituted NLRP3 inflammasome inhibitors. *Bioorg Med Chem Lett* **30**, 127560 (2020).
- Hartmann, G. Nucleic Acid Immunity. *Adv Immunol* **133**, 121-169 (2017).
- He, M., Chiang, H. H., Luo, H., Zheng, Z., Qiao, Q., Wang, L., Tan, M., Ohkubo, R., Mu, W. C., Zhao, S., Wu, H., & Chen, D. An Acetylation Switch of the NLRP3 Inflammasome Regulates Aging-Associated Chronic Inflammation and Insulin Resistance. *Cell Metab* **31**, 580-591 e585 (2020).
- He, W. T., Wan, H., Hu, L., Chen, P., Wang, X., Huang, Z., Yang, Z. H., Zhong, C. Q., & Han, J. Gasdermin D is an executor of pyroptosis and required for interleukin-1beta secretion. *Cell Res* **25**, 1285-1298 (2015).
- He, Y., Zeng, M. Y., Yang, D., Motro, B., & Nunez, G. NEK7 is an essential mediator of NLRP3 activation downstream of potassium efflux. *Nature* **530**, 354-357 (2016).
- Heilig, R., Dick, M. S., Sborgi, L., Meunier, E., Hiller, S., & Broz, P. The Gasdermin-D pore acts as a conduit for IL-1beta secretion in mice. *Eur J Immunol* **48**, 584-592 (2018).
- Heras, B., & Martin, J. L. Post-crystallization treatments for improving diffraction quality of protein crystals. *Acta Crystallogr D Biol Crystallogr* **61**, 1173-1180 (2005).
- Hill, J. R., Coll, R. C., Sue, N., Reid, J. C., Dou, J., Holley, C. L., Pelingon, R., Dickinson, J. B., Biden, T. J., Schroder, K., Cooper, M. A., & Robertson, A. A. B. Sulfonylureas as Concomitant Insulin Secretagogues and NLRP3 Inflammasome Inhibitors. *ChemMedChem* **12**, 1449-1457 (2017).
- Hill, J. R., Shao, X., Massey, N. L., Stauff, J., Sherman, P. S., Robertson, A. A. B., & Scott, P. J. H. Synthesis and evaluation of NLRP3-inhibitory sulfonylurea [(11)C]MCC950 in healthy animals. *Bioorg Med Chem Lett* **30**, 127186 (2020).
- Hiller, S., Kohl, A., Fiorito, F., Herrmann, T., Wider, G., Tschopp, J., Grutter, M. G., & Wuthrich, K. NMR structure of the apoptosis- and inflammation-related NALP1 pyrin domain. *Structure* **11**, 1199-1205 (2003).
- Hochheiser, I. V., Behrmann, H., Hagelueken, G., Rodriguez-Alcazar, J. F., Kopp, A., Latz, E., Behrmann, E., & Geyer, M. Directionality of PYD filament growth determined by the transition of NLRP3 nucleation seeds to ASC elongation. *Sci Adv* **8**, eabn7583 (2022).
- Hochheiser, I. V., Pils, M., Hagelueken, G., Moecking, J., Marleaux, M., Brinkschulte, R., Latz, E., Engel, C., & Geyer, M. Structure of the NLRP3 decamer bound to the cytokine release inhibitor CRID3. *Nature* **604**, 184-189 (2022).
- Hollingsworth, L. R., Sharif, H., Griswold, A. R., Fontana, P., Mintseris, J., Dagbay, K. B., Paulo, J. A., Gygi, S. P., Bachovchin, D. A., & Wu, H. DPP9 sequesters the C terminus of NLRP1 to repress inflammasome activation. *Nature* **592**, 778-783 (2021).
- Hopfner, K. P., & Hornung, V. Molecular mechanisms and cellular functions of cGAS-STING signalling. *Nat Rev Mol Cell Biol* **21**, 501-521 (2020).
- Hornef, M. W., Normark, B. H., Vandewalle, A., & Normark, S. Intracellular recognition of lipopolysaccharide by toll-like receptor 4 in intestinal epithelial cells. *J Exp Med* **198**, 1225-1235 (2003).
- Hornung, V., Ellegast, J., Kim, S., Brzózka, K., Jung, A., Kato, H., Poeck, H., Akira, S., Conzelmann, K.-K., Schlee, M., Endres, S., & Hartmann, G. 5'-Triphosphate RNA is the ligand for RIG-I. *Science (New York, N.Y.)* **314**, 994-997 (2006).
- Hoving, J. C., Wilson, G. J., & Brown, G. D. Signalling C-type lectin receptors, microbial recognition and immunity. *Cell Microbiol* **16**, 185-194 (2014).

- Howe, K. L., Achuthan, P., Allen, J., Allen, J., Alvarez-Jarreta, J., Amode, M. R., Armean, I. M., Azov, A. G., Bennett, R., Bhai, J., Billis, K., Boddu, S., Charkhchi, M., Cummins, C., Da Rin Fioretto, L., Davidson, C., Dodiya, K., El Houdaigui, B., Fatima, R., . . . Flicek, P. Ensembl 2021. *Nucleic Acids Res* **49**, D884-D891 (2021).
- Hu, Z., & Chai, J. Structural Mechanisms in NLR Inflammasome Assembly and Signaling. *Curr Top Microbiol Immunol* **397**, 23-42 (2016).
- Hu, Z., Yan, C., Liu, P., Huang, Z., Ma, R., Zhang, C., Wang, R., Zhang, Y., Martinon, F., Miao, D., Deng, H., Wang, J., Chang, J., & Chai, J. Crystal structure of NLRC4 reveals its autoinhibition mechanism. *Science* **341**, 172-175 (2013).
- Hu, Z., Zhou, Q., Zhang, C., Fan, S., Cheng, W., Zhao, Y., Shao, F., Wang, H. W., Sui, S. F., & Chai, J. Structural and biochemical basis for induced self-propagation of NLRC4. *Science* **350**, 399-404 (2015).
- Huang, M., Zhang, X., Toh, G. A., Gong, Q., Wang, J., Han, Z., Wu, B., Zhong, F., & Chai, J. Structural and biochemical mechanisms of NLRP1 inhibition by DPP9. *Nature* **592**, 773-777 (2021).
- Huang, W., Jiang, T., Choi, W., Qi, S., Pang, Y., Hu, Q., Xu, Y., Gong, X., Jeffrey, P. D., Wang, J., & Shi, Y. Mechanistic insights into CED-4-mediated activation of CED-3. *Genes Dev* **27**, 2039-2048 (2013).
- Huang, Y., Wang, H., Hao, Y., Lin, H., Dong, M., Ye, J., Song, L., Wang, Y., Li, Q., Shan, B., Jiang, Y., Li, H., Shao, Z., Kroemer, G., Zhang, H., Bai, L., Jin, T., Wang, C., Ma, Y., . . . Zhou, R. Myeloid PTEN promotes chemotherapy-induced NLRP3-inflammasome activation and antitumour immunity. *Nat Cell Biol* **22**, 716-727 (2020).
- Huang, Y. H., Lo, M. H., Cai, X. Y., & Kuo, H. C. Epigenetic hypomethylation and upregulation of NLRC4 and NLRP12 in Kawasaki disease. *Oncotarget* **9**, 18939-18948 (2018).
- Humphries, F., Bergin, R., Jackson, R., Delagic, N., Wang, B., Yang, S., Dubois, A. V., Ingram, R. J., & Moynagh, P. N. The E3 ubiquitin ligase Pellino2 mediates priming of the NLRP3 inflammasome. *Nat Commun* **9**, 1560 (2018).
- Indramohan, M., Stehlik, C., & Dorfleutner, A. COPs and POPs Patrol Inflammasome Activation. *J Mol Biol* **430**, 153-173 (2018).
- Inohara, N., & Nunez, G. The NOD: a signaling module that regulates apoptosis and host defense against pathogens. *Oncogene* **20**, 6473-6481 (2001).
- Ishikawa, H., & Barber, G. N. STING is an endoplasmic reticulum adaptor that facilitates innate immune signalling. *Nature* **455**, 674-678 (2008).
- Ismael, S., Nasoohi, S., & Ishrat, T. MCC950, the Selective Inhibitor of Nucleotide Oligomerization Domain-Like Receptor Protein-3 Inflammasome, Protects Mice against Traumatic Brain Injury. *J Neurotrauma* **35**, 1294-1303 (2018).
- Janeway, C. A., Jr., & Medzhitov, R. Innate immune recognition. *Annu Rev Immunol* **20**, 197-216 (2002).
- Jeru, I., Duquesnoy, P., Fernandes-Alnemri, T., Cochet, E., Yu, J. W., Lackmy-Port-Lis, M., Grimprel, E., Landman-Parker, J., Hentgen, V., Marlin, S., McElreavey, K., Sarkisian, T., Grateau, G., Alnemri, E. S., & Amselem, S. Mutations in NALP12 cause hereditary periodic fever syndromes. *Proc Natl Acad Sci U S A* **105**, 1614-1619 (2008).
- Jeru, I., Hentgen, V., Normand, S., Duquesnoy, P., Cochet, E., Delwail, A., Grateau, G., Marlin, S., Amselem, S., & Lecron, J. C. Role of interleukin-1beta in NLRP12-associated autoinflammatory disorders and resistance to anti-interleukin-1 therapy. *Arthritis Rheum* **63**, 2142-2148 (2011).

## References

---

- Jessop, M., Felix, J., & Gutsche, I. AAA+ ATPases: structural insertions under the magnifying glass. *Curr Opin Struct Biol* **66**, 119-128 (2021).
- Jiang, X., & Wang, X. Cytochrome c promotes caspase-9 activation by inducing nucleotide binding to Apaf-1. *J Biol Chem* **275**, 31199-31203 (2000).
- Jin, M. S., & Lee, J. O. Structures of the toll-like receptor family and its ligand complexes. *Immunity* **29**, 182-191 (2008).
- Jin, T., Chuenchor, W., Jiang, J., Cheng, J., Li, Y., Fang, K., Huang, M., Smith, P., & Xiao, T. S. Design of an expression system to enhance MBP-mediated crystallization. *Sci Rep* **7**, 40991 (2017).
- Jin, T., Huang, M., Jiang, J., Smith, P., & Xiao, T. S. Crystal structure of human NLRP12 PYD domain and implication in homotypic interaction. *PLoS One* **13**, e0190547 (2018).
- Jin, T., Perry, A., Jiang, J., Smith, P., Curry, J. A., Unterholzner, L., Jiang, Z., Horvath, G., Rathinam, V. A., Johnstone, R. W., Hornung, V., Latz, E., Bowie, A. G., Fitzgerald, K. A., & Xiao, T. S. Structures of the HIN domain:DNA complexes reveal ligand binding and activation mechanisms of the AIM2 inflammasome and IFI16 receptor. *Immunity* **36**, 561-571 (2012).
- Jin, Y., Wu, W., Zhang, W., Zhao, Y., Wu, Y., Ge, G., Ba, Y., Guo, Q., Gao, T., Chi, X., Hao, H., Wang, J., & Feng, F. Involvement of EGF receptor signaling and NLRP12 inflammasome in fine particulate matter-induced lung inflammation in mice. *Environ Toxicol* **32**, 1121-1134 (2017).
- Jorgensen, I., & Miao, E. A. Pyroptotic cell death defends against intracellular pathogens. *Immunol Rev* **265**, 130-142 (2015).
- Jumper, J., Evans, R., Pritzel, A., Green, T., Figurnov, M., Ronneberger, O., Tunyasuvunakool, K., Bates, R., Zidek, A., Potapenko, A., Bridgland, A., Meyer, C., Kohl, S. A. A., Ballard, A. J., Cowie, A., Romera-Paredes, B., Nikolov, S., Jain, R., Adler, J., . . . Hassabis, D. Highly accurate protein structure prediction with AlphaFold. *Nature* **596**, 583-589 (2021).
- Juruss, E., Engel, D., Star, K., Monson, K., Brandi, J., Felberg, L. E., Brookes, D. H., Wilson, L., Chen, J., Liles, K., Chun, M., Li, P., Gohara, D. W., Dolinsky, T., Konecny, R., Koes, D. R., Nielsen, J. E., Head-Gordon, T., Geng, W., . . . Baker, N. A. Improvements to the APBS biomolecular solvation software suite. *Protein Sci* **27**, 112-128 (2018).
- Kabsch, W. Automatic processing of rotation diffraction data from crystals of initially unknown symmetry and cell constants. *Journal of Applied Crystallography* **26**, 795-800 (1993).
- Kagan, J. C., Su, T., Horng, T., Chow, A., Akira, S., & Medzhitov, R. TRAM couples endocytosis of Toll-like receptor 4 to the induction of interferon-beta. *Nat Immunol* **9**, 361-368 (2008).
- Kamitsukasa, Y., Nakano, K., Murakami, K., Hirata, K., Yamamoto, M., Shimizu, T., & Ohto, U. The structure of NLRP9 reveals a unique C-terminal region with putative regulatory function. *FEBS Lett* (2022).
- Kang, K., Huang, L., Li, Q., Liao, X., Dang, Q., Yang, Y., Luo, J., Zeng, Y., Li, L., & Gou, D. An improved Tet-on system in microRNA overexpression and CRISPR/Cas9-mediated gene editing. *J Anim Sci Biotechnol* **10**, 43 (2019).
- Kankkunen, P., Teirila, L., Rintahaka, J., Alenius, H., Wolff, H., & Matikainen, S. (1,3)-beta-glucans activate both dectin-1 and NLRP3 inflammasome in human macrophages. *J Immunol* **184**, 6335-6342 (2010).
- Kanzaki, S., Tamura, S., Ito, T., Wakabayashi, M., Saito, K., Kato, S., Ohta, Y., Sekita, Y., & Kimura, T. Involvement of Nlrp9a/b/c in mouse preimplantation development. *Reproduction* **160**, 181-191 (2020).

- Karlsson, M., Zhang, C., Mear, L., Zhong, W., Digre, A., Katona, B., Sjostedt, E., Butler, L., Odeberg, J., Dusart, P., Edfors, F., Oksvold, P., von Feilitzen, K., Zwahlen, M., Arif, M., Altay, O., Li, X., Ozcan, M., Mardinoglu, A., . . . Lindskog, C. A single-cell type transcriptomics map of human tissues. *Sci Adv* **7** (2021).
- Kaur, H., Abreu, B., Akhmetzyanov, D., Lakatos-Karoly, A., Soares, C. M., Prisner, T., & Glaubitz, C. Unexplored Nucleotide Binding Modes for the ABC Exporter MsbA. *J Am Chem Soc* **140**, 14112-14125 (2018).
- Kaur, H., Lakatos-Karoly, A., Vogel, R., Noll, A., Tampe, R., & Glaubitz, C. Coupled ATPase-adenylate kinase activity in ABC transporters. *Nat Commun* **7**, 13864 (2016).
- Kawai, T., & Akira, S. The role of pattern-recognition receptors in innate immunity: update on Toll-like receptors. *Nat Immunol* **11**, 373-384 (2010).
- Kawasaki, T., & Kawai, T. Toll-like receptor signaling pathways. *Front Immunol* **5**, 461 (2014).
- Kawashima, A., Karasawa, T., Tago, K., Kimura, H., Kamata, R., Usui-Kawanishi, F., Watanabe, S., Ohta, S., Funakoshi-Tago, M., Yanagisawa, K., Kasahara, T., Suzuki, K., & Takahashi, M. ARIH2 Ubiquitinates NLRP3 and Negatively Regulates NLRP3 Inflammasome Activation in Macrophages. *J Immunol* **199**, 3614-3622 (2017).
- Kayagaki, N., Kornfeld, O. S., Lee, B. L., Stowe, I. B., O'Rourke, K., Li, Q., Sandoval, W., Yan, D., Kang, J., Xu, M., Zhang, J., Lee, W. P., McKenzie, B. S., Ulas, G., Payandeh, J., Roose-Girma, M., Modrusan, Z., Reja, R., Sagolla, M., . . . Dixit, V. M. NINJ1 mediates plasma membrane rupture during lytic cell death. *Nature* **591**, 131-136 (2021).
- Kayagaki, N., Stowe, I. B., Lee, B. L., O'Rourke, K., Anderson, K., Warming, S., Cuellar, T., Haley, B., Roose-Girma, M., Phung, Q. T., Liu, P. S., Lill, J. R., Li, H., Wu, J., Kummerfeld, S., Zhang, J., Lee, W. P., Snipas, S. J., Salvesen, G. S., . . . Dixit, V. M. Caspase-11 cleaves gasdermin D for non-canonical inflammasome signalling. *Nature* **526**, 666-671 (2015).
- Kelley, N., Jeltema, D., Duan, Y., & He, Y. The NLRP3 Inflammasome: An Overview of Mechanisms of Activation and Regulation. *Int J Mol Sci* **20** (2019).
- Kennedy, C. R., Goya Grocin, A., Kovacic, T., Singh, R., Ward, J. A., Shenoy, A. R., & Tate, E. W. A Probe for NLRP3 Inflammasome Inhibitor MCC950 Identifies Carbonic Anhydrase 2 as a Novel Target. *ACS Chem Biol* **16**, 982-990 (2021).
- Kersse, K., Verspurten, J., Vanden Berghe, T., & Vandenabeele, P. The death-fold superfamily of homotypic interaction motifs. *Trends Biochem Sci* **36**, 541-552 (2011).
- Keuler, T., Ferber, D., Marleaux, M., Geyer, M., & Gutschow, M. Structure-Stability Relationship of NLRP3 Inflammasome-Inhibiting Sulfonylureas. *ACS Omega* **7**, 8158-8162 (2022).
- Khan, S., & Zaki, H. Crosstalk between NLRP12 and JNK during Hepatocellular Carcinoma. *Int J Mol Sci* **21** (2020).
- Kim, H. E., Du, F., Fang, M., & Wang, X. Formation of apoptosome is initiated by cytochrome c-induced dATP hydrolysis and subsequent nucleotide exchange on Apaf-1. *Proc Natl Acad Sci U S A* **102**, 17545-17550 (2005).
- Kim, Y. K., Shin, J. S., & Nahm, M. H. NOD-Like Receptors in Infection, Immunity, and Diseases. *Yonsei Med J* **57**, 5-14 (2016).
- Kingeter, L. M., & Lin, X. C-type lectin receptor-induced NF-kappaB activation in innate immune and inflammatory responses. *Cell Mol Immunol* **9**, 105-112 (2012).
- Kortmann, J., Brubaker, S. W., & Monack, D. M. Cutting Edge: Inflammasome Activation in Primary Human Macrophages Is Dependent on Flagellin. *J Immunol* **195**, 815-819 (2015).

## References

---

- Krauss, J. L., Zeng, R., Hickman-Brecks, C. L., Wilson, J. E., Ting, J. P., & Novack, D. V. NLRP12 provides a critical checkpoint for osteoclast differentiation. *Proc Natl Acad Sci U S A* **112**, 10455-10460 (2015).
- Krissinel, E., & Henrick, K. Inference of macromolecular assemblies from crystalline state. *J Mol Biol* **372**, 774-797 (2007).
- Kuemmerle-Deschner, J. B., Wittkowski, H., Tyrrell, P. N., Koetter, I., Lohse, P., Ummenhofer, K., Reess, F., Hansmann, S., Koitschev, A., Deuter, C., Bialkowski, A., Foell, D., & Benseler, S. M. Treatment of Muckle-Wells syndrome: analysis of two IL-1-blocking regimens. *Arthritis Res Ther* **15**, R64 (2013).
- Kufer, T. A., & Sansonetti, P. J. NLR functions beyond pathogen recognition. *Nat Immunol* **12**, 121-128 (2011).
- Kumar, S., Ingle, H., Prasad, D. V., & Kumar, H. Recognition of bacterial infection by innate immune sensors. *Crit Rev Microbiol* **39**, 229-246 (2013).
- Labbe, K., McIntire, C. R., Doiron, K., Leblanc, P. M., & Saleh, M. Cellular inhibitors of apoptosis proteins cIAP1 and cIAP2 are required for efficient caspase-1 activation by the inflammasome. *Immunity* **35**, 897-907 (2011).
- Lacabanne, D., Wiegand, T., Wili, N., Kozlova, M. I., Cadalbert, R., Klose, D., Mulikdjanian, A. Y., Meier, B. H., & Bockmann, A. ATP Analogues for Structural Investigations: Case Studies of a DnaB Helicase and an ABC Transporter. *Molecules* **25** (2020).
- Lachmann, H. J., Kone-Paut, I., Kuemmerle-Deschner, J. B., Leslie, K. S., Hachulla, E., Quartier, P., Gitton, X., Widmer, A., Patel, N., & Hawkins, P. N. Use of Canakinumab in the Cryopyrin-Associated Periodic Syndrome. *New England Journal of Medicine* **360**, 2416-2425 (2009).
- Laliberte, R. E., Perregaux, D. G., Hoth, L. R., Rosner, P. J., Jordan, C. K., Peese, K. M., Egger, J. F., Dombroski, M. A., Geoghegan, K. F., & Gabel, C. A. Glutathione s-transferase omega 1-1 is a target of cytokine release inhibitory drugs and may be responsible for their effect on interleukin-1beta posttranslational processing. *J Biol Chem* **278**, 16567-16578 (2003).
- Lamkanfi, M., Mueller, J. L., Vitari, A. C., Misaghi, S., Fedorova, A., Deshayes, K., Lee, W. P., Hoffman, H. M., & Dixit, V. M. Glyburide inhibits the Cryopyrin/Nalp3 inflammasome. *J Cell Biol* **187**, 61-70 (2009).
- Larquet, E., Schreiber, V., Boisset, N., & Richet, E. Oligomeric assemblies of the Escherichia coli MalT transcriptional activator revealed by cryo-electron microscopy and image processing. *J Mol Biol* **343**, 1159-1169 (2004).
- Laskowski, R. A., & Swindells, M. B. LigPlot+: multiple ligand-protein interaction diagrams for drug discovery. *J Chem Inf Model* **51**, 2778-2786 (2011).
- Lassig, C., Matheisl, S., Sparrer, K. M., de Oliveira Mann, C. C., Moldt, M., Patel, J. R., Goldeck, M., Hartmann, G., Garcia-Sastre, A., Hornung, V., Conzelmann, K. K., Beckmann, R., & Hopfner, K. P. ATP hydrolysis by the viral RNA sensor RIG-I prevents unintentional recognition of self-RNA. *Elife* **4** (2015).
- Latz, E., Verma, A., Visintin, A., Gong, M., Sirois, C. M., Klein, D. C., Monks, B. G., McKnight, C. J., Lamphier, M. S., Duprex, W. P., Espevik, T., & Golenbock, D. T. Ligand-induced conformational changes allosterically activate Toll-like receptor 9. *Nat Immunol* **8**, 772-779 (2007).
- Latz, E., Xiao, T. S., & Stutz, A. Activation and regulation of the inflammasomes. *Nat Rev Immunol* **13**, 397-411 (2013).
- Lee, B. L., Moon, J. E., Shu, J. H., Yuan, L., Newman, Z. R., Schekman, R., & Barton, G. M. UNC93B1 mediates differential trafficking of endosomal TLRs. *Elife* **2**, e00291 (2013).

- Lee, B. L., Stowe, I. B., Gupta, A., Kornfeld, O. S., Roose-Girma, M., Anderson, K., Warming, S., Zhang, J., Lee, W. P., & Kayagaki, N. Caspase-11 auto-proteolysis is crucial for noncanonical inflammasome activation. *J Exp Med* **215**, 2279-2288 (2018).
- Lee, D. J., Du, F., Chen, S. W., Nakasaki, M., Rana, I., Shih, V. F. S., Hoffmann, A., & Jamora, C. Regulation and Function of the Caspase-1 in an Inflammatory Microenvironment. *J Invest Dermatol* **135**, 2012-2020 (2015).
- Lee, J. K., Kim, S. H., Lewis, E. C., Azam, T., Reznikov, L. L., & Dinarello, C. A. Differences in signaling pathways by IL-1beta and IL-18. *Proc Natl Acad Sci U S A* **101**, 8815-8820 (2004).
- Lee, J. Y., Seo, D., You, J., Chung, S., Park, J. S., Lee, J. H., Jung, S. M., Lee, Y. S., & Park, S. H. The deubiquitinating enzyme, ubiquitin-specific peptidase 50, regulates inflammasome activation by targeting the ASC adaptor protein. *FEBS Lett* **591**, 479-490 (2017).
- Lee, S. H., & Dominguez, R. Regulation of actin cytoskeleton dynamics in cells. *Mol Cells* **29**, 311-325 (2010).
- Lee, S. M., Yip, T. F., Yan, S., Jin, D. Y., Wei, H. L., Guo, R. T., & Peiris, J. S. M. Recognition of Double-Stranded RNA and Regulation of Interferon Pathway by Toll-Like Receptor 10. *Front Immunol* **9**, 516 (2018).
- Leipe, D. D., Koonin, E. V., & Aravind, L. STAND, a class of P-loop NTPases including animal and plant regulators of programmed cell death: multiple, complex domain architectures, unusual phyletic patterns, and evolution by horizontal gene transfer. *J Mol Biol* **343**, 1-28 (2004).
- Lemaitre, B., Nicolas, E., Michaut, L., Reichhart, J. M., & Hoffmann, J. A. The dorsoventral regulatory gene cassette spatzle/Toll/cactus controls the potent antifungal response in Drosophila adults. *Cell* **86**, 973-983 (1996).
- Leng, F., Yin, H., Qin, S., Zhang, K., Guan, Y., Fang, R., Wang, H., Li, G., Jiang, Z., Sun, F., Wang, D. C., & Xie, C. NLRP6 self-assembles into a linear molecular platform following LPS binding and ATP stimulation. *Sci Rep* **10**, 198 (2020).
- Levinsohn, J. L., Newman, Z. L., Hellmich, K. A., Fattah, R., Getz, M. A., Liu, S., Sastalla, I., Leppla, S. H., & Moayeri, M. Anthrax lethal factor cleavage of Nlrp1 is required for activation of the inflammasome. *PLoS Pathog* **8**, e1002638 (2012).
- Li, D., & Wu, M. Pattern recognition receptors in health and diseases. *Signal Transduct Target Ther* **6**, 291 (2021).
- Li, X., Dong, Z., Liu, Y., Song, W., Pu, J., Jiang, G., Wu, Y., Liu, L., & Huang, X. A Novel Role for the Regulatory Nod-Like Receptor NLRP12 in Anti-Dengue Virus Response. *Front Immunol* **12**, 744880 (2021).
- Li, X., Shu, C., Yi, G., Chaton, C. T., Shelton, C. L., Diao, J., Zuo, X., Kao, C. C., Herr, A. B., & Li, P. Cyclic GMP-AMP synthase is activated by double-stranded DNA-induced oligomerization. *Immunity* **39**, 1019-1031 (2013).
- Li, X., Thome, S., Ma, X., Amrute-Nayak, M., Finigan, A., Kitt, L., Masters, L., James, J. R., Shi, Y., Meng, G., & Mallat, Z. MARK4 regulates NLRP3 positioning and inflammasome activation through a microtubule-dependent mechanism. *Nat Commun* **8**, 15986 (2017).
- Li, Y., Fu, T. M., Lu, A., Witt, K., Ruan, J., Shen, C., & Wu, H. Cryo-EM structures of ASC and NLRC4 CARD filaments reveal a unified mechanism of nucleation and activation of caspase-1. *Proc Natl Acad Sci U S A* **115**, 10845-10852 (2018).
- Li, Y., Huang, H., Liu, B., Zhang, Y., Pan, X., Yu, X. Y., Shen, Z., & Song, Y. H. Inflammasomes as therapeutic targets in human diseases. *Signal Transduct Target Ther* **6**, 247 (2021).



## References

---

- Liao, K. C., & Mogridge, J. Activation of the Nlrp1b inflammasome by reduction of cytosolic ATP. *Infect Immun* **81**, 570-579 (2013).
- Lich, J. D., Williams, K. L., Moore, C. B., Arthur, J. C., Davis, B. K., Taxman, D. J., & Ting, J. P. Monarch-1 suppresses non-canonical NF-kappaB activation and p52-dependent chemokine expression in monocytes. *J Immunol* **178**, 1256-1260 (2007).
- Lin, K. M., Hu, W., Troutman, T. D., Jennings, M., Brewer, T., Li, X., Nanda, S., Cohen, P., Thomas, J. A., & Pasare, C. IRAK-1 bypasses priming and directly links TLRs to rapid NLRP3 inflammasome activation. *Proc Natl Acad Sci U S A* **111**, 775-780 (2014).
- Lisa, M. N., Cvirkaite-Krupovic, V., Richet, E., Andre-Leroux, G., Alzari, P. M., Haouz, A., & Danot, O. Double autoinhibition mechanism of signal transduction ATPases with numerous domains (STAND) with a tetratricopeptide repeat sensor. *Nucleic Acids Res* **47**, 3795-3810 (2019).
- Liu, F., Niu, Q., Fan, X., Liu, C., Zhang, J., Wei, Z., Hou, W., Kanneganti, T. D., Robb, M. L., Kim, J. H., Michael, N. L., Sun, J., Soong, L., & Hu, H. Priming and Activation of Inflammasome by Canarypox Virus Vector ALVAC via the cGAS/IFI16-STING-Type I IFN Pathway and AIM2 Sensor. *J Immunol* **199**, 3293-3305 (2017).
- Liu, H., & Naismith, J. H. An efficient one-step site-directed deletion, insertion, single and multiple-site plasmid mutagenesis protocol. *BMC Biotechnol* **8**, 91 (2008).
- Liu, J., Qian, C., & Cao, X. Post-Translational Modification Control of Innate Immunity. *Immunity* **45**, 15-30 (2016).
- Liu, X., Pichulik, T., Wolz, O. O., Dang, T. M., Stutz, A., Dillen, C., Delmiro Garcia, M., Kraus, H., Dickhofer, S., Daiber, E., Munzenmayer, L., Wahl, S., Rieber, N., Kummerle-Deschner, J., Yazdi, A., Franz-Wachtel, M., Macek, B., Radsak, M., Vogel, S., . . . Weber, A. N. R. Human NACHT, LRR, and PYD domain-containing protein 3 (NLRP3) inflammasome activity is regulated by and potentially targetable through Bruton tyrosine kinase. *J Allergy Clin Immunol* **140**, 1054-1067 e1010 (2017).
- Liu, X., Zhang, Z., Ruan, J., Pan, Y., Magupalli, V. G., Wu, H., & Lieberman, J. Inflammasome-activated gasdermin D causes pyroptosis by forming membrane pores. *Nature* **535**, 153-158 (2016).
- Liu, Y., Zhai, H., Alemayehu, H., Hopkins, L. J., Borgeaud, A. C., Heroven, C., Howe, J. D., Boulanger, J., Bryant, C. E., & Modis, Y. Cryo-electron tomography of ASC signalling sites in pyroptotic cells. *bioRxiv* (2021).
- Lord, C. A., Savitsky, D., Sitcheran, R., Calame, K., Wright, J. R., Ting, J. P., & Williams, K. L. Blimp-1/PRDM1 mediates transcriptional suppression of the NLR gene NLRP12/Monarch-1. *J Immunol* **182**, 2948-2958 (2009).
- Lu, A., Li, Y., Schmidt, F. I., Yin, Q., Chen, S., Fu, T. M., Tong, A. B., Ploegh, H. L., Mao, Y., & Wu, H. Molecular basis of caspase-1 polymerization and its inhibition by a new capping mechanism. *Nat Struct Mol Biol* **23**, 416-425 (2016).
- Lu, A., Li, Y., Yin, Q., Ruan, J., Yu, X., Egelman, E., & Wu, H. Plasticity in PYD assembly revealed by cryo-EM structure of the PYD filament of AIM2. *Cell Discov* **1** (2015).
- Lu, A., Magupalli, V. G., Ruan, J., Yin, Q., Atianand, M. K., Vos, M. R., Schroder, G. F., Fitzgerald, K. A., Wu, H., & Egelman, E. H. Unified polymerization mechanism for the assembly of ASC-dependent inflammasomes. *Cell* **156**, 1193-1206 (2014).
- Lu, A., & Wu, H. Structural mechanisms of inflammasome assembly. *FEBS J* **282**, 435-444 (2015).
- Lu, C., Wang, A., Wang, L., Dorsch, M., Ocain, T. D., & Xu, Y. Nucleotide binding to CARD12 and its role in CARD12-mediated caspase-1 activation. *Biochem Biophys Res Commun* **331**, 1114-1119 (2005).

- Lu, C., Xu, H., Ranjith-Kumar, C. T., Brooks, M. T., Hou, T. Y., Hu, F., Herr, A. B., Strong, R. K., Kao, C. C., & Li, P. The structural basis of 5' triphosphate double-stranded RNA recognition by RIG-I C-terminal domain. *Structure* **18**, 1032-1043 (2010).
- Lukasik, E., & Takken, F. L. STANDING strong, resistance proteins instigators of plant defence. *Curr Opin Plant Biol* **12**, 427-436 (2009).
- Lunemann, J. D., Malhotra, S., Shinohara, M. L., Montalban, X., & Comabella, M. Targeting Inflammasomes to Treat Neurological Diseases. *Ann Neurol* **90**, 177-188 (2021).
- MacDonald, J. A., Wijekoon, C. P., Liao, K. C., & Muruve, D. A. Biochemical and structural aspects of the ATP-binding domain in inflammasome-forming human NLRP proteins. *IUBMB Life* **65**, 851-862 (2013).
- Madeira, F., Park, Y. M., Lee, J., Buso, N., Gur, T., Madhusoodanan, N., Basutkar, P., Tivey, A. R. N., Potter, S. C., Finn, R. D., & Lopez, R. The EMBL-EBI search and sequence analysis tools APIs in 2019. *Nucleic Acids Res* **47**, W636-W641 (2019).
- Maekawa, S., Ohto, U., Shibata, T., Miyake, K., & Shimizu, T. Crystal structure of NOD2 and its implications in human disease. *Nat Commun* **7**, 11813 (2016).
- Magupalli, V. G., Negro, R., Tian, Y., Hauenstein, A. V., Di Caprio, G., Skillern, W., Deng, Q., Orning, P., Alam, H. B., Maliga, Z., Sharif, H., Hu, J. J., Evavold, C. L., Kagan, J. C., Schmidt, F. I., Fitzgerald, K. A., Kirchhausen, T., Li, Y., & Wu, H. HDAC6 mediates an aggresome-like mechanism for NLRP3 and pyrin inflammasome activation. *Science* **369** (2020).
- Malik, A., & Kanneganti, T. D. Inflammasome activation and assembly at a glance. *J Cell Sci* **130**, 3955-3963 (2017).
- Mambwe, B., Neo, K., Javanmard Khameneh, H., Leong, K. W. K., Colantuoni, M., Vacca, M., Muimo, R., & Mortellaro, A. Tyrosine Dephosphorylation of ASC Modulates the Activation of the NLRP3 and AIM2 Inflammasomes. *Front Immunol* **10**, 1556 (2019).
- Man, S. M., Hopkins, L. J., Nugent, E., Cox, S., Gluck, I. M., Turlomousis, P., Wright, J. A., Cicuta, P., Monie, T. P., & Bryant, C. E. Inflammasome activation causes dual recruitment of NLRC4 and NLRP3 to the same macromolecular complex. *Proc Natl Acad Sci U S A* **111**, 7403-7408 (2014).
- Man, S. M., & Kanneganti, T. D. Converging roles of caspases in inflammasome activation, cell death and innate immunity. *Nat Rev Immunol* **16**, 7-21 (2016).
- Mangan, M. S. J., Olhava, E. J., Roush, W. R., Seidel, H. M., Glick, G. D., & Latz, E. Targeting the NLRP3 inflammasome in inflammatory diseases. *Nat Rev Drug Discov* **17**, 588-606 (2018).
- Mantovani, A., Dinarello, C. A., Molgora, M., & Garlanda, C. Interleukin-1 and Related Cytokines in the Regulation of Inflammation and Immunity. *Immunity* **50**, 778-795 (2019).
- Mao, L., Kitani, A., Hiejima, E., Montgomery-Recht, K., Zhou, W., Fuss, I., Wiestner, A., & Strober, W. Bruton tyrosine kinase deficiency augments NLRP3 inflammasome activation and causes IL-1beta-mediated colitis. *J Clin Invest* **130**, 1793-1807 (2020).
- Mariathasan, S., Newton, K., Monack, D. M., Vucic, D., French, D. M., Lee, W. P., Roose-Girma, M., Erickson, S., & Dixit, V. M. Differential activation of the inflammasome by caspase-1 adaptors ASC and Ipaf. *Nature* **430**, 213-218 (2004).
- Marleaux, M., Anand, K., Latz, E., & Geyer, M. Crystal structure of the human NLRP9 pyrin domain suggests a distinct mode of inflammasome assembly. *FEBS Lett* **594**, 2383-2395 (2020).
- Marquetet, E., & Richet, E. How integration of positive and negative regulatory signals by a STAND signaling protein depends on ATP hydrolysis. *Mol Cell* **28**, 187-199 (2007).

## References

---

- Marshall, J. S., Warrington, R., Watson, W., & Kim, H. L. An introduction to immunology and immunopathology. *Allergy Asthma Clin Immunol* **14**, 49 (2018).
- Martin, B. N., Wang, C., Willette-Brown, J., Herjan, T., Gulen, M. F., Zhou, H., Bulek, K., Franchi, L., Sato, T., Alnemri, E. S., Narla, G., Zhong, X. P., Thomas, J., Klinman, D., Fitzgerald, K. A., Karin, M., Nunez, G., Dubyak, G., Hu, Y., & Li, X. IKKalpha negatively regulates ASC-dependent inflammasome activation. *Nat Commun* **5**, 4977 (2014).
- Martino, L., Holland, L., Christodoulou, E., Kunzelmann, S., Esposito, D., & Rittinger, K. The Biophysical Characterisation and SAXS Analysis of Human NLRP1 Uncover a New Level of Complexity of NLR Proteins. *PLoS One* **11**, e0164662 (2016).
- Martinon, F., Burns, K., & Tschopp, J. The inflammasome: a molecular platform triggering activation of inflammatory caspases and processing of proIL-beta. *Mol Cell* **10**, 417-426 (2002).
- Martinon, F., Mayor, A., & Tschopp, J. The inflammasomes: guardians of the body. *Annu Rev Immunol* **27**, 229-265 (2009).
- Maruta, N., Burdett, H., Lim, B. Y. J., Hu, X., Desa, S., Manik, M. K., & Kobe, B. Structural basis of NLR activation and innate immune signalling in plants. *Immunogenetics* **74**, 5-26 (2022).
- Mathern, D. R., & Heeger, P. S. Molecules Great and Small: The Complement System. *Clin J Am Soc Nephrol* **10**, 1636-1650 (2015).
- Matsushima, N., Tanaka, T., Enkhbayar, P., Mikami, T., Taga, M., Yamada, K., & Kuroki, Y. Comparative sequence analysis of leucine-rich repeats (LRRs) within vertebrate toll-like receptors. *BMC Genomics* **8**, 124 (2007).
- Matyszewski, M., Zheng, W., Lueck, J., Antiochos, B., Egelman, E. H., & Sohn, J. Cryo-EM structure of the NLRC4(CARD) filament provides insights into how symmetric and asymmetric supramolecular structures drive inflammasome assembly. *J Biol Chem* **293**, 20240-20248 (2018).
- Matyszewski, M., Zheng, W., Lueck, J., Mazanek, Z., Mohideen, N., Lau, A. Y., Egelman, E. H., & Sohn, J. Distinct axial and lateral interactions within homologous filaments dictate the signaling specificity and order of the AIM2-ASC inflammasome. *Nat Commun* **12**, 2735 (2021).
- Mayor, A., Martinon, F., De Smedt, T., Petrilli, V., & Tschopp, J. A crucial function of SGT1 and HSP90 in inflammasome activity links mammalian and plant innate immune responses. *Nat Immunol* **8**, 497-503 (2007).
- McAndrew, C. C., Napolitano, N. M., Vompe, A. D., Wewers, M. D., & Gavrillin, M. A. ASC phosphorylation at Y146 regulates inflammasome activation and pyroptosis. *The Journal of Immunology* **200**, 115.112-115.112 (2018).
- McKee, C. M., & Coll, R. C. NLRP3 inflammasome priming: A riddle wrapped in a mystery inside an enigma. *J Leukoc Biol* **108**, 937-952 (2020).
- McQuin, C., Goodman, A., Chernyshev, V., Kamensky, L., Cimini, B. A., Karhohs, K. W., Doan, M., Ding, L., Rafelski, S. M., Thirstrup, D., Wiegand, W., Singh, S., Becker, T., Caicedo, J. C., & Carpenter, A. E. CellProfiler 3.0: Next-generation image processing for biology. *PLoS Biol* **16**, e2005970 (2018).
- Medzhitov, R. Origin and physiological roles of inflammation. *Nature* **454**, 428-435 (2008).
- Medzhitov, R., Preston-Hurlburt, P., & Janeway, C. A., Jr. A human homologue of the Drosophila Toll protein signals activation of adaptive immunity. *Nature* **388**, 394-397 (1997).
- Menges, C. W., Altomare, D. A., & Testa, J. R. FAS-associated factor 1 (FAF1): diverse functions and implications for oncogenesis. *Cell Cycle* **8**, 2528-2534 (2009).

- Mertens, M., & Singh, J. A. Anakinra for rheumatoid arthritis: a systematic review. *J Rheumatol* **36**, 1118-1125 (2009).
- Meunier, E., & Broz, P. Evolutionary Convergence and Divergence in NLR Function and Structure. *Trends Immunol* **38**, 744-757 (2017).
- Miller, A. D. Essentials of chemical biology: structure and dynamics of biological macromolecules. *WILEY* (2008).
- Mitchell, P. S., Sandstrom, A., & Vance, R. E. The NLRP1 inflammasome: new mechanistic insights and unresolved mysteries. *Curr Opin Immunol* **60**, 37-45 (2019).
- Moghaddas, F., Zeng, P., Zhang, Y., Schutzle, H., Brenner, S., Hofmann, S. R., Berner, R., Zhao, Y., Lu, B., Chen, X., Zhang, L., Cheng, S., Winkler, S., Lehmborg, K., Canna, S. W., Czabotar, P. E., Wicks, I. P., De Nardo, D., Hedrich, C. M., . . . Masters, S. L. Autoinflammatory mutation in NLRC4 reveals a leucine-rich repeat (LRR)-LRR oligomerization interface. *J Allergy Clin Immunol* **142**, 1956-1967 e1956 (2018).
- Montalban, X., Arnold, D. L., Weber, M. S., Staikov, I., Piasecka-Stryczynska, K., Willmer, J., Martin, E. C., Dangond, F., Syed, S., Wolinsky, J. S., & Evobrutinib Phase 2 Study, G. Placebo-Controlled Trial of an Oral BTK Inhibitor in Multiple Sclerosis. *N Engl J Med* **380**, 2406-2417 (2019).
- Monteleone, M., Stanley, A. C., Chen, K. W., Brown, D. L., Bezbradica, J. S., von Pein, J. B., Holley, C. L., Boucher, D., Shakespear, M. R., Kapetanovic, R., Rolfes, V., Sweet, M. J., Stow, J. L., & Schroder, K. Interleukin-1beta Maturation Triggers Its Relocation to the Plasma Membrane for Gasdermin-D-Dependent and -Independent Secretion. *Cell Rep* **24**, 1425-1433 (2018).
- Monteleone, M., Stow, J. L., & Schroder, K. Mechanisms of unconventional secretion of IL-1 family cytokines. *Cytokine* **74**, 213-218 (2015).
- Moriarty, N. W., Grosse-Kunstleve, R. W., & Adams, P. D. electronic Ligand Builder and Optimization Workbench (eLBOW): a tool for ligand coordinate and restraint generation. *Acta Crystallogr D Biol Crystallogr* **65**, 1074-1080 (2009).
- Mortimer, L., Moreau, F., MacDonald, J. A., & Chadee, K. NLRP3 inflammasome inhibition is disrupted in a group of auto-inflammatory disease CAPS mutations. *Nat Immunol* **17**, 1176-1186 (2016).
- Motta, V., Soares, F., Sun, T., & Philpott, D. J. NOD-like receptors: versatile cytosolic sentinels. *Physiol Rev* **95**, 149-178 (2015).
- Moustaqil, M., Ollivier, E., Chiu, H. P., Van Tol, S., Rudolffi-Soto, P., Stevens, C., Bhumkar, A., Hunter, D. J. B., Freiberg, A. N., Jacques, D., Lee, B., Sierecki, E., & Gambin, Y. SARS-CoV-2 proteases PLpro and 3CLpro cleave IRF3 and critical modulators of inflammatory pathways (NLRP12 and TAB1): implications for disease presentation across species. *Emerg Microbes Infect* **10**, 178-195 (2021).
- Mullins, B., & Chen, J. NLRP9 in innate immunity and inflammation. *Immunology* **162**, 262-267 (2021).
- Munoz-Planillo, R., Kuffa, P., Martinez-Colon, G., Smith, B. L., Rajendiran, T. M., & Nunez, G. K(+) efflux is the common trigger of NLRP3 inflammasome activation by bacterial toxins and particulate matter. *Immunity* **38**, 1142-1153 (2013).
- Murphy, K. M. Janeway's immunobiology (9th edition ed.). *Garland Science* (2017).
- Nagyoszi, P., Nyul-Toth, A., Fazakas, C., Wilhelm, I., Kozma, M., Molnar, J., Hasko, J., & Krizbai, I. A. Regulation of NOD-like receptors and inflammasome activation in cerebral endothelial cells. *J Neurochem* **135**, 551-564 (2015).
- Nakanishi, K. Unique Action of Interleukin-18 on T Cells and Other Immune Cells. *Front Immunol* **9**, 763 (2018).

## References

---

- Negroni, A., Pierdomenico, M., Cucchiara, S., & Stronati, L. NOD2 and inflammation: current insights. *J Inflamm Res* **11**, 49-60 (2018).
- Newman, J., Egan, D., Walter, T. S., Meged, R., Berry, I., Ben Jelloul, M., Sussman, J. L., Stuart, D. I., & Perrakis, A. Towards rationalization of crystallization screening for small- to medium-sized academic laboratories: the PACT/JCSG+ strategy. *Acta Crystallogr D Biol Crystallogr* **61**, 1426-1431 (2005).
- Newstead, S., Ferrandon, S., & Iwata, S. Rationalizing alpha-helical membrane protein crystallization. *Protein Sci* **17**, 466-472 (2008).
- Ng, J. T., Dekker, C., Reardon, P., & von Delft, F. Lessons from ten years of crystallization experiments at the SGC. *Acta Crystallographica Section D* **72**, 224-235 (2016).
- Niu, T., De Rosny, C., Chautard, S., Rey, A., Patoli, D., Gros Lambert, M., Cosson, C., Lagrange, B., Zhang, Z., Visvikis, O., Hacot, S., Hologne, M., Walker, O., Wong, J., Wang, P., Ricci, R., Henry, T., Boyer, L., Petrilli, V., & Py, B. F. NLRP3 phosphorylation in its LRR domain critically regulates inflammasome assembly. *Nat Commun* **12**, 5862 (2021).
- Nold, M. F., Nold-Petry, C. A., Zepp, J. A., Palmer, B. E., Bufler, P., & Dinarello, C. A. IL-37 is a fundamental inhibitor of innate immunity. *Nat Immunol* **11**, 1014-1022 (2010).
- Normand, S., Waldschmitt, N., Neerinx, A., Martinez-Torres, R. J., Chauvin, C., Couturier-Maillard, A., Boulard, O., Cobret, L., Awad, F., Huot, L., Ribeiro-Ribeiro, A., Lautz, K., Ruez, R., Delacre, M., Bondu, C., Williams, M., Scott, C., Segal, A., Amselem, S., . . . Chamaillard, M. Proteasomal degradation of NOD2 by NLRP12 in monocytes promotes bacterial tolerance and colonization by enteropathogens. *Nat Commun* **9**, 5338 (2018).
- Novick, D., Kim, S., Kaplanski, G., & Dinarello, C. A. Interleukin-18, more than a Th1 cytokine. *Semin Immunol* **25**, 439-448 (2013).
- Nyul-Toth, A., Kozma, M., Nagyoszi, P., Nagy, K., Fazakas, C., Hasko, J., Molnar, K., Farkas, A. E., Vegh, A. G., Varo, G., Galajda, P., Wilhelm, I., & Krizbai, I. A. Expression of pattern recognition receptors and activation of the non-canonical inflammasome pathway in brain pericytes. *Brain Behav Immun* **64**, 220-231 (2017).
- Ogura, T., Whiteheart, S. W., & Wilkinson, A. J. Conserved arginine residues implicated in ATP hydrolysis, nucleotide-sensing, and inter-subunit interactions in AAA and AAA+ ATPases. *J Struct Biol* **146**, 106-112 (2004).
- Ohto, U., Kamitsukasa, Y., Ishida, H., Zhang, Z., Murakami, K., Hiramata, C., Maekawa, S., & Shimizu, T. Structural basis for the oligomerization-mediated regulation of NLRP3 inflammasome activation. *Proc Natl Acad Sci U S A* **119**, e2121353119 (2022).
- Page, R., Grzechnik, S. K., Canaves, J. M., Spraggon, G., Kreusch, A., Kuhn, P., Stevens, R. C., & Lesley, S. A. Shotgun crystallization strategy for structural genomics: an optimized two-tiered crystallization screen against the *Thermotoga maritima* proteome. *Acta Crystallogr D Biol Crystallogr* **59**, 1028-1037 (2003).
- Paik, S., Kim, J. K., Silwal, P., Sasakawa, C., & Jo, E. K. An update on the regulatory mechanisms of NLRP3 inflammasome activation. *Cell Mol Immunol* **18**, 1141-1160 (2021).
- Pajouhesh, H., & Lenz, G. R. Medicinal chemical properties of successful central nervous system drugs. *NeuroRx* **2**, 541-553 (2005).
- Palazon-Riquelme, P., Worboys, J. D., Green, J., Valera, A., Martin-Sanchez, F., Pellegrini, C., Brough, D., & Lopez-Castejon, G. USP7 and USP47 deubiquitinases regulate NLRP3 inflammasome activation. *EMBO Rep* **19** (2018).
- Paludan, S. R., Pradeu, T., Masters, S. L., & Mogensen, T. H. Constitutive immune mechanisms: mediators of host defence and immune regulation. *Nat Rev Immunol* **21**, 137-150 (2021).

- Papin, S., Duquesnoy, P., Cazeneuve, C., Pantel, J., Coppey-Moisan, M., Dargemont, C., & Amselem, S. Alternative splicing at the MEFV locus involved in familial Mediterranean fever regulates translocation of the marenostriin/pyrin protein to the nucleus. *Hum Mol Genet* **9**, 3001-3009 (2000).
- Park, B. S., Song, D. H., Kim, H. M., Choi, B. S., Lee, H., & Lee, J. O. The structural basis of lipopolysaccharide recognition by the TLR4-MD-2 complex. *Nature* **458**, 1191-1195 (2009).
- Park, H. H., Lo, Y. C., Lin, S. C., Wang, L., Yang, J. K., & Wu, H. The death domain superfamily in intracellular signaling of apoptosis and inflammation. *Annu Rev Immunol* **25**, 561-586 (2007).
- Park, K., Shen, B. W., Parmeggiani, F., Huang, P. S., Stoddard, B. L., & Baker, D. Control of repeat-protein curvature by computational protein design. *Nat Struct Mol Biol* **22**, 167-174 (2015).
- Park, Y. H., Wood, G., Kastner, D. L., & Chae, J. J. Pyrin inflammasome activation and RhoA signaling in the autoinflammatory diseases FMF and HIDS. *Nat Immunol* **17**, 914-921 (2016).
- Patel, J. R., Jain, A., Chou, Y. Y., Baum, A., Ha, T., & Garcia-Sastre, A. ATPase-driven oligomerization of RIG-I on RNA allows optimal activation of type-I interferon. *EMBO Rep* **14**, 780-787 (2013).
- Patente, T. A., Pinho, M. P., Oliveira, A. A., Evangelista, G. C. M., Bergami-Santos, P. C., & Barbuto, J. A. M. Human Dendritic Cells: Their Heterogeneity and Clinical Application Potential in Cancer Immunotherapy. *Front Immunol* **9**, 3176 (2018).
- Pathak, M., Vani, V., Sharma, S., & Seshagiri, P. B. Expression of IL-1beta and implantation serine proteases is required for mouse blastocyst hatching. *Reproduction* **161**, 123-133 (2021).
- Pelegrin, P., & Surprenant, A. Pannexin-1 mediates large pore formation and interleukin-1beta release by the ATP-gated P2X7 receptor. *EMBO J* **25**, 5071-5082 (2006).
- Perregaux, D. G., McNiff, P., Laliberte, R., Hawryluk, N., Peurano, H., Stam, E., Egger, J., Griffiths, R., Dombroski, M. A., & Gabel, C. A. Identification and characterization of a novel class of interleukin-1 post-translational processing inhibitors. *J Pharmacol Exp Ther* **299**, 187-197 (2001).
- Piippo, N., Korhonen, E., Hytti, M., Skottman, H., Kinnunen, K., Josifovska, N., Petrovski, G., Kaamiranta, K., & Kauppinen, A. Hsp90 inhibition as a means to inhibit activation of the NLRP3 inflammasome. *Sci Rep* **8**, 6720 (2018).
- Pinheiro, A. S., Eibl, C., Ekman-Vural, Z., Schwarzenbacher, R., & Peti, W. The NLRP12 pyrin domain: structure, dynamics, and functional insights. *J Mol Biol* **413**, 790-803 (2011).
- Pinheiro, A. S., Proell, M., Eibl, C., Page, R., Schwarzenbacher, R., & Peti, W. Three-dimensional structure of the NLRP7 pyrin domain: insight into pyrin-pyrin-mediated effector domain signaling in innate immunity. *J Biol Chem* **285**, 27402-27410 (2010).
- Platnich, J. M., & Muruve, D. A. NOD-like receptors and inflammasomes: A review of their canonical and non-canonical signaling pathways. *Arch Biochem Biophys* **670**, 4-14 (2019).
- Poli, G., Brancorsini, S., Cochetti, G., Barillaro, F., Egidi, M. G., & Mearini, E. Expression of inflammasome-related genes in bladder cancer and their association with cytokeratin 20 messenger RNA. *Urol Oncol* **33**, 505 e501-507 (2015).
- Proell, M., Riedl, S. J., Fritz, J. H., Rojas, A. M., & Schwarzenbacher, R. The Nod-like receptor (NLR) family: a tale of similarities and differences. *PLoS One* **3**, e2119 (2008).
- Py, B. F., Kim, M. S., Vakifahmetoglu-Norberg, H., & Yuan, J. Deubiquitination of NLRP3 by BRCC3 critically regulates inflammasome activity. *Mol Cell* **49**, 331-338 (2013).
- Radaev, S., Li, S., & Sun, P. D. A survey of protein-protein complex crystallizations. *Acta Crystallogr D Biol Crystallogr* **62**, 605-612 (2006).

## References

---

- Radian, A. D., Khare, S., Chu, L. H., Dorfleutner, A., & Stehlik, C. ATP binding by NLRP7 is required for inflammasome activation in response to bacterial lipopeptides. *Mol Immunol* **67**, 294-302 (2015).
- Ramachandran, G. N., Ramakrishnan, C., & Sasisekharan, V. Stereochemistry of polypeptide chain configurations. *J Mol Biol* **7**, 95-99 (1963).
- Ranjan, P., Singh, N., Kumar, A., Neerincx, A., Kremmer, E., Cao, W., Davis, W. G., Katz, J. M., Gangappa, S., Lin, R., Kufer, T. A., & Sambhara, S. NLRC5 interacts with RIG-I to induce a robust antiviral response against influenza virus infection. *Eur J Immunol* **45**, 758-772 (2015).
- Rao, Z., Chen, X., Wu, J., Xiao, M., Zhang, J., Wang, B., Fang, L., Zhang, H., Wang, X., Yang, S., & Chen, Y. Vitamin D Receptor Inhibits NLRP3 Activation by Impeding Its BRCC3-Mediated Deubiquitination. *Front Immunol* **10**, 2783 (2019).
- Read, R. J. Pushing the boundaries of molecular replacement with maximum likelihood. *Acta Crystallogr D Biol Crystallogr* **57**, 1373-1382 (2001).
- Rehwinkel, J., & Gack, M. U. RIG-I-like receptors: their regulation and roles in RNA sensing. *Nat Rev Immunol* **20**, 537-551 (2020).
- Ren, G., Zhang, X., Xiao, Y., Zhang, W., Wang, Y., Ma, W., Wang, X., Song, P., Lai, L., Chen, H., Zhan, Y., Zhang, J., Yu, M., Ge, C., Li, C., Yin, R., & Yang, X. ABRO1 promotes NLRP3 inflammasome activation through regulation of NLRP3 deubiquitination. *EMBO J* **38** (2019).
- Reubold, T. F., Hahne, G., Wohlgemuth, S., & Eschenburg, S. Crystal structure of the leucine-rich repeat domain of the NOD-like receptor NLRP1: implications for binding of muramyl dipeptide. *FEBS Lett* **588**, 3327-3332 (2014).
- Reubold, T. F., Wohlgemuth, S., & Eschenburg, S. Crystal structure of full-length Apaf-1: how the death signal is relayed in the mitochondrial pathway of apoptosis. *Structure* **19**, 1074-1083 (2011).
- Richards, N., Schaner, P., Diaz, A., Stuckey, J., Shelden, E., Wadhwa, A., & Gumucio, D. L. Interaction between pyrin and the apoptotic speck protein (ASC) modulates ASC-induced apoptosis. *J Biol Chem* **276**, 39320-39329 (2001).
- Rider, P., Carmi, Y., Guttman, O., Braiman, A., Cohen, I., Voronov, E., White, M. R., Dinarello, C. A., & Apte, R. N. IL-1alpha and IL-1beta recruit different myeloid cells and promote different stages of sterile inflammation. *J Immunol* **187**, 4835-4843 (2011).
- Ridker, P. M., Everett, B. M., Thuren, T., MacFadyen, J. G., Chang, W. H., Ballantyne, C., Fonseca, F., Nicolau, J., Koenig, W., Anker, S. D., Kastelein, J. J. P., Cornel, J. H., Pais, P., Pella, D., Genest, J., Cifkova, R., Lorenzatti, A., Forster, T., Kobalava, Z., . . . Group, C. T. Antiinflammatory Therapy with Canakinumab for Atherosclerotic Disease. *N Engl J Med* **377**, 1119-1131 (2017).
- Riedl, S. J., Li, W., Chao, Y., Schwarzenbacher, R., & Shi, Y. Structure of the apoptotic protease-activating factor 1 bound to ADP. *Nature* **434**, 926-933 (2005).
- Robert, X., & Gouet, P. Deciphering key features in protein structures with the new ENDscript server. *Nucleic Acids Res* **42**, W320-324 (2014).
- Robinson, K. S., Teo, D. E. T., Tan, K. S., Toh, G. A., Ong, H. H., Lim, C. K., Lay, K., Au, B. V., Lew, T. S., Chu, J. J. H., Chow, V. T. K., Wang, Y., Zhong, F. L., & Reversade, B. Enteroviral 3C protease activates the human NLRP1 inflammasome in airway epithelia. *Science* **370** (2020).
- Robinson, K. S., Toh, G. A., Rozario, P., Bayat, S., Sun, Z., Bauernfried, S., Nadkarni, R., Harapas, C. R., Lim, C. K., Chu, W., Tan, K. Y., Bonnard, C., Sobota, R., Connolly, J. E., Masters, S. L., Chen, K. W., Ho, L., Hornung, V., & Zhong, F. L. Human NLRP1 is activated by ZAKα-driven ribotoxic stress response. *bioRxiv* (2022).

- Rodgers, M. A., Bowman, J. W., Fujita, H., Orazio, N., Shi, M., Liang, Q., Amatya, R., Kelly, T. J., Iwai, K., Ting, J., & Jung, J. U. The linear ubiquitin assembly complex (LUBAC) is essential for NLRP3 inflammasome activation. *J Exp Med* **211**, 1333-1347 (2014).
- Rossmann, M. G. The molecular replacement method. *Acta Crystallogr A* **46 ( Pt 2)**, 73-82 (1990).
- Rost, B. Twilight zone of protein sequence alignments. *Protein Eng* **12**, 85-94 (1999).
- Ruhl, S., Shkarina, K., Demarco, B., Heilig, R., Santos, J. C., & Broz, P. ESCRT-dependent membrane repair negatively regulates pyroptosis downstream of GSDMD activation. *Science* **362**, 956-960 (2018).
- Rupp, B. Biomolecular Crystallography: Principles, Practice, and Application to Structural Biology. *CRC Press LLC* (2009).
- Saito, T., Hirai, R., Loo, Y. M., Owen, D., Johnson, C. L., Sinha, S. C., Akira, S., Fujita, T., & Gale, M., Jr. Regulation of innate antiviral defenses through a shared repressor domain in RIG-I and LGP2. *Proc Natl Acad Sci U S A* **104**, 582-587 (2007).
- Sancho, D., & Reis e Sousa, C. Signaling by myeloid C-type lectin receptors in immunity and homeostasis. *Annu Rev Immunol* **30**, 491-529 (2012).
- Sandall, C. F., Ziehr, B. K., & MacDonald, J. A. ATP-Binding and Hydrolysis in Inflammasome Activation. *Molecules* **25** (2020).
- Sandstrom, A., Mitchell, P. S., Goers, L., Mu, E. W., Lesser, C. F., & Vance, R. E. Functional degradation: A mechanism of NLRP1 inflammasome activation by diverse pathogen enzymes. *Science* **364** (2019).
- Scheffzek, K., Ahmadian, M. R., Kabsch, W., Wiesmuller, L., Lautwein, A., Schmitz, F., & Wittinghofer, A. The Ras-RasGAP complex: structural basis for GTPase activation and its loss in oncogenic Ras mutants. *Science* **277**, 333-338 (1997).
- Schmid-Burgk, J. L., Chauhan, D., Schmidt, T., Ebert, T. S., Reinhardt, J., Endl, E., & Hornung, V. A Genome-wide CRISPR (Clustered Regularly Interspaced Short Palindromic Repeats) Screen Identifies NEK7 as an Essential Component of NLRP3 Inflammasome Activation. *J Biol Chem* **291**, 103-109 (2016).
- Schmidt, A., Schwerd, T., Hamm, W., Hellmuth, J. C., Cui, S., Wenzel, M., Hoffmann, F. S., Michallet, M. C., Besch, R., Hopfner, K. P., Endres, S., & Rothenfusser, S. 5'-triphosphate RNA requires base-paired structures to activate antiviral signaling via RIG-I. *Proc Natl Acad Sci U S A* **106**, 12067-12072 (2009).
- Schnappauf, O., Chae, J. J., Kastner, D. L., & Aksentijevich, I. The Pyrin Inflammasome in Health and Disease. *Front Immunol* **10**, 1745 (2019).
- Schroder, K., & Tschopp, J. The inflammasomes. *Cell* **140**, 821-832 (2010).
- Schuberth-Wagner, C., Ludwig, J., Bruder, A. K., Herzner, A. M., Zillinger, T., Goldeck, M., Schmidt, T., Schmid-Burgk, J. L., Kerber, R., Wolter, S., Stumpel, J. P., Roth, A., Bartok, E., Drosten, C., Coch, C., Hornung, V., Barchet, W., Kummerer, B. M., Hartmann, G., & Schlee, M. A Conserved Histidine in the RNA Sensor RIG-I Controls Immune Tolerance to N1-2'O-Methylated Self RNA. *Immunity* **43**, 41-51 (2015).
- Schwaid, A. G., & Spencer, K. B. Strategies for Targeting the NLRP3 Inflammasome in the Clinical and Preclinical Space. *J Med Chem* **64**, 101-122 (2021).
- Semino, C., Carta, S., Gattorno, M., Sitia, R., & Rubartelli, A. Progressive waves of IL-1beta release by primary human monocytes via sequential activation of vesicular and gasdermin D-mediated secretory pathways. *Cell Death Dis* **9**, 1088 (2018).



## References

---

- Sester, D. P., Thygesen, S. J., Sagulenko, V., Vajjhala, P. R., Cridland, J. A., Vitak, N., Chen, K. W., Osborne, G. W., Schroder, K., & Stacey, K. J. A novel flow cytometric method to assess inflammasome formation. *J Immunol* **194**, 455-462 (2015).
- Shao, L., Liu, Y., Wang, W., Li, A., Wan, P., Liu, W., Shereen, M. A., Liu, F., Zhang, W., Tan, Q., Wu, K., Liu, Y., & Wu, J. SUMO1 SUMOylates and SENP3 deSUMOylates NLRP3 to orchestrate the inflammasome activation. *FASEB J* **34**, 1497-1515 (2020).
- Sharif, H., Wang, L., Wang, W. L., Magupalli, V. G., Andreeva, L., Qiao, Q., Hauenstein, A. V., Wu, Z., Nunez, G., Mao, Y., & Wu, H. Structural mechanism for NEK7-licensed activation of NLRP3 inflammasome. *Nature* **570**, 338-343 (2019).
- Sharma, N., Saxena, S., Agrawal, I., Singh, S., Srinivasan, V., Arvind, S., Epari, S., Paul, S., & Jha, S. Differential Expression Profile of NLRs and AIM2 in Glioma and Implications for NLRP12 in Glioblastoma. *Sci Rep* **9**, 8480 (2019).
- Shaw, M. H., Reimer, T., Kim, Y. G., & Nunez, G. NOD-like receptors (NLRs): bona fide intracellular microbial sensors. *Curr Opin Immunol* **20**, 377-382 (2008).
- Shaw, P. J., Lamkanfi, M., & Kanneganti, T. D. NOD-like receptor (NLR) signaling beyond the inflammasome. *Eur J Immunol* **40**, 624-627 (2010).
- Shen, C., Li, R., Negro, R., Cheng, J., Vora, S. M., Fu, T. M., Wang, A., He, K., Andreeva, L., Gao, P., Tian, Z., Flavell, R. A., Zhu, S., & Wu, H. Phase separation drives RNA virus-induced activation of the NLRP6 inflammasome. *Cell* **184**, 5759-5774 e5720 (2021).
- Shen, C., Lu, A., Xie, W. J., Ruan, J., Negro, R., Egelman, E. H., Fu, T. M., & Wu, H. Molecular mechanism for NLRP6 inflammasome assembly and activation. *Proc Natl Acad Sci U S A* **116**, 2052-2057 (2019).
- Shi, F., Yang, Y., Kouadir, M., Xu, W., Hu, S., & Wang, T. Inflammasome-independent role of NLRP12 in suppressing colonic inflammation regulated by Blimp-1. *Oncotarget* **7**, 30575-30584 (2016).
- Shi, H., Wang, Y., Li, X., Zhan, X., Tang, M., Fina, M., Su, L., Pratt, D., Bu, C. H., Hildebrand, S., Lyon, S., Scott, L., Quan, J., Sun, Q., Russell, J., Arnett, S., Jurek, P., Chen, D., Kravchenko, V. V., . . . Beutler, B. NLRP3 activation and mitosis are mutually exclusive events coordinated by NEK7, a new inflammasome component. *Nat Immunol* **17**, 250-258 (2016).
- Shi, J., Zhao, Y., Wang, K., Shi, X., Wang, Y., Huang, H., Zhuang, Y., Cai, T., Wang, F., & Shao, F. Cleavage of GSDMD by inflammatory caspases determines pyroptotic cell death. *Nature* **526**, 660-665 (2015).
- Shi, J., Zhao, Y., Wang, Y., Gao, W., Ding, J., Li, P., Hu, L., & Shao, F. Inflammatory caspases are innate immune receptors for intracellular LPS. *Nature* **514**, 187-192 (2014).
- Singh, D. P., Kaur, G., Bagam, P., Pinkston, R., & Batra, S. Membrane microdomains regulate NLRP10- and NLRP12-dependent signalling in A549 cells challenged with cigarette smoke extract. *Arch Toxicol* **92**, 1767-1783 (2018).
- Song, H., Liu, B., Huai, W., Yu, Z., Wang, W., Zhao, J., Han, L., Jiang, G., Zhang, L., Gao, C., & Zhao, W. The E3 ubiquitin ligase TRIM31 attenuates NLRP3 inflammasome activation by promoting proteasomal degradation of NLRP3. *Nat Commun* **7**, 13727 (2016).
- Song, N., Liu, Z. S., Xue, W., Bai, Z. F., Wang, Q. Y., Dai, J., Liu, X., Huang, Y. J., Cai, H., Zhan, X. Y., Han, Q. Y., Wang, H., Chen, Y., Li, H. Y., Li, A. L., Zhang, X. M., Zhou, T., & Li, T. NLRP3 Phosphorylation Is an Essential Priming Event for Inflammasome Activation. *Mol Cell* **68**, 185-197 e186 (2017).
- Spalinger, M. R., Kasper, S., Gottier, C., Lang, S., Atrott, K., Vavricka, S. R., Scharl, S., Raselli, T., Frey-Wagner, I., Gutte, P. M., Grutter, M. G., Beer, H. D., Contassot, E., Chan, A. C., Dai, X.,

- Rawlings, D. J., Mair, F., Becher, B., Falk, W., . . . Scharl, M. NLRP3 tyrosine phosphorylation is controlled by protein tyrosine phosphatase PTPN22. *J Clin Invest* **126**, 1783-1800 (2016).
- Spalinger, M. R., Lang, S., Gottier, C., Dai, X., Rawlings, D. J., Chan, A. C., Rogler, G., & Scharl, M. PTPN22 regulates NLRP3-mediated IL1B secretion in an autophagy-dependent manner. *Autophagy* **13**, 1590-1601 (2017).
- Stein, C., Caccamo, M., Laird, G., & Leptin, M. Conservation and divergence of gene families encoding components of innate immune response systems in zebrafish. *Genome Biol* **8**, R251 (2007).
- Strowig, T., Henao-Mejia, J., Elinav, E., & Flavell, R. Inflammasomes in health and disease. *Nature* **481**, 278-286 (2012).
- Stutz, A., Horvath, G. L., Monks, B. G., & Latz, E. ASC speck formation as a readout for inflammasome activation. *Methods Mol Biol* **1040**, 91-101 (2013).
- Stutz, A., Kolbe, C. C., Stahl, R., Horvath, G. L., Franklin, B. S., van Ray, O., Brinkschulte, R., Geyer, M., Meissner, F., & Latz, E. NLRP3 inflammasome assembly is regulated by phosphorylation of the pyrin domain. *J Exp Med* **214**, 1725-1736 (2017).
- Sun, Z., Liu, Q., Qu, G., Feng, Y., & Reetz, M. T. Utility of B-Factors in Protein Science: Interpreting Rigidity, Flexibility, and Internal Motion and Engineering Thermostability. *Chem Rev* **119**, 1626-1665 (2019).
- Swanson, K. V., Deng, M., & Ting, J. P. The NLRP3 inflammasome: molecular activation and regulation to therapeutics. *Nat Rev Immunol* **19**, 477-489 (2019).
- Swatek, K. N., & Komander, D. Ubiquitin modifications. *Cell Res* **26**, 399-422 (2016).
- Tadaki, H., Saito, H., Nishimura-Tadaki, A., Imagawa, T., Kikuchi, M., Hara, R., Kaneko, U., Kishi, T., Miyamae, T., Miyake, N., Doi, H., Tsurusaki, Y., Sakai, H., Yokota, S., & Matsumoto, N. De novo 19q13.42 duplications involving NLRP gene cluster in a patient with systemic-onset juvenile idiopathic arthritis. *J Hum Genet* **56**, 343-347 (2011).
- Tafoya, S., & Bustamante, C. Molecular switch-like regulation in motor proteins. *Philos Trans R Soc Lond B Biol Sci* **373** (2018).
- Takeuchi, O., & Akira, S. Pattern recognition receptors and inflammation. *Cell* **140**, 805-820 (2010).
- Tameling, W. I., Vossen, J. H., Albrecht, M., Lengauer, T., Berden, J. A., Haring, M. A., Cornelissen, B. J., & Takken, F. L. Mutations in the NB-ARC domain of I-2 that impair ATP hydrolysis cause autoactivation. *Plant Physiol* **140**, 1233-1245 (2006).
- Tang, J., Tu, S., Lin, G., Guo, H., Yan, C., Liu, Q., Huang, L., Tang, N., Xiao, Y., Pope, R. M., Rajaram, M. V. S., Amer, A. O., Ahmer, B. M., Gunn, J. S., Wozniak, D. J., Tao, L., Coppola, V., Zhang, L., Langdon, W. Y., . . . Zhang, J. Sequential ubiquitination of NLRP3 by RNF125 and Cbl-b limits inflammasome activation and endotoxemia. *J Exp Med* **217** (2020).
- Tapia-Abellan, A., Angosto-Bazarra, D., Alarcon-Vila, C., Banos, M. C., Hafner-Bratkovic, I., Oliva, B., & Pelegrin, P. Sensing low intracellular potassium by NLRP3 results in a stable open structure that promotes inflammasome activation. *Sci Adv* **7**, eabf4468 (2021).
- Tapia-Abellan, A., Angosto-Bazarra, D., Martinez-Banaclocha, H., de Torre-Minguela, C., Ceron-Carrasco, J. P., Perez-Sanchez, H., Arostegui, J. I., & Pelegrin, P. MCC950 closes the active conformation of NLRP3 to an inactive state. *Nat Chem Biol* **15**, 560-564 (2019).
- Tenthorey, J. L., Haloupek, N., Lopez-Blanco, J. R., Grob, P., Adamson, E., Hartenian, E., Lind, N. A., Bourgeois, N. M., Chacon, P., Nogales, E., & Vance, R. E. The structural basis of flagellin detection by NAIP5: A strategy to limit pathogen immune evasion. *Science* **358**, 888-893 (2017).

- Tian, M., Peng, Y., & Zheng, J. Metabolic Activation and Hepatotoxicity of Furan-Containing Compounds. *Drug Metab Dispos* **50**, 655-670 (2022).
- Tian, X., Pascal, G., & Monget, P. Evolution and functional divergence of NLRP genes in mammalian reproductive systems. *BMC Evol Biol* **9**, 202 (2009).
- Travassos, L. H., Carneiro, L. A., Ramjeet, M., Hussey, S., Kim, Y. G., Magalhaes, J. G., Yuan, L., Soares, F., Chea, E., Le Bourhis, L., Boneca, I. G., Allaoui, A., Jones, N. L., Nunez, G., Girardin, S. E., & Philpott, D. J. Nod1 and Nod2 direct autophagy by recruiting ATG16L1 to the plasma membrane at the site of bacterial entry. *Nat Immunol* **11**, 55-62 (2010).
- Truax, A. D., Chen, L., Tam, J. W., Cheng, N., Guo, H., Koblansky, A. A., Chou, W. C., Wilson, J. E., Brickey, W. J., Petrucelli, A., Liu, R., Cooper, D. E., Koenigsnecht, M. J., Young, V. B., Netea, M. G., Stienstra, R., Sartor, R. B., Montgomery, S. A., Coleman, R. A., & Ting, J. P. The Inhibitory Innate Immune Sensor NLRP12 Maintains a Threshold against Obesity by Regulating Gut Microbiota Homeostasis. *Cell Host Microbe* **24**, 364-378 e366 (2018).
- Tsu, B. V., Beierschmitt, C., Ryan, A. P., Agarwal, R., Mitchell, P. S., & Daugherty, M. D. Diverse viral proteases activate the NLRP1 inflammasome. *Elife* **10** (2021).
- Tuladhar, S., & Kanneganti, T. D. NLRP12 in innate immunity and inflammation. *Mol Aspects Med* **76**, 100887 (2020).
- Turvey, S. E., & Broide, D. H. Innate immunity. *J Allergy Clin Immunol* **125**, S24-32 (2010).
- Ulland, T. K., Jain, N., Hornick, E. E., Elliott, E. I., Clay, G. M., Sadler, J. J., Mills, K. A., Janowski, A. M., Volk, A. P., Wang, K., Legge, K. L., Gakhar, L., Bourdi, M., Ferguson, P. J., Wilson, M. E., Cassel, S. L., & Sutterwala, F. S. Nlrp12 mutation causes C57BL/6J strain-specific defect in neutrophil recruitment. *Nat Commun* **7**, 13180 (2016).
- UniProt, C. UniProt: the universal protein knowledgebase in 2021. *Nucleic Acids Res* **49**, D480-D489 (2021).
- Valverde, P., Martinez, J. D., Canada, F. J., Arda, A., & Jimenez-Barbero, J. Molecular Recognition in C-Type Lectins: The Cases of DC-SIGN, Langerin, MGL, and L-Sectin. *Chembiochem* **21**, 2999-3025 (2020).
- Van Gijn, M. E., Ceccherini, I., Shinar, Y., Carbo, E. C., Slofstra, M., Arostegui, J. I., Sarrabay, G., Rowczenio, D., Omoyimni, E., Balci-Peynircioglu, B., Hoffman, H. M., Milhavet, F., Swertz, M. A., & Touitou, I. New workflow for classification of genetic variants' pathogenicity applied to hereditary recurrent fevers by the International Study Group for Systemic Autoinflammatory Diseases (INSAID). *J Med Genet* **55**, 530-537 (2018).
- Vande Walle, L., Stowe, I. B., Sacha, P., Lee, B. L., Demon, D., Fossoul, A., Van Hauwermeiren, F., Saavedra, P. H. V., Simon, P., Subrt, V., Kostka, L., Stivala, C. E., Pham, V. C., Staben, S. T., Yamazoe, S., Konvalinka, J., Kayagaki, N., & Lamkanfi, M. MCC950/CRID3 potentially targets the NACHT domain of wild-type NLRP3 but not disease-associated mutants for inflammasome inhibition. *PLoS Biol* **17**, e3000354 (2019).
- Vijay, K. Toll-like receptors in immunity and inflammatory diseases: Past, present, and future. *Int Immunopharmacol* **59**, 391-412 (2018).
- Vladimer, G. I., Weng, D., Paquette, S. W., Vanaja, S. K., Rathinam, V. A., Aune, M. H., Conlon, J. E., Burbage, J. J., Proulx, M. K., Liu, Q., Reed, G., Meccas, J. C., Iwakura, Y., Bertin, J., Goguen, J. D., Fitzgerald, K. A., & Lien, E. The NLRP12 inflammasome recognizes *Yersinia pestis*. *Immunity* **37**, 96-107 (2012).
- Volkman, H. E., Cambier, S., Gray, E. E., & Stetson, D. B. Tight nuclear tethering of cGAS is essential for preventing autoreactivity. *Elife* **8** (2019).

- Walter, T. S., Meier, C., Assenberg, R., Au, K. F., Ren, J., Verma, A., Nettleship, J. E., Owens, R. J., Stuart, D. I., & Grimes, J. M. Lysine methylation as a routine rescue strategy for protein crystallization. *Structure* **14**, 1617-1622 (2006).
- Wan, P., Zhang, Q., Liu, W., Jia, Y., Ai, S., Wang, T., Wang, W., Pan, P., Yang, G., Xiang, Q., Huang, S., Yang, Q., Zhang, W., Liu, F., Tan, Q., Zhang, W., Wu, K., Liu, Y., & Wu, J. Cullin1 binds and promotes NLRP3 ubiquitination to repress systematic inflammasome activation. *FASEB J* **33**, 5793-5807 (2019).
- Wang, H. F. NLRP12-associated systemic autoinflammatory diseases in children. *Pediatr Rheumatol Online J* **20**, 9 (2022).
- Wang, J., Zhang, Q., Xu, L., Lv, C., Liu, R., Zhang, M., & Tan, W. A case of episodic and refractory arthritis due to a novel variant of NLRP12. *Ann Rheum Dis* **81**, e33 (2022).
- Wang, L., Manji, G. A., Grenier, J. M., Al-Garawi, A., Merriam, S., Lora, J. M., Geddes, B. J., Briskin, M., DiStefano, P. S., & Bertin, J. PYPAF7, a novel PYRIN-containing Apaf1-like protein that regulates activation of NF-kappa B and caspase-1-dependent cytokine processing. *J Biol Chem* **277**, 29874-29880 (2002).
- Wang, Q., Gao, H., Clark, K. M., Mugisha, C. S., Davis, K., Tang, J. P., Harlan, G. H., DeSelm, C. J., Presti, R. M., Kutluay, S. B., & Shan, L. CARD8 is an inflammasome sensor for HIV-1 protease activity. *Science* **371** (2021).
- Wang, Q., Liu, F., Zhang, M., Zhou, P., Xu, C., Li, Y., Bian, L., Liu, Y., Yao, Y., Wang, F., Fang, Y., & Li, D. NLRP12 Promotes Mouse Neutrophil Differentiation through Regulation of Non-canonical NF-kappaB and MAPK(ERK1/2) Signaling. *Int J Biol Sci* **14**, 147-155 (2018).
- Wang, W., Hu, D., Feng, Y., Wu, C., Song, Y., Liu, W., Li, A., Wang, Y., Chen, K., Tian, M., Xiao, F., Zhang, Q., Chen, W., Pan, P., Wan, P., Liu, Y., Lan, H., Wu, K., & Wu, J. Paxillin mediates ATP-induced activation of P2X7 receptor and NLRP3 inflammasome. *BMC Biol* **18**, 182 (2020).
- Wang, W., Hu, D., Wu, C., Feng, Y., Li, A., Liu, W., Wang, Y., Chen, K., Tian, M., Xiao, F., Zhang, Q., Shereen, M. A., Chen, W., Pan, P., Wan, P., Wu, K., & Wu, J. STING promotes NLRP3 localization in ER and facilitates NLRP3 deubiquitination to activate the inflammasome upon HSV-1 infection. *PLoS Pathog* **16**, e1008335 (2020).
- Wegele, H., Muller, L., & Buchner, J. Hsp70 and Hsp90--a relay team for protein folding. *Rev Physiol Biochem Pharmacol* **151**, 1-44 (2004).
- Wendler, P., Ciniawsky, S., Kock, M., & Kube, S. Structure and function of the AAA+ nucleotide binding pocket. *Biochim Biophys Acta* **1823**, 2-14 (2012).
- Williams, C. J., Headd, J. J., Moriarty, N. W., Prisant, M. G., Videau, L. L., Deis, L. N., Verma, V., Keedy, D. A., Hintze, B. J., Chen, V. B., Jain, S., Lewis, S. M., Arendall, W. B., 3rd, Snoeyink, J., Adams, P. D., Lovell, S. C., Richardson, J. S., & Richardson, D. C. MolProbity: More and better reference data for improved all-atom structure validation. *Protein Sci* **27**, 293-315 (2018).
- Williams, K. L., Lich, J. D., Duncan, J. A., Reed, W., Rallabhandi, P., Moore, C., Kurtz, S., Coffield, V. M., Accavitti-Loper, M. A., Su, L., Vogel, S. N., Braunstein, M., & Ting, J. P. The CATERPILLER protein monarch-1 is an antagonist of toll-like receptor-, tumor necrosis factor alpha-, and Mycobacterium tuberculosis-induced pro-inflammatory signals. *J Biol Chem* **280**, 39914-39924 (2005).
- Wu, C., Su, Z., Lin, M., Ou, J., Zhao, W., Cui, J., & Wang, R. F. NLRP11 attenuates Toll-like receptor signalling by targeting TRAF6 for degradation via the ubiquitin ligase RNF19A. *Nat Commun* **8**, 1977 (2017).

## References

---

- Wu, X., Wu, F. H., Wang, X., Wang, L., Siedow, J. N., Zhang, W., & Pei, Z. M. Molecular evolutionary and structural analysis of the cytosolic DNA sensor cGAS and STING. *Nucleic Acids Res* **42**, 8243-8257 (2014).
- Xia, S., Zhang, Z., Magupalli, V. G., Pablo, J. L., Dong, Y., Vora, S. M., Wang, L., Fu, T. M., Jacobson, M. P., Greka, A., Lieberman, J., Ruan, J., & Wu, H. Gasdermin D pore structure reveals preferential release of mature interleukin-1. *Nature* **593**, 607-611 (2021).
- Xing, J., Zhou, X., Fang, M., Zhang, E., Minze, L. J., & Zhang, Z. DHX15 is required to control RNA virus-induced intestinal inflammation. *Cell Rep* **35**, 109205 (2021).
- Xu, Q., Rife, C. L., Carlton, D., Miller, M. D., Krishna, S. S., Elsliger, M. A., Abdubek, P., Astakhova, T., Chiu, H. J., Clayton, T., Duan, L., Feuerhelm, J., Grzechnik, S. K., Hale, J., Han, G. W., Jaroszewski, L., Jin, K. K., Klock, H. E., Knuth, M. W., . . . Wilson, I. A. Crystal structure of a novel archaeal AAA+ ATPase SSO1545 from *Sulfolobus solfataricus*. *Proteins* **74**, 1041-1049 (2009).
- Yan, N., Chai, J., Lee, E. S., Gu, L., Liu, Q., He, J., Wu, J. W., Kokel, D., Li, H., Hao, Q., Xue, D., & Shi, Y. Structure of the CED-4-CED-9 complex provides insights into programmed cell death in *Caenorhabditis elegans*. *Nature* **437**, 831-837 (2005).
- Yan, Y., Jiang, W., Liu, L., Wang, X., Ding, C., Tian, Z., & Zhou, R. Dopamine controls systemic inflammation through inhibition of NLRP3 inflammasome. *Cell* **160**, 62-73 (2015).
- Yang, D., He, Y., Munoz-Planillo, R., Liu, Q., & Nunez, G. Caspase-11 Requires the Pannexin-1 Channel and the Purinergic P2X7 Pore to Mediate Pyroptosis and Endotoxic Shock. *Immunity* **43**, 923-932 (2015).
- Yang, J., Liu, Z., & Xiao, T. S. Post-translational regulation of inflammasomes. *Cell Mol Immunol* **14**, 65-79 (2017).
- Yang, X. D., Li, W., Zhang, S., Wu, D., Jiang, X., Tan, R., Niu, X., Wang, Q., Wu, X., Liu, Z., Chen, L. F., Qin, J., & Su, B. PLK4 deubiquitination by Spata2-CYLD suppresses NEK7-mediated NLRP3 inflammasome activation at the centrosome. *EMBO J* **39**, e102201 (2020).
- Yanling, Q., Xiaoning, C., Fei, B., Liyun, F., Huizhong, H., & Daqing, S. Inhibition of NLRP9b attenuates acute lung injury through suppressing inflammation, apoptosis and oxidative stress in murine and cell models. *Biochem Biophys Res Commun* **503**, 436-443 (2018).
- Ye, Z., Lich, J. D., Moore, C. B., Duncan, J. A., Williams, K. L., & Ting, J. P. ATP binding by monarch-1/NLRP12 is critical for its inhibitory function. *Mol Cell Biol* **28**, 1841-1850 (2008).
- Yin, Q., Fu, T. M., Li, J., & Wu, H. Structural biology of innate immunity. *Annu Rev Immunol* **33**, 393-416 (2015).
- Yoneyama, M., & Fujita, T. RNA recognition and signal transduction by RIG-I-like receptors. *Immunol Rev* **227**, 54-65 (2009).
- Yu, J. W., Fernandes-Alnemri, T., Datta, P., Wu, J., Juliana, C., Solorzano, L., McCormick, M., Zhang, Z., & Alnemri, E. S. Pyrin activates the ASC pyroptosome in response to engagement by autoinflammatory PSTPIP1 mutants. *Mol Cell* **28**, 214-227 (2007).
- Zaki, M. H., Vogel, P., Malireddi, R. K., Body-Malapel, M., Anand, P. K., Bertin, J., Green, D. R., Lamkanfi, M., & Kanneganti, T. D. The NOD-like receptor NLRP12 attenuates colon inflammation and tumorigenesis. *Cancer Cell* **20**, 649-660 (2011).
- Zamoshnikova, A., Gross, C. J., Schuster, S., Chen, K. W., Wilson, A., Tacchini-Cottier, F., & Schroder, K. NLRP12 is a neutrophil-specific, negative regulator of in vitro cell migration but does not modulate LPS- or infection-induced NF-kappaB or ERK signalling. *Immunobiology* **221**, 341-346 (2016).

- Zanoni, I., Ostuni, R., Marek, L. R., Barresi, S., Barbalat, R., Barton, G. M., Granucci, F., & Kagan, J. C. CD14 controls the LPS-induced endocytosis of Toll-like receptor 4. *Cell* **147**, 868-880 (2011).
- Zelensky, A. N., & Gready, J. E. The C-type lectin-like domain superfamily. *FEBS J* **272**, 6179-6217 (2005).
- Zhang, A., Xing, J., Xia, T., Zhang, H., Fang, M., Li, S., Du, Y., Li, X. C., Zhang, Z., & Zeng, M. S. EphA2 phosphorylates NLRP3 and inhibits inflammasomes in airway epithelial cells. *EMBO Rep* **21**, e49666 (2020).
- Zhang, B., Chassaing, B., Shi, Z., Uchiyama, R., Zhang, Z., Denning, T. L., Crawford, S. E., Puijssers, A. J., Iskarpatyoti, J. A., Estes, M. K., Dermody, T. S., Ouyang, W., Williams, I. R., Vijay-Kumar, M., & Gewirtz, A. T. Viral infection. Prevention and cure of rotavirus infection via TLR5/NLRC4-mediated production of IL-22 and IL-18. *Science* **346**, 861-865 (2014).
- Zhang, H., & Kurgan, L. Improved prediction of residue flexibility by embedding optimized amino acid grouping into RSA-based linear models. *Amino Acids* **46**, 2665-2680 (2014).
- Zhang, L., Chen, S., Ruan, J., Wu, J., Tong, A. B., Yin, Q., Li, Y., David, L., Lu, A., Wang, W. L., Marks, C., Ouyang, Q., Zhang, X., Mao, Y., & Wu, H. Cryo-EM structure of the activated NAIP2-NLRC4 inflammasome reveals nucleated polymerization. *Science* **350**, 404-409 (2015).
- Zhang, X., & Wigley, D. B. The 'glutamate switch' provides a link between ATPase activity and ligand binding in AAA+ proteins. *Nat Struct Mol Biol* **15**, 1223-1227 (2008).
- Zhang, X., Wu, J., Du, F., Xu, H., Sun, L., Chen, Z., Brautigam, C. A., Zhang, X., & Chen, Z. J. The cytosolic DNA sensor cGAS forms an oligomeric complex with DNA and undergoes switch-like conformational changes in the activation loop. *Cell Rep* **6**, 421-430 (2014).
- Zhang, Z., Meszaros, G., He, W. T., Xu, Y., de Fatima Magliarelli, H., Mailly, L., Mihlan, M., Liu, Y., Puig Gamez, M., Goginashvili, A., Pasquier, A., Bielska, O., Neven, B., Quartier, P., Aebersold, R., Baumert, T. F., Georgel, P., Han, J., & Ricci, R. Protein kinase D at the Golgi controls NLRP3 inflammasome activation. *J Exp Med* **214**, 2671-2693 (2017).
- Zheng, D., Liwinski, T., & Elinav, E. Inflammasome activation and regulation: toward a better understanding of complex mechanisms. *Cell Discov* **6**, 36 (2020).
- Zhong, F. L., Mamai, O., Sborgi, L., Boussofara, L., Hopkins, R., Robinson, K., Szeverenyi, I., Takeichi, T., Balaji, R., Lau, A., Tye, H., Roy, K., Bonnard, C., Ahl, P. J., Jones, L. A., Baker, P. J., Lacina, L., Otsuka, A., Fournie, P. R., . . . Reversade, B. Germline NLRP1 Mutations Cause Skin Inflammatory and Cancer Susceptibility Syndromes via Inflammasome Activation. *Cell* **167**, 187-202 e117 (2016).
- Zhong, Y., Kinio, A., & Saleh, M. Functions of NOD-Like Receptors in Human Diseases. *Front Immunol* **4**, 333 (2013).
- Zhou, M., Li, Y., Hu, Q., Bai, X. C., Huang, W., Yan, C., Scheres, S. H., & Shi, Y. Atomic structure of the apoptosome: mechanism of cytochrome c- and dATP-mediated activation of Apaf-1. *Genes Dev* **29**, 2349-2361 (2015).
- Zhu, Q., & Kanneganti, T. D. Cutting Edge: Distinct Regulatory Mechanisms Control Proinflammatory Cytokines IL-18 and IL-1beta. *J Immunol* **198**, 4210-4215 (2017).
- Zhu, S., Ding, S., Wang, P., Wei, Z., Pan, W., Palm, N. W., Yang, Y., Yu, H., Li, H. B., Wang, G., Lei, X., de Zoete, M. R., Zhao, J., Zheng, Y., Chen, H., Zhao, Y., Jurado, K. A., Feng, N., Shan, L., . . . Flavell, R. A. Nlrp9b inflammasome restricts rotavirus infection in intestinal epithelial cells. *Nature* **546**, 667-670 (2017).

## List of Publications

Hochheiser, I. V., Pils, M., Hagelueken, G., Moecking, J., **Marleaux, M.**, Brinkschulte, R., Latz, E., Engel, C., & Geyer, M. Structure of the NLRP3 decamer bound to the cytokine release inhibitor CRID3. *Nature* **604**, 184-189 (2022). DOI: 10.1038/s41586-022-04467-w

Keuler, T., Ferber, D., **Marleaux, M.**, Geyer, M., & Gutschow, M. Structure-Stability Relationship of NLRP3 Inflammasome-Inhibiting Sulfonylureas. *ACS Omega* **7**, 8158-8162 (2022). DOI: 10.1021/acsomega.2c00125

Keuler, T., Gatterdam, K., Akbal, A., Lovotti, M., **Marleaux, M.**, Geyer, M., Latz, E., & Gutschow, M. Development of Fluorescent and Biotin Probes Targeting NLRP3. *Front Chem* **9**, 642273 (2021). DOI: 10.3389/fchem.2021.642273

**Marleaux, M.**, Anand, K., Latz, E., & Geyer, M. Crystal structure of the human NLRP9 Pysin domain suggests a distinct mode of inflammasome assembly. *FEBS Lett* **594**, 2383-2395 (2020). DOI: 10.1002/1873-3468.13865